ASME
SETTING THE STANDARD

Transactions of the ASME, Journal of Fluids Engineering
(ISSN 0098-2202) is published monthly by
The American Society of Mechanical Engineers,
Three Park Avenue, New York, NY 10016.
Periodicals postage paid at New York, NY
and additional mailing offices.
POSTMASTER: Send address changes to Transactions of the
ASME, Journal of Fluids Engineering, c/o THE AMERICAN
SOCIETY OF MECHANICAL ENGINEERS,
22 Law Drive, Box 2300, Fairfield, NJ 07007-2300.
CHANGES OF ADDRESS must be received at Society
headquarters seven weeks before they are to be effective.
Please send old label and new address.

Journal of Fluids Engineering

Published Monthly by ASME

VOLUME 131 • NUMBER 6 • JUNE 2009

RESEARCH PAPERS

Flows in Complex Systems

Fundamental Issues and Canonical Flows

Multiphase Flows

Techniques and Procedures

TECHNICAL BRIEFS

(Contents continued on inside back cover)

This journal is printed on acid-free paper, which exceeds the ANSI Z39.48-1992 specification for permanence of paper and library materials. ♾™
♻ 85% recycled content, including 10% post-consumer fibers.

(Contents continued)

ERRATA

The ASME Journal of Fluids Engineering is abstracted and indexed in the following:

Applied Science & Technology Index, Chemical Abstracts, Chemical Engineering and Biotechnology Abstracts (Electronic equivalent of Process and Chemical Engineering), Civil Engineering Abstracts, Computer & Information Systems Abstracts, Corrosion Abstracts, Current Contents, Ei EncompassLit, Electronics & Communications Abstracts, Engineered Materials Abstracts, Engineering Index, Environmental Engineering Abstracts, Environmental Science and Pollution Management, Excerpta Medica, Fluidex, Index to Scientific Reviews, INSPEC, International Building Services Abstracts, Mechanical & Transportation Engineering Abstracts, Mechanical Engineering Abstracts, METADEX (The electronic equivalent of Metals Abstracts and Alloys Index), Petroleum Abstracts, Process and Chemical Engineering, Referativnyi Zhurnal, Science Citation Index, SciSearch (The electronic equivalent of Science Citation Index), Shock and Vibration Digest, Solid State and Superconductivity Abstracts, Theoretical Chemical Engineering

Systematic Approaches for Design of Distribution Manifolds Having the Same Per-Port Outflow

Andrew W. Chen
3M Company,
Building 260-6N-04,
St. Paul, MN 55144
e-mail: awchen@mmm.com

Ephraim M. Sparrow
Mechanical Engineering,
University of Minnesota,
Minneapolis, MN 55455
e-mail: esparrow@umn.edu

Two geometric modalities were investigated to determine their effects on the degree of uniformity of the flow issuing from a manifold through a discrete set of exit ports. The goal of the investigation was to demonstrate how these geometric parameters can be used to achieve a high degree of exit-flow uniformity. The first investigated modality is the area ratio, which compares the total outflow area of all the exit ports with the cross-sectional area of the manifold. The second modality is the extent of pressure loading downstream of the exit ports of the manifold. The investigation was facilitated by numerical simulation for which an appropriate turbulence model was used. Three parameters were varied during the course of the research: (a) the area ratio, (b) the downstream pressure loading characterized by the length-to-diameter ratio of the outflow tubes that are attached to the exit ports, and (c) the Reynolds number. It was found that the area ratio parameter had a marked effect on the uniformity of the outflow from the manifold. Quantitative values of the area ratio corresponding to specified degrees of uniformity (i.e., 2%, 5%, and 10%) were identified. This information can be used as a guideline for manifold design. The imposition of the downstream pressure loading was also demonstrated to have a significant effect on the degree of uniformity, but that effect was not as strong as the effect of the area ratio. The manifold pressure was found to increase from the inlet of the manifold to the downstream end of the manifold. The direction of the jetlike discharge from the exit ports of the manifold into a large collection domain was found to vary along the length of the manifold, with inclined jets emanating from the upstream end and perpendicular jets at the downstream end. Over the range of investigated Reynolds numbers, from 40,000 to 200,000, the degree of uniformity of the mass effusion from the exit ports was found to be unaffected. The results of the numerical simulations were confirmed by experiments. [DOI: 10.1115/1.3111256]

1 Introduction

One of the most commonly encountered problems in fluid mechanics is the *manifold problem*. There are two types of manifolds: the distribution manifold and the collection manifold. A distribution manifold usually has a single inlet and multiple exits. An ideal distribution manifold is one having the same flow rate at each exit port of the manifold. In contrast, a collection manifold has numerous inlets and a single exit. In a system consisting of a distribution manifold, a collection manifold, and interconnecting ducts, the collection manifold must be taken into account in the design of an ideal or near-ideal distribution manifold.

The focus of this paper is to investigate two methodologies for attainment of ideal performance of distribution manifolds. These methodologies include: (a) varying the ratio of the total cross-sectional area of the exit ports to the cross-sectional area of the manifold and (b) increasing the pressure drop in the ducting system, which is situated downstream of the distribution manifold (downstream pressure loading).

Collection manifolds may be encountered in various types. For example, the discharge from the interconnecting ducts may create an array of jets whose impingement on an elevated-temperature surface creates an effective cooling modality. The space through which the jets pass may be regarded as a collection manifold. In this case, the discharge passes into a zone of relatively constant pressure.

There is an extensive literature describing a variety of approaches to the manifold problem. The quantitative history of manifold design may be traced back to the 1950s. Several decades thereafter, and to a lesser extent even up to the present era, one-dimensional models have been used extensively for the design of manifolds [1–11]. The use of a one-dimensional approach to model a situation that is intrinsically three-dimensional requires many simplifying assumptions that may compromise the accuracy of the obtained results. Therefore, in more recent times, numerical simulation has been used in manifold design.

Among the new technologies in which manifolds play an essential role is the fuel cell [12–16]. The advent of microfabrication techniques has enabled the creation of microdimensional fluid-flow devices that involve manifolds [17–25]. Chemical assessment, analysis, and reaction devices frequently make use of fluid-flow manifolds [26,27]. The most enduring and still the most common application of manifolds is in automotive and other propulsion devices [28–34]. Manifolds are widely used for flow distribution and collection in heat exchangers [18,35,36]. Polymer processing equipment may also incorporate manifolds for the distribution of the liquid melt in dies [37]. This literature review underscores the importance of manifolds in contemporary technologies and testifies to the need for continuous research.

2 Physical Description of the Modalities for Attainment of Exit Flow Uniformity

The physical system to be investigated here is shown schematically in Fig. 1. As seen in the figure, the system consists of a development region, which delivers fully developed flow to a distribution manifold whose length is 724 mm. The manifold encompasses an array of 39 circular exit ports, with a center-to-center distance of 19.05 mm. These exit ports may be mated to outflow

Contributed by the Fluids Engineering Division of ASME for publication in the JOURNAL OF FLUIDS ENGINEERING. Manuscript received January 18, 2008; final manuscript received November 29, 2008; published online May 13, 2009. Assoc. Editor: Zvi Rusak.

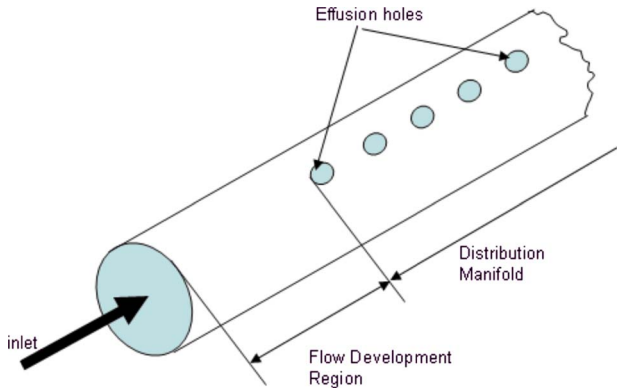

Fig. 1 Schematic of the physical system

tubes which convey the discharge of the distribution manifold to the inlet ports of a collection manifold. This arrangement is shown schematically in Fig. 2.

The first approach to the attainment of the same outflow from all the exit ports is to vary the ratio of the exit ports' cross-sectional area to the manifold's cross-sectional area. This variation was achieved by varying the diameter of the manifold while the number and diameter of the exit ports were held fixed at 6 mm. The area ratios investigated are 0.695, 0.538, 0.345, and 0.135.

The second approach to the attainment of near-ideal performance of a distribution manifold is the tailoring of the pressure drop downstream of the exit ports. The tailoring is based on the hypothesis that per-port outflow uniformity can be achieved when the internal end-to-end pressure rise in the manifold is small compared with the pressure drop, which the flow experiences as it passes through a piping system downstream of the manifold. The investigation of this approach is to be performed by systematically varying the length-to-diameter ratio of the tubes, which interconnect the distribution and collection manifolds. In practice, if the flow in the tubes emerges into a free space instead of being discharged into a collection manifold, the jets thus exposed may serve in applications involving impingement heat transfer.

A schematic, which identifies the parameters relevant to the numerical simulation, is presented in Fig. 3. That figure shows a cross-sectional cut across the manifold and through a representative exit port that is fitted with an outflow tube. The internal diameter of the distribution manifold is denoted by D, and the diameter of the circular exit port and the outflow tube is d. Additionally, the thickness of the wall of the manifold is t, and the axial length of the outflow tube is denoted by £. Note that £ is measured outward from the interior wall of the manifold. The ratio $£/d$ was varied systematically, which resulted in a systematic variation in the pressure drop downstream of the collection manifold. The smallest possible value of $£/d$ is t/d, which, for the case under consideration, is 0.532. All told, the investigated values of $£/d$ encompassed 0.532, 5, 15, and 45.

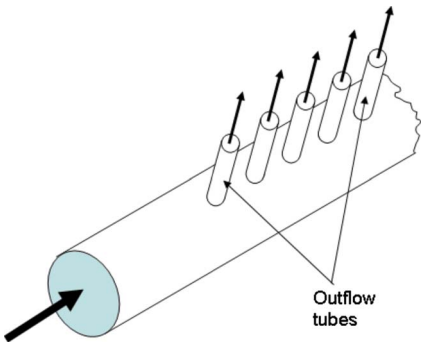

Fig. 2 The distribution manifold fitted with outflow tubes to convey its discharge to a collection manifold

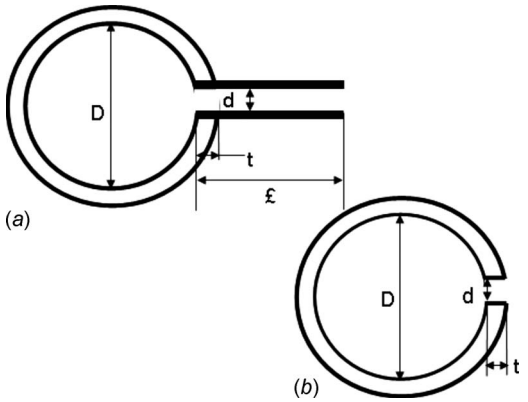

Fig. 3 Cross-sectional views revealed by a plane perpendicular to the axis of the distribution manifold: (*a*) view with an outlet tube in place and (*b*) view without an outlet tube

3 Governing Equations for Turbulent Flow in a Pipe

For the majority of applications involving manifolds, the flow is turbulent. Therefore, it is necessary to use a form of the Navier–Stokes equations that encompasses turbulence. One such form is the so-called Reynolds-averaged Navier–Stokes (RANS) equations. For an incompressible constant-properties flow, these equations are

For the x-momentum,

$$\rho\left[\frac{\partial}{\partial x}(u^2)+\frac{\partial}{\partial y}(uv)+\frac{\partial}{\partial z}(uw)\right]=-\frac{\partial p}{\partial x}+\frac{\partial}{\partial x}\left(\mu_{\text{eff}}\frac{\partial u}{\partial x}\right)+\frac{\partial}{\partial y}\left(\mu_{\text{eff}}\frac{\partial u}{\partial y}\right)+\frac{\partial}{\partial z}\left(\mu_{\text{eff}}\frac{\partial u}{\partial z}\right) \tag{1}$$

Fot the y-momentum,

$$\rho\left[\frac{\partial}{\partial x}(vu)+\frac{\partial}{\partial y}(v^2)+\frac{\partial}{\partial z}(vw)\right]=-\frac{\partial p}{\partial y}+\frac{\partial}{\partial x}\left(\mu_{\text{eff}}\frac{\partial v}{\partial x}\right)+\frac{\partial}{\partial y}\left(\mu_{\text{eff}}\frac{\partial v}{\partial y}\right)+\frac{\partial}{\partial z}\left(\mu_{\text{eff}}\frac{\partial v}{\partial z}\right) \tag{2}$$

For the z-momentum,

$$\rho\left[\frac{\partial}{\partial x}(wu)+\frac{\partial}{\partial y}(wv)+\frac{\partial}{\partial z}(w^2)\right]=-\frac{\partial p}{\partial z}+\frac{\partial}{\partial x}\left(\mu_{\text{eff}}\frac{\partial w}{\partial x}\right)+\frac{\partial}{\partial y}\left(\mu_{\text{eff}}\frac{\partial w}{\partial y}\right)+\frac{\partial}{\partial z}\left(\mu_{\text{eff}}\frac{\partial w}{\partial z}\right) \tag{3}$$

In these equations, u, v, and w are the velocity components; x, y, and z are the Cartesian coordinates; ρ is the density; and μ_{eff} is the effective viscosity defined as

$$\mu_{\text{eff}}=\mu+\mu_t \tag{4}$$

where μ is the molecular viscosity, and μ_t is the so-called turbulent viscosity. In the vast majority of turbulence models, the turbulent viscosity μ_t is taken to be isotropic.

In addition to momentum conservation, represented by Eqs. (1)–(3), the flow must obey conservation of mass, which is

$$\frac{\partial u}{\partial x} + \frac{\partial v}{\partial y} + \frac{\partial w}{\partial z} = 0 \tag{5}$$

The numerical solutions were executed by means of FLUENT 6.8.

3.1 Turbulence Models. A central issue, which has a major impact on the accuracy of the results extracted from the numerical simulations, is the appropriateness of the selected turbulence model. In simple flows, it is well established that results of adequate accuracy can be obtained by using any one of several turbulence models. In complex flows, such as that being considered here, great care must be taken to establish the appropriateness of the turbulence model. To this end, the authors have performed experiments that serve to discriminate among the available models [38]. For that study, three models were used to generate solutions for flow in a multi-exit manifold. The outcome of that study was that the realizable k-ε (REAL) model provided results that best matched the experimental data. Consequently, the realizable k-ε will be used here.

3.2 Boundary Conditions and Solution Domain. The solution domain is that space in which the numerical computations are performed. The selection of the domain is tightly linked to the specification of the boundary conditions because it is on the surfaces of the solution domain that boundary conditions are specified. Therefore, it is necessary first to establish where there are known boundary conditions and then to use that information to select the solution domain. Another factor in the selection of the solution domain is the storage capacity of the computer and the time required to achieve a converged solution. These factors become important when a very large solution domain is selected.

If reference is made to Fig. 1, it can be envisioned that jets emerge from the exit ports into the surrounding environment. By the same token, jets can also be envisioned emerging from the downstream ends of the outflow tubes. From the standpoint of economical use of computational resources, there is a temptation to close the solution domain at the outlets of the exit ports of Fig. 1. In the case of Fig. 2, a similar temptation would be to close the solution domain at the ends of the outlet tubes. The boundary conditions that might be assigned at those locations would be a pressure equal to the ambient pressure. The assignment of the ambient pressure at those locations begs the question about whether the mixing, which takes place as the jets mix with the ambient air, can have a substantial effect on the state of the fluid leaving the exit ports or the ends of the outlet tubes. To address this question, a systematic study was made in which the location of the solution domain closure was varied. That variation first assumed that the domain closed at the exit cross sections and subsequently at the locations farther and farther away from the exits. The effect of these different placements on the mass flow rates emerging from the manifold was carefully monitored. It was found that within plotting accuracy (1/2%), the mass flow rates were independent of the locations of the closure of the solution domain.

Once the solution domain placement had been established, boundary conditions could be assigned. The upstream end of the solution domain was at the cross section of the inlet of the flow development region. The length of the flow development region was chosen to ensure that the flow was fully developed at the inlet cross section of the manifold. With regard to the downstream end of the solution domain, there are two cases to consider—that in the absence of downstream loading and that of the presence of downstream loading. For the former, the standard no-slip and impermeability conditions were imposed. In the case of the latter, the discussion conveyed in the preceding paragraph applies. All other surfaces of the solution domain coincided with the solid walls of the manifold and of the outlet tubes.

The prescribed inlet boundary condition was a uniform velocity chosen so as to yield preselected values of the Reynolds number. The outlet boundary conditions encompassed the prescribed ambient pressure plus zero derivatives of the dependent variables in the streamwise direction. Finally, the no-slip and impermeability conditions were applied at all solid surfaces.

3.3 Accuracy and Convergence. In order to achieve the requisite accuracy, the discretization of the solution domain required use of a very large number of elements. As will be discussed shortly, a number of geometries of varying complexities were dealt with. For the most complex of these, about 3,500,000 elements were employed, while for the simplest geometry, approximately 1,500,000 were used. A mesh independence study was made to ensure the adequacy of these discretizations. To this end, the number of elements was reduced by a factor of 8 relative to the maximum element numbers. When the results for the two meshes were plotted, they fell on top of each other.

The convergence of the numerical solutions was examined by monitoring the values of a key parameter during the course of the iterative solution protocol. The parameter chosen for this study was the mass flow rates at the individual exits. The iterations were continued until these quantities became constant within 0.1%.

4 Results and Discussion

The quantity of most immediate practical interest is the streamwise distribution of the exit-port mass flow rates. In particular, the impact of the two modalities, exit-to-manifold area ratio and downstream pressure loading, on the degree of uniformity of the exit-port flow rates will be examined in detail. Furthermore, a complete characterization of the fluid efflux from the exit ports includes the departure angle, as well as the magnitude of the outflow. Consequently, the departure angles will be displayed as a function of the same two parameters that are used for the characterization of the magnitude of the outflow. A second focus of the presentation of the results is the streamwise pressure variation within the manifold, as well as the overall pressure difference across the system as a whole. Finally, key features of the flow field will be exhibited to provide physical insights to the manifold problem. The accuracy of the numerical predictions is confirmed by experiments described in Sec. 5 of this paper.

4.1 Streamwise Variations in the Per-Exit-Port Flow Rate.

4.1.1 Without Downstream Loading. Attention will first be focused on the effect of the area ratio $A_{\text{ports}}/A_{\text{manifold}}$ on the per-exit-port flow rate. This information is presented in Fig. 4 for an intermediate value of the Reynolds number, Re=110,000. The effect of the Reynolds number will be displayed shortly. The ordinate of Fig. 4 is the ratio of per-port mass flow rate to the average mass flow rate corresponding to a uniform prorating of the total flow among the individual ports. The abscissa is the axial distance along the length of the manifold, with $x=0$ corresponding to the location of the first exit port and $x=L$ corresponding to the location of last port. The results that are displayed in Fig. 4 and in subsequent figures are shown as continuous curves since, had they been plotted as discrete points, the points would form a more-or-less continuous curve.

Inspection of the figure reveals the area ratio $A_{\text{ports}}/A_{\text{manifold}}$ has a marked effect on the degree of uniformity of the effusing flow rate. As the area ratio decreases, the rate of efflux becomes more and more uniform. In particular, for the smallest area ratio of the 0.135, uniformity to within $\pm 2\%$ is achieved.

The solid lines displayed in the figure correspond to the original manifold configuration equipped with 39 exit ports, and the indicated area ratios correspond to that situation. Upon completion of the numerical simulations for that situation, it was deemed appropriate to seek to evaluate the universality of the results. To that end, a manifold of the same length as that of the original manifold was considered, but with 19 exit ports instead of the original 39. The results for that case are displayed as a dashed line in the figure. Attention will first be focused on the results for the 39-exit manifold, and the significance of the dashed curve will be dis-

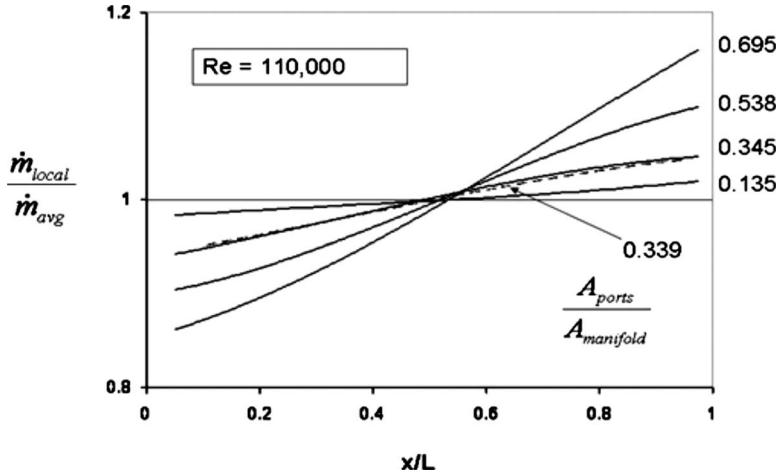

Fig. 4 Streamwise distribution of the rate of fluid flow effusing from individual exit ports, Re=110,000

cussed thereafter.

From the standpoint of practice, it is convenient to have a guideline (a *rule of thumb*) for selecting a value of the area ratio that would provide a nearly uniform efflux. For most practical purposes, a streamwise variation in the efflux that is equal to or less than $\pm 5\%$ is sufficient. With this criterion, Fig. 4 indicates that

$$\frac{A_{\text{ports}}}{A_{\text{manifold}}} \leq 0.35 \tag{6}$$

is a suitable criterion.

Attention will now be turned to the dashed line displayed in Fig. 4. As was noted earlier, the manifold represented by that line is different from the manifold that corresponds to the other curve in the figure. The area ratio for the alternative manifold is virtually identical to that of one of the cases for the original manifold. Despite the differences in the geometries of the two manifolds, which have a common area ratio, the distributions of the per-port mass flow rates are virtually the same. This finding suggests that the results conveyed in Fig. 4 may be more universal than might have been expected on the basis of their origins.

The effect of the Reynolds number on the $\dot{m}_n/\dot{m}_{\text{avg}}$ ratio will now be considered. This effect is examined for the two extreme area ratios among those investigated, $A_{\text{ports}}/A_{\text{manifold}}=0.135$ and 0.695. These results are conveyed in Fig. 5 for both area ratios. For $A_{\text{ports}}/A_{\text{manifold}}=0.135$, the Reynolds-number-related deviations are on the order of $\frac{1}{2}\%$, while those for the $A_{\text{ports}}/A_{\text{manifold}}=0.695$ manifold are about 1%. This outcome serves to generalize the results since, at minimum, it is assured that the results of Fig. 4 for Re=110,000 are applicable for all Reynolds numbers in the range from 40,000 to 200,000. It also suggests that moderate extrapolation outside of this Reynolds number range can be made.

The final quantity for which results are to be presented in this section of the paper is the relationship between the total mass flow rate $\dot{m}_{\text{tot}}$, which is distributed by the manifold, and the overall pressure drop, which is responsible for creating that mass flow rate. This information is displayed in Fig. 6, where the overall pressure drop is plotted on the ordinate and $\dot{m}_{\text{tot}}$ is represented on the abscissa. The discrete data points correspond to Reynolds numbers of 40,000, 110,000, and 200,000 and to area ratios $A_{\text{ports}}/A_{\text{manifold}}=0.135$, 0.345, 0.538, and 0.695. Inspection of the figure shows that despite the wide ranges of the Reynolds number and the area ratio, all of the results fall on a common correlating line, suggesting that the results are universal. Indeed, the correlation factor $R^2=1$. The equation for the correlating line is

$$p - p_{\text{amb}} = (775{,}553)(\dot{m}^2) \tag{7}$$

In particular, the equation indicates that the overall pressure drop depends on the square of the mass flow rate. This dependence is indicative of the dominance of inertial losses.

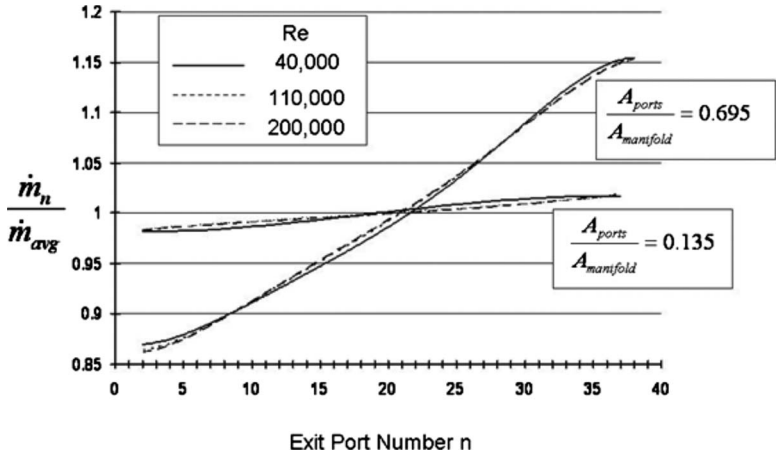

Fig. 5 Effect of Reynolds number on the streamwise variation in the per-port effusing mass flow rate, $A_{\text{ports}}/A_{\text{manifold}}=0.135$ and 0.695

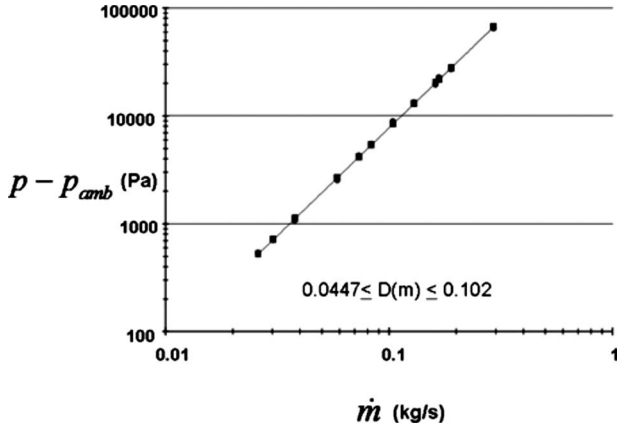

Fig. 6 Relationship between the overall pressure difference and the total mass flow rate for Re=40,000, 110,000, and 200,000 and for $A_{ports}/A_{manifold}$ between 0.135 and 0.695

4.1.2 With Downstream Loading. As was set forth in Sec. 1, the second approach to the attainment of outflow uniformity is to increase the pressure drop downstream of the exit ports. A method of attaining downstream loading is to affix outflow tubes to the exit ports of the manifold, as illustrated in Fig. 2. To parametrize the downstream pressure drop, the length-to-diameter ratio £/d, where £ and d are defined in Fig. 3, is used. Since the wall thickness of the manifold proper provides a minimum value of £, the parameterization starts with the £/d for the wall itself. Subsequently, outflow tubes of various lengths were added to the parametrization. The values of £/d resulting from this approach are 0.564, 5, 15, and 45. The per-port outflows for these cases were monitored and the results are brought together in Fig. 7. The figure corresponds to the area ratio $A_{ports}/A_{manifold}=0.695$. This case was chosen for presentation because in the absence of downstream loading, it displayed the largest variation in $\dot{m}_n/\dot{m}_{avg}$. The figure addresses the extent to which downstream loading reduces that variation.

Figure 7 displays distributions of the $\dot{m}_n/\dot{m}_{avg}$ ratio whose general shape mirrors that of Fig. 4. There are, however, important differences in detail. The most significant of these differences is that the smallest departures of the $\dot{m}_n/\dot{m}_{avg}$ ratio from 1.0 that were achieved due to $A_{ports}/A_{manifold}$ are not attained with increasing £/d ratio. As can be seen from Fig. 7, the smallest deviations from 1.0 are approximately 5%, whereas those displayed in Fig. 4 are approximately 2%. Although it may be argued that further increases in £/d might be successful in driving the $\dot{m}_n/\dot{m}_{avg}$ ratio to smaller deviations from 1.0, it is believed that using values of £/$d>45$ would be unacceptable in practical applications. On this basis, it may be concluded that the variations in $A_{ports}/A_{manifold}$ are a more suitable way to achieve uniformity of the per-port mass flow rate than are variations in £/d.

The results of Fig. 7 are specific to Re=110,000. The effect of varying the Reynolds number is presented in Fig. 8. The figure makes the clear statement that the $\dot{m}_n/\dot{m}_{avg}$ distributions are, for all practical purposes, independent of the Reynolds number. This conclusion is not limited to specific values of $A_{ports}/A_{manifold}$ and of £/d that parametrize Fig. 8: rather, it applies to all of the cases considered here.

4.2 In-Manifold Pressure Variations.

4.2.1 Without Downstream Loading. It was demonstrated in the preceding section that the mass flow rate emanating from the exit ports increases in the direction from the manifold inlet to its downstream end. This trend is reinforced by examination of the pressure variations along the length of the manifold. Figure 9 conveys this information for the various area ratios $A_{ports}/A_{manifold}=0.135$, 0.345, 0.538, and 0.695. The plotted results correspond to Re=110,000; however, it will soon be demonstrated that the trends that are in evidence in Fig. 9 are applicable to a wide range of Reynolds numbers. The most noteworthy observation that can be extracted from the figure is that there is a streamwise *pressure rise* along the manifold. This observation has been verified by the authors by means of experimental data. In those experiments, described in Ref. [38], a cylindrical-pipe manifold fitted with an array of exit ports of rectangular shape was utilized. Axial pressure distributions were measured and reported in Fig. 5 of Ref. [38]. Figure 5 clearly shows that the pressure increases with increasing downstream distances from the inlet of the manifold.

A qualitative explanation of the axial pressure rise can be offered on the basis of momentum considerations. From a simple balance of momentum transport and forces, it can be shown that the pressure variation along the length of the manifold is impacted by friction, which causes a pressure drop, and deceleration, which causes a pressure rise. From the numerical evidence offered here, as well as the experimental evidence offered in Ref. [38], it is clear that the deceleration-based pressure rise dominates the friction-based pressure drop.

The finding that a fluid can flow from a zone of lower pressure to a zone of higher pressure is by no means novel. For such a flow

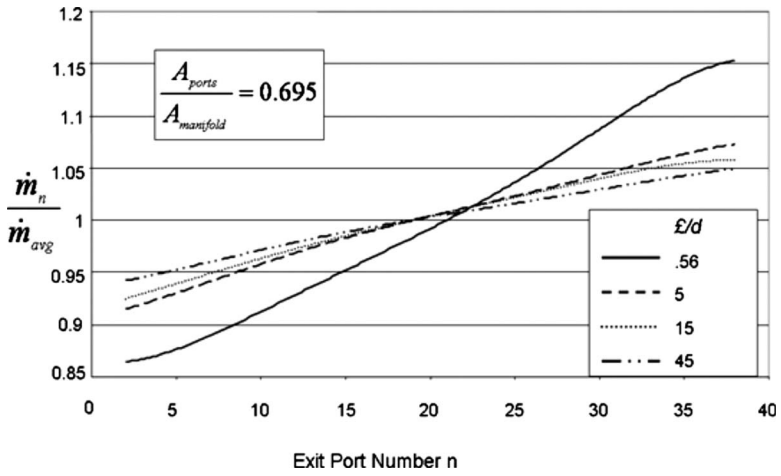

Fig. 7 Effect of the £/d ratio of the outflow tubes on the streamwise variation in the per-port mass flow rate, Re=110,000 and $A_{ports}/A_{manifold}=0.695$

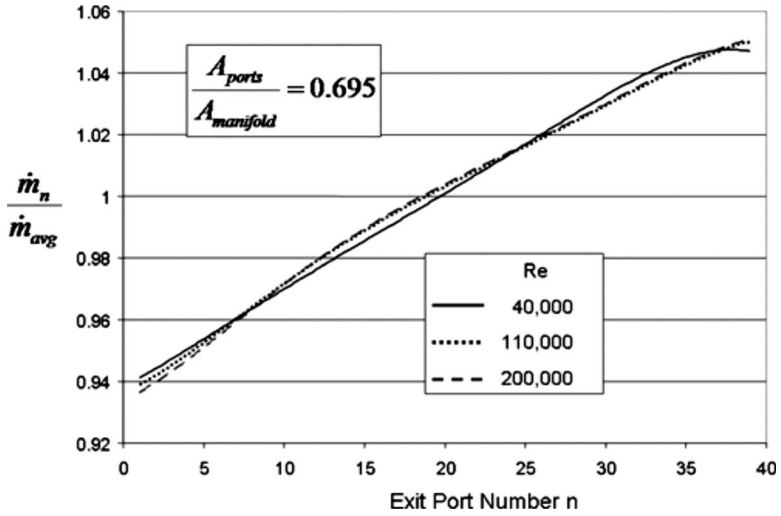

Fig. 8 Effect of the Reynolds number on the streamwise distribution of the per-port mass flow rate, £/d=45 and $A_{ports}/A_{manifold}$=0.695

to occur, it is only necessary that the flow possesses sufficient momentum to overcome the adverse pressure gradient. For example, in the classic situation of a cylinder in crossflow, the turbulent boundary does not separate until the angular position of 120 deg with respect to the forward stagnation point is reached. The momentum possessed by the turbulent boundary layer is sufficient to overcome the adverse pressure gradient, which is in effect at angular positions greater than 90 deg.

Further inspection of Fig. 9 indicates that the larger the area ratio, the larger is the pressure rise. To rationalize this finding, it is first relevant to note that all the cases appearing in Fig. 9 correspond to the same Reynolds number at the inlet of the manifold. Since ρ and μ are constant, it follows that a constant Reynolds number means that the product $\bar{U}D$ is also constant, where $\bar{U}$ is the mean velocity at the inlet, and D is the diameter of the manifold. Therefore, the smaller the pipe diameter, the larger is the mean velocity $\bar{U}$, and for future reference, $\bar{U}^2$ is inversely proportional to D^2.

Next, it may be noted that the area ratio $A_{ports}/A_{manifold}$ is, for the case A_{ports}=constant, also inversely proportional to D^2. Then, it follows that $\bar{U}^2$ is proportional to the area ratio $A_{ports}/A_{manifold}$. If attention is now focused on the momentum-based pressure rise in the absence of friction, a momentum balance gives that the pressure rise is, approximately, proportional to the difference between the value of $\bar{U}^2$ at the inlet to the manifold and the value of $\bar{U}^2$ at the downstream end of the manifold. Since the latter is essentially zero, it follows that the momentum-based pressure rise is proportional to the manifold-inlet value of $\bar{U}^2$. This hypothesis is supported by Fig. 6.

The foregoing argument only requires that the momentum be zero at the downstream end of the manifold, but the means by which that state is attained is not relevant to the argument.

Since $\bar{U}^2$ is proportional to the area ratio $A_{ports}/A_{manifold}$, it follows that the momentum-based pressure rise should be proportional to the area ratio. This outcome, which has been deduced here by means of physical reasoning, is numerically verified by making use of the information conveyed by Fig. 9. The excellent agreement of the simulation-based result with the physical-based deduction adds strong support to the simulation model and its implementation.

4.2.2 With Downstream Loading. Attention will now be turned to the in-manifold pressure variation for the case in which downstream pressure loading is applied by means of outflow tubes of different length characterized parametrically by £/d. The numerical simulation provides information for the response of the in-manifold pressure variations to various magnitudes of downstream pressure loading. These results are conveyed by Fig. 10, the format of which is identical to that of Fig. 9. The figure shows that the end-to-end pressure rise is nearly identical for all of the various downstream loadings. This outcome can be rationalized by the argument that was used in the forgoing to predict the pressure rise in the presence of different values of the area ratio $A_{ports}/A_{manifold}$. That argument indicates that the pressure rise is directly proportional to the value of $\bar{U}^2$ at the inlet of the manifold. Since the value of $\bar{U}^2$ at the inlet is not affected by the extent of the downstream pressure loading, it follows that the in-manifold pressure rise should not depend on £/d.

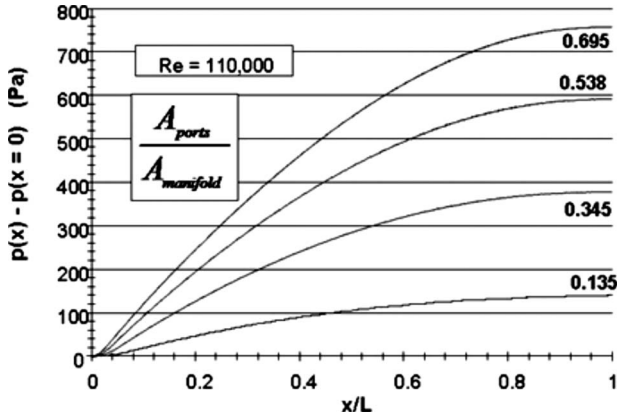

Fig. 9 Streamwise variations in the manifold pressure for various area ratios $A_{ports}/A_{manifold}$=0.135, 0.345, 0.538, and 0.695 and for Re=110,000

4.3 Departure Angles of Fluid Leaving the Exit Ports. Another measure of the performance of the manifold is the angle at which the jets effuse from the exit ports in the absence of downstream loading. Of particular relevance is the dependence of the departure angle on the streamwise position of the exit port (exit-port number n) and on the area ratio $A_{ports}/A_{manifold}$. Figure 11 compares the departure angles at the upstream end of the manifold (n=1, 2, and 3) for the lowest and highest values of the area ratio,

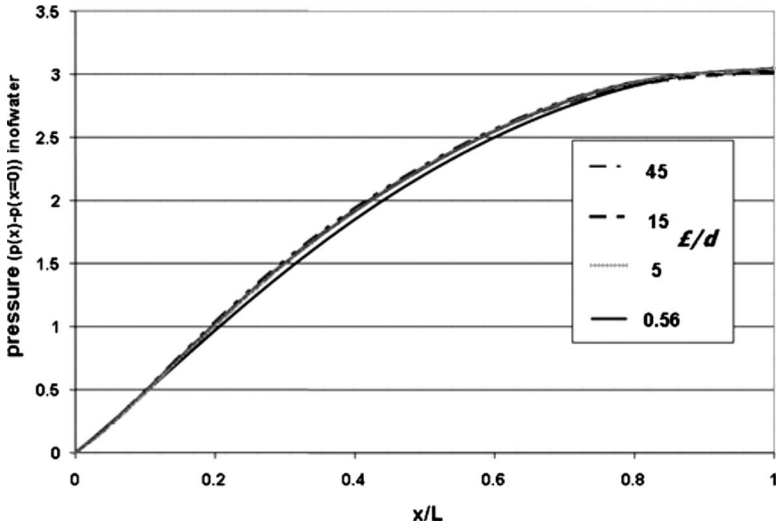

Fig. 10 Streamwise variations in the manifold pressure for £/d=0.564, 5, 15, and 45 and for Re=110,000

0.135 and 0.695. This information is presented in Fig. 11, with the (a) part corresponding to the higher value of the area ratio and with the (b) part corresponding to the lower value. In appraising the information conveyed in Fig. 11, it is important to note that the direction of fluid flow is from left to right. Not unexpectedly, the direction of the effusing flow is somewhat inclined with respect to the axis of the ports. The degree of inclination reflects the streamwise momentum that is carried out of the manifold through the respective ports. Of practical importance is the fact that for the smaller-area-ratio case, 0.135, the direction of the flow effusing from a port is nearly parallel to the axis of the port. On the other hand, for the higher-area-ratio case, 0.695, there is a significant inclination.

Attention is next turned to the variation in the departure angles as a function of the streamwise position of the exit ports. To this end, information similar to that of Fig. 11, but information for ports 37– 39 is presented in Fig. 12. As before, the (a) part of the figure is for the area ratio of 0.695 and the (b) part of the figure is for the area ratio of 0.135. An overall appraisal of Fig. 12 indicates an outflow that is more or less aligned with the axis of the port. This conclusion appears to be valid for both of the area ratios. When Figs. 11 and 12 are taken together, it may be concluded there is a significant evolution in the departure angle as a function of the exit-port number for the area ratio of 0.695. The evolution is such that the initial off-axis departure tends more and more toward on-axis departure. On the other hand, for the area ratio of 0.135, there is little evolution of the departure angle along the length of the manifold since the initial departure angles are nearly axial.

In practice, knowledge of the departure angles has relevance to impingement jet heat transfer. In that regard, it is known that perpendicular impingement provides the highest heat transfer coefficient relative to impingement at nonperpendicular angles.

5 Comparison With Experimental Data

To confirm the accuracy of the numerical simulations, experiments have been performed for a representative case. This case is characterized by $A_{\text{ports}}/A_{\text{manifold}}$=0.695 without downstream loading. The experiments were performed with air for two Reynolds numbers, 40,000 and 110,000. The fluid velocities were such that the Mach number was less than 0.1, so that compressibility was not a factor.

The experimental data are compared with the numerical predictions in Fig. 13. It can be clearly seen from the figure that the predictions are in excellent agreement with the data.

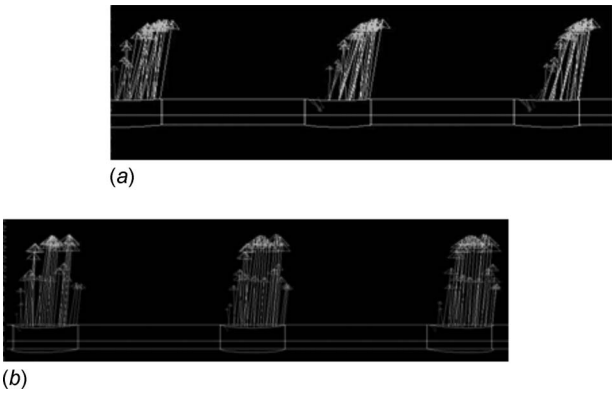

Fig. 11 Departure angles at exit ports 1, 2, and 3; (*a*) $A_{\text{ports}}/A_{\text{manifold}}$=0.695 and (*b*) $A_{\text{ports}}/A_{\text{manifold}}$=0.135; Re =110,000

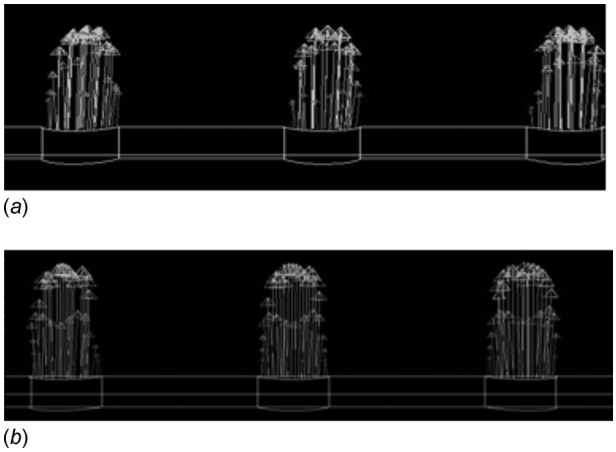

Fig. 12 Departure angles at exit ports 37, 38, and 39; (*a*) $A_{\text{ports}}/A_{\text{manifold}}$=0.695 and (*b*) $A_{\text{ports}}/A_{\text{manifold}}$=0.135; Re =110,000

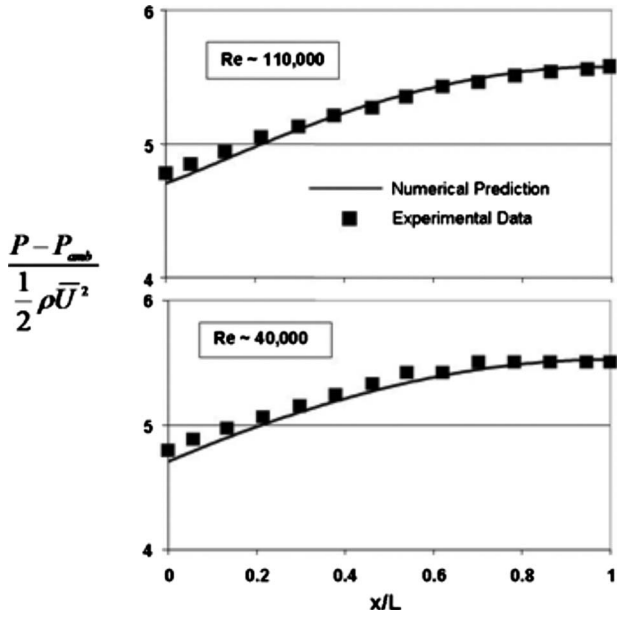

Fig. 13 Comparison of numerical predictions for $A_{ports}/A_{manifold}=0.695$ without downstream loading with experimental data

6 Concluding Remarks

The goal of this investigation was to quantitatively explore the use of two modalities for designing distribution manifolds, which provide uniform effusion of mass through all the exit ports. The two investigated modalities are (a) variations in the magnitude of the area ratio $A_{ports}/A_{manifold}$ and (b) varying the pressure loading downstream of the manifold exits by means of the magnitude of $£/d$. In these parameters, A_{ports} is the total cross-sectional area through which the fluid exits the manifold, and $A_{manifold}$ is the cross-sectional area of the manifold. In addition, £ is the length of the outflow tubes attached to the each of the exit ports, and d is the diameter of these tubes.

The investigation was facilitated by numerical simulation. In common with the conditions encountered in most engineering applications, the flow was regarded as turbulent. The selection of an appropriate turbulence model for flows in manifolds is a critical issue. A careful study of various candidate turbulence models was performed in Ref. [38]. It was found there that from among three candidate models, the realizable k-ε (REAL) model provided results, which were in best agreement with experimental data. The area ratio $A_{ports}/A_{manifold}$ was varied over the range from 0.135 to 0.695, and the downstream pressure loading parameter was varied by means of the $£/d$ ratio over the range from 0.564 to 45. The effect of the Reynolds number at the inlet of the manifold on the results was investigated by extending the calculations over the Reynolds number range from 40,000 to 200,000.

The results of the numerical simulations in the absence of downstream loading enabled quantitative evaluations of the effect of the foregoing parameters on the degree of uniformity of the mass outflow from the exit ports. For the area ratio cases, it was found that mass outflow uniformity of $\pm 2\%$ could be achieved by use of $A_{ports}/A_{manifold}=0.14$. Uniformity to $\pm 5\%$ and $\pm 10\%$ could be obtained for area ratios of 0.35 and 0.54, respectively. These results provide definitive information for manifold design in general.

The effect of downstream loading on the uniformity of the outflow was also quantified. For the largest downstream loading considered here, $£/d=45$, uniformity to $\pm 5\%$ was attained. The illustrated effect (Fig. 7) on the degree of uniformity with increasing $£/d$ suggested that diminishing returns had set in for $£/d=45$ and, therefore, it was deemed inefficient to pursue further increases in the $£/d$ beyond 45.

Another result of interest is the pressure increase along the length of the manifold. This pressure rise occurs as a consequence of the decrease in axial momentum as the fluid flows longitudinally along the length of the manifold. The pressure rise associated with the momentum decrease overwhelms the naturally occurring pressure drop due to friction. The extent of the pressure rise varied with the magnitude of $A_{ports}/A_{manifold}$, increasing with increases in the area ratio. In addition to the numerical values of the longitudinal pressure increase from the simulations, a separate prediction was made based on a simplified analytical model. The agreement between these separate approaches was found to be excellent, thereby lending support to the numerical simulations. In contrast to the significant effect of $A_{ports}/A_{manifold}$ on the pressure rise, it was found that the downstream pressure loading, represented by variations in $£/d$, had virtually no effect on the magnitude of the pressure increase. This outcome was confirmed by an analytical prediction based on the simplified model.

The Reynolds number was found to have only a slight effect on the uniformity of the mass effusion from the exit-port array.

The accuracy of the numerical predictions was verified by laboratory experiments.

Acknowledgment

The authors gratefully acknowledge the support of the 3M Company during the execution of this research.

Nomenclature

A_{ports} = cross-sectional area of manifold
$A_{manifold}$ = total cross-sectional area of all the exit ports
D = diameter of manifold
d = diameter of exit ports and downstream tubes
L = length of manifold
£ = length of downstream tubes
$\dot{m}$, $\dot{m}_{tot}$ = total rate of mass outflow from the manifold
$\dot{m}_{avg}$ = average rate of mass efflux from an exit port
$\dot{m}_n$, $\dot{m}_{local}$ = local per-port mass flow rate
n = a number identifying a given exit port
p = pressure
p_{amb} = pressure of the surrounding
Re = Reynolds number, $\rho\bar{U}D/\mu$
t = wall thickness of manifold
$\bar{U}$ = mean velocity of inlet manifold
u, v, and w = velocity components
x, y, and z = coordinates
μ = molecular viscosity
μ_{eff} = effective viscosity, Eq. (4)
μ_t = turbulent viscosity
ρ = density

References

[1] Koestel, A., and Tuve, G. L., 1948, "The Discharge of Air From a Long Slot," Heat./Piping/Air Cond., **20**(1), pp. 153–157.
[2] Spengos, A. C., and Kaiser, R. B., 1963, "Tapered Manifold Flow Spreader," Tappi J., **46**, pp. 195–200.
[3] Leydorf, G. F., Jr., Minty, R. G., and Fingeroot, M., 1972, "Design Refinement of Induction Exhaust Systems Using Steady-State Flow Bench Techniques," SAE Paper No. 720214, p. 23.
[4] Bajura, R. A., and Jones, E. H., 1976, "Flow Distribution Manifolds," ASME J. Fluids Eng., **98**, pp. 654–666.
[5] Furzer, I. A., 1980, "Steady State Flow Distributions in a Plate Column Fitted With a Manifold," Chem. Eng. Sci., **35**, pp. 1291–1298.
[6] Hsu, C., 1985, "How to Achieve Balanced Cooling With Internal Manifolding," Proceedings of the Annual Technical Conference, Society of Plastics Engineers, pp. 759–760.
[7] Riggs, J. B., 1987, "Developing of Algebraic Design Equations for Dividing, Combining, Parallel and Reverse Flow Manifolds," Ind. Eng. Chem. Res., **26**, pp. 129–133.

[8] Jones, G. F., and Lior, N., 1994, "Flow Distribution in Manifolded Solar Collectors With Negligible Buoyancy Effects," Sol. Energy, **52**, pp. 289–300.
[9] Chen, C., Jen, P., and Lai, F. S., 1997, "Optimization of the Coathanger Manifold Via Computer Simulation and an Orthogonal Array Method," Polym. Eng. Sci., **37**, pp. 188–196.
[10] Pan, J. P., Liu, T. J., and Wu, P. Y., 1999, "Theoretical Analysis on Extrusion Die Flow of Electronic Packaging Materials," AIChE J., **45**, pp. 424–431.
[11] Argyropoulos, P., Scott, K., and Taama, W. M., 2000, "Hydrodynamic Modeling of Direct Methanol Liquid Feed Fuel Cell Stacks," J. Appl. Electrochem., **30**, pp. 899–913.
[12] Koh, J.-H., Seo, H.-K., Lee, C. G., Yoo, Y.-S., and Lim, H. C., 2003, "Pressure and Flow Distribution in Internal Gas Manifolds of Fuel-Cell Stack," J. Power Sources, **115**(1), pp. 54–65.
[13] Ma, Z., Venkataraman, R., and Farooque, M., 2004, "Study of the Gas Flow Distribution and Heat Transfer for Externally Manifolded Fuel Cell Stack Module Using Computational Fluid Dynamics Method," ASME J. Fuel Cell Sci. Technol., **1**(1), pp. 49–55.
[14] Schenone, C., 2005, "Gas Distribution for Molten Carbonate Fuel Cells," Proceedings for the First European Fuel Cell Technology and Applications Conference, Dec.
[15] Jiao, K., Zhou, B., and Quan, P., 2006, "Liquid Water Transport in Parallel Serpentine Channels With Manifolds on Cathode Side of PEM Fuel Cell Stack," J. Power Sources, **154**(1), pp. 124–137.
[16] Wang, H. X., and Wang, Y.-X., 2007, "Estimation Method for the Nonuniform Degree of Fluid Distribution in Fuel Cell Stacks," Journal of Tianjin University Science and Technology, **40**(3), pp. 371–376.
[17] Amador, C., Gavriilidis, A., and Angeli, P., 2004, "Flow Distribution in Different Microreactor Scale-Out Geometries and the Effect of Manufacturing Tolerances and Channel Blockage," Chem. Eng. J., **101**(1–3), pp. 379–390.
[18] Tonomura, O., Tanaka, S., Noda, M., Kano, M., Hasebe, S., and Hashimoto, I., 2004, "CFD-Based Optimal Design of Manifold in Plate-Fin Micro Devices," Chem. Eng. J., **101**(1–3), pp. 397–402.
[19] Eason, C., Dalton, T., Davies, M., O'Mathuna, C., and Slattery, O., 2005, "Direct Comparison Between Five Different Microchannels, Part 2: Experimental Description and Flow Friction Measurement," Heat Transfer Eng., **26**(3), pp. 89–98.
[20] Furlani, E. P., 2005, "Thermal Modulation and Instability of Newtonian Liquid Microjets," 2005 NSTI Nanotechnology Conference and Trade Show—NSTI Nanotech 2005 Technical Proceedings, pp. 668–671.
[21] Tonkovich, A., Kuhlmann, D., Rogers, A., McDaniel, J., Fitzgerald, S., Arora, R., and Yuschack, T., 2005, "Microchannel Technology Scale-Up to Commercial Capacity," Chem. Eng. Res. Des., **83**(6A), pp. 634–639.
[22] Emerson, D. R., Cieslicki, K., Gu, X., and Barber, R. W., 2006, "Biometric Design of Microfluidic Manifolds Based on a Generalized Murray's Law," Lab Chip, **6**(3), pp. 447–454.
[23] Zhang, Z., and Li, Y., 2003, "CFD Simulations on Inlet Configuration of Plate-Fin Heat Exchangers," Cryogenics, **43**(12), pp. 673–678.
[24] Tiselj, I., Hetsroni, G., Mavko, B., Mosyak, A., Pogrebnyak, B., and Sengal, Z., 2004, "Effect of Axial Conduction on the Heat Transfer in Microchannel," Int. J. Heat Mass Transfer, **47**, pp. 2551–2565.
[25] Klein, D., Hetsroni, G., and Mosyak, A., 2005, "Heat Transfer Characteristics of Water and APG Surfactant Solution in Micro-Channel Heat Sink," Int. J. Multiphase Flow, **31**, pp. 393–415.
[26] Nozal, L., Arce, L., Simonet, B. M., Rios, A., and Valcarcel, M., 2004, "Rapid Determination of Trace Levels of Tetracyclines in Surface Water Using a Continuous Flow Manifold Coupled to a Capillary Electrophoresis System," Anal. Chim. Acta, **517**(1–2), pp. 89–94.
[27] Yebra-Biurrun, M. C., Moreno-Cid, A., and Cancela-Perez, S., 2005, "Fast Online Ultrasonic-Assisted Extraction Coupled to a Flow Injection-Atomic Absorption Spectrometric System for Zinc Determination in Meat Samples," Talanta, **66**(3), pp. 691–695.
[28] Kale, S. C., and Ganesan, V., 2004, "Investigation of the Flow Field in the Various Regions of Intake Manifold of a S.I. Engine," Ind. J. Eng. Mater. Sci., **11**(2), pp. 85–92.
[29] Persoons, T., Van den Bulck, E., and Fausto, S., 2004, "Study of Pulsating Flow in Close-Coupled Catalyst Manifolds Using Phase Locked Hot-Wire Anemometry," Exp. Fluids, **36**(2), pp. 217–232.
[30] D'Errico, G., and Onorati, A., 2006, "Thermo-Fluid Dynamic Modeling of a Six-Cylinder Spark Ignition Engine With a Secondary Air Injection System," Int. J. Engine Res., **7**(1), pp. 1–16.
[31] Cyklis, P., and Hendla, R., 2005, "Influence of Real Gas Model on the Simulation of Pressure Pulsation in the Reciprocating Compressor Manifolds," Archives of Thermodynamics, **26**(3), pp. 21–35.
[32] Ma, F., Choi, J.-Y., and Yang, V., 2005, "Thrust Chamber Dynamics and Propulsive Performance of Single-Tube Pulse Detonation Engines," J. Propul. Power, **21**(3), pp. 512–526.
[33] Xu, B., Liang, F., and Cai, S., 2005, "Numerical Analysis and Visualization of Natural Gas Jet With Multi-Point Injection System," Chin. J. Mech. Eng., **18**(4), pp. 550–554.
[34] Ryu, J., Cheong, C., Kim, S., and Lee, S., 2005, "Computation of Internal Aerodynamic Noise From a Quick-Opening Throttle Valve Using Frequency-Domain Acoustic Analogy," Appl. Acoust., **66**(11), pp. 1278–1308.
[35] Hrnjak, P. S., 2004, "Flow Distribution Issues in Parallel Flow Heat Exchangers," ASHRAE Trans., **110** Part 1, pp. 301–306.
[36] Vist, S., and Pettersen, J., 2004, "Two-Phase Flow Distribution in Compact Heat Exchanger Manifolds," Exp. Therm. Fluid Sci., **28**(2–3), pp. 209–215.
[37] Wu, T., Jiang, B., Xu, S., and Bi, C., 2006, "Nonisothermal Comprehensive 3D Analysis of Polymer Melt Flow in a Coat Hanger Die," Polym. Eng. Sci., **46**(4), pp. 406–415.
[38] Chen, A. W., and Sparrow, E. M., 2009, "Turbulence Modeling for Flow in a Distribution Manifold," Int. J. Heat Mass Transfer, **52**(5-6), pp. 1573–1581.

A Numerical Investigation of the Flow Past a Generic Side Mirror and its Impact on Sound Generation

Jonas Ask
Environment and Fluid Dynamics Centre,
Volvo Car Corporation,
SE-405 31 Göteborg, Sweden

Lars Davidson
Professor
Department of Applied Mechanics,
Division of Fluid Dynamics,
Chalmers University of Technology,
SE-412 96 Göteborg, Sweden

The case investigated is the flow past a generic side mirror mounted on a flat plate at the Reynolds number of $Re_D = 5.2 \times 10^5$ based on the mirror diameter. The present work studies both flow and acoustic sources by evaluating two second-order advection schemes, different levels of turbulence modeling, and three different grids. The advection schemes discussed in the present study are a second-order upwind scheme and a monotonic central scheme. The turbulence models investigated cover three levels of modeling. These are the original formulation of the detached eddy simulation (DES) model, the Smagorinsky–Lilly sub-grid scale (SGS) model with near-wall damping, and a dynamic Smagorinsky model. The different grids are as follows: a primary grid where all parameter studies are conducted and a second grid with significantly higher wake resolution and to some extent also increased plate resolution, while maintaining the resolution at the front side of the mirror. The final grid uses a significantly higher plate resolution and a wake resolution similar to that of grid two, but a comparably lower mirror front side resolution as compared with the two other grids. The general outcome of this work is that the estimation of the grid cutoff frequency through a relation of the velocity fluctuation and the grid size matches both the experimental results and trend lines perfectly. Findings from the flow field show that the horseshoe vortex in front of the mirror causes pressure fluctuations with a magnitude exceeding the maximum levels at the rear side of the mirror. Its location and unsteady properties are perfectly captured in the final simulation as compared with the experiments conducted by Daimler–Chrysler. A laminar separation at the front side of the mirror is more or less found for all wall resolved cases except the DES simulation. The third grid fails to predict this flow feature, but it is shown that this effect has no significant effect on either the static pressure sensors at the mirror surface or at the dynamic sensors located downstream of the mirror. The simulation also supports the fundamental frequency based on the eddy convection in the mirror shear layer, which is shown to be twice as high as the frequency peak found in the lateral force spectra.
[DOI: 10.1115/1.3129122]

1 Introduction

Flow induced noise experienced by the driver or passengers of a ground vehicle can be a consequence of different flow or fluid-structure phenomena occurring in low Mach number flows. Exposed components such as side mirrors, A-pillars, rails, tires, and underfloor details generate flow structures, and these are the primary sources of noise generation around the vehicle above approximately 120 km/h. The present work studies the flow past a generic side mirror mounted on a flat plate. This geometry has been the subject of several studies [1–5]. Höld et al. [1] and Siegert et al. [2] conducted both experimental and numerical investigations to predict sound generation and propagation at the Reynolds number of $Re_D = 7.066 \times 10^5$ based on the mirror diameter. They conducted unsteady Reynolds averaged Navier–Stokes (URANS) simulations for three different mesh densities and used an acoustic analogy to compute the radiated sound based on the wall pressure fluctuations and their temporal derivative [6,7]. The simulation in their work covered 0.1 s. A similar study at the Reynolds number of $Re_D = 5.2 \times 10^5$ was reported in Ref. [3], which focused on differences in sound generation and propagation in comparison of URANS and the detached eddy simulation (DES) modeling technique [8]. Their longest simulation covered 0.26 s, and the grid density was twice the highest resolved case in Refs. [1,2]. The results of Rung's DES simulations [3] generally showed an overprediction of the low frequency fluctuating pressure levels for most surface-mounted sensors and microphones. Their findings showed however a major improvement in acoustic results using the DES model as compared with the URANS results.

The generic side mirror is geometrically similar to both the sphere and the cylinder, perhaps best known for their drag crisis around a critical Reynolds number. This great difference in drag force is the consequence of laminar versus turbulent separation over the object. The Reynolds number for the present simulation is close to the critical Reynolds number for both the sphere and the cylinder. According to Schlichting [9], the drag force coefficient over a circular cylinder drops 0.7 over the interval $3.0 \times 10^5 < Re_D < 5.0 \times 10^5$. Similar results are also found for the sphere, where the force coefficient drops 0.31 over the interval $2.5 \times 10^5 < Re_D < 4 \times 10^5$. Constantinescu and Squires [10] mentioned a critical Reynolds number of $Re_{cr} \approx 3.7 \times 10^5$ for the sphere, which agrees well with Schlichting [9]. If an analogy is made between the flow state over the side mirror and the corresponding sphere and cylinder, the boundary layer over the generic side mirror in the present state is close to its critical value. Personal communication and results obtained from Daimler–Chrysler

Contributed by the Fluids Engineering Division of ASME for publication in the JOURNAL OF FLUIDS ENGINEERING. Manuscript received October 19, 2007; final manuscript received March 19, 2009; published online May 14, 2009. Assoc. Editor: Dimitris Drikakis. Paper presented at the 12th AIAA/CEAS Aeroacoustics Conference, Cambridge, MA, May 8–10 2006.

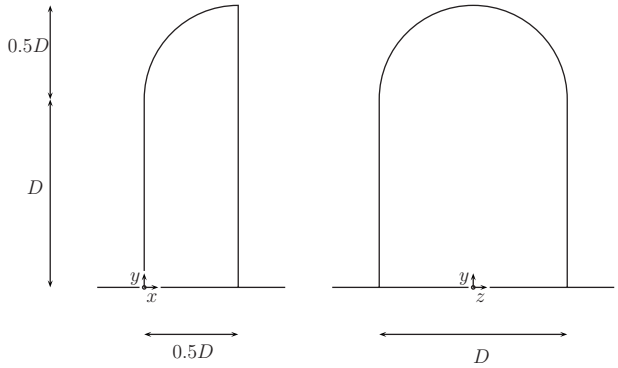

Fig. 1 Mirror geometry: side view and front view, respectively

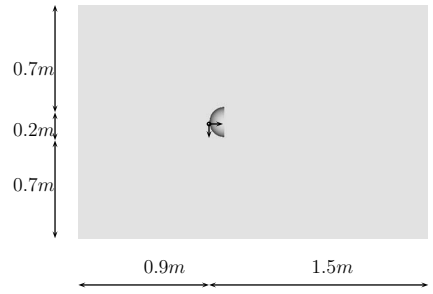

Fig. 2 Mirror and plate: *x*–*z* plane

[11] showed that the flow state over the mirror is actually subcritical. Regardless of the importance of this flow feature with respect to the sound sources, this constitutes a true challenge for any code and turbulence model to accurately predict both the size and location of the separation point.

With regards to the spatial discretization of the convective fluxes for DES, a general recommendation was made by Strelets [12] and was further applied in Refs. [10,13–15]. He suggested central difference schemes in the wake combined with high-order upwind-biased schemes in the Reynolds averaged Navier–Stokes (RANS) and Euler regions if the pure central differenced scheme proved unstable. The central schemes are known to have stability issues when operating in RANS mode, especially for cells with large aspect ratios. On the other hand, upwind-biased schemes are commonly considered too dissipative for large eddy simulations (LES). Different spatial discretization practices have been reported in the literature in connection with DES. In the most extreme cases, a fifth-order upwind-biased scheme was applied in the Euler and RANS regions combined with a fourth-order central scheme in the wake [14,15]. In Refs. [10,13], a fifth-order upwind scheme was used close to the walls and over the Euler region and was combined with a second-order central difference scheme in the wake region. However, several authors have also reported acceptable results for second and third-order upwind-biased schemes [3,16] involving separated flows.

Although the geometry is fairly simple it poses several challenges. A few are laminar to turbulent transition of the plate boundary layer, a laminar separation close to the mirror trailing edge, prediction of the size and unsteadiness of the horseshoe vortex, and the size of the recirculation zone in the turbulent wake. The main scope of the present paper is therefore to investigate the degree to which these flow features can be predicted using a commercial code, second-order advection schemes, and a mesh topology typically used in industrial applications.

The paper is organized as follows. Section 2 describes the geometry. Section 3 presents the cases considered and discusses the numerical approaches used in the present simulations. The findings from the parameter study are covered in Secs. 4–6, which treat the effects of the two advection schemes, the different turbulence models, and the three grids. This is followed by the results sections, consisting of flow field results (Sec. 7) and fluctuating surface pressure results (Sec. 8) for the most finely resolved cases. Conclusions are given in Sec. 9 and acknowledgments in Sec. 10. An appendix is also included that gives the locations of the static and dynamic pressure sensors (Appendix).

2 Case Description

The mirror consists of a half cylinder with a diameter of $D=0.2$ m blunted by a quarter sphere on top, which gives a total height of $H=0.3$ m. The geometry and origin of the coordinate system are shown in Fig. 1 and its position on the plate is represented in Fig. 2. The upstream part of the mirror will, in the following text, be referred to as the *front side* and the downstream flat side will be referred to as the *rear side*. The Reynolds number based on the mirror diameter is $\mathrm{Re}_D=5.2\times10^5$ with a freestream velocity of 39 m/s.

3 Methodology

The code used in this paper is the unstructured FLUENT commercial solver [17]. It is based on a control volume formulation to convert the governing equations to a solvable set of algebraic equations. The code at the present state uses a collocated scheme with cell-centered storage of both scalars and vectors. In the present work, the incompressible segregated solver is used with an implicit SIMPLEC pressure-velocity coupling algorithm. The domain is bounded by an inlet 3.0 m upstream of the mirror and an outlet 6.0 m downstream of the mirror. In the lateral extension the far-field boundaries are positioned 3.0 m on opposite sides of the mirror. In the plate-normal direction a far-field boundary is located 3.0 m above the plate. The inlet boundary condition for the DES case follows the "trip-less" approach proposed by Shur et al. [18], with an initial steady state inlet turbulence intensity of 0.1% and a turbulent inlet length scale of 0.1 m followed by a zero inlet turbulent viscosity. For the LES cases no perturbations are applied at the inlet. The cases are summarized in Table 1.

Table 1 requires some additional explanation. The first of the three different grids is (S), a block structured grid generated in ICEM HEXA 5.1 with low Reynolds resolution at the mirror front side. Grid (QS) is a quasistructured grid, where the near-field region is resolved by a block structured hexahedral grid similar to grid type (S) but with finer wake resolution and, to some extent, finer plate resolution. The outer region in the (QS) grid contains a rapidly growing unstructured grid with an overbridging layer of pyramids to enable the node and face. The final grid (U) is a hex-dominant unstructured grid generated in HARPOON 2.4C with isotropic resolution boxes in the mirror wake and above the plate. Closest to the walls, three layers of 1 mm cells resolve the geometry and the near-wall region. Above the plate the maximum cell size permitted is 2 mm, which is kept up to 25 mm perpendicular to the plate. The wake resolution is kept at a maximum of 4 mm at a distance of 0.4 m downstream of the rear side of the mirror. In

Table 1 Description of the conducted cases

	Case parameters			
ID	Grid topology	Turbulence treatment	Spatial discretization scheme	Number of cells ($\times10^6$)
M1SA2UD	S	DES (S-A)	2UD	5.83
M1SABCD	S	DES (S-A)	BCD	5.83
M1DS2UD	S	Dyn Smag	2UD	5.83
M1DSBCD	S	Dyn Smag	BCD	5.83
M1SLBCD	S	Smag–Lilly	BCD	5.83
M2SLBCD	QS	Smag–Lilly	BCD	11.8
M3SLBCD	U	Smag–Lilly	BCD	31.1

this text n^+ will refer to the wall-normal direction, s^+ to the streamwise direction, and l^+ to the lateral direction. At solid boundaries the log-law is applied for cells located in the range of $30<n^+<300$, and the viscous sublayer is assumed to be resolved for cell centroids located at $n^+<5$. A blending of the wall shear stress is carried out in the intermediate region. The log-law is assumed to be valid over a major part of the plate while resolving the viscous sublayer over the front side of the mirror.

The mirror front side n^+ values are less than 1.5 for the (S) and (QS) grids and less than 120 for the (U) grid. Corresponding s^+ and l^+ values are typically 30–40 and 80–90, respectively, for the (S) and (QS) grids and less than 120 in both directions for the (U) grid due to the cubic isotropic cells. Maximum n^+ values occur close to the plate's leading edge and are approximately 400 for grid (S) and 200 for grid (QS). For grid (U) the maximum n^+ is approximately 100 at the plate's leading edge. These levels decrease rapidly downstream of the plate until transition occurs, where they again increases.

For the M2SLBCD case a time-step size of $1\times10e^{-5}$ s was used; for all other cases the time-step size was kept twice as large, i.e., $2\times10e^{-5}$ s. The maximum Courant–Friedrichs–Lewy (CFL) number ranges from $3<\mathrm{CFL}_{\mathrm{conv}}<14$ for the (S) grid depending on the model and $22<\mathrm{CFL}_{\mathrm{conv}}<26$ for the two finer grids (QS) and (U). The maximum levels are typically found close to the trailing edge of the mirror and is limited to just a few cells. All cases cover 0.4 s of physical time.

The different turbulence models are given in column three of Table 1. Starting with DES, one of the most important aspects of the original formulations is to prevent grid-induced separation. No shielding between the inner and outer flows exists in FLUENT, which means that the user has to take an eventual grid-induced separation into account when building the grid. Here, an a priori estimate of the boundary layer thickness is used from a laminar Blasius solution for cylinder flows [9]. At the present Reynolds number the estimated boundary layer thickness is $\delta\approx0.59$ mm, which is resolved by ten cells in the wall-normal direction. To prevent an eventual grid-induced separation in the DES case, the following relation must be fulfilled [19]:

$$C_{\mathrm{DES}}\Delta > \mathcal{O}(1)\delta \tag{1}$$

In Eq. (1), Δ is the maximum extension of the cell, $C_{\mathrm{DES}}=0.65$, and δ is the boundary layer thickness. For cells located at the front side of the mirror close to the trailing edge, this requirement is fulfilled by at least one order of magnitude.

The dynamic Smagorinsky constant C_v is clipped at 0 and 0.23, and the test filter comprises the computational cell and the neighboring cells that share the same faces. For hexahedral cells used in the present work the ratio between the test filter and the grid filter is approximately 2.1 or $9^{1/3}$. The dynamic Smagorinsky constant is solved by seeking C_v for which the error norm E is minimized as follows:

$$E = \left(L_{ij} - \frac{\delta_{ij}}{3}L_{kk} - C_v M_{ij}\right)^2 \tag{2}$$

where

$$M_{ij} = -2(\tilde{\Delta}^2|\tilde{\bar{S}}|\tilde{\bar{S}}_{ij} - \bar{\Delta}^2\widetilde{|\bar{S}|\bar{S}_{ij}}) \tag{3}$$

They then set $\partial E/\partial C_v=0$, resulting in

$$C_v = \frac{L_{ij}M_{ij}}{M_{ij}M_{ij}} \tag{4}$$

For a more detailed description, see Ref. [20].

In the Smagorinsky–Lilly model the eddy viscosity is computed as follows:

$$\nu_t = \rho L_s^2|\bar{S}| \tag{5}$$

where

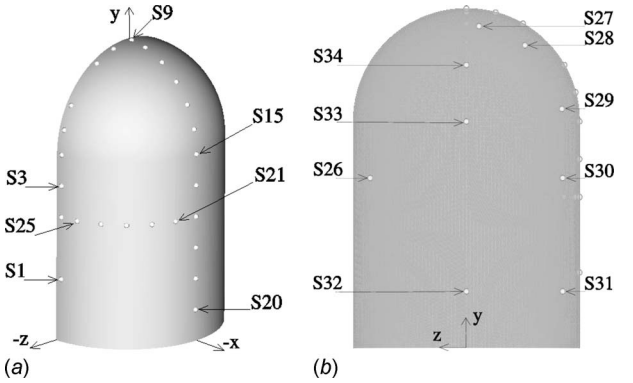

Fig. 3 Location of static pressure sensors over the front and rear side of the mirror: (*a*) Static sensor distribution over the front side and (*b*) static senor distribution over the rear side

$$|\bar{S}| = \sqrt{2\bar{S}_{ij}\bar{S}_{ij}} \tag{6}$$

and

$$L_s = \min(\kappa d, C_s V^{1/3}) \tag{7}$$

In Eq. (7), $C_s=0.1$ and d denotes the distance to the nearest wall.

The advection schemes used for the different cases are presented in column four where (2UD) is a second-order upwind-biased scheme and the (BCD) scheme is the bounded central difference scheme. The BCD scheme is essentially a second-order central scheme with a wiggle detector for wavelengths of $2\Delta x$ or less. For these occasions it locally blends with a second-order upwind scheme or, in the worst case, a first-order upwind scheme.

Figure 3 shows the location of the static pressure sensors. Sensors S1-S25 are located on the front side of the mirror and sensors S26-S34 are located on the rear side of the mirror.

The dynamic pressure sensors are distributed over the plate and the rear side of the mirror according to Fig. 4. The results for the dynamic pressure sensors obtained from Daimler–Chrysler [11] were low pass filtered using a Butterworth filter with a stop-band frequency of 2000 Hz and a bin width of 10 Hz. To reproduce these results the time sequences were resampled and split into windows containing 4096 samples for all cases conducted except for case M2SLBCD, which contained windows sizes of 8192 samples due to a sampling frequency of 100k Hz compared with 50k Hz for the other cases. Furthermore, each window was Hanning filtered with a 50% overlap.

From a wind noise perspective the wall pressure levels are by far the most important result owing to the representation of the physical excitation of the exterior structure. The fluctuating pressure level is computed in the following way:

$$\mathrm{SPL} = 10\log_{10}\frac{\hat{p}}{p_{\mathrm{ref}}^2} \tag{8}$$

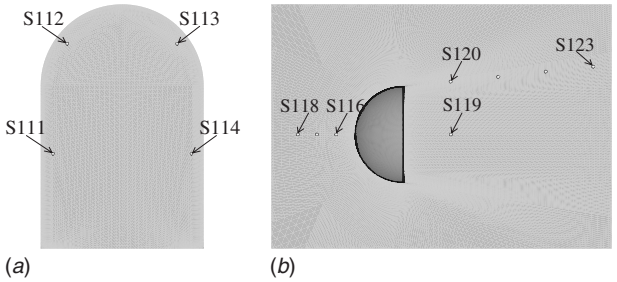

Fig. 4 Location of dynamic pressure sensors over the rear side of the mirror and the plate: (*a*) Dynamic sensor distribution over the rear side and (*b*) dynamic senor distribution over the plate

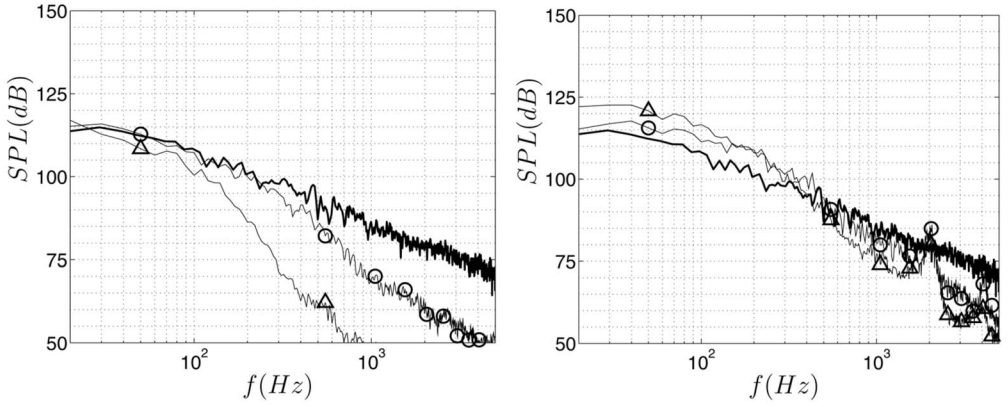

(a) DES model results at sensor S119, Experiment (-), M1SABCD (○), M1SA2UD (△)

(b) Dynamic Smagorinsky model results at S119, Experiment (-), M1DSBCD (○), M1DS2UD (△)

Fig. 5 Effect of advection scheme at sensor S119, DES and Dynamic Smagorinsky models

where $p_{\text{ref}}=2.0\cdot10^{-5}$ Pa is the reference pressure, and $\hat{p}$ is the filtered Fourier transformed results of the fluctuating pressure.

The cutoff frequency is estimated as $f_{\max}=|u_{p,\text{rms}}|/(2\Delta x_p)$, where $u_{p,\text{rms}}$ is the root mean square (rms) of the resolved fluctuating velocity magnitude and Δx_p is the local near-wall grid spacing. The number of grid points per wavelength is estimated as $\lambda_{\max}/\Delta x_p$, where $\lambda_{\max}=U_\infty/f_{\max}$.

4 Effect of Discretization Scheme

The discretization scheme has both a local and a global effect on the flow. The two schemes are thus evaluated as far downstream as possible for two different flow regimes: at the symmetry plane in the mirror wake S119 and at the farthest downstream sensor position S123 in the shear layer of the mirror. The schemes are investigated for both the DES model and for the dynamic Smagorinsky model shown in Figs. 5 and 6.

The LES case results obtained by the two advection schemes return very similar levels at sensor S119 (Fig. 5(*b*)), while the DES model returns significantly lower levels above 100 Hz for the 2UD scheme (Fig. 5(*a*)). Similar trends are also found for sensor S123, with a rapid decay of the fluctuations when the DES model is used in combination with the pure upwind scheme (Fig. 6(*a*)). At sensor S123 the experiments show a peak at approximately 40 Hz, which is best represented by the BCD scheme in combination with the dynamic model. In summary, combining the DES model with the upwind scheme seems to be a truly unsuccessful combination. As early as at 300 Hz the level is at best about 10 dB lower than both the experiments and the BCD scheme. It appears from these results that the BCD scheme is the best choice of the two schemes, primarily due to a low sensitivity to the turbulence model.

5 Effect of Turbulence Treatment

An upstream separation line can clearly be identified in the oil film visualization picture (Fig. 7(*a*)) located at approximately $0.15D$, measured from the rear side edge of the mirror. Instantaneous LES and DES results of the wall shear stress are also presented in Figs. 7(*b*) and 8 and indicate fair agreement in the separation at the front side of the mirror for the LES cases as compared with the experiments (Fig. 7(*a*)). The DES case lacks this feature completely (Fig. 8(*b*)), due to an excessive production of turbulent viscosity preventing the occurrence of the separation.

The downstream effects of the different models are not as apparent (Figs. 9(*a*) and 9(*b*)). At positions S119–S122 the DES model underpredicts the results by about 5 dB at 500 Hz. These effects become less pronounced further downstream and, at posi-

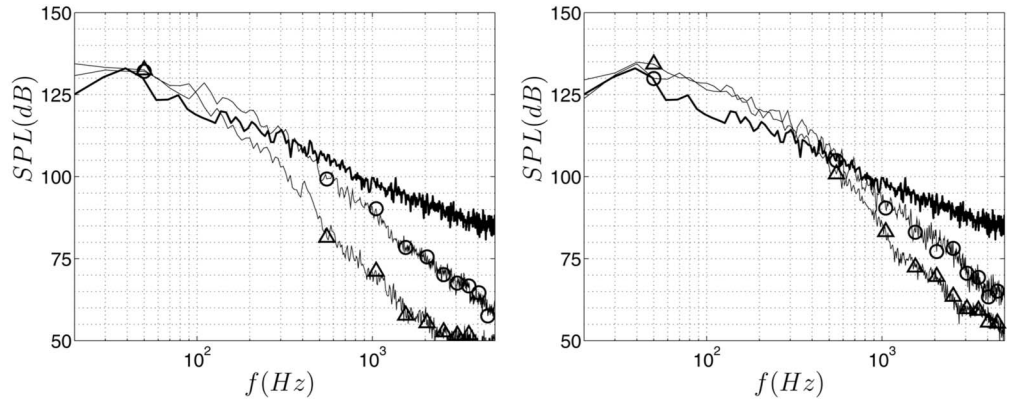

(a) DES model results at sensor S123, Experiment (-), M1SABCD (○), M1SA2UD (△)

(b) Dynamic Smagorinsky model results at S123, Experiment (-), M1DSBCD (○), M1DS2UD (△)

Fig. 6 Effect of advection scheme at sensor S123, DES and Dynamic Smagorinsky model, respectively

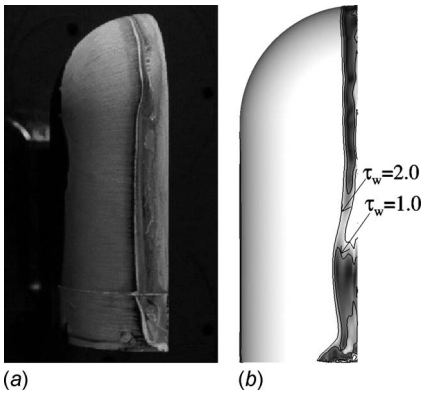

Fig. 7 Oil film visualization and snapshot of wall shear stresses for the M1SLBCD case: (*a*) Oil film visualization (courtesy of Daimler Chrysler Research and Technology), and (*b*) wall shear stress, M1SLBCD, $0 < \tau_{wall} < 2.0$

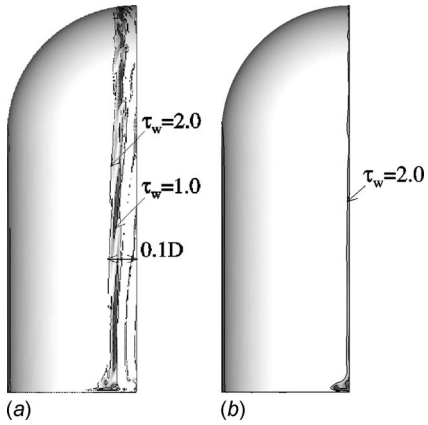

Fig. 8 Snapshot of wall shear stresses for the M1DSBCD and M1SABCD casese: (*a*) Wall shear stress, M1DSBCD, $0 < \tau_{wall} < 2.0$ and (*b*) wall shear stress, M1SABCD, $0 < \tau_{wall} < 2.0$

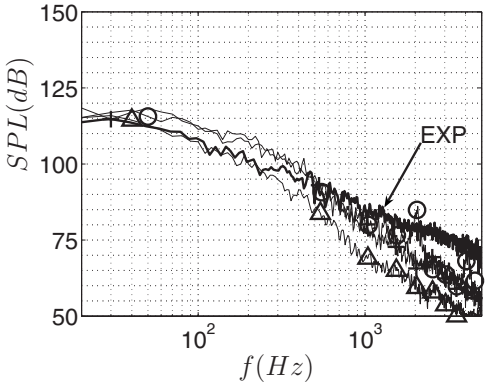

(a) Effect of different turbulence models at sensor S119, Experiments (-), M1DSBCD (∘), M1SABCD (△), M1SLBCD (+)

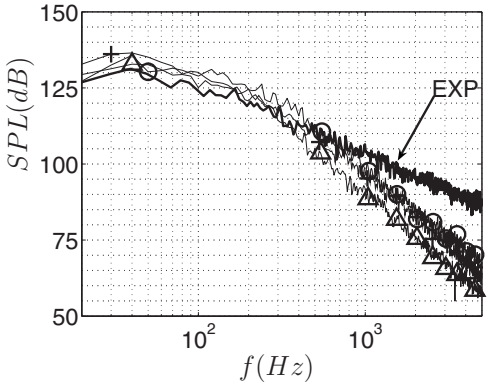

(b) Effect of different turbulence models at sensor S121, Experiments (-), M1DSBCD (∘), M1SABCD (△), M1SLBCD (+)

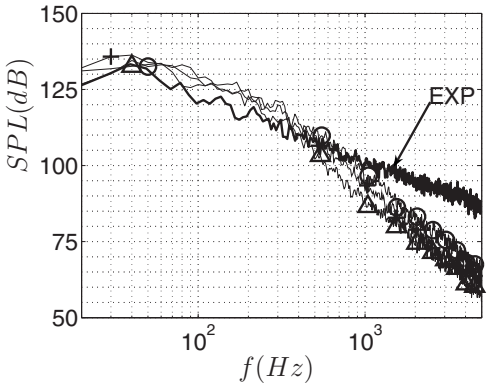

(c) Effect of different turbulence models at sensor S122, Experiments (-), M1DSBCD (∘), M1SABCD (△), M1SLBCD (+)

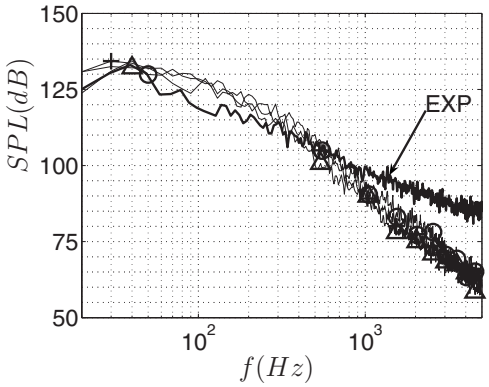

(d) Effect of different turbulence models at sensor S123, Experiments (-), M1DSBCD (∘), M1SABCD (△), M1SLBCD (+)

Fig. 9 Effect of different turbulence models

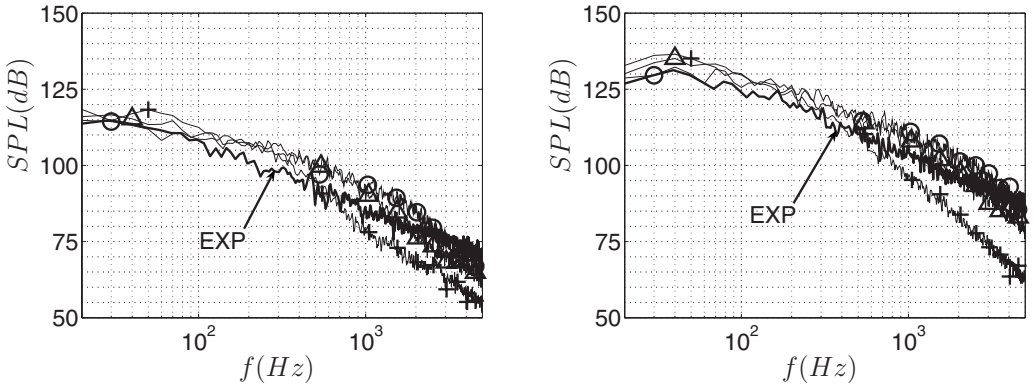

(a) Effect of resolution at sensor S119, Experiment (-), M1SLBCD (+), M2SLBCD (△), M3SLBCD (○)

(b) Effect of resolution at sensor S121, Experiment (-), M1SLBCD (+), M2SLBCD (△), M3SLBCD (○)

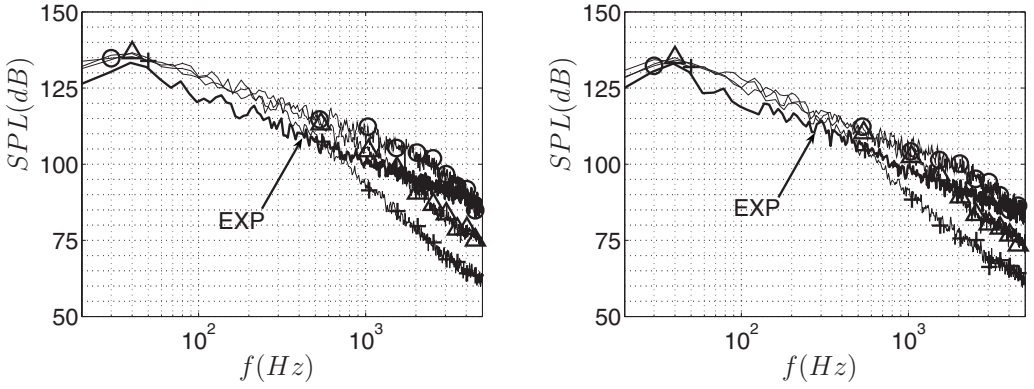

(c) Effect of resolution at sensor S122, Experiment (-), M1SLBCD (+), M2SLBCD (△), M3SLBCD (○)

(d) Effect of resolution at sensor S123, Experiment (-), M1SLBCD (+), M2SLBCD (△), M3SLBCD (○)

Fig. 10 Effect of resolution at four different positions in the mirror wake

tion S123, the differences between the models have almost vanished. Measurements at sensors S121–S123 show a peak at 40 Hz. This peak is fairly well predicted by all models.

A drawback of the dynamic model is the oscillations that occur at multiples of 1000 Hz (Fig. 9(*a*)). Thus, in summary, the DES model seems to underpredict the levels in the near wake of the mirror and the dynamic model shows tendencies to oscillate in the wake. The best candidate among the models investigated is therefore the Smagorinsky–Lilly model, which was also found to be the fastest in terms of CPU hours.

6 Effect of Resolution

The final part of the parameter study primarily contains the effect of different resolution levels. As in Secs 4 and 5 the comparison is made at the four sensor positions in the mirror wake (S119–S123). These results are presented in Figs. 10(*a*)–10(*d*). All simulations return almost identical pressure levels in the frequency range of 20–400 Hz but typically overpredict the level in this region by 5 dB as compared with the experiments. Increased wake and plate resolution has the effect of delaying the decay of the fluctuation levels at increased frequencies (Figs. 10(*a*)–10(*d*)). The trend is however that the 5 dB overprediction found in the low frequency region is present over the whole frequency range. Even though the M3SLBCD case fails to predict the separation point at the front side of the mirror due to the use of wall functions, no apparent effect in the downstream pressure levels can be found.

The computed grid cutoff frequencies at sensors S119–S123 are summarized in Table 2 for the three grids.

The cutoff frequencies in Figs. 10(*a*)–10(*d*) actually mark the starting point for a more pronounced decay of the levels, and a rough estimate is that a 2.5 times finer cell distribution gives a 2.5 times higher grid cutoff frequency.

7 Flow Field Results

In the following text a more thorough examination will be made of the flow field for the case M3SLBCD and, to some extent, case M2SLBCD.

Table 2 Cutoff frequency for the surface sensors

Cutoff frequency for first off-wall cells						
	M1SLBCD		M2SLBCD		M3SLBCD	
Sensor	f_{max} (Hz)	Grid pnts/ λ_{max}	f_{max} (Hz)	Grid pnts/ λ_{max}	f_{max} (Hz)	Grid pnts/ λ_{max}
S119	490	8.3	1210	9.1	1950	10
S121	671	4.8	1670	5.4	3900	5
S122	709	4.5	1590	5.6	3975	4.9
S123	582	5.5	1460	6.1	3475	5.6

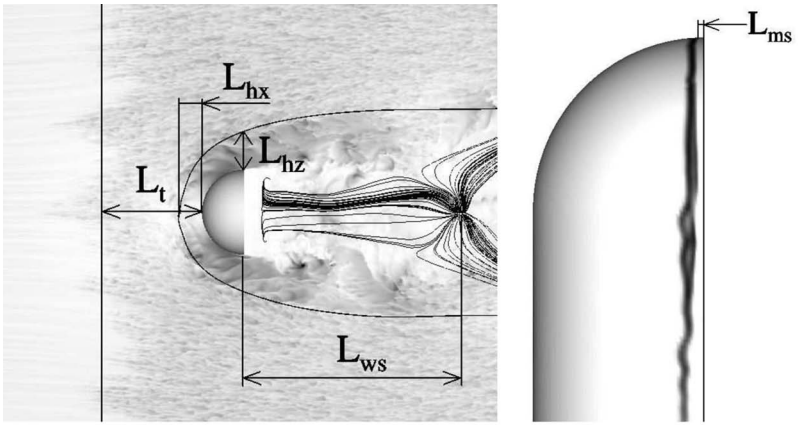

(a) Plate flow structures, M3SLBCD (b) Mirror flow structures, M2SLBCD

Fig. 11 Characterization of dominating flow structures

Freestream air reaches the plate's leading edge forming a laminar boundary layer at the farthest upstream part of the plate (Fig. 11). Local transition streaks occur further downstream of the plate (at L_t upstream of the mirror) and, at approximately $0.5D$ upstream of the mirror, the plate's boundary layer is fully turbulent. Along the symmetry plane of the mirror the flow becomes stagnant as it approaches the front side of the mirror, which results in a horseshoe vortex centered approximately 6 mm above the plate and at position L_{hx} in the streamwise direction (Table 3). At the trailing edge of the mirror close to the plate, shedded vortices interact with the plate's boundary layer causing two symmetric regions with high pressure fluctuations. Their directions with respect to the symmetry plane of the mirror are mainly determined by the mirror wake and, to some extent, the size and proximity of the horseshoe vortex L_{hz}. Above the plate boundary layer undisturbed freestream air meets the front side of the mirror and accelerates along its surface. The boundary layer of the mirror remains laminar until separation occurs close to the mirror's trailing edge. The center of this recirculation bubble is located at the distance L_{ms} from the mirror's trailing edge. Judging from Fig. 11(*b*) versus Fig. 7(*a*) the simulations show a delayed separation point as compared with the experiment. This laminar separation is the starting point for the mirror's wake and the recirculation zone that ends at L_{ws}.

The location of the static pressure sensors were shown in Fig. 3 and the results for these locations are presented in Fig. 12 for both the M2SLBCD and M3SLBCD cases as well as the experimental results [11]. Sensors S1–S9 in region (I) are located 6 mm upstream of the mirror's rear side (Fig. 3(*a*)). Judging from the oil film visualization (Fig. 7(*a*)), their locations are in the flow separated region. All simulations conducted indicate a delayed separation point or fail to predict this feature completely compared with the experiments, which results in an excessive velocity magnitude and a lower pressure as a consequence (Fig. 12). Sensors in region (II) are located along the mirror's symmetry plane starting with the most topward positioned point S10 located 2.6 mm upstream of the mirror's trailing edge. The flow is attached at this sensor position while the measured flow has detached causing a higher pressure as compared with the simulations. At sensors S11 to S20, experimental and simulated mean pressures match perfectly and converge toward $C_p = 1.0$ at the last sensors in this region. Sensor region (III) is located at the mirror's front side 133 mm above the plate. As for sensor S10, sensor S25 is positioned at 2.6 mm, measured from the mirror's trailing edge, and again highlights the misrepresentation of the separation point in the simulations. Both simulations show an even lower pressure at S25 as compared with that at sensor S10 and thus indicate a higher flow speed at this location as compared with sensor S10. The mean pressure over the front side of the mirror shows otherwise good agreement with the experimental results and, on the rear side, region (IV), almost perfect agreement between the two LES cases and the experiment is obtained, even though the M3SLBCD case uses wall functions over the whole front side of the mirror.

Figure 13(*a*) shows the spectral content of lateral and streamwise force coefficients. In the lateral force coefficient a peak is found at 18.3 Hz. A much weaker peak is also found for the streamwise force coefficient at a frequency of 36.5 Hz. The lateral force coefficient is believed to relate to the vortex shedding by a

Table 3 Locations of flow structures found

Identification	Mirror offset (m)
L_t	0.208
L_{hx}	0.0525
L_{hz}	0.0906
L_{ws}	0.5165
L_{ms}	0.002

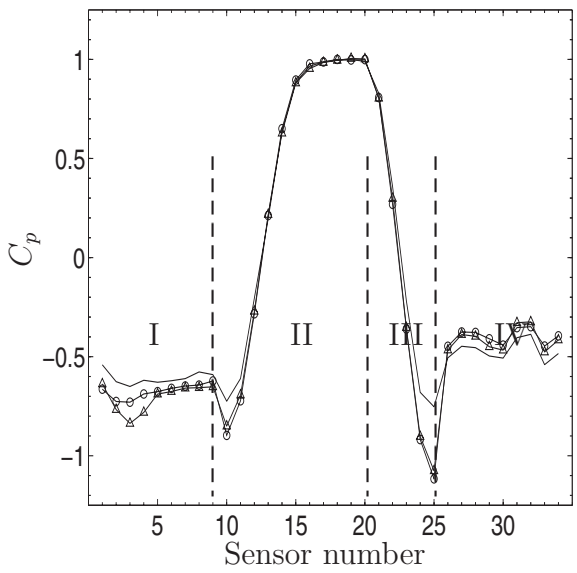

Fig. 12 Mean pressure over mirror: (-) measured, (△) M2SLBCD, and (○) M3SLBCD

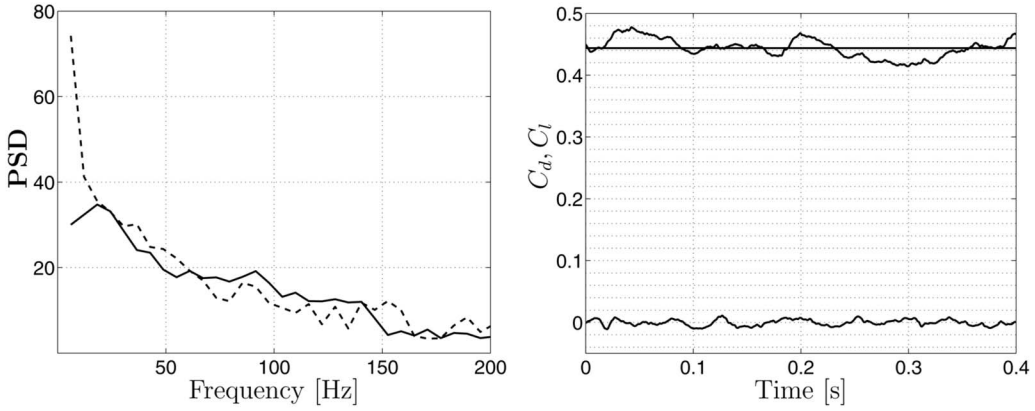

(a) Power Spectral Density versus frequency,(−) lateral force coefficient, (−−) streamwise force coefficient

(b) Time traces of streamwise and lateral mirror forces

Fig. 13 Force coefficient results for the M3SLBCD case

factor of two since two vortices, one rotating clockwise and one co-rotating vortex, are contained within one full period. This shedding frequency, 36.5 Hz, corresponds to the peak found in the mirror's shear layer at sensors S121 to S123 and results in a Strouhal number based on the mirror diameter and the freestream velocity of approximately S_t=0.19. This means that 14 vortex sheddings are contained in the present simulations. Figure 13(*b*) gives the time traces for both the streamwise and lateral force coefficients together with the time-averaged streamwise force coefficient, which is computed to be $\overline{C_d}$=0.4437.

8 Surface Pressure Fluctuations Results

Contours of the mirror and plate pressure fluctuations are shown in Fig. 14 together with the locations of the dynamic pressure sensors. The highest levels are recovered at the plate close to sensors S120 to S123 at the breakup of the detached mirror shear layer. The levels in this region are more than twice as large as over the rear side of the mirror. Upstream of the mirror the horseshoe vortex leaves a clear footprint on the plate, indicating fluctuation levels exceeding the maximum levels at the mirror's rear side.

Pressure fluctuations returned by the dynamic pressure sensors as well as the corresponding computed signals for the M3SLBCD case are presented in the frequency plane in Figs. 15–20. The locations of these sensors are given in the Appendix and, visually, in Fig. 14.

Four sensors are located at the mirror rear side, S111–S114, and the results for these sensors are shown in Figs. 15(*a*) and 15(*b*) The fluctuations at the rear side of the mirror are determined mainly by flow structures in the wake and are accurately predicted up to the grid cutoff frequency indicated by the vertical line. The four sensors show no tonal content and the fluctuations decay rapidly with increased frequency up to the predicted cut-off frequencies.

Sensors S116–S118 are located upstream of the mirror along the mirror's symmetry plane. It is obvious that their purpose is to capture the horseshoe vortex in front of the mirror. S116 is the sensor located closest to the mirror and the levels at this position are accurately predicted up to 1500 Hz with a peak level of about 120 dB, which is significantly higher than the levels at the mirror's rear side. The result for sensor S117 is similar to that for sensor S116, indicating that both sensors are located close to the horseshoe vortex core. Compared with the mirror's rear side sensors, both sensors show a flat low frequency part between 20 Hz and 200 Hz where most of the energy is concentrated. Above this region the levels decay rapidly, contrary to the result for sensor S118. The sensor located farthest upstream S118, shows significantly lower levels as compared with sensors S117 and S116, and the simulation overpredicts the levels by approximately 10 dB. A possible explanation is too early a transition point along the plate, but no experimental results exist to justify this hypothesis. Among the sensors investigated this sensor also turns out to have the flattest curve and indicates a signal with a white noise character and no dominating frequencies. Similar to sensors S116, S117, and S118, sensor S119 is located along the mirror's symmetry plane but is, in contrast, located in the wake downstream of the mirror. The trend for this sensor is similar to that of the sensors at the rear side of the mirror but has a slower decay of the fluctua-

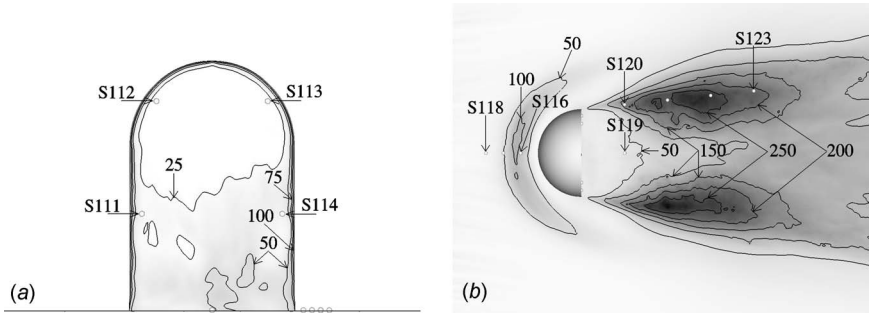

Fig. 14 RMS of wall pressure (Pa) and sensor positions for the M3SLBCD case: (*a*) RMS of pressure on the rear side of the mirror and (*b*) RMS of pressure fluctuations over the plate

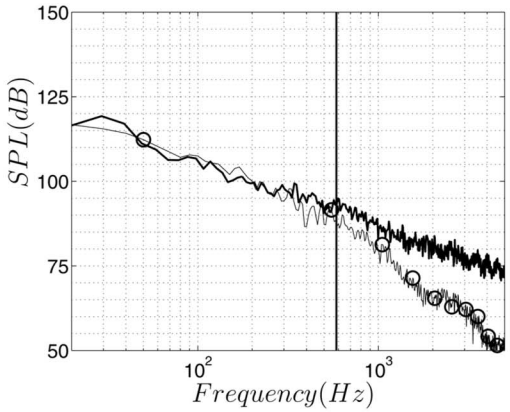

(a) SPL at surface sensor S111, (-) Measured, (○) M3SLBCD

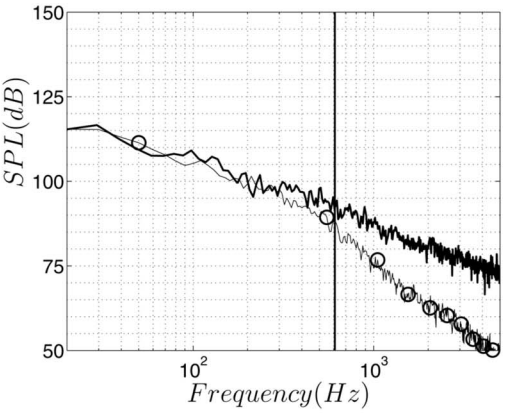

(b) SPL at surface sensor S114, (-) Measured, (○) M3SLBCD

Fig. 15 SPL at sensors S111 and S114

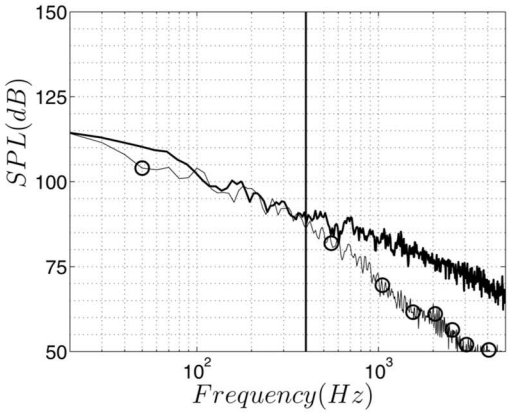

(a) SPL at surface sensor S112, (-) Measured, (○) M3SLBCD

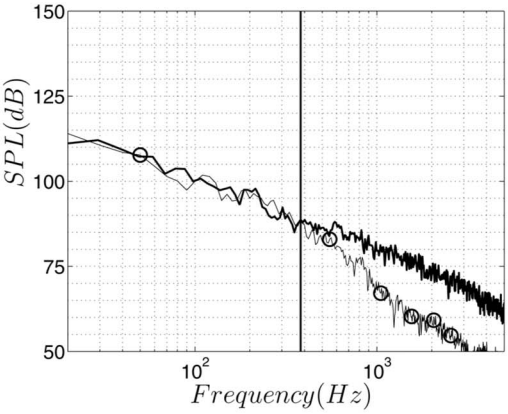

(b) SPL at surface sensor S113, (-) Measured, (○) M3SLBCD

Fig. 16 SPL at sensors S112 and S113

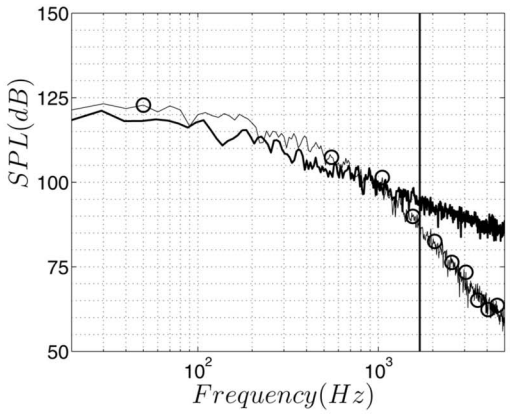

(a) SPL at surface sensor S116, (-) Measured, (○) M3SLBCD

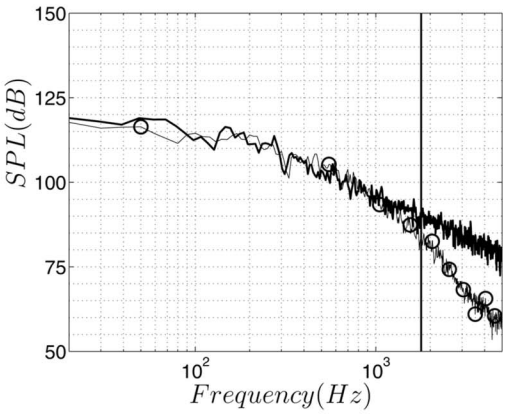

(b) SPL at surface sensor S117, (-) Measured, (○) M3SLBCD

Fig. 17 SPL at sensors S116 and S117

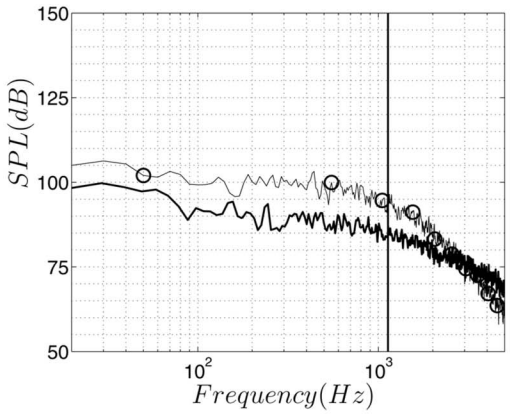

(a) SPL at surface sensor S118, (-) Measured, (∘) M3SLBCD

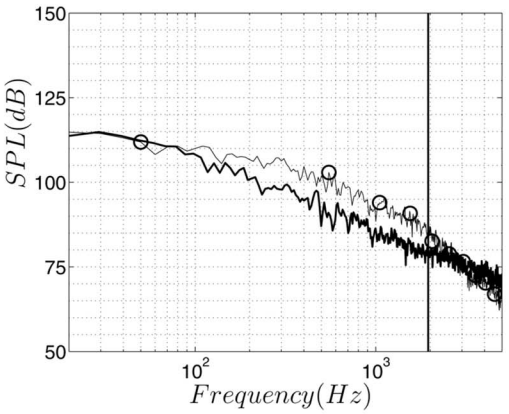

(b) SPL at surface sensor S119, (-) Measured, (∘) M3SLBCD

Fig. 18 SPL at sensors S118 and S119

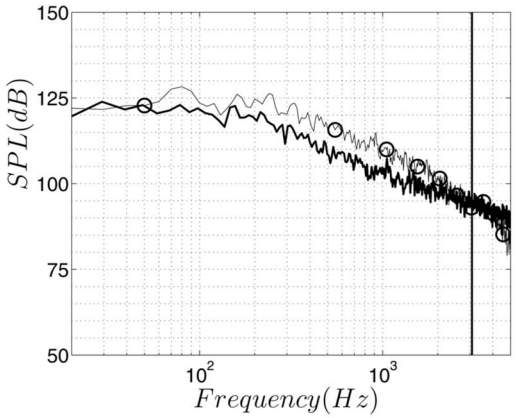

(a) SPL at surface sensor S120, (-) Measured, (∘) M3SLBCD

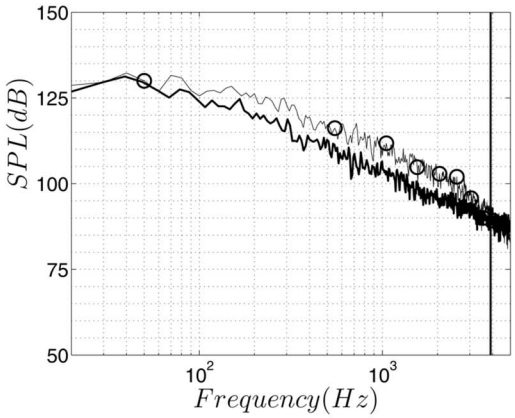

(b) SPL at surface sensor S121, (-) Measured, (∘) M3SLBCD

Fig. 19 SPL at sensors S120 and S121

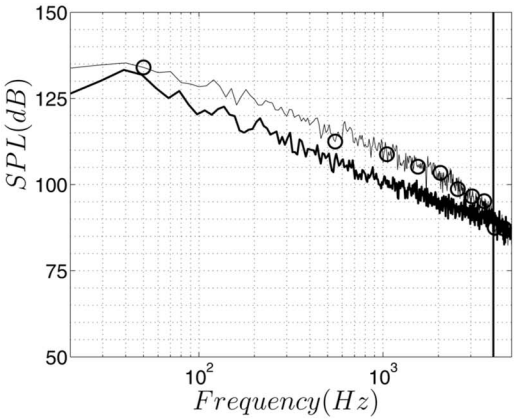

(a) SPL at surface sensor S122, (-) Measured, (∘) M3SLBCD

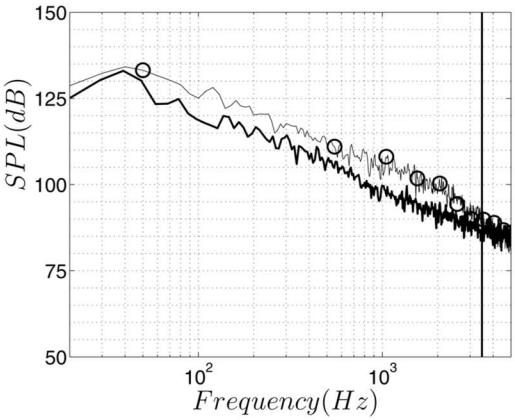

(b) SPL at surface sensor S123, (-) Measured, (∘) M3SLBCD

Fig. 20 SPL at sensors S122 and S123

tions as compared with these sensors, which is explained by its more downstream position, where there exists a wider range of scales.

Sensors S120 and S121 are those positioned farthest upstream in the mirror's shear layer; the results are shown in Figs. 19(*a*) and 19(*b*). The results in the case of sensor S120 are similar to those for sensor S116, with a flat low frequency region followed by a rapid decay at increasing frequencies. At sensor S121, 0.1 m downstream of sensor S120, the signal character changes slightly to gain a more tonal character with a peak at approximately 40 Hz. This peak becomes more pronounced further downstream at sensors S122 and S123 (Figs. 20(*a*) and 20(*b*)).

A general trend in the wall pressure results is that the levels are perfectly predicted at the rear side of the mirror and at the plate upstream of the front side of the mirror. In the mirror's wake and along the mirror's shear layer the simulation catches the trends perfectly but overpredicts the fluctuations by about 5 dB.

9 Conclusion

This paper covers predictions of both the flow field and the acoustic sources of a generic side mirror mounted on a flat plate. The Reynolds number is 5.2×10^5 based on the diameter of the mirror and the corresponding Mach number for this flow field is $Ma_\infty=0.11$. Owing to the low Mach number, the flow field is solved on the basis of an assumption of incompressibility. In the first part of the paper a parameter study is conducted by means of different advection schemes, turbulence models, and three levels of grid resolution. The general outcome of the work is as follows.

An estimation of the local grid cutoff is given by relating the velocity fluctuation with the near-wall grid spacing. This estimate first of all marks the starting point for a more rapid decay of the fluctuation levels. Second, for most sensors, it also marks the frequency at which the simulated results cross or leave the measured levels. This technique is shown to predict the grid cutoff for both structured and unstructured grids.

The choice of advection scheme, i.e., a second-order upwind or second-order hybrid scheme, has little effect on the downstream pressure fluctuations as long as the DES model is avoided.

As concerns turbulence modeling, the DES model should be avoided if fluctuations are of interest. Both the dynamic model and the Smagorinsky–Lilly model with near wall damping give a significant improvement in the representation of the wide range of turbulent scales and have the potential to capture both the laminar separation point and the point of transition from a laminar to a turbulent boundary layer. Although the dynamic model and the Smagorinsky–Lilly model give similar results, oscillations are to be expected when using the dynamic model, which suggests that the simpler Smagorinsky–Lilly model is preferable.

The computed mean pressure levels at the mirror surface are in good agreement with the experimental results except for the sensors located near the mirror laminar separation line and are fairly independent of whether the mirror's boundary layer is resolved or replaced by wall functions. The computed shedding frequency is 37 Hz based on the lateral force coefficient, resulting in a Strouhal number of about $S_t=0.19$, and the mean streamwise force coefficient is computed to be $\overline{C_d}=0.4437$ on the basis of the projected area of the mirror.

The fundamental frequency based on the spectral peaks at sensors S121–S123 were both computed and found from the experiments to be approximately $f_n=40$ Hz. The fundamental frequency based on convection of the shear layer disturbances is due to the alternating rotating vortices from the shear layer instabilities, with twice as high a frequency as the lateral force coefficient, which supports the findings regarding the Strouhal number. A perfect match between measured and computed results is found for sensors located at the rear side of the mirror and upstream of the mirror at the mirror's symmetry plane. One exception exists however for sensor S118, indicating a possibly too early a transition point in the simulation. All sensors in the mirror's wake and in the mirror's shear layer captures the trends perfectly but show an overprediction of the intermediate frequency region by about 5 dB in the case of the simulations.

Acknowledgment

This work was supported by the Volvo Car Corporation and the Swedish Agency for Innovation Systems (VINNOVA). We would also like to express our gratitude to Dr. Franz R. Klimetzek at Daimler Chrysler, who let us use their experimental data and pictures.

Appendix

Table 4 shows the locations of the static and dynamic sensors.

Table 4 Location of dynamic and static pressure sensors

Positions of dynamic pressure sensors			
Sensor ID	*x*	*y*	*z*
S111	0.100	0.1167	0.0850
S112	0.100	0.2517	0.0674
S113	0.100	0.2517	−0.0674
S114	0.100	0.1167	−0.0850
S116	−0.0400	0.00	−0.0000
S117	−0.0800	0.00	−0.0000
S118	−0.1200	0.00	−0.0000
S119	0.2000	0.00	−0.0000
S120	0.1995	0.00	−0.1105
S121	0.2989	0.00	−0.1209
S122	0.3984	0.00	−0.1314
S123	0.4978	0.00	−0.1418
Positions of static pressure sensors			
Sensor ID	*x*	*y*	*z*
S1	0.0940	0.0667	−0.0998
S2	0.0940	0.1333	−0.0998
S3	0.0940	0.1667	−0.0998
S4	0.0940	0.2000	−0.0998
S5	0.0940	0.2258	−0.0964
S6	0.0940	0.2499	−0.0864
S7	0.0940	0.2864	−0.0499
S8	0.0940	0.2964	−0.0258
S9	0.0940	0.2998	0.0000
S10	0.0741	0.2966	0.0000
S11	0.0500	0.2866	0.0000
S12	0.0293	0.2707	0.0000
S13	0.0134	0.2500	0.0000
S14	0.0034	0.2259	0.0000
S15	0.0000	0.2000	0.0000
S16	0.0000	0.1667	0.0000
S17	0.0000	0.1333	0.0000
S18	0.0000	0.1000	0.0000
S19	0.0000	0.0667	0.0000
S20	0.0000	0.0333	0.0000
S21	0.0034	0.1333	−0.0259
S22	0.0134	0.1333	−0.0500
S23	0.0293	0.1333	−0.0707
S24	0.0500	0.1333	−0.0866
S25	0.0741	0.1333	−0.0966
S26	0.1000	0.1500	0.0850
S27	0.1000	0.2843	−0.0111
S28	0.1000	0.2674	−0.0517
S29	0.1000	0.2111	−0.0843
S30	0.1000	0.1500	−0.0850
S31	0.1000	0.0500	−0.0850
S32	0.1000	0.0500	0.0000
S33	0.1000	0.2000	0.0000
S34	0.1000	0.2500	0.0000

References

[1] Höld, R., Brenneis, A., and Eberle, A., 1999, "Numerical Simulation of Aeroacoustic Sound Generated by Generic Bodies Placed on a Plate: Part I—Prediction of Aeroacoustic Sources," Fifth AIAA/CEAS Aeroacoustics Conference, Seattle, WA, May 10–12, Paper No. AIAA-99-1896.

[2] Siegert, R., Schwartz, V., and Reichenberger, J., 1999, "Numerical Simulation of Aeroacoustic Sound Generated by Generic Bodies Placed on a Plate: Part II—Prediction of Radiated Sound Pressure," Fifth AIAA/CEAS Aeroacoustics Conference, Seattle, WA, May 10–12, Paper No. AIAA-99-1895.

[3] Rung, T., Eschricht, D., Yan, J., and Thiele, F., 2002, "Sound Radiation of the Vortex Flow Past a Generic Side Mirror," Eighth AIAA/CEAS Aeroacoustics Conference, Breckenridge, CO, Jun. 17–19, Paper No. AIAA-2002-2340.

[4] EXA, 2003, "Validation Update: Model Mirror," Aeroacoustic Consortium 2003/2004 Presentation, Aug. 20.

[5] Bipin, L., Sandeep, S., and Jieyong, X., 2003, "Computational Aeroacoustic Analysis of a Generic Side View Mirror," Noise and Vibration Conference and Exhibition, Traverse City, MI, May 5–8, Paper No. SAE-2003-01-1698.

[6] Ffowcs Williams, J. E. and Hawkings, D. L., 1969, "Sound Generation by Turbulence and Surfaces in Arbitrary Motion," Philos. Trans. R. Soc. London, Ser. A, **264**(1151), pp. 321–342.

[7] Brentner, K. S. and Farassat, F., 2003, "Modeling Aerodynamically Generated Sound of Helicopter Rotors," Prog. Aerosp. Sci., **39**, pp. 83–120.

[8] Spalart, P., Jou, W.-H., Strelets, M., and Allmaras, S. R., 1997, "Comments on the Feasibility of LES for Wings, and on a Hybrid RANS/LES Approach," First AFOSR International Conference on DNS/LES. Advances in DNS/LES, pp. 137–147.

[9] Schlichting, H., 1969, *Boundary Layer Theory*, Springer, New York.

[10] Constantinescu, G. S. and Squires, K. D., 2003, "LES and DES Investigations of Turbulent Flow Over a Sphere at Re=10000," Flow, Turbul. Combust., **70**, pp. 267–298.

[11] Klimetzek, F., 2005, private communication.

[12] Strelets, M., 2001, "Detached Eddy Simulation of Massively Separated Flows," 39th AIAA Aerospace Sciences Meeting and Exhibit, Reno, NV, Jan. 8–11, Paper No. AIAA-2001-0879.

[13] Constantinescu, G. S. and Squires, K. D., 2004, "Numerical Investigations of Flow Over a Sphere in the Subcritical and Supercritical Regimes," Phys. Fluids, **16**, pp. 1449–1466.

[14] Spalart, P., Hedges, L., Shur, M., and Travin, A., 2003, "Simulation of Active Flow Control on a Stalled Airfoil," Flow, Turbul. Combust., **71**, pp. 361–373.

[15] Hedges, L. S., Travin, A. K. and Spalart, P., 2002, "Detached-Eddy Simulations Over a Simplified Landing Gear," ASME J. Fluids Eng., **124**, pp. 413–423.

[16] Schmidt, S. and Thiele, F., 2003, "Detached Eddy Simulation of Flow Around A-Airfoil," Flow, Turbul. Combust., **71**, pp. 261–278.

[17] FLUENT Inc., 2004, FLUENT 6.2 Documentation.

[18] Shur, M., Spalart, P., Strelets, M., and Travin, A., 1996, "Navier–Stokes Simulation of Shedding Turbulent Flow Past a Circular Cylinder and a Cylinder With Backward Splitter Plate," Computational Fluid Dynamics '96, Proceedings of the Third ECCOMAS Computational Fluid Dynamics Conference, Sept. 9–13, pp. 676–682.

[19] Menter, F., Kuntz, M., and Bender, R., 2003, "A Scale-adaptive Simulation Model for Turbulent Flow Predictions," 41st Aerospace Science Meeting and Exhibit, Jan. 6–9, Paper No. AIAA-2003-0767.

[20] Kim, S. E., 2004, "Large Eddy Simulation Using Unstructured Meshes and Dynamic Subgrid-Scale Turbulence Model," 34st AIAA Fluid Dynamics Conference and Exhibit, Jun., Paper No. AIAA-2004-2548.

Exit Flow Behavior of Axial Fan Flows With/Without Impingement

D. Sui

S. S. Wang

J. R. Mao

School of Energy and Power Engineering,
Xi'an Jiatong University,
Xi'an 710049, P.R.C.

T. Kim
e-mail: tongbeum@gmail.com

T. J. Lu
e-mail: tjlu@mail.xjtu.edu.cn

MOE Key Laboratory for Strength and Vibration,
Xi'an Jiaotong University,
Xi'an 710049, P.R.C.

The exit flow patterns of an axial flow fan widely used in electronics cooling are experimentally characterized both in free exit and in the presence of a flat impingement plate. The axial fan is rotated with 12.0 V input from a dc power supply, leading to a nominal Reynolds number of $Re = 9.0 \times 10^3$ based on fan diameter. One shear layer each is found to form between the exit flow from the axial fan and the surrounding fluid at rest, and between the exit flow and the flow along the fan axis. In addition to creating a highest wall pressure region (the primary stagnation region), the presence of the flat plate induces a flow recirculation zone (the secondary stagnation region) at the plate center. When the fan exit-to-plate spacing normalized by fan diameter (H/D) equals to about 0.6, the wall pressure is minimized in the secondary stagnation region due to the maximized "recirculation" as a result of intensified flow interaction. Within the range considered ($0.2 \leq H/D \leq 2.0$) and with the case of $H/D \sim 0.6$ serving as a reference, the flow interaction tends to be suppressed by the proximity of the plate at $H/D = 0.2$ and weakened due to the momentum dissipation at $H/D \sim 2.0$. [DOI: 10.1115/1.3130246]

Keywords: axial fan, impingement, secondary stagnation, separation distance

1 Introduction

The considerable heat removal capability of an impinging jet has led to its widespread use in various engineering applications. Among these, much attention was paid to using impinging jet cooling as a possible solution for the ever increasing intensity of heat dissipation in electronic devices due to compactness requirement [1–5].

In conventional impinging jets, a steady high momentum flow with its maximum velocity located at the center of the jet is issued through a circular nozzle/orifice, followed by impingement on a heat source. Such impinging jets, including single and multiple arrays on flat/modified surfaces, were extensively studied [1–6].

Although numerous efforts were made to enhance the thermal performance using such impinging jets, cooling flows in conventional (and commercially available) heat sinks are mainly driven by an axial flow fan (Fig. 1). The mechanisms associated with the axial fan flows differ from those of the conventional impinging jets: (1) Due to the presence of a hub housing the dc driving motor, a large flow area at the central part of the impinging flow is displaced over roughly 25% of the total flow area and the impingement (direct impact of the emerged high momentum flow) therefore occurs at target surface areas off from the driving fan axis; (2) the impinging flow is highly unsteady and periodic as a result of the rotating fan blades, in sharp contrast with the mostly steady flow in conventional jets; (3) the spacing between the fan exit and the target plate (or fin height) is relatively short, typically half the fan diameter, due to heat sink size restrictions; and (4) no potential core exists, while its existence in conventional jets is known to be influential on impinging heat transfer characteristics (especially for short separation distances).

Recent flow analysis of such axial flow fans was reported by Yen and Lin [7]. Obtained flow data without the impingement of the fan exit flow (i.e., free exit) show that the exit flow separated from the fan hub tends to contract toward the fan axis before convecting downstream parallel to the fan axis. Unlike the flow that emerged from the conventional jets, the highest momentum flow exists radially off from the fan axis, with its radial location coincident with the midspan of the fan blades at the axial measurement plane equal to the fan hub diameter. However, no measurement for fan exit flows impinging on a target plate was performed.

With a target plate placed downstream of the exit flow, the flow is decelerated as it approaches the plate, eventually stagnating on it. This implies that the flow pattern gradually changes within the fan exit-to-flat plate spacing (defined here as the separation distance), resulting from the upstream penetration of the potential field. Furthermore, the intensity of the potential field penetration is expected to increase as the separation distance is reduced. According to Refs. [8,9] for conventional impinging jets, there exists an optimum separation distance for maximum stagnation heat transfer, which is partly attributed to the potential core of the jets. Conversely, no potential core is expected to exist in axial fan flows and it is yet unclear if an optimum separation distance still exists.

This paper aims to investigate experimentally the detailed patterns of axial fan flows impinging on a flat plate. For comparison, axial fan flow patterns in free exit conditions are also measured. With the impingement, particular emphasis is placed upon the "secondary stagnation region" on the plate where recirculated flows meet and interact. The separation distance H (normalized by the fan diameter D) is systematically varied in the range of $0.2 \leq H/D \leq 2.0$ while the axial flow fan is rotated with 12.0 V input from a dc power supply, corresponding to a nominal Reynolds number of 9.0×10^3 (based on D).

2 Experimental Setup and Conditions

2.1 Axial Fan Exit Flow Test Rig. A schematic of the purpose-built test rig for examining the exit flow field associated with an axial flow fan is shown in Fig. 2. To facilitate the measurement of the mean flow velocity drawn by the axial fan, a circular flow tube was connected to the fan inlet. A Perspex™ flat plate having the size of 0.3 m(height) × 0.3 m(width) × 0.01 m(thickness) is mounted on a linear traverse system, allowing for systematic variation in the exit-to-plate spacing (H). Both the axial axis of the exit flow and the center of the plate are coincident with the z-axis, as illustrated in Fig. 2, where V_z, V_r, and V_t denote the velocity component of fluid flow in the axial,

Contributed by the Fluids Engineering Division of ASME for publication in the JOURNAL OF FLUIDS ENGINEERING. Manuscript received June 19, 2008; final manuscript received April 13, 2009; published online May 14, 2009. Assoc. Editor: Chunill Hah.

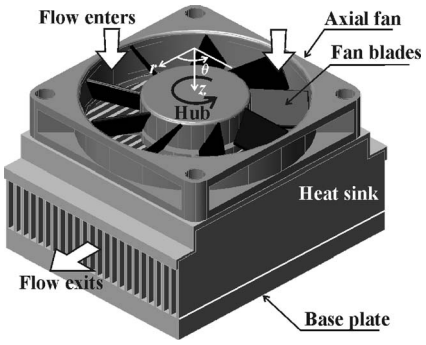

Fig. 1 An axial fan and fin heat sink utilized for central processing unit cooling

radial, and tangential directions, respectively.

The axial flow fan tested in this present study has seven forward-swept fan blades and is ducted with a gap (tip clearance) between the blade tip and the casing. The ratio of tip clearance to blade span δ/S is 0.03. Prior to the flow measurements, the response of the fan rotation speed to input voltage was measured using a Hall-effect sensor, which was used subsequently to synchronize blade position signal with the particle image velocimetry (PIV) system for phase lock averaging. It was found that the fan steadily rotates, for example, within $\pm 0.5\%$ at 2577 rpm with 12.0 V input from a dc power supply. Details of the blades and fan unit are listed in Table 1.

2.2 Velocity and Pressure Measurements. The inlet velocity profile was measured by traversing a Pitot tube placed at $3D$ upstream of the axial fan. The mean incoming flow velocity c_z was calculated from the measured inlet velocity profile. A total of 31 flush mounted static pressure tappings were radially distributed on the flat plate. All of the tappings and stagnation pressure probes were connected to a differential pressure transducer (48 J-type, Scanivalve™), which sends data via an RS232 cable to a data acquisition personal computer.

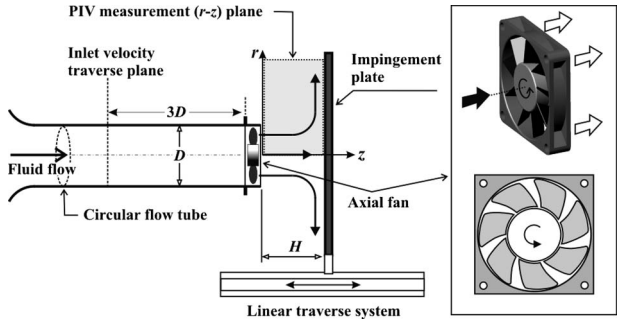

Fig. 2 Schematic of fan exit flow test rig and particle image velocimetry measurement planes

Table 1 Parameters of blades and fan unit tested in this present study

Fan unit	Fan diameter, D	67 mm
	Hub diameter, d	34 mm
	Fan rotation speed at 12.0 V	2577 ± 12 rpm
	Rotor tip speed, V_{tip}, at 12.0 V	9.01 ± 0.04 m/s
	No. of blades	7
	Tip clearance, δ	0.5 mm
Blades	Blade span, S	16.5 mm
	Chord at hub (at tip)	17 mm (24 mm)
	Forward swept angle	30 deg
	Pitch angle at hub (at tip)	+50 deg (+30 deg)
	Twist angle	−20 deg
	Tip clearance-blade span ratio, δ/S	0.03

The particle image velocimetry (Gemini-200–15, LaVision™) composed of a double pulsed neodymium doped:yttrium aluminium garnet (Nd:YAG) laser generator, a charge coupled device (CCD) camera (ImagePro, LaVision™), and a seed particle generator was used to measure the velocity fields of the fan exit flow. A 1 mm thick laser sheet was created by an optical system and aligned with the fan axis for the r-z plane flow measurement (see Fig. 2). Prior to the measurement, the plate was painted in black to minimize reflection.

The time interval of the laser pulse (dt) needs to satisfy the following equation [10]:

$$1000(Vdt)B \leq (dW)/4$$

where V (m/s) is the velocity of seed particles, B (pixel/mm) is the magnification of the CCD camera, and dW is the width of the interrogation window. Prior to the measurement, the average velocity V_0 (m/s) of seed particles is obtained based on the prediction time interval dt_0 (s) of the laser pulses. To improve the precision of PIV measurements, the following iteration was conducted to obtain an optimal dt for the experiment:

$$dt_{i+1}(s) = 0.25dW/(1000(BV_i))$$

$$(i = 0,1,2,3,\ldots)$$

where the initial velocity V_i was estimated based on the measured mass flow rates. The iteration was continued until the value of dt matched the average velocity of the flow field.

Based on the flow velocity and the focal length of the CCD camera to the measurement plane, the time interval (Δt) of each pair of the captured images (2048×2048 pixels) was then set to be 80 μs. The instantaneous velocity fields were subsequently obtained using a cross correlation analysis with an interrogation window of 64×64 pixels and a 50% overlap of vector-to-vector spacing. In total, 40 instantaneous flow images were captured with a sampling frequency of 5 Hz, which is 11.6% of the fan rotation frequency (43 Hz), followed by ensemble averaging.

2.3 Data Reduction Parameters and Uncertainties. The Reynolds number, Re, is defined based on the fan diameter D and the mean axial velocity c_z of the incoming flow through the circular flow tube as

$$\mathrm{Re} = \frac{\rho c_z D}{\mu} \tag{1}$$

where μ and ρ are the viscosity and the density of air, respectively. To evaluate the wall pressure on the target plate, the wall pressure coefficient C_p is defined as

$$C_p = \frac{p_s - p_{\mathrm{in}}}{\rho V_{\mathrm{tip}}^2/2} \tag{2}$$

where p_s is the static pressure measured on the plate, p_{in} is the reference static pressure measured at $3D$ upstream from the axial fan, and V_{tip} is the speed of fan blade tip.

The measurement uncertainties associated with the wall static pressure and the corresponding pressure coefficient were estimated following the method reported by Coleman and Steele [11] (based on 20:1 odds) and found to be within 0.1% and 1.7%, respectively. Note that only random errors were considered. It was assumed that the bias (systematic) errors could be minimized by careful calibrations.

For error analysis of the PIV measurements, it was assumed that the fan exit flow was well traced by seed particles and the time interval of each pair of pulse laser sheets was set accurately. The latter implies that the errors in the r-z plane velocity components were mainly induced by measurement errors in the displace-

ments of the seed particles. According to Wernet [10], the displacement estimates σ_D is primarily determined by the ratio of the correlation peak width d_r (unit: pixel) to the average particle displacement D_P (unit: pixel) across the interrogation window (subregion), expressed as

$$\sigma_D = \frac{d_r}{D_p} \tag{3}$$

where

$$D_p = \Delta t \times V_0 \times 1000/\bar{B} \tag{4}$$

Here, V_0 and $\bar{B}$ are the actual average velocity of seed particles in the flow field and the ratio of the actual particle displacement (unit: millimeters) to the corresponding total number of pixels the seed particles travel (unit: pixel), respectively. Following Wernet [12], the uncertainties of the r-z velocity components measured in this study using PIV were estimated to be within 2.5%.

3 Free Exit Flow of Axial Flow Fan

3.1 Overall Flow Patterns. First, consider flow from the axial fan ejected into the fluid at rest in the absence of a flat plate (i.e., free exit). Figures 3(*a*) and 3(*b*) show the ensemble average velocity vectors in the r-z plane and the radial profiles of the axial velocity in five selected axial planes: $z/D=0.25$, $z/D=0.5$, $z/D=1.0$, $z/D=1.5$, and $z/D=2.0$, where z is the axial location from the fan exit.

The highest axial velocity appears to emerge from the midspan of the fan blades. At $z/D=0.25$, the axial velocity in the radial range of $|r/D|<0.2$ is nearly zero and the flow in the regime $|r/D|\leq 0.6$ remains undisturbed. The exit flow streams tend to contract toward the fan axis until $z/D=0.5$ and then convect downstream parallel to the fan axis until the axial position of $z/D=1.0$ is reached, followed by a radial diversion when $z/D<1.0$. Such diversion is attributed to the centrifugal force generated by the tangential flow motion in the axial range of $0.5<z/D<1.0$. The observation above is consistent with the data reported by Yen and Lin [7].

According to the overall exit flow pattern in the r-z plane shown in Fig. 3, three distinct flow regions may be classified, as follows: First, the "exit flow region" is a region where high momentum flow emerges from the axial fan. Second, the "inner flow region" is a region where the flow is surrounded by the exit flow (region). Finally, the "outer flow region" is a region where the surrounding fluid at rest is present. Consequently, one shear layer each forms at the boundary between the exit and outer flow regions (as in the conventional jets), and between the exit and inner flow regions. The latter is a unique feature of the exit flow generated by the axial fan, with the displaced flow formed at the central part of the exit flow. Note that only one shear layer between the exit and outer flow regions is formed in the conventional jets [6].

3.2 Radial and Tangential Flow Behaviors. Since the flow emerging from the present axial fan is three dimensional (3D), it is instructive to examine the radial and tangential flow motions in addition to the axial motion. To this end, the radial profiles of both velocity components are sliced in a way similar to that carried out for the axial component (Fig. 3(*b*)) and are presented in Figs. 4(*a*) and 4(*b*). During the analysis, the velocity components measured using PIV were normalized by the blade tip speed V_{tip}, which was calculated to be 9.01 m/s for 2577 rpm.

In comparison, the radial motion at $z/D=0.25$ is much weaker (i.e., less than $0.1V_{\text{tip}}$ (Fig. 4(*a*)) than the axial motion, the latter as large as $0.4V_{\text{tip}}$ (Fig. 3(*b*)). As previously discussed, the flow contracts, having a positive radial velocity when $r/D<0$ and a negative value when $r/D>0$. On the other hand, the tangential motion is found to be as pronounced as the axial motion, reaching about 60% of the axial peak velocity, as displayed in Fig. 4(*b*). At an axial plane (e.g., $z/D=0.25$), the change of sign of the tangential

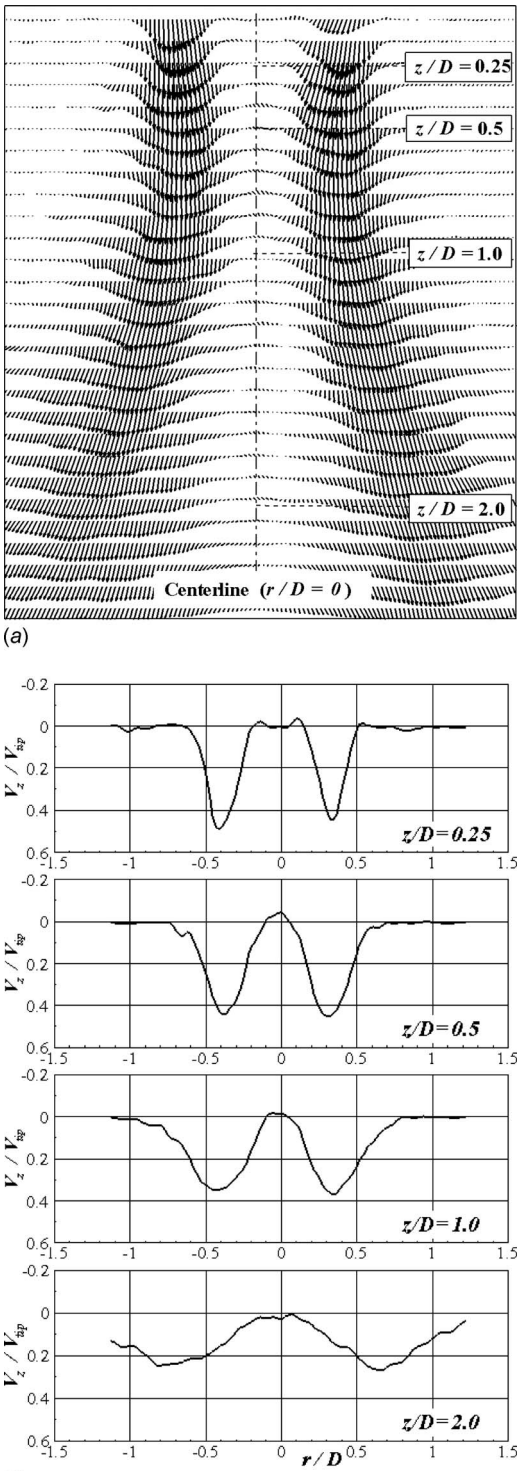

Fig. 3 Overall exit flow structures obtained from PIV measurements for Re=9.0×10³: (*a*) ensemble average velocity vectors and (*b*) radial profiles of axial velocity, at five selected axial planes

velocity occurs when $|r/D|>0.75$. The tangential motion of the exit flow causes shear between the exit flow and the surrounding fluid at rest. For this axial plane ($z/D=0.25$) placed relatively close to the fan, the tangential velocity is strong enough (having up to 30% of the blade tip speed, i.e., $V_t \sim 0.3V_{\text{tip}}$) to generate recognizable counter-rotating vortices.

Further downstream, the magnitude of the peak axial velocity is

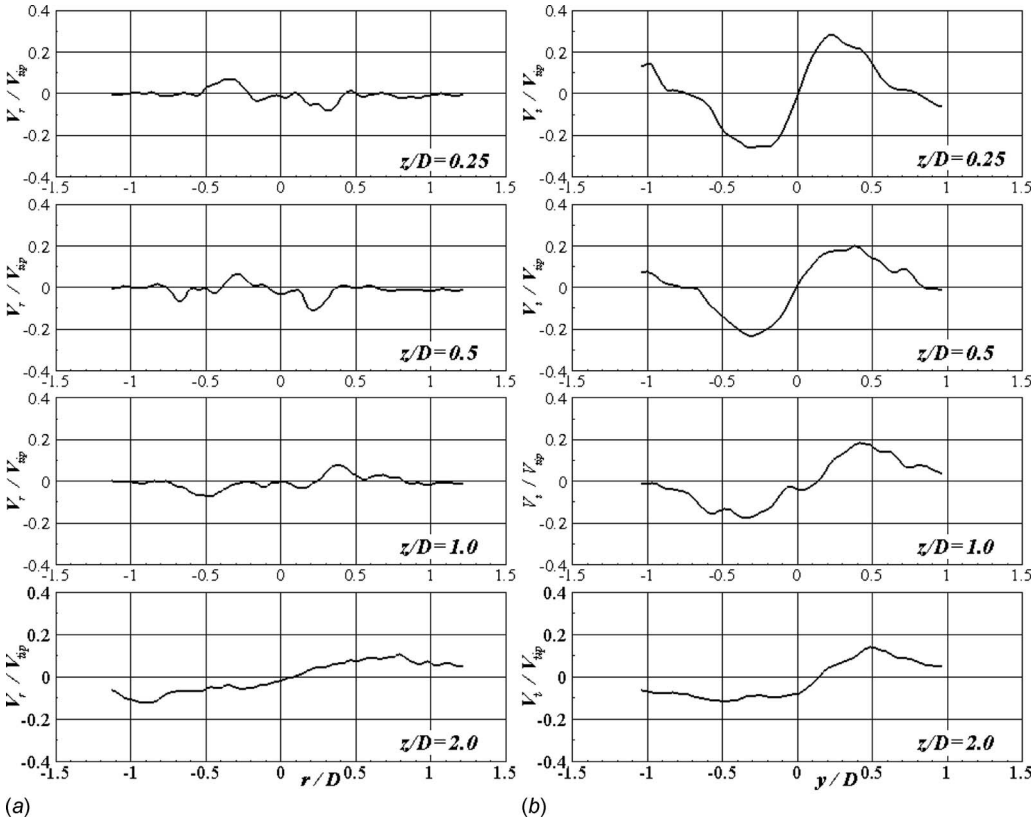

Fig. 4 Radial distributions of (*a*) radial and (*b*) tangential velocity components obtained from PIV measurements for Re=9.0×10³

reduced, with its radial location moving outward. For example, at $z/D=2.0$, the axial velocity at the peaks is about half that measured at $z/D=0.25$, and the radial location of the peaks is now located at $r/D=\pm 0.75$. Meanwhile, the magnitude change of the tangential velocity is pronounced, with the peak value reduced from $0.3V_{tip}$ at $z/D=0.25$ to $0.1V_{tip}$ at $z/D=2.0$.

4 Exit Flows of Axial Fan With Impingement

4.1 Overall Flow Structures. Of particular interest is how the exit flow patterns vary when a flat plate is present downstream and how the local wall pressure distribution on the flat plate changes as the separation distance between the fan and the plate is varied. To this end, PIV flow measurements between the fan exit and flat plate as well as static pressure measurements on the flat plate were performed. Figure 5 displays the velocity vector fields in the r-z plane for $H/D=1.0$, 0.5, and 0.25, respectively.

In general, the fan exit flows is decelerated axially and deflected radially outward as it approaches the flat plate, as shown by the ensemble average velocity vectors in the r-z plane (Fig. 5). The presence of flow recirculation toward the center of the plate (i.e., $r/D=0$) distinguishes the overall exit flow patterns (Fig. 5) from those without impingement (Fig. 3(*a*)) [13]. The recirculated flows meet and interact near the central portion of the flat plate. Conventionally, this region is called the secondary stagnation region, compared with the primary stagnation region where the exit flow impinges directly on the plate [14]. In the secondary stagnation region, the flow interaction causes recirculation toward the axial fan exit.

To obtain more details of the impingement flow, Fig. 5 is sliced in a way similar to that carried out for free exit axial fan flows (Figs. 3(*b*) and 4) at an axial plane close to the flat plate (e.g., $z/H=0.9$). The obtained radial distributions of the axial and radial velocity components are plotted in Figs. 6(*a*) and 6(*b*), respec-

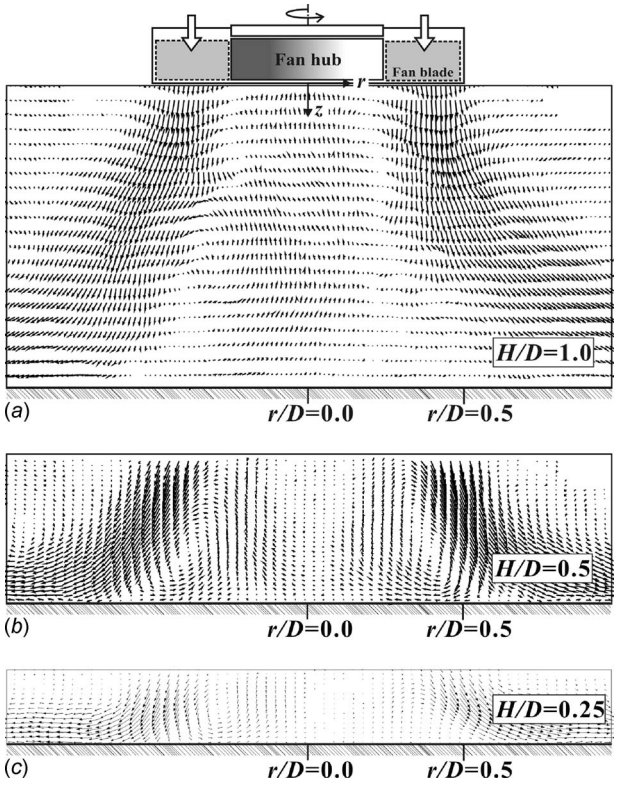

Fig. 5 The *r-z* plane velocity vectors for varying exit-to-plate spacings: (*a*) *H*/*D*=1.0, (*b*) *H*/*D*=0.5, and (*c*) *H*/*D*=0.25

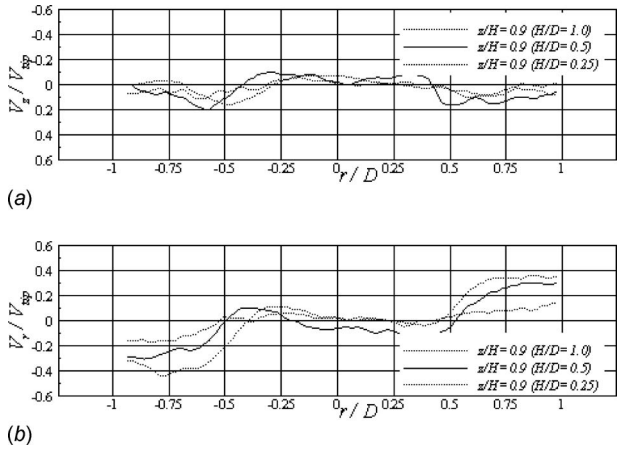

Fig. 6 Radial distributions of axial and radial velocity components of the axial fan flow for a fixed relative axial location, e.g., $z/H=0.9$ within the exit-to-plate spacings ($H/D=0.25$, 0.5, and 1.0); (*a*) axial velocity profile and (*b*) radial velocity profile

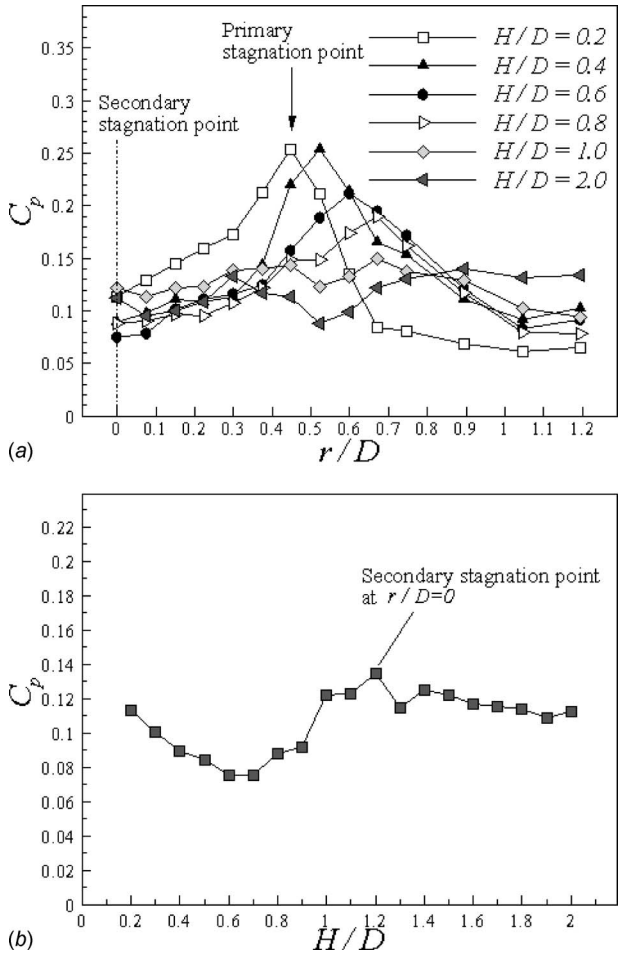

Fig. 7 Distributions of wall pressure coefficient C_p: (*a*) radial distribution, and (*b*) variation in C_p at the secondary stagnation point ($r/D=0$) with the exit-to-plate spacing

tively. It is seen that as the separation distance is increased from $H/D=0.25$ to $H/D=0.5$, the flow region where a stronger negative axial velocity exists becomes widened whereas a further increase in the separation distance to $H/D=1.0$ reduces its radial extent. Moreover, among the three separation distances considered, the peak of the axial velocity impinging on the plate is highest for $H/D=0.5$. Also, from the radial velocity component shown in Fig. 6(*b*) for the same axial plane ($z/H=0.9$), it is seen that the radial velocity toward the center of the plate at $H/D=0.5$ is larger than that at either $H/D=0.25$ or $H/D=1.0$.

The radial profiles of the axial and radial velocities displayed in Fig. 6 indicate that, when the separation distance is relatively short (e.g., $H/D=0.25$), radial flow is dominant near the plate. At larger separation distances (e.g., $H/D=1.0$), both of the velocity components decrease before the exit flow reaches the plate due to increased flow mixing with the surrounding fluid. The present flow data suggest that flow recirculation toward the axial fan from the plate is strongest when the separation distance reaches approximately $H/D=0.5$.

4.2 Distribution of Static Wall Pressure on Flat Plate. To investigate further the influence of exit flow patterns (especially in the secondary stagnation region), the radial distribution of wall pressure on the target plate was measured. Figure 7(*a*) plots the wall pressure coefficient C_p defined in Eq. (2) as a function of radial position r/D for selected separation distances ($H/D=0.2$, 0.4, 0.6, 0.8, 1.0, and 2.0).

The peaks of the wall pressure coefficient on the plate (Fig. 7(*a*)) appear to be associated with the impingement of high velocity peaks (see Fig. 6). Since only the time averaged values were measured using the pneumatic pressure tappings, the obtained pressure distribution is symmetric with respect to the fan axis ($r/D=0$) regardless of the separation distance. Note that for $H/D=0.2$, the static pressure is low in the secondary stagnation region but higher than other regions except in that of the primary stagnation region. The static pressure then monotonically increases before peaking at $r/D=\pm 0.45$ (primary stagnation region). Outward away from the peaks, the wall pressure coefficient decreases.

As the plate is moved away (downstream) from the fan exit (e.g., $H/D=0.4$, 0.6, 0.8, 1.0, and 2.0), the highest pressure region tends to be widened and the peak pressure values decrease (except for the case of $H/D=0.4$, which has a peak pressure similar to that for $H/D=0.2$). The reduction in the peak pressure is caused by the dissipation of momentum before the exit flow reaches the plate (see also Fig. 6). Furthermore, the location of the peak pressure moves radially outward as the separation distance is increased. It is suggested that when convecting downstream, the exit flow is affected by the centrifugal force generated by its tangential motion, causing the radial shift of the primary stagnation point.

4.3 Wall Pressure in Secondary Stagnation Region. The importance of the secondary stagnation region in conventional multijet arrays is associated with the uniformity requirement of local heat transfer distribution, for example, during the tempering of glass plate and the annealing of metal sheets. The flow between two neighboring jets is typically recirculation dominant, analogous to the case considered in the present study (see Fig. 5). For axial fan flow impinging on fin heat sinks (or a target plate), unfortunately, a heat source (e.g., the central processing unit or CPU) is usually located at an area under the direct influence of the secondary stagnation region. Despite its importance, studies on the flow and heat transfer behaviors in the secondary stagnation region are scarce [14]. While only the flow and pressure behaviors in the secondary stagnation region are of concern below, the corresponding heat transfer behavior will be examined in a separate study.

Consider first the wall static pressure coefficient in the secondary stagnation region. As can be seen from Fig. 7(*a*), in this region, the increase in the separation distance from $H/D=0.2$ to $H/D=0.6$ results in a decrease in C_p whereas a further increase to $H/D=2.0$ causes an increase in C_p. This implies that, at $H/D=0.6$, the flow in the secondary stagnation region undergoes a "transition," as observed in Fig. 6

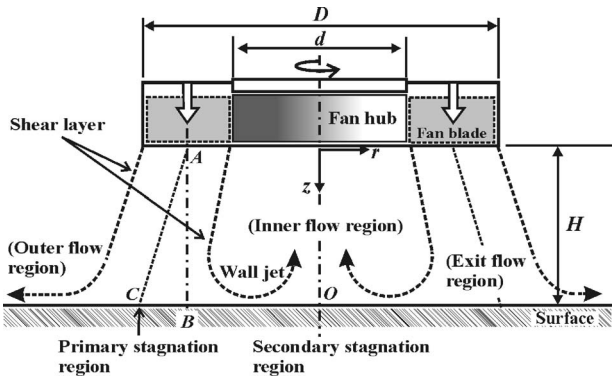

Fig. 8 Sketch of overall exit flows emerging from an axial flow fan

To elaborate this transition, the pressure coefficient at the secondary stagnation point (i.e., $r/D=0$) was plotted in Fig. 7(*b*) as a function of the separation distance. The wall static pressure coefficient decreases as the separation distance is increased up to $H/D=0.6$, reducing correspondingly the wall static pressure at $r/D=0$. This reduction in the wall static pressure is attributed to the intensified recirculation as the separation distance is increased to $H/D=0.6$. On the other hand, a further increase in H/D leads to an increase in C_p until $H/D=1.2$, which is then followed by a gradual decrease as H/D is increased to 2.0, as displayed in Fig. 7(*b*).

The observed variation in C_p at the secondary stagnation point implies that, at $H/D=0.6$, flow recirculation from the plate is maximized due to intensified flow interaction of recirculated flows in the secondary stagnation region, which is consistent with the flow patterns displayed in Figs. 5 and 6. It can also be inferred from these results that, within the range considered ($0.2 \leq H/D \leq 2.0$) and with the case of $H/D=2.0$ serving as a reference, the flow interaction tends to be suppressed by the proximity of the plate at $H/D=0.2$ and weakened due to the momentum dissipation at $H/D=2.0$.

4.4 Sketch of Overall Exit Flow Patterns. Based on the overall flow features observed with the PIV flow data and wall pressure distribution, a sketch of the axial fan exit flow impinging on a flat plate may be made, as illustrated in Fig. 8. Three different flow regions can be summarized as follows.

(1) *Exit flow region*. The flow emerging from the fan stagnates on the flat plate. Due to the high pressure formed in the secondary stagnation region and the centrifugal force resulting from the tangential motion of the exit flow, the axis *AC* of the impinging flow coinciding with the primary stagnation region is not parallel to the fan axis (i.e., the *z*-axis or the axis *AB*).
(2) *Inner flow region*. The flow recirculates toward the fan axis after the impingement, forming the secondary stagnation region where two flow streams recirculating in opposite directions in the *r*-*z* plane meet and interact. Furthermore, highly vortical flows that are confined between the fan hub and the impingement plate exist in this region.
(3) *Outer flow region*. The flow is at rest. In a small closed system, the flow in this region may be drawn by the axial fan.

5 Practical Significance

To demonstrate how the present results can be used in practice, consider the case of an axial fan exit flow impinging on a conventional fin heat sink. The overall size of the heat sink (especially that of the base heat spreader plate) is typically as large as the axial fan. The fan exit-to-plate spacing (H/D) is less than half the fan diameter, limited by the fin height. A square-shaped heat source (e.g., CPU) is attached to the central portion of the base plate, occupying approximately 15% of the total plate area.

For $H/D=0.5$, which is the typical fin height, the present results suggest that the primary stagnation point is located radially between $r/D=0.5$ and $r/D=0.6$. In other words, the exit flow impinges on the edge of the base plate of the heat sink. Consequently, the heat source is posed mainly in the secondary stagnation region. On the other hand, a base plate having a finite thickness (e.g., approximately 10% of the base plate width) and made of a highly thermal conducting material (e.g., aluminum) allows the lateral spreading of heat. However, despite the lateral spreading of heat through the base plate and then the fins, a further design improvement of conventional fin heat sinks driven by an axial fan is required so that the heat transfer performance in the secondary stagnation region can be enhanced. We will address this issue in a separate study.

6 Conclusions

The flow patterns of a free exit flow emerging from an axial fan and its impingement on a flat plate were characterized experimentally. The following conclusions were drawn.

(1) While a shear layer is formed between the exit flow and the outer flow (surrounding the fluid at rest) as in a conventional jet, another distinct shear layer is formed between the exit flow and the inner flow. The latter is a unique feature of the exit flow generated by the axial fan, with the displaced flow area located at the central portion of the exit flow.
(2) The impingement of the axial fan flow causes a secondary stagnation region at the center of the impingement plate, coinciding with the fan axis. The overall flow patterns in the secondary stagnation region are analogous to those in two neighboring jet-to-jet arrays, apart from the tangential motion in the former.
(3) The exit flow patterns change as the normalized fan exit-to-plate spacing (H/D) is varied and, under the conditions considered in the present study, an optimal spacing of $H/D=0.6$ exists, which maximizes the recirculated flow interaction in the secondary stagnation region.

Acknowledgment

This work was supported by the National Basic Research Program of China (Contract No. 2006CB601203), the National Natural Science Foundation of China (Contract Nos. 50676075, 10632060, and 10825210), the National 111 Project of China (Contract No. B06024), and the National High Technology Research and Development Program of China (Contract No. 2006AA03Z519).

Nomenclature

Cp = pressure coefficient
c_z = mean incoming flow velocity (m/s)
d = fan hub diameter (m)
D = fan diameter (m)
H = exit-to-plate spacing (m)
N = fan rotation speed (rpm)
p_{in} = inlet static pressure measured at $3D$ upstream from the fan (Pa)
p_s = static pressure on a flat plate (Pa)
r, z, θ = coordinates
Re = Reynolds number based on the fan diameter
S = fan blade span (m)
V_z, V_r, V_t = axial, radial, and tangential velocity components of fan exit flow (m/s)
V_{tip} = fan blade tip speed (m/s)
V_0 = average velocity of seed particle (m/s)

Δt = time interval of each pair of pulse laser sheets (μs)
σ_D = displacement estimates
D_P = average particle displacement across the interrogation window (subregion) (pixel)

Greek Symbols

δ = tip clearance (m)
μ = viscosity (kg/ms)
ρ = air density (kg/m^3)

References

[1] Saini, M., and Webb, R., 2003, "Heat Rejection Limits of Air Cooled Plane Fin Heat Sinks for Computer Cooling," IEEE Trans. Compon. Packag. Technol., **26**, pp. 71–79.
[2] Chu, R. C., Simons, R. E., Ellsworth, M. J., Schmidt, R. R., and Cozzolino, V., 2004, "Review of Cooling Technologies for Computer Products," IEEE Trans. Device Mater. Reliab., **4**, pp. 568–585.
[3] El-Sheikh, H. A., and Garimella, S. V., 2000, "Enhancement of Air Jet Impingement Heat Transfer Using Pin-Fin Heat Sink," IEEE Trans. Compon. Packag. Technol., **23**, pp. 300–308.
[4] El-Sheikh, H. A., and Garimella, S. V., 2000, "Heat Transfer From Pin-Fin Heat Sinks Under Multiple Impinging Jets," IEEE Trans. Adv. Packag., **23**, pp. 113–120.
[5] Brignoni, L. A., and Garimella, S. V., 1999, "Experimental Optimization of Confined Air Jet Impingement on a Pin Fin Heat Sink," IEEE Trans. Compon. Packag. Technol., **22**, pp. 399–404.
[6] Martin, H., 1977, "Heat and Mass Transfer Between Impinging Gas Jets and Solid Surfaces," Adv. Heat Transfer, **13**, pp. 1–60.
[7] Yen, S. C., and Lin, F. K. T., 2006, "Exit Flow Field and Performance of Axial Flow Fans," ASME J. Fluids Eng., **128**, pp. 332–340.
[8] Huang, L., and El-Genk, M. S., 1994, "Heat Transfer of an Impinging Jet on a Flat Surface," Int. J. Heat Mass Transfer, **37**, pp. 1915–1923.
[9] Baughn, J. W., and Shimizu, S., 1989, "Heat Transfer Measurements From a Surface With Uniform Heat Flux and an Impinging Jet," ASME J. Heat Transfer, **111**, pp. 1096–1098.
[10] Wernet, M. P., 2000, "Application of DPIV to Study Both Steady State and Transient Turbomachinery Flows," Opt. Laser Technol., **32**, pp. 497–525.
[11] Coleman, H. W., and Steele, W. G., 1999, *Experimentation and Uncertainty Analysis for Engineers*, 2nd ed., Wiley, New York.
[12] Wernet, M. P., 1991, "Particle Pisplacement Tracking Applied to Air Flows," Proceedings of the Fourth International Conference on Laser Anemometry, pp. 327–335.
[13] Ichimiya, K., 2003, "Heat Transfer Characteristics of an Annular Turbulent Impinging Jet With a Confined Wall Measured by Thermosensitive Liquid Crystal," Heat Mass Transfer, **39**, pp. 545–551.
[14] Can, M., 2003, "Experimental Optimization of Air Jets Impinging on a Continuously Moving Flat Plate," Heat Mass Transfer, **39**, pp. 509–517.

Reynolds Number Effects on the Performance Characteristic of a Small Regenerative Pump

Shin-Hyoung Kang
Seoul National University,
599 Gwanak-ro,
Gwanak-gu,
Seoul 151-742, Korea
e-mail: kangsh@snu.kr

Su-Hyun Ryu
Korea Institute of Nuclear Safety,
34 Gwahak-ro,
Yuseong-gu,
Daejeon 305-338, Korea
e-mail: k653rsh@kins.re.kr

This paper studies the effect of the Reynolds number on the performance characteristics of a small regenerative pump. Since regenerative pumps have low specific speeds, they are usually applicable to small devices such as micropumps. As the operating Reynolds number decreases, nondimensional similarity parameters such as flow and head coefficients and efficiency become dependent on the Reynolds number. In this study, the Reynolds number based on the impeller diameter and rotating speed varied between 5.52×10^3 *and* 1.33×10^6*. Complex three-dimensional flow structures of internal flow vary with the Reynolds numbers. The coefficients of the loss models are obtained by using the calculated through flows in the impeller. The estimated performances obtained by using one-dimensional modeling agreed reasonably well with the numerically calculated performances. The maximum values of flow and head coefficients depended on the Reynolds number when it is smaller than* 2.65×10^5*. The critical value of the Reynolds number for loss coefficient and maximum efficiency variations with Reynolds number was* 1.0×10^5*.*
[DOI: 10.1115/1.3026629]

1 Introduction

Regenerative pumps create high pressure head at low flow rates and have low specific speeds. Recently, they have been widely used for fuel supply systems in automobiles. They have also been used as a blower for the hydrogen supplying system in fuel cell vehicles.

Performance analysis and testing of regenerative pumps have been conducted since the 1950s. Wilson et al. [1] and Iversen [2] studied the flow inside the pump and developed a loss model based on their experiments. Shimosaka and Yamazaki [3] measured the performance of an open channel type pump for various numbers of vanes, clearances, and channel areas. Hollenberg [4] studied the effects of the Reynolds number on the performance variation in regenerative pumps. In the 1990s, Hübel et al. [5] visualized the internal flow of an automotive fuel pump and compared it to the calculated three-dimensional flows. Badami [6] developed a new design for a side channel type regenerative pump after he studied the performance results for different clearances, number of vanes, blade angles, and areas of the side channels. However, it has been still difficult to design regenerative pumps based on generally accepted rules.

The regenerative pumps shown in Fig. 1 have a simple assembly consisting of an impeller and a casing, which has an inlet and outlet. The side channel has a stripper between the inlet and outlet ports. Very complex flow is generated by the flow circulation that develops in the moving impeller vane and the side channel. A helical-shaped flow appears from the inlet to the outlet due to the circulating flow except in the stripper region separating the inlet from the outlet port. Since the flow in the vane is highly three-dimensional with a relatively large internal loss, the efficiency of the regenerative pumps is lower than those of other turbo-type pumps at low specific speeds. However, they operate at one order smaller values of specific speed than the centrifugal pumps. The impeller is very simple to manufacture even for small machines. Figure 2 shows a longitudinal cross section of the pump at section A-A of Fig. 1.

We focus on the potential of the regenerative pumps for application to very small devices, such as micropumps. In such a case, the Reynolds number becomes very small and the through flow can be considered to be a laminarlike flow. Kang et al. [7] studied the flow structures and design parameters of the regenerative pump at high Reynolds numbers. However, the data accumulated for high Reynolds numbers cannot be used, and extensive design data for low Reynolds numbers are needed. Therefore, in this study, we used numerical simulation to study the effects of the Reynolds number on the performance characteristics of a small regenerative pump to investigate its potential for application to small systems. First, we compared the flow characteristics of the pump between a high and low Reynolds number. Second, we assumed a new loss model and verified it numerically. Finally, we checked the variations in the performance characteristics by one-dimensional analysis for various Reynolds numbers.

2 A Pump Model and Calculation Method

The test model shown in Table 1 has a curved leading edge, which reduces the incidence loss of vanes and increases the momentum exchange within the circulatory flow. There are 45 equally spaced vanes in the periphery of the impeller. As the flow comes in through the inlet, the vane applies work on the fluid and increases the flow pressure. After the transient region near the inlet, the pressure increases linearly and the flow becomes periodic in the vane-to-vane region of the impeller. However, the flow becomes transient again as the vane approaches the discharge outlet and the stripper. The flow is unsteady in the vane as it passes the transient regions of the inlet and outlet of the pump and generates extra pressure loss. However, the vane shape is usually designed based on the performance of the vane in a fully developed flow region, where the pressure increases linearly. Therefore, flow calculations are performed in a vane-to-vane region of the impeller and side channel. The effects of the inlet and outlet ports and the stripper on the hydrodynamic performance of the pump should be taken into account to predict the pump performance. Figure 3 shows the flow domain to be applied for numerical calculations. The hatched region is the blade. The upstream and downstream boundaries are located between two blades. The pe-

Contributed by the Fluids Engineering Division of ASME for publication in the JOURNAL OF FLUIDS ENGINEERING. Manuscript received March 5, 2007; final manuscript received September 30, 2008; published online May 15, 2009. Assoc. Editor: Yu-Tai Lee.

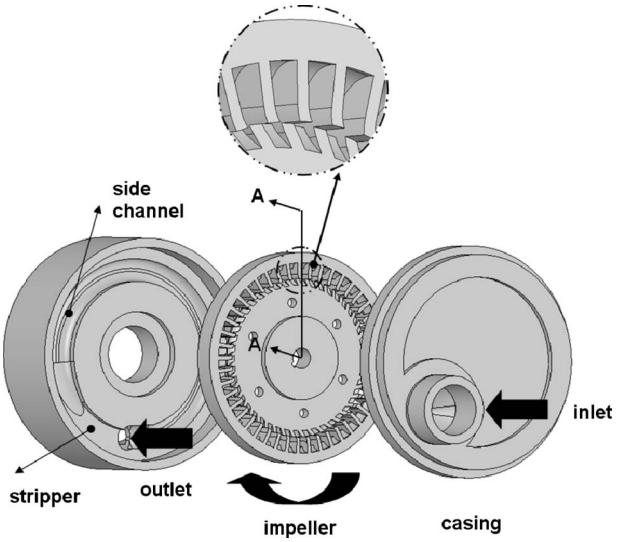

Fig. 1 Regenerative pump assembly

riodic condition of all variables is applied on both planes. The plane 1-2-3-4 is the sliding surface between the moving impeller and the stationary casing with the side channel. The planes 5-6-7-8 and 9-10-11-12 are the plane of symmetry between the rear and front blades. All the solid surfaces including the blade are moving; however, the channel wall is stationary.

CFX-TASCFLOW is used in this study, and the basic specifications of the pump are summarized in Table 1. The working fluid is gasoline, and the Reynolds number is calculated based on the outer diameter of the channel and the rotating speed. We used a relative frame of reference for the impeller and vanes because the impeller rotates relative to the side channel wall. We assumed the flow to be turbulent. A low Reynolds number κ-ε turbulence model was adopted to consider the low-speed viscous effects through the pump. We adopted the generated grid and numbers of the nodes in the study of flow at high Reynolds numbers by Kang et al. [7]. Extra nodes were allocated near the walls for y^+ to be 1.0–2.0. The total number of the nodes is about 490,000.

Head rise is usually obtained for a given flow rate. However, the flow is calculated for a given value of head rise in the study. The flow rate is obtained integrating the tangential component of velocity in the side channel. The variation in pressure rise can be thought of as a superposition of a component linearly increasing in the circumferential direction and a periodic fluctuation set in one vane space. By specifying the body force corresponding to the linearly increasing pressure rise per vane, the flow can be calculated using periodic boundary conditions of all variables on the inlet and outlet planes of the calculation domain. The body force [7] is given as follows:

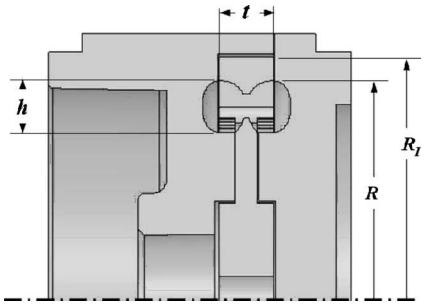

Fig. 2 Section view of a regenerative pump

Table 1 Specifications of simulated impeller parameters

Blade array (front)	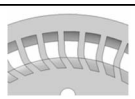	Blade array (side)	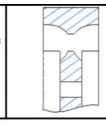
Blade array (up)			
A	4.06 mm^2	ν	$5.4\times10^{-7}\,m^2/s$
Z	45	ρ	$750\,kg/m^3$
h	3.5 mm	N	7500 rpm
t	3.8 mm	Re	6.63×10^5
R	15 mm	ϕ_{op}	0.666
R_I	16.65 mm	ψ_{op}	3.650

$$f_\theta = \frac{\rho g H}{r(2\pi - \theta_s)} \tag{1}$$

The flow rate is obtained by integrating the velocity distribution on the exit plane.

3 Calculated and Measured Performances

For a low Reynolds number, we have no experimental data for the present test model. Instead, we compared the experimental results with numerical results to verify our calculations for a high Reynolds number ($\mathrm{Re}=6.63\times10^5$). The details of the experimental results are described in this paper by Lim and Kang [8].

Figure 4 shows the measured performance data for different gaps between the impeller and the casing wall. There are three sources of leakage flow rate: the inner leakage Q_1, the outer leakage Q_2, and the leakage through the stopper Q_3. When the three leakages and the flow reduction corresponding to the inlet and outlet pressure losses Q_{io} were corrected by Lim and Kang [8] using the correlations suggested by Shim and Kang [9], the scattered data collapsed into a single performance line, as shown in Fig. 4. However, the uncertainty band of performance of one vane space with consideration of the uncertainty of the measured gap (0.13–0.20 mm) is shown in Fig. 4. The calculated performance is in good agreement with the corrected performance of the measured data. Hence, the numerical results were reasonable for

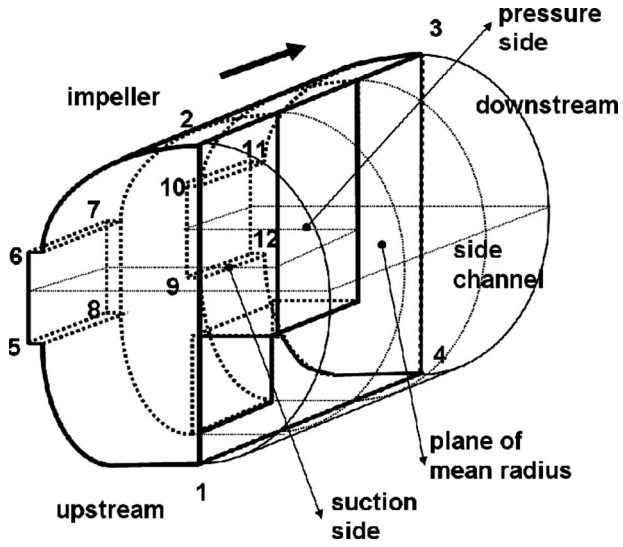

Fig. 3 Domain for numerical calculations

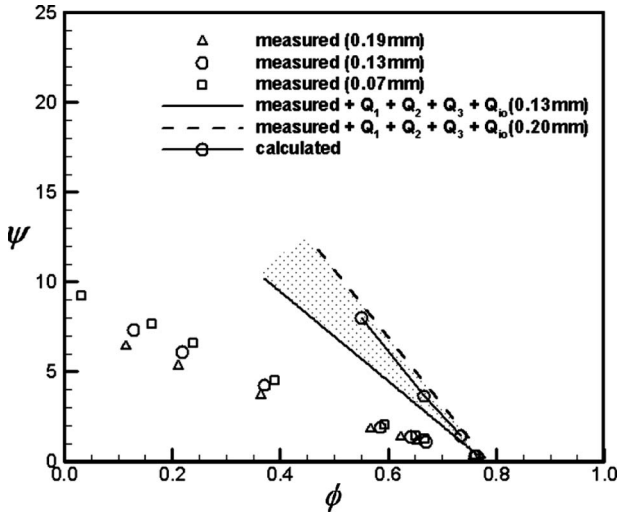

Fig. 4 Comparison between measured and calculated head versus flow coefficients

studying the performance characteristics of a small regenerative pump. We also calculated the performance for three different numbers of nodes: 90,000, 490,000, and 1,120,000. The calculated flow coefficients for the design head coefficient, 3.650, were 0.660, 0.666, and 0.667, respectively. For the present study, 490,000 nodes were considered sufficient. We focused on the hydrodynamic behavior in one vane-to-vane space with zero leakage even for a small size pump in the present study.

4 Flow Characteristics

A highly three-dimensional flow passes the vane and the side channel. The variation in the flow characteristics is numerically investigated at high and low Reynolds numbers. The flow field of the high Reynolds number $Re=6.63\times10^5$ is calculated as well as that of the low Reynolds number $Re=6.63\times10^3$. The regenerative pump is operated at the design point and the streamlines, tangential velocity components, and static pressure contours are compared at the suction and pressure side planes and at the plane of the mean radius shown in Fig. 3.

The internal flow structures are presented for the case of a high Reynolds number ($Re=6.63\times10^5$) from Figs. 5–8. The results of the suction side plane are shown in Fig. 5. The vortex core of the circulatory flows in Fig. 5(*a*) appears in the side channel region. Tangential velocity components are large over the impeller tip, as shown in Fig. 5(*b*), where the swirling flow is also strong. The rates of momentum exchanges are dominant here rather than over the hub. The static pressure is low over a large portion of the channel region where the vortex core appears (see Fig. 5(*c*)).

The results on the periodic boundary at the middle of the vanes are shown in Fig. 6. The vortex core in Fig. 6(*a*) moves into the center region of the pump. High tangential velocity appears over the tip, as shown in Fig. 6(*b*), and relatively low velocity near the hub. The static pressure in Fig. 6(*c*) becomes minimum at the vortex core. The tangential velocity and static pressure are radically stratified from the hub to the tip.

The results on the pressure side plane are shown in Fig. 7. The vortex core in Fig. 7(*a*) moves into the center of the vane. High tangential velocity appears near the vane tip of the side channel, as shown in Fig. 7(*b*). The static pressure distributions shown in Fig. 7(*c*) are generally high over the vane and especially near the tip region.

The results of the plane of mean radius are shown in Fig. 8. Figure 8(*a*) shows the formation of two radial vortices due to the flow around the pressure and suction surfaces of the vane. The contours of the tangential velocity components are shown in Fig. 8(*b*). The maximum tangential motion occurs near the vane corner on the pressure side. The static pressure is large on the pressure

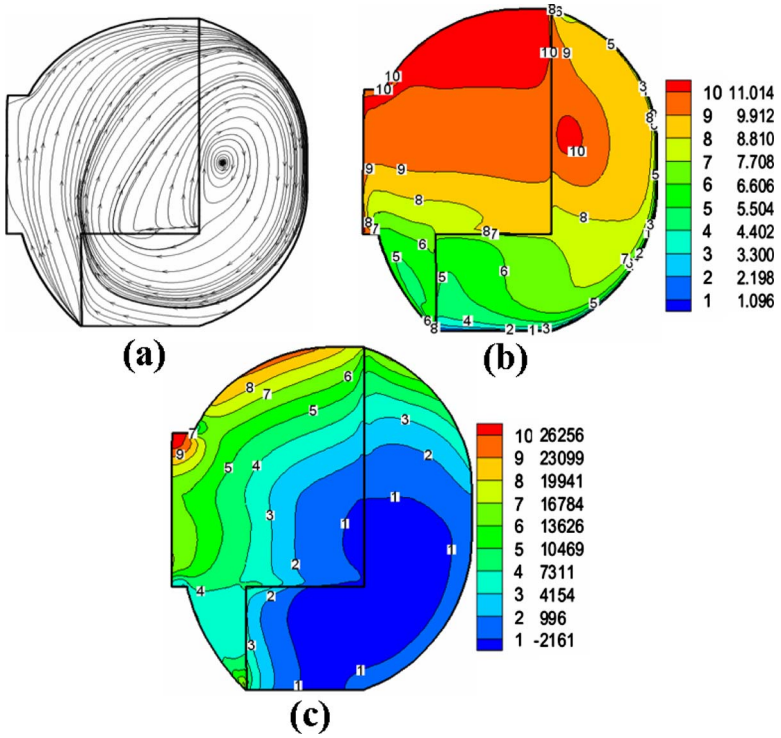

Fig. 5 Flow distributions at the suction side of the blade ($Re=6.63\times10^5$): (*a*) streamlines, (*b*) tangential velocity, and (*c*) static pressure distributions

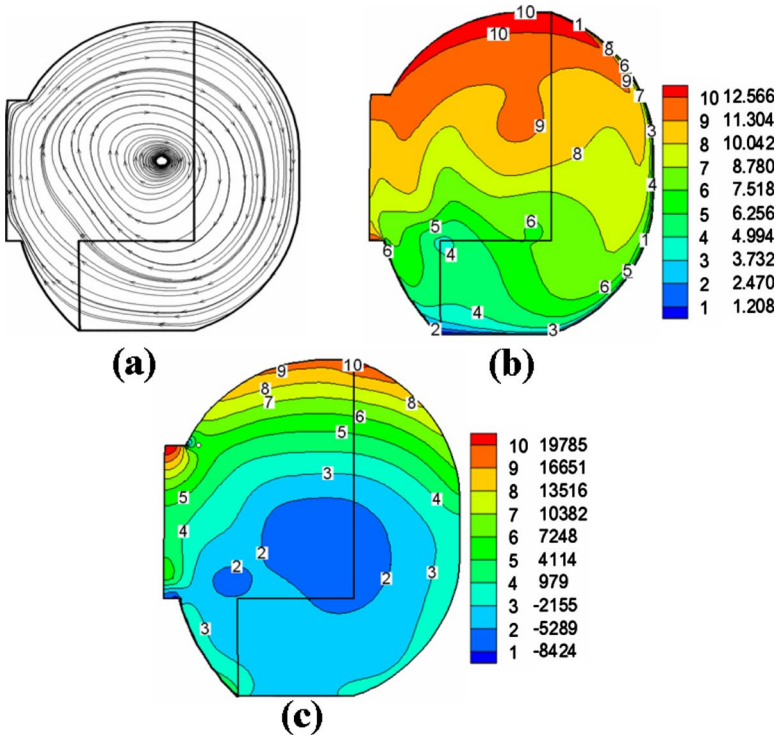

Fig. 6 Flow distributions at the periodic boundary of the blades (Re=6.63 $\times 10^5$): (*a*) streamlines, (*b*) tangential velocity, and (*c*) static pressure distributions

surface and small on the suction surface in Fig. 8(*c*). The flow in the vane is highly three-dimensional and is composed of strong tangential and radial vortex cores.

The flow structures for the case of a low Reynolds number Re=6.63×10^3 are presented from Figs. 9–12. The results on the suction side plane are shown in Fig. 9. The vortex core of the circulatory flows, shown in Fig. 10(*a*), does not appear in the side channel region. When the Reynolds number is small, the circulatory flows are not well developed due to the strong viscous effects near the channel wall. The tangential velocity components are

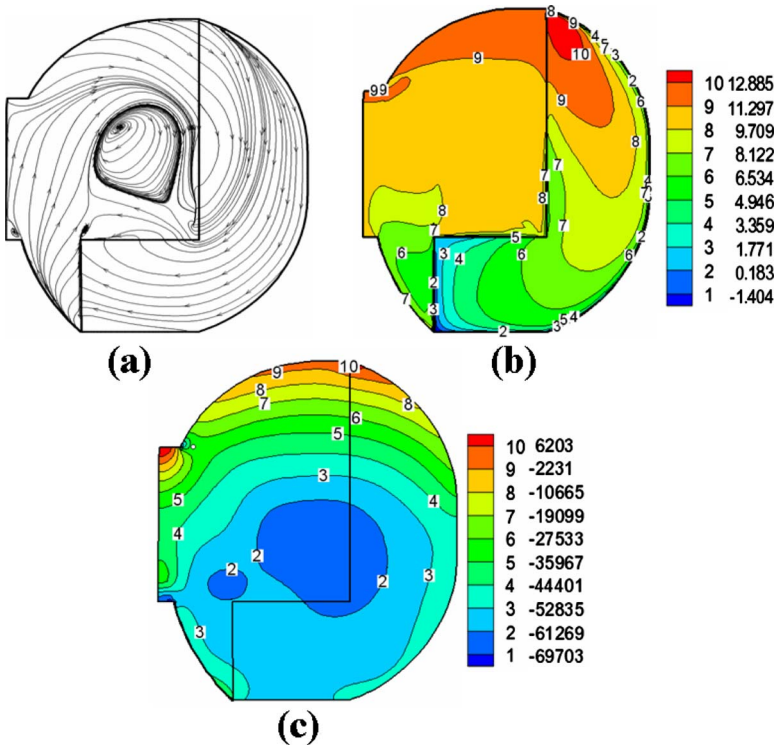

Fig. 7 Flow distributions at the pressure side of the blade (Re=6.63×10^5): (*a*) streamlines, (*b*) tangential velocity, and (*c*) static pressure distributions

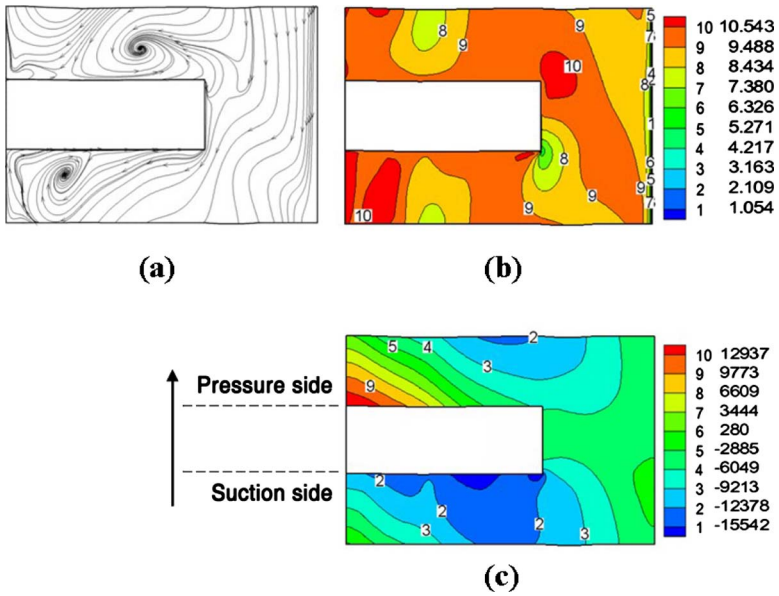

Fig. 8 Flow distributions at the plane of mean radius ($Re=6.63\times10^5$): (*a*) streamlines, (*b*) tangential velocity, and (*c*) static pressure distributions

large in the vane region, as shown in Fig. 9(*b*). The static pressure is low in the channel region and shows a locally high pressure at the interface region in Fig. 9(*c*). The results for the periodic boundary between vanes are shown in Fig. 10. The streamline in Fig. 10(*a*) is similar to that for a high Reynolds number. The tangential velocity shown in Fig. 10(*b*) shows high speed near the blade tip corner and small speed near the hub side channel. Minimum static pressure occurs at the impeller hub, as shown in Fig. 10(*c*).

The results on the pressure side plane are shown in Fig. 11. The vortex core in Fig. 11(*a*) is not the same as that on the suction side. The circulatory flows are insufficient to drive the high energy flow into the side channel; therefore, high tangential velocity occurs in the blade region for this case of a low Reynolds number (see Fig. 11(*b*)). The static pressure distributions in Fig. 11(*c*) are high at both the tip of the vane and the channel region.

The results for the plane of mean radius are shown in Fig. 12. Figure 12(*a*) shows the formation of one radial vortex at the suc-

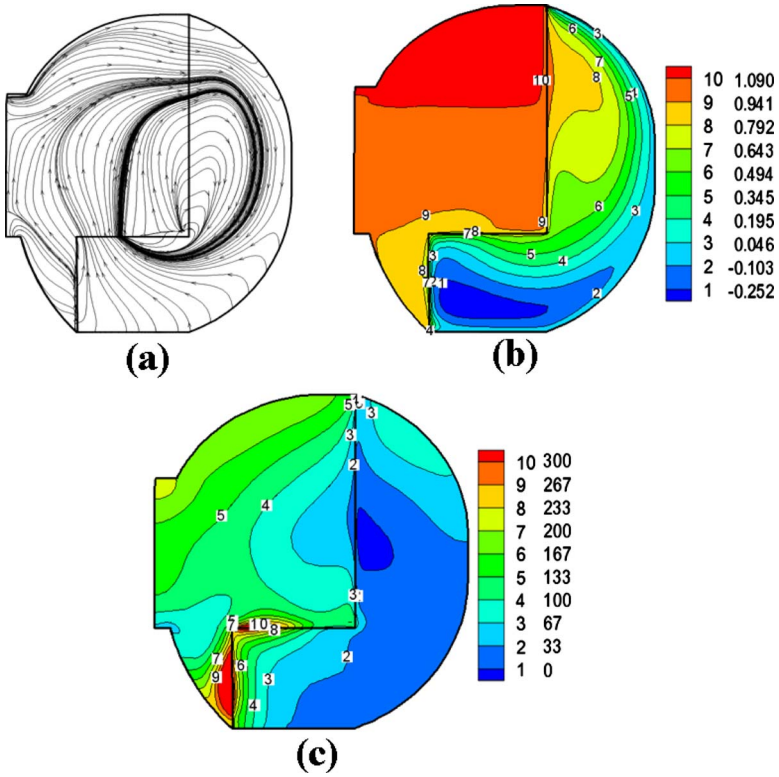

Fig. 9 Flow distributions at the suction side of the blade ($Re=6.63\times10^3$): (*a*) streamlines, (*b*) tangential velocity, and (*c*) static pressure distributions

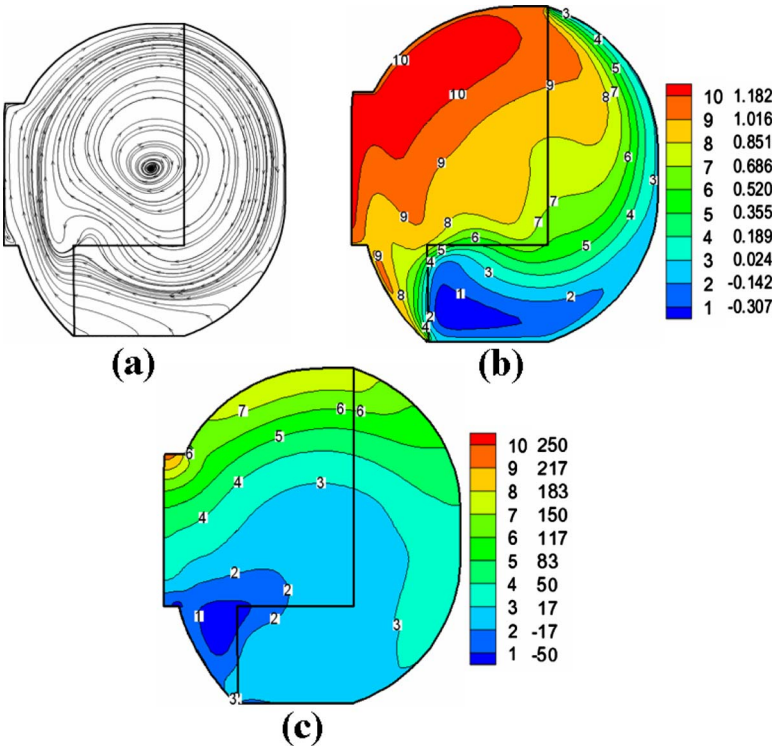

Fig. 10 Flow distributions at the periodic boundary of the blades (Re $=6.63\times10^3$): (*a*) streamlines, (*b*) tangential velocity, and (*c*) static pressure distributions

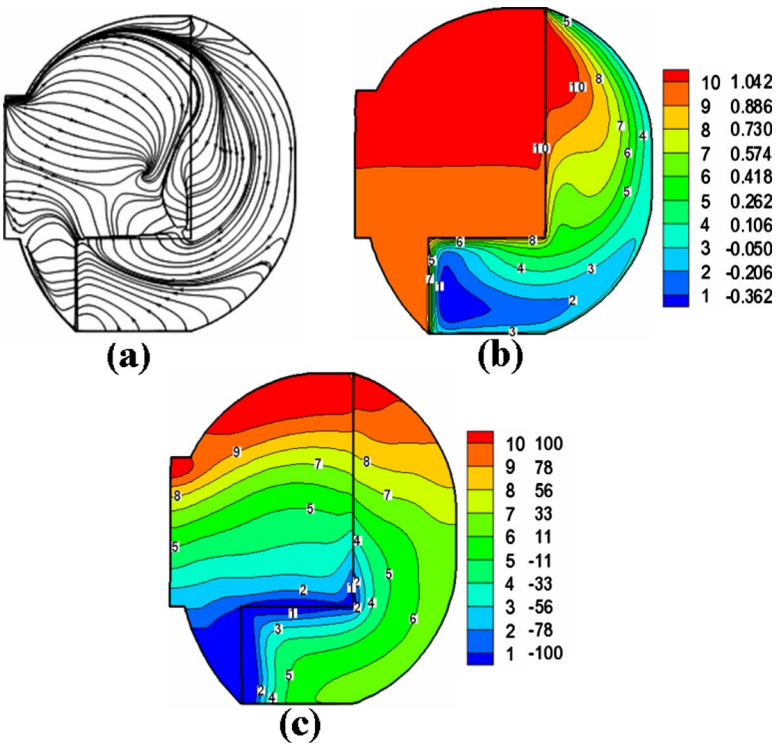

Fig. 11 Flow distributions at the pressure side of the blade (Re=6.63 $\times10^3$: (*a*) streamlines, (*b*) tangential velocity, and (*c*) static pressure distributions

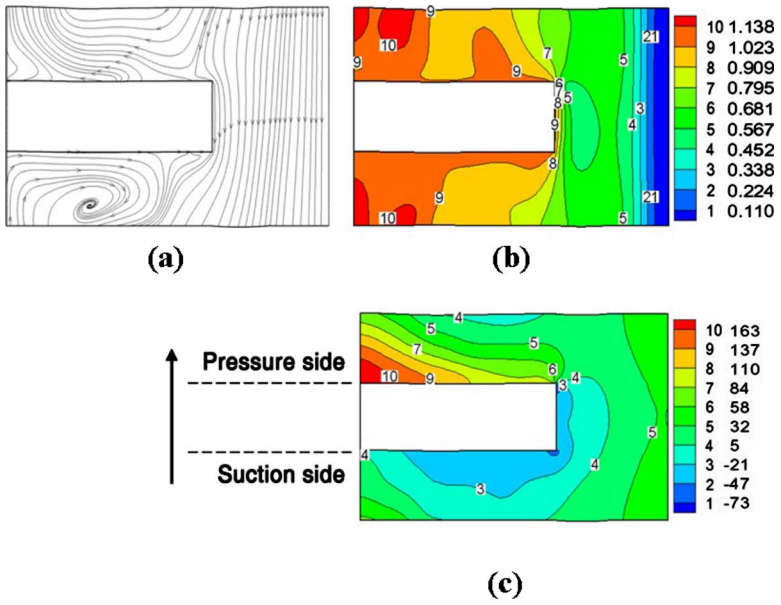

Fig. 12 Flow distributions at the plane of mean radius (Re=6.63×10³): (*a*) streamlines, (*b*) tangential velocity, and (*c*) static pressure distributions

tion side corner. The vortex on the pressure surface does not appear in this case. The contours of the tangential velocity component are shown in Fig. 12(*b*). Tangential velocity is low at both the vane and the channel. The static pressure is uniformly distributed on the pressure and suction surfaces, as shown in Fig. 12(*c*).

5 One-Dimensional Analysis and Loss Model

The design and performance analyses are usually done based on a one-dimensional analysis. Some important relations for head rise, torque, and hydraulic efficiency in one vane space are summarized here [1,7].

$$g\Delta H = \frac{\Delta Q_c}{Q_s}(V_{t2}U_2 - V_{t1}U_1) - g\Delta H_{\text{loss}} \tag{2}$$

$$\Delta T = \frac{\rho Q_s}{\omega}(g\Delta H + g\Delta H_{\text{loss}}) \tag{3}$$

$$\eta = \frac{Q}{Q_s}\left(\frac{g\Delta H}{g\Delta H + g\Delta H_{\text{loss}}}\right) \tag{4}$$

Q_s is the flow rate in the side channel when the local velocity is the rigid body rotating speed $V_t=\omega r$. ΔQ_c is the circulatory flow rate in one vane space. The internal flow of the side channel is a strongly swirling through flow. However, the internal loss is usually estimated using the model for a fully developed pipe flow.

$$g\Delta H_{\text{loss}} = k_f \frac{L}{2D_h}\left(\frac{Q}{A}\right)^2 \tag{5}$$

Nondimensionalized equation (5) becomes

$$\Delta\psi_{\text{loss}} = K_t\phi^2 \tag{6}$$

The theoretical head rise without flow loss is given by momentum exchanges as follows:

$$\Delta\psi_{\text{th}} = \frac{\Delta\phi_c}{\phi_s}\left(\frac{V_{t2}U_2 - V_{t1}U_1}{U^2}\right) \tag{7}$$

Equation (2) using Eqs. (6) and (7) becomes as follows:

$$\Delta\psi = \Delta\psi_{\text{th}} - \Delta\psi_{\text{loss}} \tag{8}$$

It is usually assumed that the pressure coefficient is a linear function of the flow coefficient.

$$\Delta\psi = \Delta\psi_m(1 - \phi/\phi_m) \tag{9}$$

By converting Eqs. (3) and (4) to its nondimensional forms and using the loss model given by Eq. (6), we obtain

$$\Delta\tau = \tfrac{1}{2}\phi_s(\Delta\psi + K_t\phi^2) \tag{10}$$

$$\eta = \frac{\phi}{\phi_s}\left(\frac{\Delta\psi}{\Delta\psi + K_t\phi^2}\right) \tag{11}$$

6 Performance Characteristics

The performance curves shown in Fig. 13 are obtained from the three-dimensional numerical calculations. Reynolds numbers are changed by changing the rotational speed of the impeller. The flow coefficient and head coefficient maintain a linear relation regardless of the Reynolds number. In a range of calculations, the performance curve shows good similarity for $\text{Re} \geq 2.65\times10^5$. However, for $\text{Re} \geq 2.65\times10^5$, the performance curve depends on the Reynolds number.

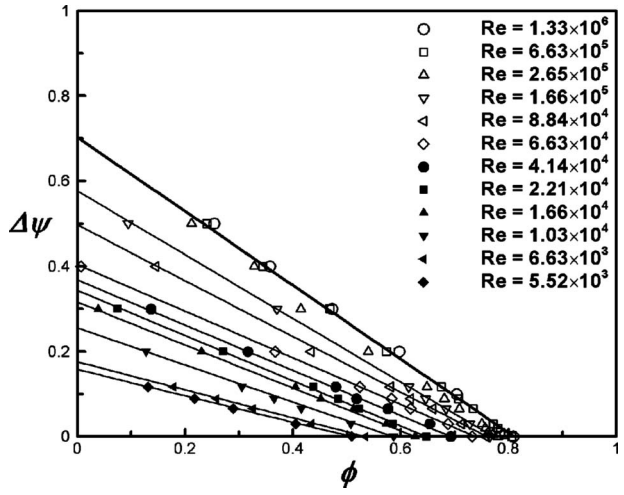

Fig. 13 Variations in pressure coefficients with flow coefficients for various Reynolds numbers

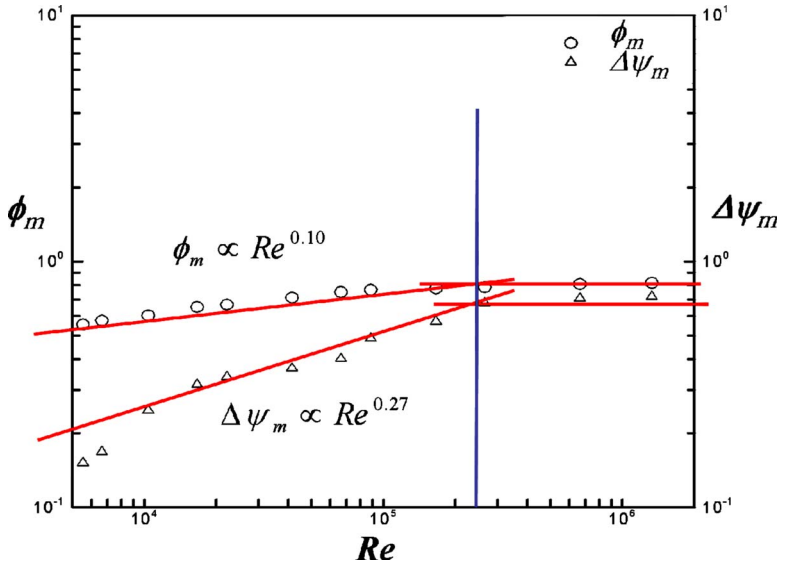

Fig. 14 Variations in maximum flow and shut-off head coefficient with Reynolds number

Important parameters are the maximum flow coefficient and the shut-off head coefficient in the performance curve. Figure 14 shows the variations in the two parameters with Reynolds number. For $\mathrm{Re} \geq 2.65 \times 10^5$, they show constant values; however, the maximum flow coefficient decreases smoothly as the Reynolds number decreases as $\phi_m \propto \mathrm{Re}^{0.10}$. The flow rate for a given pressure rise reduces due to the viscous effects caused by the decrease in the Reynolds number. For a given flow rate, a relatively large viscous shear reduces the head rise, and the shut-off head coefficient decreases as the Reynolds number decreases as $\Delta\psi_m \propto \mathrm{Re}^{0.27}$. This result is confirmed by the theoretical head rise. The relevant parameters of the theoretical head rise are the circulatory flows and momentum exchanges, as shown in Eq. (7). Figures 15 and 16 show the variations in the two parameters. At the same flow coefficient, the circulatory flow and momentum exchanges have a larger reduction at a low Reynolds number than at a high Reynolds number. Variations in the theoretical head rise with the Reynolds number are shown in Fig. 16. The theoretical head rise has a linear relation with the flow coefficient and reduces as the Reynolds number decreases. Therefore, the shut-off head coefficient also reduces.

Based on Eq. (8), we estimated the amount of internal pressure loss. The internal pressure loss is the difference between the actual pressure head rise and the theoretical head rise, which can be obtained from the calculation of the momentum transfer from Eq. (7). Since the difference is too small to be accurately estimated from the momentum transfer, it can be obtained from the values of torque by using Eq. (10).

Figure 17 shows the internal pressure loss with the flow coefficients. The circulatory flow strongly depends on the head coefficient and reduces as the flow coefficient increases, as shown in Fig. 15. When the pressure loss is fitted by Eq. (6), the loss coefficients shown in Fig. 18 are shown to be a function of the Reynolds number. When the Reynolds number is sufficiently large, i.e., $\mathrm{Re} \geq 1.0 \times 10^5$, the loss coefficients vary as $K_t \propto \mathrm{Re}^{-0.18}$. However, for $\mathrm{Re} \leq 1.0 \times 10^5$, the loss coefficients vary as $K_t \propto \mathrm{Re}^{-0.56}$.

Using Eqs. (10) and (11), the values of efficiency are obtained and shown in Fig. 19. At low flow rate, the efficiency increases proportionally with the flow coefficient since the loss is relatively small. However, as the flow coefficient increases, the loss becomes relatively large and pressure rise is small. Therefore, the efficiency drops to zero after peaking at the design point. The values of maximum efficiency and the corresponding flow coeffi-

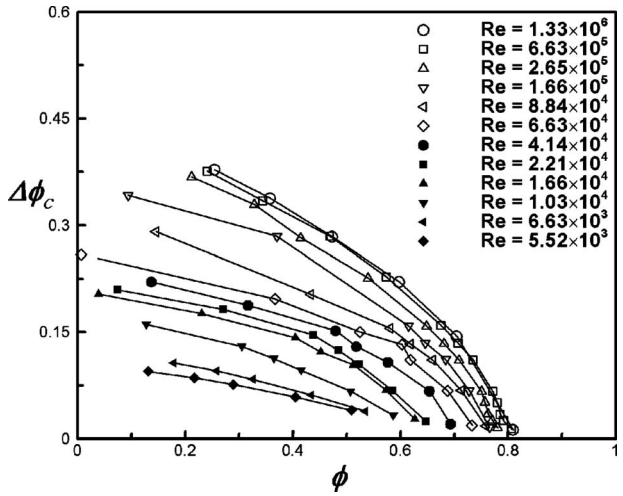

Fig. 15 Variations in circulatory flow coefficient with Reynolds number

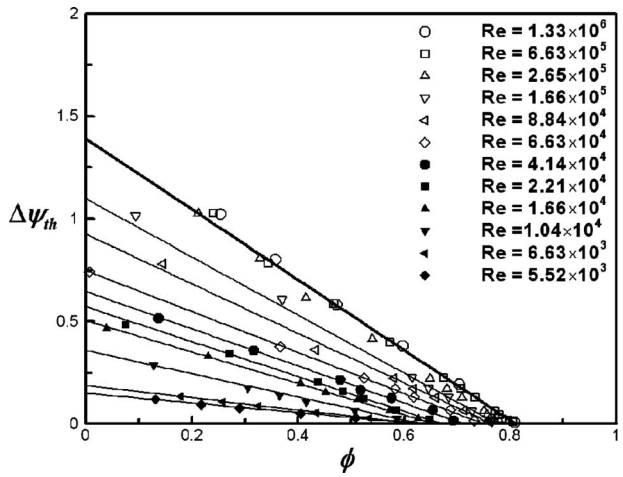

Fig. 16 Variations in theoretical head rise with Reynolds number

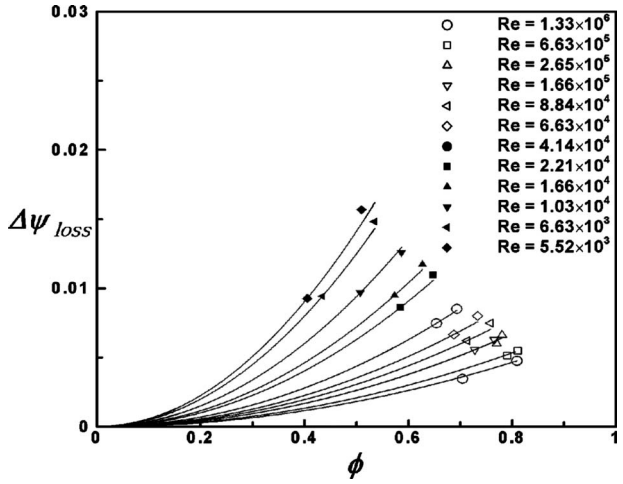

Fig. 17 Variations in head loss coefficient with flow coefficient

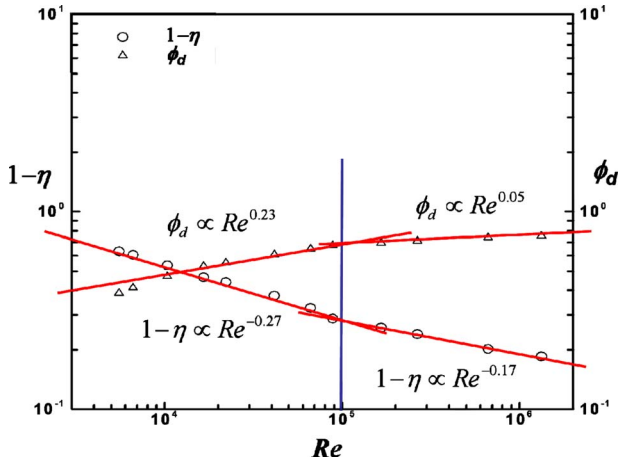

Fig. 20 Variations in maximum hydraulic efficiency and flow coefficient with Reynolds number

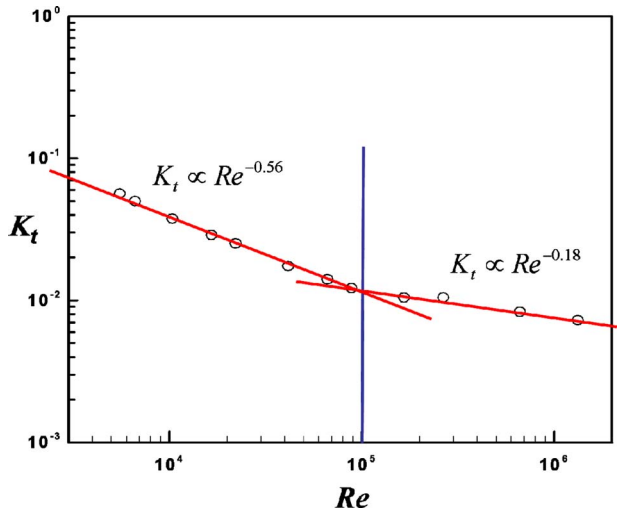

Fig. 18 Variations in loss coefficient with Reynolds number

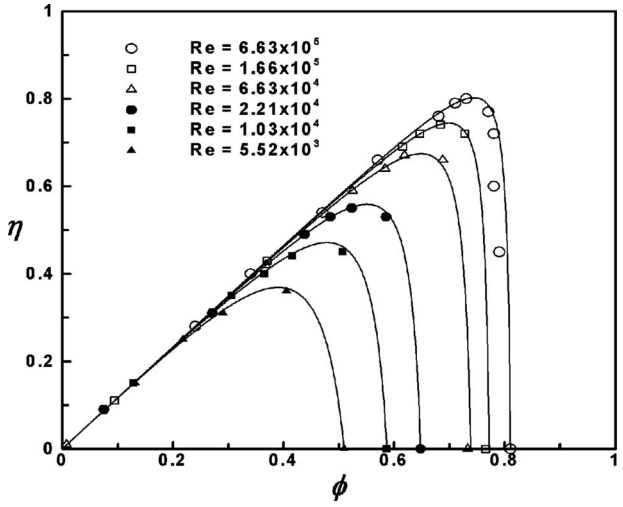

Fig. 19 Variation in hydraulic efficiency curves

cient decrease as the Reynolds number decreases, as shown in Fig. 20. When the Reynolds number is large, i.e., $Re \geq 1.0 \times 10^5$, $1-\eta_d \propto Re^{-0.17}$, and $\phi_d \propto Re^{0.05}$. However, for $Re \leq 1.0 \times 10^5$, $1-\eta_d \propto Re^{-0.27}$, and $\phi_d \propto Re^{0.23}$.

7 Conclusions

From the numerical studies of the effects of the Reynolds number on the flow and performance characteristics of a small regenerative pump, the following conclusions were obtained.

(1) Highly three-dimensional flow occurred in the inner region of a regenerative pump. Since the viscous effects near the channel and the vane wall became large for low Reynolds flows, the total momentum exchange was reduced considerably.
(2) The head-flow curves showed a linear relation, regardless of the Reynolds number. The maximum values of flow and shut-off head coefficients decreased as the Reynolds number decreased.
(3) The loss coefficient also strongly depended on the Reynolds number.
(4) The flow coefficient corresponding to the maximum efficiency decreased as the Reynolds number decreased.
(5) From the above conclusions, the variations in the values of important design parameters with Reynolds number should be carefully considered for the application of a small regenerative pump to very small devices.

Acknowledgment

This study was financially supported by the Micro-Thermal Engineering Research Center at Seoul National University. We also acknowledge the contribution of Mr. Y.H. Kim, who carried out additional calculations to reconfirm grid sensitivity.

Nomenclature

A = side channel area
D = outer diameter of the blade (=$2R$)
D_h = hydraulic diameter
f_θ = body force
g = gravity acceleration
h = width of the vane
H = head
t = thickness of the impeller
K_f = friction loss coefficient
N = rotating speed
P = pressure

Q = flow rate
Q_c = circulatory flow rate
Q_s = rigid body flow rate
R = outer radius of the blade
r = mean streamline radius
T = torque
Re = Reynolds number ($=UD/\upsilon$)
U = impeller speed ($=\omega R$)
V_t = tangential flow speed
V_c = circulatory flow velocity
Z = number of blade
ω = angular speed
θ_s = stripper angle
ρ = density
υ = kinematic viscosity
ψ = head coefficient ($=gH/U^2$)
ϕ = flow coefficient ($=Q/UA$)
ϕ_c = circulatory flow coefficient ($=Q_c/UA$)
ϕ_s = rigid body flow coefficient ($=Q_s/UA$)
τ = torque coefficient ($=T/\rho U^2 AD$)
η = hydraulic efficiency

Subscript

m = maximum values
t = values at the tip
1 = inlet of the vane
2 = outlet of the vane

References

[1] Wilson, W. A., Santalo, M. A., and Oelrich, J. A., 1955, "A Theory of the Fluid-Dynamic Mechanism of Regenerative Pumps," Trans. ASME, **77**, pp. 1303–1316, Paper No. 54-A-59.

[2] Iversen, H. W., 1955, "Performance of the Periphery Pump," Trans. ASME, **53**, pp. 19–28, Paper No. 53-A-102.

[3] Shimosaka, M., and Yamazaki, S., 1960, "Research on the Characteristics of Regenerative Pump," Bull. JSME, **3**(10), pp. 185–190.

[4] Hollenberg, J. W., 1987, "Reynolds Number Effects on Regenerative Pump Performance," ASME J. Eng. Ind., **109**(4), pp. 392–395.

[5] Hübel, M., Blättel, B., and Stroh, W., 1995, "Investigation on Fluid Mechanics of the Regenerative Pump Used in Gasoline Injection Systems," SAE Technical Paper Series No. 950077, pp. 131–139.

[6] Badami, M., 1997, "Theoretical and Experimental Analysis of Transitional and New Periphery Pumps," SAE Technical Paper Series No. 971074, pp. 44–55.

[7] Kang, S. H., Ryu, S. H., Lim, H. S., and Shim, C. Y., 2004, "Performance Characteristics of Side Channel Type Regenerative Pump," Trans. KSME B, **28**(12), pp. 1600–1607.

[8] Lim, H. S., and Kang, S. H., 2005, "Performance Characteristics of Side Channel Type Regenerative Pump," Trans. KSME B, **29**(3), pp. 306–313.

[9] Shim, C. Y., and Kang, S. H., 2003, "Though Flow Analysis and Leakage Flow of a Regenerative Pump," KSME Int. J., **27**(8), pp. 1015–1022.

One-Dimensional Unsteady Periodic Flow Model with Boundary Conditions Constrained by Differential Equations

Nhan T. Nguyen
NASA Ames Research Center,
Moffett Field, CA 94035

This paper describes a modeling method for closed-loop unsteady fluid transport systems based on 1D unsteady Euler equations with nonlinear forced periodic boundary conditions. A significant feature of this model is the incorporation of dynamic constraints on the variables that control the transport process at the system boundaries as they often exist in many transport systems. These constraints result in a coupling of the Euler equations with a system of ordinary differential equations that model the dynamics of auxiliary processes connected to the transport system. Another important feature of the transport model is the use of a quasilinear form instead of the flux-conserved form. This form lends itself to modeling with measurable conserved fluid transport variables and represents an intermediate model between the primitive variable approach and the conserved variable approach. A wave-splitting finite-difference upwind method is presented as a numerical solution of the model. An iterative procedure is implemented to solve the nonlinear forced periodic boundary conditions prior to the time-marching procedure for the upwind method. A shock fitting method to handle transonic flow for the quasilinear form of the Euler equations is presented. A closed-loop wind tunnel is used for demonstration of the accuracy of this modeling method. [DOI: 10.1115/1.3130244]

1 Introduction

A transport system is a system that carries information from one point to another point within the system. Examples of transport systems are numerous such as fluid flow in gas distribution pipelines [1], air traffic systems [2], and highway traffic systems [3], just to name a few. The underlying mathematical principle of a transport system is the hyperbolic partial differential equation that models such a system as a continuum whose information varies in space and time [4]. This equation is used to model a wave propagation behavior in many transport systems since information is carried from one point to another point within the continuum by wave actions. Associated with the hyperbolic partial differential equation are boundary conditions that specify the configurations of these systems. If the information is carried in one direction without returning to its starting position, then we say that the system is open-loop. An example of an open-loop transport system is gas flow through an aircraft engine. On the other hand, if the information returns to its starting position, then the system is said to be closed-loop. An example of a closed-loop transport system is the circulatory system in a biological system. The flow of information is usually supplied at the system boundary by a forced process that provides a motive force to propagate the information as waves. A common device for accomplishing this objective in fluid transport systems is a pump that supplies a positive pressure wave to displace the fluid volume in the flow direction. In this study, we will focus on such a closed-loop fluid transport system that is energized by a positive-displacement device such as a turbomachinery compressor. While the focus is on a fluid transport system, the underlying principle is sufficiently general for other types of transport systems.

This study is motivated by the need for modeling a closed-loop wind tunnel system, which is a good example of a closed-loop transport system. We now introduce a real problem of Mach number control in a wind tunnel. Referring to Fig. 1, the NASA Ames 11 ft transonic wind tunnel (TWT) is a closed-circuit wind tunnel capable of delivering an air speed from Mach 0.2 to Mach 1.5 in a test section measured 11 ft wide $\times$ 11 ft high. The air flow is delivered by a three-stage compressor driven by four synchronous induction ac motors with a total input power of 236,000 hp as shown in Fig. 2. The compressor is a variable-geometry machine equipped with inlet guide vanes (IGVs) having adjustable trailing edge flaps driven by two 10 hp dc motors. The Mach number in the test section M_∞, hence the flow throughout the wind tunnel circuit, is controlled by a combination of the compressor speed ω and the IGV flap position θ as shown in Fig. 3. In the context of the present study, the flow inside a wind tunnel is governed by the hyperbolic equations, and the control inputs are applied at the system boundaries where the compressor is situated. The compressor control inputs are regulated by the actuator dynamics of the drive motors and the IGV system.

The Mach number control is normally accomplished by adjusting the IGV flap position at a fixed compressor speed, which must be regulated at discrete set points at all times in order to avoid blade vibration. Thus, the flow condition, as well as the compressor speed, must be controlled simultaneously. A typical operation of a wind tunnel involves aerodynamic measurements on a subscale test model of a flight vehicle. During a typical test, the test model inside the test section is pitched through a series of angles of attack. As the angle of attack increases, the momentum loss across the test model generates a flow disturbance that causes the Mach number to drift from its set point. Thus, to handle this disturbance, a feedback control strategy is necessary to regulate the Mach number. Currently, the Mach number feedback control is based on an ad hoc empirical model and is unable to keep up with a continuous change in test model's angle of attack due to the noncollocation of the Mach number sensing in the test section and the control action in the compressor. The spatial separation between the test section and the compressor results in a fluid transport delay, which causes the feedback control action to always lag

Contributed by the Fluids Engineering Division of ASME for publication in the JOURNAL OF FLUIDS ENGINEERING. Manuscript received November 2, 2007; final manuscript received April 13, 2009; published online May 12, 2009. Review conducted by Joseph Katz.

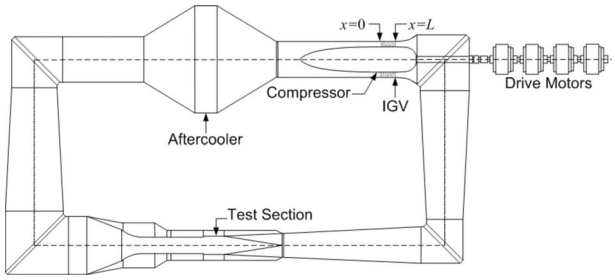

Fig. 1 Closed-circuit wind tunnel (NASA Ames 11 ft TWT)

the Mach number sensing. In order to improve the Mach number control strategy, a model-predictive control has been proposed whereby the control action would be based on a physics-based model that would be able to predict with sufficient accuracy the transient behavior of fluid flow in the wind tunnel [5].

Past efforts in the mathematical modeling of a wind tunnel usually have attempted to simplify the complexity of the fluid dynamics aspects of a wind tunnel to a great extent. One simplified approach is to describe the unsteady flow through a wind tunnel by a pseudo-steady-state compressible flow, which neglects the time transient behavior of the flow field [6]. This approach has been used in the past for designing the Mach number control of the 11 ft TWT [7]. Other simplified methods have also been considered. For example, Soeterboek et al. [8] described a method of modeling the test section Mach number by an experimental transfer function coupled with a time delay. A model-predictive Mach number control has also been proposed by Motter and Principe [9] whereby the disturbance is estimated as a function of the test model's angle of attack by fitting measurement data to a functional approximation method such as a recursive least square or neural network algorithm. The predicted disturbance model would then be used to establish a feedforward optimal control law that would minimize the disturbance to the Mach number. In all these studies, no unsteady fluid flow model based on fluid physics has been attempted.

With regard to general 1D unsteady flow, there have been numerous studies of this type of model. Ben-Artzi and Falcovitz [10] described a unified approach of generalized Riemann problem that comprises some of the most commonly used numerical methods for computing 1D unsteady flow process. Various authors in the field of computational fluid dynamics (CFD) such as Hirsch [11], Laney [12], and Wendt [13] have published many well-known numerical algorithms based on the flux-conserved form of the 1D unsteady Euler equations. Characteristic methods had been frequently used in the study of 1D unsteady flow before the advent of CFD by Shapiro [14]. Wylie and Streeter [15] also used characteristic methods to compute 1D unsteady flow in hydraulics. In the modern context of CFD, the flux-conserved numerical methods are the preferred approach since the flux conservation affords many advantages such as shock capturing and numerical consistency. However, in certain special applications such as this study, a flow process may involve several complex behaviors such as follows: (1) The boundary conditions are enforced by another real flow process that is modeled by a dimensional analysis involving physical quantities such as mass flow, stagnation pressure, and stagnation temperature, (2) the inflow and outflow boundary conditions are inseparable as they are functionally related to nonlinear period boundary conditions, and (3) the viscous loss effect is involved and is empirically modeled as stagnation pressure losses. In these cases, an alternate non-flux-conserved approach may be more advantageous than the flux-conserved approach, which may result in a complicated formulation that otherwise could be avoided.

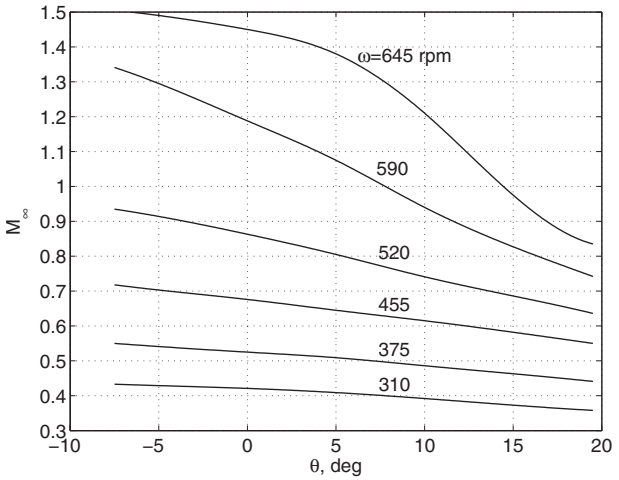

Fig. 3 NASA Ames 11 ft TWT Mach number envelope

The paper presents the development of a computational hyperbolic model for a closed-loop fluid system based on the 1D unsteady Euler equations. The hyperbolic model is an intermediate model between the flux-conserved form and the non-flux-conserved form that affords a certain advantage for flow with dissipation and varying area. A nonlinear forced periodic boundary condition is imposed on the model to describe a forced process that generates the flow of information. This boundary condition in turn is coupled to a system of ordinary differential equations that represent the dynamics of auxiliary systems that actually drive the information flow in a closed-loop system. We also present an explicit scheme of a wave-splitting, finite-difference upwind method for solving this hyperbolic model. The computational results for a closed-loop wind tunnel model show a very good agreement with experimental data.

2 Closed-Loop Transport Model

2.1 Hyperbolic Equations in Quasilinear Form. Fluid transport phenomena are governed by the conservation laws of

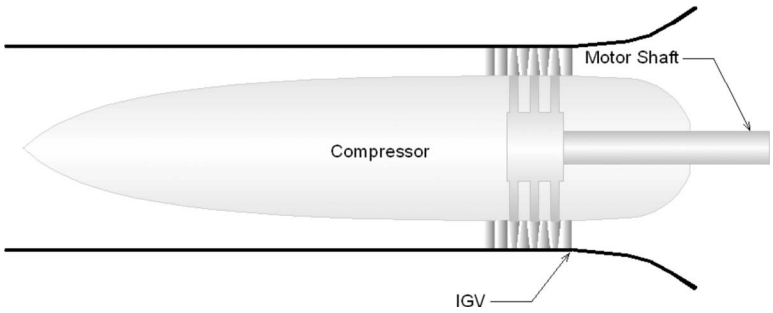

Fig. 2 Wind tunnel compressor

mass, momentum, and energy. These equations are hyperbolic in nature. For 1D internal flow, the governing unsteady Euler equations are expressed in a flux-conserved form as [14]

$$\frac{\partial \mathbf{U}}{\partial t} + \frac{\partial \mathbf{F}(\mathbf{U},x)}{\partial x} + \mathbf{Q}(\mathbf{U},x) = \mathbf{0}, \quad \forall\, x \in (0,L), \quad t \in (0,T) \tag{1}$$

where $\mathbf{U}(x,t):[0,L]\times[0,T]\rightarrow\mathbb{R}^n$ is a vector of transport variables with $n=3$, $\mathbf{F}(\mathbf{U},x)$ is a flux vector of conserved quantities, and $\mathbf{Q}(\mathbf{U},x)$ is a nonhomogeneous dissipative source term. In the vector form, $\mathbf{U}$, $\mathbf{F}$, and $\mathbf{Q}$ are defined as

$$\mathbf{U}(x,t) = \begin{bmatrix} \rho A \\ \rho u A \\ \rho A c_v T + \frac{1}{2}\rho u^2 A \end{bmatrix}, \quad \mathbf{F}(\mathbf{U},x) = \begin{bmatrix} \rho u A \\ \rho u^2 A + pA \\ \rho u A c_p T + \frac{1}{2}\rho u^3 A \end{bmatrix}$$

$$\mathbf{Q}(\mathbf{U},x) = \begin{bmatrix} 0 \\ -p\frac{dA}{dx} + \frac{1}{2}\rho u^2 A \frac{f}{D} \\ -\frac{dQ}{dx} \end{bmatrix} \tag{2}$$

where ρ is the density, p is the pressure, u is the flow speed, T is the temperature, A is the varying flow area, f is the friction factor, D is the hydraulic diameter, dQ/dx is the heat transfer gradient, c_v is the constant-volume specific heat, and c_p is the constant-pressure specific heat.

Equation (1) admits a continuous solution as well as a discontinuous solution. When a shock is present, a discontinuous solution describes the evolution of the shock discontinuity, which requires Eq. (1) to be cast in a weak form in order to handle the infinite spatial derivative of the flux vector through the shock. The weak form solution relates the information on either side of the discontinuity to the integral form of Eq. (1), which results in the well-known Rankine–Hugoniot relations [12].

Suppose the vector $\mathbf{U}$ can be expressed as a function of some flow variables $\mathbf{y}$ so that

$$\mathbf{U}(x,t) = \mathbf{U}(\mathbf{y}(x,t)) \tag{3}$$

Then by explicit differentiation, Eq. (1) can be rewritten in a quasilinear, non-flux-conserved form as

$$\frac{\partial \mathbf{y}}{\partial t} + \mathbf{A}(\mathbf{y},x)\frac{\partial \mathbf{y}}{\partial x} + \mathbf{B}(\mathbf{y},x) = \mathbf{0} \tag{4}$$

where $\mathbf{A}(\mathbf{y},x):\mathbb{R}^n\times[0,T]\rightarrow\mathbb{R}^n\times\mathbb{R}^n$ is a characteristic matrix and $\mathbf{B}(\mathbf{y},x):\mathbb{R}^n\times[0,L]\rightarrow\mathbb{R}^n$ is a nonhomogeneous dissipative source term such that

$$\mathbf{A} = \left(\frac{\partial \mathbf{U}}{\partial \mathbf{y}}\right)^{-1}\left(\frac{\partial \mathbf{F}}{\partial \mathbf{U}}\right)\left(\frac{\partial \mathbf{U}}{\partial \mathbf{y}}\right) \tag{5}$$

$$\mathbf{B} = \left(\frac{\partial \mathbf{U}}{\partial \mathbf{y}}\right)^{-1}\left(\frac{\partial \mathbf{F}}{\partial x} + \mathbf{Q}\right) \tag{6}$$

Equation (4) is a system of first-order, quasilinear strictly hyperbolic equations due to the fact that the matrix $\mathbf{A}$ has n real, distinct eigenvalues such that

$$\lambda_1(\mathbf{A}) < \lambda_2(\mathbf{A}) < \cdots < \lambda_n(\mathbf{A}) \tag{7}$$

for all $\mathbf{y}(x,t)\in\mathbb{R}^n$, $x\in[0,L]$, and $t\in[0,T]$. Under this condition, the matrix $\mathbf{A}$ is diagonalizable using a similarity transformation

$$\mathbf{A} = \mathbf{\Phi}\mathbf{\Lambda}\mathbf{\Phi}^{-1} \tag{8}$$

where $\mathbf{\Phi}$ is a matrix of the right eigenvectors and $\mathbf{\Lambda}$ is a diagonal matrix of the right eigenvalues of $\mathbf{A}$ as follows:

$$\mathbf{\Lambda} = \begin{bmatrix} u+c & 0 & 0 \\ 0 & u & 0 \\ 0 & 0 & u-c \end{bmatrix} \tag{9}$$

with c as the speed of sound.

The eigenvalues are the wave speeds of the fluid transport systems, and the direction of the wave propagation is called a characteristic direction. For subsonic transport, the information in the fluid medium is carried in both the upstream and downstream directions by one upstream wave speed $u-c$ and two downstream wave speeds u and $u+c$. Since $x\in[0,L]$, then for the information to be transported in the upstream direction, data must exist at the boundary $x=L$. Similarly, data must also exist at the boundary $x=0$ in order for information to be carried downstream in the flow. The number of upstream and downstream boundary conditions must match the number of upstream and downstream wave speeds. This is known as the boundary condition compatibility [12].

Premultiplying Eq. (4) by $\mathbf{\Phi}^{-1}$, we obtain the characteristic form of the hyperbolic partial differential equation

$$\mathbf{\Phi}^{-1}\mathbf{y}_t + \mathbf{\Lambda}\mathbf{\Phi}^{-1}\mathbf{y}_x + \mathbf{\Phi}^{-1}\mathbf{B} = \mathbf{0} \tag{10}$$

Equations (1) and (4) are completely equivalent, but there are significant differences in the numerical implementation of these equations. The flux-conserved form of Eq. (1) yields a solution that is conserved throughout the domain of x, resulting in a correct steady-state solution. For example, examining the first row of Eq. (1), it is clear that the steady-state solution requires that the mass flux variable ρuA be constant with respect to x. This is a well-known result in fluid mechanics. In the numerical implementation, this mass flux conservation is incorporated directly into the solution method in order to guarantee that the general time unsteady solution will converge to the correct steady-state solution [13].

On the other hand, the quasilinear, non-flux-conserved form of Eq. (4) can take on a wide range of expressions, some of which are more advantageous than others from a numerical implementation standpoint. For example, one common quasilinear form of Eq. (4) is

$$\frac{\partial}{\partial t}\begin{bmatrix} p \\ u \\ c^2 \end{bmatrix} + \begin{bmatrix} u & \gamma p & 0 \\ \frac{c^2}{\gamma p} & u & 0 \\ 0 & (\gamma-1)c^2 & u \end{bmatrix}\frac{\partial}{\partial x}\begin{bmatrix} p \\ u \\ c^2 \end{bmatrix} + \begin{bmatrix} \gamma p u\frac{dA}{Adx} - \frac{(\gamma-1)\gamma p u^3}{2c^2}\frac{f}{D} - \frac{\gamma-1}{A}\frac{dQ}{dx} \\ \frac{u^2}{2}\frac{f}{D} \\ (\gamma-1)c^2 u\frac{dA}{Adx} - \frac{(\gamma-1)\gamma u^3}{2}\frac{f}{D} - \frac{(\gamma-1)c^2}{pA}\frac{dQ}{dx} \end{bmatrix} = \begin{bmatrix} 0 \\ 0 \\ 0 \end{bmatrix} \tag{11}$$

where γ is the specific heat ratio. In this form, the variables p, u, and c^2 are called primitive variables or basic variables.

The right eigenvector matrix $\mathbf{\Phi}$ for Eq. (11) is computed as

$$\mathbf{\Phi} = \begin{bmatrix} \frac{\gamma p}{(\gamma-1)c^2} & 0 & \frac{\gamma p}{(\gamma-1)c^2} \\ \frac{1}{(\gamma-1)c} & 0 & -\frac{1}{(\gamma-1)c} \\ 1 & 1 & 1 \end{bmatrix} \tag{12}$$

Then the characteristic form of Eq. (11) becomes

$$\begin{bmatrix} \frac{(\gamma-1)c^2}{2\gamma p}\frac{\partial p}{\partial t} + \frac{(\gamma-1)c}{2}\frac{\partial u}{\partial t} \\ -\frac{(\gamma-1)c^2}{\gamma p}\frac{\partial p}{\partial t} + \frac{\partial c^2}{\partial t} \\ \frac{(\gamma-1)c^2}{2\gamma p}\frac{\partial p}{\partial t} - \frac{(\gamma-1)c}{2}\frac{\partial u}{\partial t} \end{bmatrix} + \begin{bmatrix} u+c & 0 & 0 \\ 0 & u & 0 \\ 0 & 0 & u-c \end{bmatrix} \begin{bmatrix} \frac{(\gamma-1)c^2}{2\gamma p}\frac{\partial p}{\partial x} + \frac{(\gamma-1)c}{2}\frac{\partial u}{\partial x} \\ -\frac{(\gamma-1)c^2}{\gamma p}\frac{\partial p}{\partial x} + \frac{\partial c^2}{\partial x} \\ \frac{(\gamma-1)c^2}{2\gamma p}\frac{\partial p}{\partial x} - \frac{(\gamma-1)c}{2}\frac{\partial u}{\partial x} \end{bmatrix}$$

$$+ \begin{bmatrix} \frac{(\gamma-1)c^2u}{2}\frac{dA}{Adx} + \frac{(\gamma-1)c^2u^2 - (\gamma-1)^2cu^3}{4c}\frac{f}{D} - \frac{(\gamma-1)^2c^2}{2\gamma pA}\frac{dQ}{dx} \\ -\frac{(\gamma-1)u^3}{2}\frac{f}{D} - \frac{(\gamma-1)c^2}{\gamma pA}\frac{dQ}{dx} \\ \frac{(\gamma-1)c^2u}{2}\frac{dA}{Adx} - \frac{(\gamma-1)c^2u^2 + (\gamma-1)^2cu^3}{4c}\frac{f}{D} - \frac{(\gamma-1)^2c^2}{2\gamma pA}\frac{dQ}{dx} \end{bmatrix} = \begin{bmatrix} 0 \\ 0 \\ 0 \end{bmatrix} \tag{13}$$

The three characteristic directions are defined by $(dx/dt)_{1,2,3} = u \pm c, u$ such that on these characteristic directions, the total derivative of a quantity is computed as

$$\left(\frac{d}{dt}\right)_i = \frac{\partial}{\partial t} + \left(\frac{dx}{dt}\right)_i \frac{\partial}{\partial x} \tag{14}$$

where $i=1,2,3$ denotes the characteristic direction.

Therefore, we can write out Eq. (13) as

$$\frac{c}{\gamma p}\left(\frac{dp}{dt}\right)_{1,2} \pm \left(\frac{du}{dt}\right)_{1,2} + cu\frac{dA}{Adx} \pm \frac{cu^2 \mp (\gamma-1)u^3}{2c}\frac{f}{D} - \frac{(\gamma-1)c}{\gamma pA}\frac{dQ}{dx} = 0 \tag{15}$$

$$-\frac{1}{p}\left(\frac{dp}{dt}\right)_3 + \frac{\gamma}{(\gamma-1)c^2}\left(\frac{dc^2}{dt}\right)_3 - \frac{\gamma u^3}{2c^2}\frac{f}{D} - \frac{1}{pA}\frac{dQ}{dx} = 0 \tag{16}$$

We recall that the entropy of a perfect gas is defined as

$$ds = \frac{\gamma R}{\gamma-1}\frac{dT}{T} - R\frac{dp}{p} = R\left(\frac{\gamma}{\gamma-1}\frac{dc^2}{c^2} - \frac{dp}{p}\right) \tag{17}$$

Then, substituting Eq. (17) into Eq. (16) yields

$$\left(\frac{ds}{dt}\right)_3 = \frac{u^3}{2T}\frac{f}{D} + \frac{1}{\rho TA}\frac{dQ}{dx} \tag{18}$$

From Eq. (15), it can be seen that the pressure and flow speed propagate at wave speeds $u \pm c$, while Eq. (18) shows that the entropy propagates at a wave speed u. Equation (18) also implies an important thermodynamic property that, for an adiabatic flow, the friction factor must be positive to ensure that entropy change is positive according to the second law of thermodynamics. For a perfect gas, the isentropic relationship between the density and pressure is expressed as

$$\frac{\rho}{\rho_0} = \left(\frac{p}{p_0}\right)^{1/k} \tag{19}$$

We substitute Eq. (19) into Eq. (15) and then integrate the resulting equation along with Eq. (18). Upon simplification, we get

$$\left(u \pm \frac{2c}{\gamma-1}\right)_{1,3} = \int \left[\mp cu\frac{dA}{Adx} - \frac{cu^2 \mp (\gamma-1)u^3}{2c}\frac{f}{D} \pm \frac{(\gamma-1)c}{\gamma pA}\frac{dQ}{dx}\right]dt \tag{20}$$

$$(s)_2 = \int R\left(\frac{\gamma u^3}{2c^2}\frac{f}{D} + \frac{1}{pA}\frac{dQ}{dx}\right)dt \tag{21}$$

For inviscid, adiabatic flow with a constant area, we see that the integral terms in the right hand sides of Eqs. (20) and (21) vanish, thus rendering the expressions on the left hand sides constant. As a result, the expressions on the right hand sides $u \pm 2c/(k-1)$ and s are the well-known Riemann invariants, which are conserved along the characteristic directions $(dx/dt)_{1,2,3} = u \pm c, u$ for inviscid, adiabatic flow [12]. For viscous flow, these Riemann invariants are no longer conserved along the characteristic directions. However, the Riemann invariant concept is important in studying shock capturing methods that involve discontinuous solutions.

The flux-conserved form of Eq. (1) is very popular in computational fluid dynamics because it addresses the conservation laws directly for flow with shock discontinuities. On the other hand, the quasilinear form of Eq. (4) using the primitive variables such as Eq. (11) in general does not necessarily preserve the conservation features of the transport physics because the flux variables as reconstructed from the primitive variables may not be necessarily conserved. However, the advantage of using a flux-conserved form is not without a trade-off. The fact that the momentum flux variable is usually not a directly measurable quantity can potentially result in an increased complexity in formulating numerical methods for certain physical applications whereby the boundary conditions are specified in terms of directly measurable quantities.

From Eq. (1), we note that the mass flux variable is the same as the mass flow $\dot{m} = \rho uA$ in a 1D flow, and the energy flux variable takes on the meaning of the enthalpy $\dot{m}c_pT_0$ of the fluid, where T_0 is the stagnation temperature. Since the mass flow is always conserved, the stagnation temperature therefore is also conserved for an adiabatic process and thus is proportional to the energy flux variable. On the other hand, the momentum flux variable is generally not conserved for shock free, inviscid flow with a varying area. Instead, we can replace the momentum flux variable with the stagnation pressure p_0 as a variable that is generally conserved for shock free, inviscid flow. Thus, this leads us to consider the following quasilinear form in terms of the mass flow, the stagnation pressure, and the stagnation temperature:

$$\frac{\partial}{\partial t}\begin{bmatrix}\dot{m}\\ p_0\\ T_0\end{bmatrix}+\begin{bmatrix}u & \frac{pA}{p_0} & \frac{\dot{m}u}{2T_0}\\ \frac{\rho_0 c^2}{\rho A} & u\left[1-\frac{(\gamma-1)T}{T_0}\right] & \frac{\rho_0 c^2 u}{T_0}\\ \frac{(\gamma-1)T}{\rho A} & -\frac{(\gamma-1)^2 uT}{\gamma p_0} & u\left[1+\frac{(\gamma-1)T}{T_0}\right]\end{bmatrix}$$

$$\times\frac{\partial}{\partial x}\begin{bmatrix}\dot{m}\\ p_0\\ T_0\end{bmatrix}+\begin{bmatrix}\frac{\dot{m}u}{2}\frac{f}{D}\\ \frac{\rho_0 u^3}{2}\left(\frac{T_0}{T}-\gamma+1\right)\frac{f}{D}-\frac{\rho_0 c^2 u(2-\mathrm{M}^2)}{2\dot{m}c_p T}\frac{dQ}{dx}\\ -(\gamma-1)uT\frac{f}{D}\left(\frac{T_0}{T}-1\right)-\frac{\gamma u}{\dot{m}c_p}\frac{dQ}{dx}\end{bmatrix}$$

$$=\begin{bmatrix}0\\ 0\\ 0\end{bmatrix} \tag{22}$$

where ρ_0 is the stagnation density and M is the Mach number.

Equation (22) represents an intermediate model between the flux-conserved form of Eq. (1) and the quasilinear, non-flux-conserved form with primitive variables as in Eq. (11). In this form, the steady-state solution is governed by the following equation:

$$\frac{d\mathbf{Y}}{dx}=-\mathbf{C}(\mathbf{Y},x) \tag{23}$$

where $\mathbf{Y}$ is the steady-state solution and

$$\mathbf{C}(\mathbf{Y},x)=\mathbf{A}^{-1}(\mathbf{Y},x)\mathbf{B}(\mathbf{Y},x)=\begin{bmatrix}0\\ \frac{\gamma p_0 \mathrm{M}^2}{2}\left(\frac{f}{D}+\frac{1}{\dot{m}c_p T_0}\frac{dQ}{dx}\right)\\ -\frac{1}{\dot{m}c_p}\frac{dQ}{dx}\end{bmatrix} \tag{24}$$

It is obvious from Eq. (23) that the mass flow is identically conserved along the x-direction. For fluid transport without friction and heat transfer, both the stagnation pressure and stagnation temperature are conserved along the x-direction. It can be shown that the eigenvalues of the matrix $\mathbf{A}$ in both Eqs. (11) and (22) are equal to the values in Eq. (9) since the similarity transformation is invariant. Equation (22) affords a certain advantage over the flux-conserved form of Eq. (1) for subsonic flow in that it uses measurable physical quantities as variables from the boundary conditions and a stagnation pressure loss model that can significantly simplify computational methods for a real flow process.

2.2 Forced Periodic Boundary Conditions and Dynamic Constraints. In a closed-loop transport system, information is carried from one point to another point and then returned back to the starting position as illustrated in Fig. 4. To enable this information recirculation, a positive-displacement device must be embedded at the boundaries of the system. For subsonic transport, two boundary conditions at $x=0$ and one boundary condition at $x=L$ are required. For supersonic transport, three boundary conditions at $x=0$ are required. For a closed-loop system, the boundary conditions at $x=0$ are affected by the boundary conditions at $x=L$ since the information must be returned to its starting position. Thus, in general for a closed-loop system, we consider the following nonlinear forced periodic boundary condition for Eq. (4):

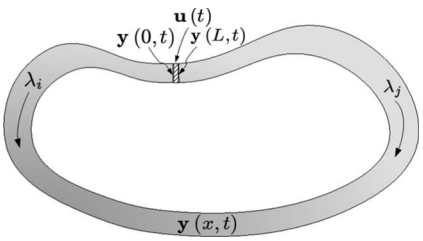

Fig. 4 Closed-loop transport system

$$\mathbf{y}(0,t)=\mathbf{g}(\mathbf{y}(L,t),\mathbf{u}),\quad \forall\, t\in(0,T) \tag{25}$$

where $\mathbf{u}(t):[0,T]\rightarrow\mathbb{R}^m$ in class C^1 is a boundary control vector, and $\mathbf{g}(\mathbf{y}(L,t),\mathbf{u}):\mathbb{R}^n\times\mathbb{R}^m\rightarrow\mathbb{R}^n$ is a forcing function that relates the transport state vectors at $x=0$ and $x=L$ and the boundary control vector $\mathbf{u}$. For a well-posed problem, we require that the boundary condition (25) be noncharacteristic such that $\mathbf{g}(\mathbf{y}(L,t),\mathbf{u})$ is nowhere tangential to any of the characteristic curves of Eq. (10) [4].

To ensure the boundary condition compatibility for all signs of the eigenvalues of $\mathbf{A}$, the Jacobian of $\mathbf{g}$ with respect to $\mathbf{y}(L,t)$ is required to be full rank or

$$\dim\frac{\partial\mathbf{g}}{\partial\mathbf{y}(L,t)}=n \tag{26}$$

where $n=3$ is the number of the eigenvalues.

To see this, we let n^+ and n^- be the numbers of the positive and negative eigenvalues, respectively. If $n^+=n$, then from Eq. (25), there are n^+ independent boundary conditions for $\mathbf{y}(0,t)$ that correspond to n^+ positive eigenvalues. Thus, the compatibility for the positive eigenvalues is satisfied. If $n^-=n$, then from Eqs. (25) and (26), there are n^- independent boundary conditions with $\mathbf{y}(L,t)$ that correspond to n^- negative eigenvalues. The compatibility for the negative eigenvalues is thus satisfied. If $0<n^+<n$, we choose n^+ independent boundary conditions with $\mathbf{y}(0,t)$ corresponding to n^+ positive eigenvalues. Then, from Eq. (26), there are n^- remaining boundary conditions with $\mathbf{y}(L,t)$ corresponding to n^- negative eigenvalues. Thus, the compatibility for the mixed-sign eigenvalues is satisfied.

The boundary condition (25) provides a control action to maintain the flow of information in a closed-loop system by the boundary control vector $\mathbf{u}$. In practice, the boundary control vector $\mathbf{u}$ ends up being controlled by an auxiliary process that effectively imposes a dynamic constraint on the boundary control action. Therefore, in general, we consider the dynamic constraint on the boundary control in Eq. (25) to be governed by a system of ordinary differential equations as follows:

$$\dot{\mathbf{u}}=\mathbf{f}(\mathbf{y}(0,t),\mathbf{y}(L,t),\mathbf{u},\mathbf{v}),\quad \forall\, t\in(0,T) \tag{27}$$

where $\mathbf{v}(t)\in\mathcal{L}^2[0,T]\rightarrow\mathbb{R}^l$ is a measurable auxiliary control vector and $\mathbf{f}(\mathbf{y}(0,t),\mathbf{y}(L,t),\mathbf{u},\mathbf{v}):\mathbb{R}^n\times\mathbb{R}^n\times\mathbb{R}^m\times\mathbb{R}^l\rightarrow\mathbb{R}^m$ is a transition function of the auxiliary process.

Equation (27) describes the time-varying process of the boundary control as influenced by the dynamics of the auxiliary process specified by the transition function $\mathbf{f}$ and the auxiliary control vector $\mathbf{v}$. The coupling with Eq. (1) is due to the existence of the transport state vectors $\mathbf{y}(0,t)$ and $\mathbf{y}(L,t)$ at the system boundaries.

To completely describe the problem, both Eqs. (4) and (27) are given the following initial conditions:

$$\mathbf{y}(x,0)=\mathbf{Y}(x) \tag{28}$$

$$\mathbf{U}(0)=\mathbf{U}_0 \tag{29}$$

where $\mathbf{Y}$ and $\mathbf{U}$ are the steady-state solutions of Eqs. (23) and (27) at the initial time, respectively. For a well-posed mixed initial-boundary value problem, the initial conditions (28) and (29) must

be compatible with the boundary condition (25) such that

$$\mathbf{Y}(0) = \mathbf{g}(\mathbf{Y}(L), \mathbf{U}_0) \tag{30}$$

The problem is now posed as follows: Given a closed-loop transport system initially at an equilibrium defined by the steady-state solutions $\mathbf{Y}(x)$ and $\mathbf{U}_0$, we would like to adjust the auxiliary control $\mathbf{v}(t)$ so as to move the system to a new equilibrium at some later time. We are interested in the evolution of the fluid transport properties during this process.

3 Computational Method

Computational methods for hyperbolic partial differential equations can be formulated based on three general discretization techniques: finite difference, finite element, and finite volume [11]. There are several methods of spatial discretization used in finite-difference methods that are designed to address numerical requirements of consistency, stability, and convergence [11–13]. Briefly, the consistency requirement expresses that the discretized equations should tend to the differential equations to which they are related when Δt and Δx tend to zero. The stability requirement states that solutions must be bounded from one time step to another. The convergence requirement asserts that numerical solutions should approach their exact solutions throughout the solution domains when Δt and Δx tend to zero. For a well-posed mixed initial-boundary value problem, stability is the necessary and sufficient condition for convergence [11].

3.1 Wave-Splitting Upwind Scheme. The simplest type of spatial discretization for a first-order, hyperbolic partial differential equation is the first-order upwind finite-difference method. In flow with shocks, spatial discretization may not have sufficient stability requirements and could cause numerical oscillations at the discontinuities. Various spatial discretization schemes such as the Lax–Wendroff method incorporate an artificial viscosity to dampen these numerical oscillations. For the conservation laws with the dissipative source term $\mathbf{B}$ in Eq. (4), the friction factor f provides a natural viscosity for the numerical solutions so that an artificial viscosity may not be needed. From Eq. (9), we see that the eigenvalue $u-c$ is positive for supersonic flow and negative for subsonic flow. Thus for supersonic flow, Eq. (4) can be readily solved using the positive-wave upwind finite-difference method. For subsonic flow, however, we employ a wave-splitting, upwind finite-difference method to account for the mixed-sign eigenvalues.

For mixed-sign eigenvalues when $u<c$, the matrix $\mathbf{A}$ can be split into a semipositive definite matrix and a seminegative definite matrix as

$$\mathbf{A} = \mathbf{A}^+ + \mathbf{A}^- \tag{31}$$

where

$$\mathbf{A}^+ = \mathbf{\Phi}\mathbf{\Lambda}^+\mathbf{\Phi}^{-1} \tag{32}$$

$$\mathbf{A}^- = \mathbf{\Phi}\mathbf{\Lambda}^-\mathbf{\Phi}^{-1} \tag{33}$$

with

$$\mathbf{\Lambda}^+ = \begin{bmatrix} u+c & 0 & 0 \\ 0 & u & 0 \\ 0 & 0 & 0 \end{bmatrix} \geq \mathbf{0}, \quad \forall\, t \in (0,T) \tag{34}$$

$$\mathbf{\Lambda}^- = \begin{bmatrix} 0 & 0 & 0 \\ 0 & 0 & 0 \\ 0 & 0 & u-c \end{bmatrix} \leq \mathbf{0}, \quad \forall\, t \in (0,T) \tag{35}$$

The characteristic equation (10) can be written in a wave-splitting form as

$$\mathbf{\Phi}^{-1}\mathbf{y}_t + \mathbf{\Lambda}^+\mathbf{\Phi}^{-1}\mathbf{y}_x + \mathbf{\Lambda}^-\mathbf{\Phi}^{-1}\mathbf{y}_x + \mathbf{\Phi}^{-1}\mathbf{B} = \mathbf{0} \tag{36}$$

Equation (36) is now discretized using a wave-splitting, first-order upwind finite-difference method as

$$\mathbf{\Phi}^{-1}\dot{\mathbf{y}}_i + \mathbf{\Lambda}^+\mathbf{\Phi}^{-1}\frac{\mathbf{y}_i - \mathbf{y}_{i-1}}{\Delta x} + \mathbf{\Lambda}^-\mathbf{\Phi}^{-1}\frac{\mathbf{y}_{i+1} - \mathbf{y}_i}{\Delta x} + \mathbf{\Phi}^{-1}\mathbf{B} = \mathbf{0} \tag{37}$$

where $i=2,3,\ldots,m-1$ denotes the index of the interior points not on the boundary such that $x_i=((i-1)/(m-1))L$ and $\mathbf{y}_i(t)=\mathbf{y}(x_i,t)$.

The following question is posed: At what grid point do we want to evaluate $\mathbf{\Phi}^{-1}$, $\mathbf{\Lambda}^+$, $\mathbf{\Lambda}^-$, and $\mathbf{B}$? That is, we want to examine the stencil of the spatial discretization. To help answer this question, we examine the discretized form of the steady-state equation (23) using a first-order spatial discretization

$$\mathbf{A}(\mathbf{Y}_{i-1}, x_{i-1})\frac{\mathbf{Y}_i - \mathbf{Y}_{i-1}}{\Delta x} + \mathbf{B}(\mathbf{Y}_{i-1}, x_{i-1}) = \mathbf{0} \tag{38}$$

This form is an explicit spatial discretization, which yields a simple method for computing the steady-state solution of Eq. (23). We see that $\mathbf{A}$ and $\mathbf{B}$ are evaluated at a prior grid point with respect to the discretization of $\mathbf{y}_x$. In order for Eq. (37) to converge to the steady-state solution based on the discretization scheme in Eq. (38), we need to maintain a numerical consistency between the steady-state form and the quasilinear form. This is done by evaluating all the matrices in Eq. (37) at a prior grid point for the positive-wave speeds and at a current grid point for the negative-wave speed. Using this approach, Eq. (37) can be decomposed into scalar equations as

$$\mathbf{\Psi}_1(\mathbf{y}_{i-1}, x_{i-1})\dot{\mathbf{y}}_i + (u_{i-1} + c_{i-1})\mathbf{\Psi}_1(\mathbf{y}_{i-1}, x_{i-1})\frac{\mathbf{y}_i - \mathbf{y}_{i-1}}{\Delta x} + \mathbf{\Psi}_1(\mathbf{y}_{i-1}, x_{i-1})\mathbf{B}(\mathbf{y}_{i-1}, x_{i-1}) = 0 \tag{39}$$

$$\mathbf{\Psi}_2(\mathbf{y}_{i-1}, x_{i-1})\dot{\mathbf{y}}_i + u_{i-1}\mathbf{\Psi}_2(\mathbf{y}_{i-1}, x_{i-1})\frac{\mathbf{y}_i - \mathbf{y}_{i-1}}{\Delta x} + \mathbf{\Psi}_2(\mathbf{y}_{i-1}, x_{i-1})\mathbf{B}(\mathbf{y}_{i-1}, x_{i-1}) = 0 \tag{40}$$

$$\mathbf{\Psi}_3(\mathbf{y}_i, x_i)\dot{\mathbf{y}}_i + (u_i - c_i)\mathbf{\Psi}_3(\mathbf{y}_i, x_i)\frac{\mathbf{y}_{i+1} - \mathbf{y}_i}{\Delta x} + \mathbf{\Psi}_3(\mathbf{y}_i, x_i)\mathbf{B}(\mathbf{y}_i, x_i) = 0 \tag{41}$$

where $\mathbf{\Psi}_k(\mathbf{y}_i, x_i)$, $k=1,2,3$ is the kth 1×3 row vector of the matrix $\mathbf{\Phi}^{-1}(\mathbf{y}_i, x_i)$.

We now combine Eqs. (39)–(41) into a vector form as

$$\dot{\mathbf{y}}_i + \mathbf{A}_{i-1}^+\frac{\mathbf{y}_i - \mathbf{y}_{i-1}}{\Delta x} + \mathbf{A}_i^-\frac{\mathbf{y}_{i+1} - \mathbf{y}_i}{\Delta x} + \mathbf{B}_{i-1}^+ + \mathbf{B}_i^- = \mathbf{0} \tag{42}$$

with

$$\mathbf{A}_{i-1}^+ = \mathbf{\Psi}^{-1}\mathbf{\Lambda}^+(\mathbf{y}_{i-1}, x_{i-1})\mathbf{\Psi} \tag{43}$$

$$\mathbf{A}_i^- = \mathbf{\Psi}^{-1}\mathbf{\Lambda}^-(\mathbf{y}_i, x_i)\mathbf{\Psi} \tag{44}$$

$$\mathbf{B}_{i-1}^+ = \mathbf{\Psi}^{-1}\begin{bmatrix} \mathbf{\Psi}_1(\mathbf{y}_{i-1}, x_{i-1})\mathbf{B}(\mathbf{y}_{i-1}, x_{i-1}) \\ \mathbf{\Psi}_2(\mathbf{y}_{i-1}, x_{i-1})\mathbf{B}(\mathbf{y}_{i-1}, x_{i-1}) \\ 0 \end{bmatrix}_{3\times 1} \tag{45}$$

$$\mathbf{B}_i^- = \mathbf{\Psi}^{-1}\begin{bmatrix} 0 \\ 0 \\ \mathbf{\Psi}_3(\mathbf{y}_i, x_i)\mathbf{B}(\mathbf{y}_i, x_i) \end{bmatrix}_{3\times 1} \tag{46}$$

where

$$\mathbf{\Psi} = \begin{bmatrix} \mathbf{\Psi}_1(\mathbf{y}_{i-1}, x_{i-1}) \\ \mathbf{\Psi}_2(\mathbf{y}_{i-1}, x_{i-1}) \\ \mathbf{\Psi}_3(\mathbf{y}_i, x_i) \end{bmatrix}_{3\times 3} \tag{47}$$

We note that in general wave-splitting schemes are less conservative than flux-splitting schemes, which better preserve the con-

servation laws across shock waves [12]. However, for continuous subsonic flow, the wave-splitting schemes can yield good results. In particular, the wave-splitting scheme in Eq. (42) ensures that the time evolution of the hyperbolic solution will converge to the correct steady-state solution if it is also discretized in the same manner. Comparing this method of wave-splitting scheme with a well-known scheme, the difference is that the matrices $\mathbf{A}_{i-1}^{+}$ and $\mathbf{A}_{i}^{-}$ are evaluated at a prior grid point for the positive-wave speeds and at a current grid point for the negative-wave speed. This method is contrasted with a typical wave-splitting scheme using a midpoint method as

$$\mathbf{A}_{i-1/2}^{+} = \mathbf{A}^{+}\left(\frac{\mathbf{y}_{i-1}+\mathbf{y}_{i}}{2}, \frac{x_{i-1}+x_{i}}{2}\right) \tag{48}$$

$$\mathbf{A}_{i+1/2}^{-} = \mathbf{A}^{-}\left(\frac{\mathbf{y}_{i}+\mathbf{y}_{i+1}}{2}, \frac{x_{i}+x_{i+1}}{2}\right) \tag{49}$$

3.2 Stability Analysis. In the presence of the nonhomogeneous source vector $\mathbf{B}$, the stability of the upwind finite-difference method could be impacted depending on the magnitude of $\mathbf{B}$. The global stability of nonlinear differential equations is very desirable, but in many cases it can be difficult to evaluate [16]. Lyapunov stability theory has been used for determining the global stability of nonlinear differential equations [16,17]. Nonetheless, finding a Lyapunov function for a nonlinear system can be quite daunting and the failure of finding one does not necessarily imply that the system is unstable. Often, local stability of a nonlinear differential equation can be inferred from global stability of the linearization about an equilibrium [17]. Suppose $\mathbf{Y}_i$ is the steady-state solution of Eq. (38), then for every $\mathbf{Y}_i \in \mathbb{R}^n$ there exists a small variation $\tilde{\mathbf{y}}_i$ around the neighborhood of $\mathbf{Y}_i$ such that if $\tilde{\mathbf{y}}_i$ is a linearized solution bounded throughout the neighborhood of $\mathbf{Y}_i$, then $\tilde{\mathbf{y}}_i$ is globally stable in a linear sense. The global stability of $\tilde{\mathbf{y}}_i$ implies a local stability of $\mathbf{y}_i$ [16,17].

Suppose $\mathbf{A}_{i-1}^{+}$, $\mathbf{A}_{i}^{-}$, $\mathbf{B}_{i-1}^{+}$, and $\mathbf{B}_{i}^{-}$ are locally Lipschitz with respect to $\mathbf{y}_{i-1}$ and $\mathbf{y}_i$, then to obtain $\tilde{\mathbf{y}}_i$, we linearize Eq. (42) as

$$\begin{aligned}\dot{\tilde{\mathbf{y}}}_i + \mathbf{A}_{i-1}^{+}\frac{\tilde{\mathbf{y}}_i - \tilde{\mathbf{y}}_{i-1}}{\Delta x} + \mathbf{A}_{i-1,\mathbf{y}_i}^{+}\left(\frac{\mathbf{y}_i - \mathbf{y}_{i-1}}{\Delta x}\right)\tilde{\mathbf{y}}_i + \mathbf{A}_{i-1,\mathbf{y}_{i-1}}^{+}\left(\frac{\mathbf{y}_i - \mathbf{y}_{i-1}}{\Delta x}\right)\tilde{\mathbf{y}}_{i-1} \\ + \mathbf{A}_{i}^{-}\frac{\tilde{\mathbf{y}}_{i+1} - \tilde{\mathbf{y}}_i}{\Delta x} + \mathbf{A}_{i,\mathbf{y}_i}^{-}\left(\frac{\mathbf{y}_{i+1} - \mathbf{y}_i}{\Delta x}\right)\tilde{\mathbf{y}}_i + \mathbf{A}_{i,\mathbf{y}_{i-1}}^{-}\left(\frac{\mathbf{y}_{i+1} - \mathbf{y}_i}{\Delta x}\right)\tilde{\mathbf{y}}_{i-1} \\ + (\mathbf{B}_{i-1,\mathbf{y}_i}^{+} + \mathbf{B}_{i,\mathbf{y}_i}^{-})\tilde{\mathbf{y}}_i + (\mathbf{B}_{i-1,\mathbf{y}_{i-1}}^{+} + \mathbf{B}_{i,\mathbf{y}_{i-1}}^{-})\tilde{\mathbf{y}}_{i-1} = \mathbf{0}\end{aligned} \tag{50}$$

Since $\mathbf{Y}_i$ is a steady-state solution, then it follows that

$$\frac{\mathbf{Y}_{i+1} - \mathbf{Y}_i}{\Delta x} = -\mathbf{C}_i \tag{51}$$

where $\mathbf{C}_i = \mathbf{A}^{-1}(\mathbf{Y}_i, x_i)\mathbf{B}(\mathbf{Y}_i, x_i)$ as defined in Eq. (23). Equation (50) then becomes

$$\begin{aligned}\dot{\tilde{\mathbf{y}}}_i + \mathbf{A}_{i-1}^{+}\frac{\tilde{\mathbf{y}}_i - \tilde{\mathbf{y}}_{i-1}}{\Delta x} + \mathbf{A}_{i}^{-}\frac{\tilde{\mathbf{y}}_{i+1} - \tilde{\mathbf{y}}_i}{\Delta x} + (\mathbf{B}_{i-1,\mathbf{y}_i}^{+} + \mathbf{B}_{i,\mathbf{y}_i}^{-} - \mathbf{A}_{i-1,\mathbf{y}_i}^{+}\mathbf{C}_{i-1} \\ - \mathbf{A}_{i,\mathbf{y}_i}^{-}\mathbf{C}_i)\tilde{\mathbf{y}}_i + (\mathbf{B}_{i-1,\mathbf{y}_{i-1}}^{+} + \mathbf{B}_{i,\mathbf{y}_{i-1}}^{-} - \mathbf{A}_{i-1,\mathbf{y}_{i-1}}^{+}\mathbf{C}_{i-1} - \mathbf{A}_{i,\mathbf{y}_{i-1}}^{-}\mathbf{C}_i)\tilde{\mathbf{y}}_{i-1} \\ = \mathbf{0}\end{aligned} \tag{52}$$

The term $\mathbf{A}_{i-1,\mathbf{y}_i}^{+}\mathbf{C}_{i-1}$ is evaluated at $\mathbf{y}_{i-1}$ and $\mathbf{y}_i$ as

$$\mathbf{A}_{i-1,\mathbf{y}_i}^{+}\mathbf{C}_{i-1} = \begin{bmatrix}\mathbf{A}_{i-1,y_{1,i}}^{+}\mathbf{C}_{i-1} & \mathbf{A}_{i-1,y_{2,i}}^{+}\mathbf{C}_{i-1} & \mathbf{A}_{i-1,y_{3,i}}^{+}\mathbf{C}_{i-1}\end{bmatrix}_{3\times 3} \tag{53}$$

where the subscript y_j, $j=1,2,3$ denotes the partial derivative with respect to the scalar quantity y_j. All the other terms $\mathbf{A}_{i,\mathbf{y}_i}^{-}\mathbf{C}_i$, $\mathbf{A}_{i-1,\mathbf{y}_{i-1}}^{+}\mathbf{C}_{i-1}$, and $\mathbf{A}_{i,\mathbf{y}_{i-1}}^{-}\mathbf{C}_i$ in Eq. (52) are then evaluated in the same manner.

If $\mathbf{y}_i$ is smooth and Δx is a small number, then it may be assumed that $\mathbf{A}_{i}^{-} \simeq \mathbf{A}_{i-1}^{-}$, $\mathbf{A}_{i-1,\mathbf{y}_i}^{+}\mathbf{C}_{i-1} \simeq \mathbf{A}_{i-1,\mathbf{y}_i}^{+}\mathbf{C}_{i-1} + \mathbf{A}_{i,\mathbf{y}_i}^{-}\mathbf{C}_i$, and $\mathbf{B}_{i-1,\mathbf{y}_i} \simeq \mathbf{B}_{i-1,\mathbf{y}_i}^{+} + \mathbf{B}_{i,\mathbf{y}_i}^{-}$. Furthermore, we recognize that

$$\begin{aligned}\mathbf{A}_{i-1}^{-1}\mathbf{A}_{i-1,\mathbf{y}_i}\mathbf{C}_{i-1} + \mathbf{A}_{i-1,\mathbf{y}_i}^{-1}\mathbf{A}_{i-1}\mathbf{C}_{i-1} \\ = 0 \Rightarrow \mathbf{A}_{i-1,\mathbf{y}_i}\mathbf{C}_{i-1} = -\mathbf{A}_{i-1}\mathbf{A}_{i-1,\mathbf{y}_i}^{-1}\mathbf{B}_{i-1}\end{aligned} \tag{54}$$

Then, it follows that

$$\mathbf{B}_{i-1,\mathbf{y}_i} - \mathbf{A}_{i-1,\mathbf{y}_i}\mathbf{C}_{i-1} = \mathbf{A}_{i-1}(\mathbf{A}_{i-1}^{-1}\mathbf{B}_{i-1,\mathbf{y}_i} + \mathbf{A}_{i-1,\mathbf{y}_i}^{-1}\mathbf{B}_{i-1}) = \mathbf{A}_{i-1}\mathbf{C}_{i-1,\mathbf{y}_i} \tag{55}$$

We now can simplify Eq. (52) as

$$\begin{aligned}\dot{\tilde{\mathbf{y}}}_i + \mathbf{A}_{i-1}^{+}\frac{\tilde{\mathbf{y}}_i - \tilde{\mathbf{y}}_{i-1}}{\Delta x} + \mathbf{A}_{i-1}^{-}\frac{\tilde{\mathbf{y}}_{i+1} - \tilde{\mathbf{y}}_i}{\Delta x} + \mathbf{A}_{i-1}\mathbf{C}_{i-1,\mathbf{y}_i}\tilde{\mathbf{y}}_i + \mathbf{A}_{i-1}\mathbf{C}_{i-1,\mathbf{y}_{i-1}}\tilde{\mathbf{y}}_{i-1} \\ \simeq \mathbf{0}\end{aligned} \tag{56}$$

where

$$\mathbf{C}_{\mathbf{y}} = \frac{\gamma p_0 \mathrm{M}^2}{1-\mathrm{M}^2}\begin{bmatrix} 0 & 0 & 0 \\ \frac{1}{\dot{m}}\left(\frac{T_0 f}{TD} + \frac{1+\gamma \mathrm{M}^2}{2\dot{m}c_p T_0}\frac{dQ}{dx}\right) & -\frac{1+\gamma \mathrm{M}^2}{2p_0}\left(\frac{f}{D} + \frac{1}{\dot{m}c_p T_0}\frac{d\bar{Q}}{dx}\right) & \frac{1}{2T_0}\left(\frac{T_0 f}{TD} + \frac{(\gamma+1)\mathrm{M}^2}{2\dot{m}c_p T_0}\frac{dQ}{dx}\right) \\ \frac{1-\mathrm{M}^2}{\gamma p_0 \mathrm{M}^2 \dot{m}^2 c_p}\frac{dQ}{dx} & 0 & 0 \end{bmatrix} \tag{57}$$

Equation (56) can be written in a form

$$\dot{\mathbf{X}} = \mathbf{S}\mathbf{X} + \mathbf{V} \tag{58}$$

where

$$\mathbf{X} = [\tilde{\mathbf{y}}_2 \ \ \tilde{\mathbf{y}}_3 \ \ \cdots \ \ \tilde{\mathbf{y}}_{m-1}]^T$$

$$\mathbf{V} = \left[\left(\frac{\mathbf{A}_1^{+}}{\Delta x} - \mathbf{A}_1\mathbf{C}_{1,\mathbf{y}_1}\right)\tilde{\mathbf{y}}_1 \ \ \mathbf{0} \ \ \cdots \ \ -\frac{\mathbf{A}_{m-2}^{-}}{\Delta x}\tilde{\mathbf{y}}_m\right]^T$$

$$\mathbf{S} = \begin{bmatrix} -\frac{|\mathbf{A}_1|}{\Delta x} - \mathbf{A}_1\mathbf{C}_{1,\mathbf{y}_2} & -\frac{\mathbf{A}_1^-}{\Delta x} & \cdots & \mathbf{0} \\ \frac{\mathbf{A}_2^+}{\Delta x} - \mathbf{A}_2\mathbf{C}_{2,\mathbf{y}_2} & -\frac{|\mathbf{A}_2|}{\Delta x} - \mathbf{A}_2\mathbf{C}_{2,\mathbf{y}_3} & -\frac{\mathbf{A}_2^-}{\Delta x} & \vdots \\ \vdots & \mathbf{0} & \ddots & -\frac{\mathbf{A}_{m-3}^-}{\Delta x} \\ \mathbf{0} & \cdots & \frac{\mathbf{A}_{m-2}^+}{\Delta x} - \mathbf{A}_{m-2}\mathbf{C}_{m-2,\mathbf{y}_{m-2}} & -\frac{|\mathbf{A}_{m-2}|}{\Delta x} - \mathbf{A}_{m-2}\mathbf{C}_{m-2,\mathbf{y}_{m-1}} \end{bmatrix} \tag{59}$$

and

$$|\mathbf{A}_i| = \mathbf{A}_i^+ - \mathbf{A}_i^-$$

For a homogeneous solution for which $\mathbf{V}=\mathbf{0}$, Eq. (58) is stable if the eigenvalues of $\mathbf{S}$ are negative [17], thereby implying that Eq. (42) is locally stable about its equilibrium. The effect of the nonhomogeneous term $\mathbf{V}$ on the stability will be discussed later. If $\mathbf{y}_i$ is smooth and Δx is small, then the eigenvalues of $\mathbf{S}$ are computed to be

$$\lambda(\mathbf{S}) = \lambda\left(-\frac{|\mathbf{A}_i|}{\Delta x} - \mathbf{A}_i\mathbf{C}_{i,\mathbf{y}_i} \pm \left[-\frac{\mathbf{A}_i^-}{\Delta x}\left(\frac{\mathbf{A}_i^+}{\Delta x} - \mathbf{A}_i\mathbf{C}_{i,\mathbf{y}_i}\right)\right]^{1/2}\right) \tag{60}$$

where $\lambda(*)$ denotes the eigenvalue operation on *, and the square root operation of the matrix can be computed using a singular value decomposition [18].

Using the fact that $\mathbf{A}_i^-\mathbf{A}_i^+=\mathbf{0}$ and $\mathbf{A}_i^-\mathbf{A}_i=\mathbf{A}_i^-\mathbf{A}_i^-$, then Eq. (60) can be simplified as

$$\lambda(\mathbf{S}) = \lambda\left(-\mathbf{A}_i^+\left(\frac{\mathbf{I}}{\Delta x} + \mathbf{C}_{i,\mathbf{y}_i}\right) + \mathbf{A}_i^-\left[\frac{\mathbf{I}}{\Delta x} - \mathbf{C}_{i,\mathbf{y}_i} \pm \left(\frac{\mathbf{C}_{i,\mathbf{y}_i}}{\Delta x}\right)^{1/2}\right]\right) \tag{61}$$

For stability, we require that $\lambda(\mathbf{S})<0$. Since $\mathbf{A}_i^+\geq\mathbf{0}$ and $\mathbf{A}_i^-\leq\mathbf{0}$, this implies that

$$\frac{\mathbf{I}}{\Delta x} + \mathbf{C}_{i,\mathbf{y}_i} > \mathbf{0} \tag{62}$$

$$\frac{\mathbf{I}}{\Delta x} - \mathbf{C}_{i,\mathbf{y}_i} \pm \left(\frac{\mathbf{C}_{i,\mathbf{y}_i}}{\Delta x}\right)^{1/2} > \mathbf{0} \tag{63}$$

where $\mathbf{I}$ is the identity matrix. Since $\lambda(\mathbf{C}_\mathbf{y})\leq\mathbf{0}$, this implies that $\mathbf{C}_{i,\mathbf{y}_i}\leq\mathbf{0}$. Equation (63) then has an imaginary part, so we only require that the real part be positive definite. Because $\mathbf{C}_{i,\mathbf{y}_i}\leq\mathbf{0}$, Eq. (63) is satisfied for all Δx. On the other hand, Eq. (62) places a restriction on Δx, which must satisfy

$$\Delta x < \frac{1}{\max|\lambda(\mathbf{C}_{i,\mathbf{y}_i})|} \tag{64}$$

where

$$\max|\lambda(\mathbf{C}_\mathbf{y})| = \frac{\gamma \mathrm{M}^2(1+\gamma \mathrm{M}^2)}{1-\mathrm{M}^2}\left(\frac{f}{D} + \frac{1}{\dot{m}c_pT_0}\frac{d\bar{Q}}{dx}\right) \tag{65}$$

We see that the presence of the nonhomogeneous source term $\mathbf{B}$ in Eq. (4) affects the stability of the wave-splitting scheme in Eq. (42), which requires that Δx be less than the reciprocal of the largest absolute eigenvalue of $\mathbf{C}_{i,\mathbf{y}}$. Thus far, we have not considered the effect of the nonhomogeneous term $\mathbf{V}$. It is obvious that the stability of Eq. (58) also requires that $\mathbf{V}$ is bounded in $t\in[0,T]$. We assume that the functions $\mathbf{g}(\mathbf{y}(L,t),\mathbf{u})$ and $\mathbf{f}$ are locally Lipschitz with respect to $\mathbf{y}_1(t)=\mathbf{y}(0,t)$, $\mathbf{y}_m(t)=\mathbf{y}(L,t)$, and $\mathbf{u}$. If $\mathbf{U}\in\mathbb{R}^m$ is the steady-state solution of Eq. (27), then there exists a small variation $\tilde{\mathbf{u}}$ around the neighborhood of $\mathbf{U}$ such that if $\tilde{\mathbf{u}}$ is bounded throughout the neighborhood of $\mathbf{U}$, then $\tilde{\mathbf{u}}$ is globally stable. Linearization of Eqs. (25) and (27) results in

$$\mathbf{V} = \left[\left(\frac{\mathbf{A}_1^+}{\Delta x} - \mathbf{A}_1\mathbf{C}_{1,\mathbf{y}_1}\right)(\mathbf{g}_{\mathbf{y}_m}\tilde{\mathbf{y}}_m + \mathbf{g}_\mathbf{u}\tilde{\mathbf{u}}) \quad \mathbf{0} \quad \cdots \quad -\frac{\mathbf{A}_{m-1}^-}{\Delta x}\tilde{\mathbf{y}}_m\right]^T \tag{66}$$

$$\dot{\tilde{\mathbf{u}}} = \mathbf{f}_\mathbf{u}\tilde{\mathbf{u}} + \mathbf{f}_{\mathbf{y}_1}\tilde{\mathbf{y}}_1 + \mathbf{f}_{\mathbf{y}_m}\tilde{\mathbf{y}}_m + \mathbf{f}_\mathbf{V}\tilde{\mathbf{v}} \tag{67}$$

The nonhomogeneous term $\mathbf{V}$ is bounded if Eq. (67) is globally stable. Since $\mathbf{V}$ is measurable in $\mathcal{L}^2$, then $\tilde{\mathbf{v}}$ is also measurable in $\mathcal{L}^2$. The local stability of Eq. (27) then requires the global stability of Eq. (67), which implies that the eigenvalues of $\mathbf{f}_\mathbf{u}$ are negative in order to ensure that the nonhomogeneous term $\mathbf{V}$ is always bounded in $t\in[0,T]$. Thus, the additional requirement for the wave-splitting scheme is

$$\lambda(\mathbf{f}_\mathbf{u}) < 0 \tag{68}$$

We have thus shown that the wave-splitting scheme in Eq. (42) is stable under certain requirements. To implement the complete computational procedure, we must also address the nonlinear dynamic constraint equation (27), which can be discretized as

$$\dot{\mathbf{u}} = \mathbf{f}(\mathbf{y}_1, \mathbf{y}_m, \mathbf{u}, \mathbf{V}) \tag{69}$$

Equations (42) and (69) are subject to the following initial conditions:

$$\mathbf{Y}_i(0) = \mathbf{Y}(x_i) \tag{70}$$

$$\mathbf{U}(0) = \mathbf{U}_0 \tag{71}$$

Both these equations can be integrated using any standard ODE numerical methods such as the Euler method or the Runge–Kutta method. We note that because of the nonlinear forced periodic boundary condition (25) and the quasilinearity of Eq. (4), Eqs. (42) and (69) must be discretized in time using an explicit scheme. For an Euler's method, the time step must be chosen to satisfy the following condition:

$$\Delta t \leq \min\left\{\frac{\Delta x}{\max_i[(1+\alpha_i)(u_i+c_i)]}, \frac{2}{\max|\lambda(\mathbf{f}_\mathbf{u})|}\right\} \tag{72}$$

The first condition is the Courant–Friedrichs–Levy (CFL) condition for Eq. (42) [11]. The second condition is the numerical stability condition for Euler's method for Eq. (69). The term $1+\alpha$ is due to the contribution of the source term $\mathbf{B}$ where

$$\alpha_i = \frac{\mu_i \Delta x}{u_i + c_i} \tag{73}$$

and

$$\mu_i = -\frac{\boldsymbol{\Psi}_1(\mathbf{y}_i,x_i)\mathbf{B}(\mathbf{y}_i,x_i) - \boldsymbol{\Psi}_1(\mathbf{y}_{i-1},x_{i-1})\mathbf{B}(\mathbf{y}_{i-1},x_{i-1})}{\boldsymbol{\Psi}_1(\mathbf{y}_i,x_i)\mathbf{y}_i - \boldsymbol{\Psi}_1(\mathbf{y}_{i-1},x_{i-1})\mathbf{y}_{i-1}} \tag{74}$$

The derivation of the CFL condition is included in the Appendix.

3.3 Boundary Condition and Characteristic Equations. To solve for Eq. (39), we need the information on the system boundaries. We can write the periodic boundary condition (25) in a component form as

$$\begin{bmatrix} \dot{m}(0,t) \\ p_0(0,t) \\ T_0(0,t) \end{bmatrix} = \begin{bmatrix} \mathbf{I}_1 \\ \mathbf{I}_2 \\ \mathbf{I}_3 \end{bmatrix} \mathbf{y}_{1,j+1} = \begin{bmatrix} g_1(\mathbf{y}_{m,j+1},\mathbf{u}_{j+1}) \\ g_2(\mathbf{y}_{m,j+1},\mathbf{u}_{j+1}) \\ g_3(\mathbf{y}_{m,j+1},\mathbf{u}_{j+1}) \end{bmatrix} \tag{75}$$

where $\mathbf{I}_k$, $k=1,2,3$, is a kth row vector of the 3×3 identity matrix, and $j=1,2,\ldots,n-1$ denotes the time index such that $t_j=((j-1)/(n-1))T$ and $\mathbf{y}_{ij}=\mathbf{y}(x_i,t_j)$. We note that the mass flow is generally conserved so that

$$g_1(\mathbf{y}_{m,j+1},\mathbf{u}_{j+1}) = \mathbf{I}_1\mathbf{y}_{m,j+1} \tag{76}$$

At the incoming boundary $x=0$, $i=1$ so that the Eq. (37) cannot admit a positive wave, which would require the solution to include a point upstream of $x=0$ that is nonexistent. Since there is only one negative wave, only the negative-wave speed characteristic equation (41) is admitted. Using Euler's method, we combine Eq. (41) with the last two components of the boundary condition (75) so that

$$\begin{bmatrix} \mathbf{I}_2 \\ \mathbf{I}_3 \\ \boldsymbol{\Psi}_3(\mathbf{y}_{1j},x_1) \end{bmatrix} \mathbf{y}_{1,j+1} - \begin{bmatrix} g_2(\mathbf{y}_{m,j+1},\mathbf{u}_{j+1}) \\ g_3(\mathbf{y}_{m,j+1},\mathbf{u}_{j+1}) \\ 0 \end{bmatrix} = \begin{bmatrix} \mathbf{0}_{1\times 3} \\ \mathbf{0}_{1\times 3} \\ \boldsymbol{\Psi}_3(\mathbf{y}_{1j},x_1) \end{bmatrix} \mathbf{y}_{1j} - \frac{\boldsymbol{\Lambda}^-(\mathbf{y}_{1j},x_1)\Delta t}{\Delta x} \begin{bmatrix} \mathbf{0}_{1\times 3} \\ \mathbf{0}_{1\times 3} \\ \boldsymbol{\Psi}_3(\mathbf{y}_{1j},x_1) \end{bmatrix} (\mathbf{y}_{2j} - \mathbf{y}_{1j}) - \begin{bmatrix} \mathbf{0}_{1\times 3} \\ \mathbf{0}_{1\times 3} \\ \boldsymbol{\Psi}_3(\mathbf{y}_{1j},x_1) \end{bmatrix} \Delta t \mathbf{B}(\mathbf{y}_{1j},x_1) \tag{77}$$

where $\mathbf{0}_{1\times 3}$ is the 1×3 zero row vector.

We next consider the boundary at $x=L$, $i=m$. The situation is now reverse whereby the solution can only admit the two positive eigenvalue characteristic equations (39) and (40) along with the first component of the boundary condition (75). These three equations are written in a matrix form as

$$\begin{bmatrix} \boldsymbol{\Psi}_1(\mathbf{y}_{m-1,j},x_{m-1}) \\ \boldsymbol{\Psi}_2(\mathbf{y}_{m-1,j},x_{m-1}) \\ \mathbf{I}_1 \end{bmatrix} \mathbf{y}_{m,j+1} - \begin{bmatrix} \mathbf{0}_{1\times 3} \\ \mathbf{0}_{1\times 3} \\ \mathbf{I}_1 \end{bmatrix} \mathbf{y}_{1,j+1} = \begin{bmatrix} \boldsymbol{\Psi}_1(\mathbf{y}_{m-1,j},x_{m-1}) \\ \boldsymbol{\Psi}_2(\mathbf{y}_{m-1,j},x_{m-1}) \\ \mathbf{0}_{1\times 3} \end{bmatrix} \mathbf{y}_{mj} - \frac{\boldsymbol{\Lambda}^+(\mathbf{y}_{m-1,j},x_{m-1})\Delta t}{\Delta x} \times \begin{bmatrix} \boldsymbol{\Psi}_1(\mathbf{y}_{m-1,j},x_{m-1}) \\ \boldsymbol{\Psi}_2(\mathbf{y}_{m-1,j},x_{m-1}) \\ \mathbf{0}_{1\times 3} \end{bmatrix} (\mathbf{y}_{mj} - \mathbf{y}_{m-1,j}) - \begin{bmatrix} \boldsymbol{\Psi}_1(\mathbf{y}_{m-1,j},x_{m-1}) \\ \boldsymbol{\Psi}_2(\mathbf{y}_{m-1,j},x_{m-1}) \\ \mathbf{0}_{1\times 3} \end{bmatrix} \Delta t \mathbf{B}(\mathbf{y}_{m-1,j},x_{m-1}) \tag{78}$$

Equations (77) and (78) are nonlinear at the time step t_{j+1} due to the boundary condition (75) and also coupled together through the term $\mathbf{y}_{1,j+1}$. Solving for $\mathbf{y}_{1,j+1}$ from Eq. (77) and substituting into Eq. (78) then yield

$$\begin{aligned} &\begin{bmatrix} \boldsymbol{\Psi}_1(\mathbf{y}_{m-1,j},x_{m-1}) \\ \boldsymbol{\Psi}_2(\mathbf{y}_{m-1,j},x_{m-1}) \\ \mathbf{I}_1 \end{bmatrix} \mathbf{y}_{m,j+1} - \begin{bmatrix} \mathbf{0}_{1\times 3} \\ \mathbf{0}_{1\times 3} \\ \mathbf{I}_1 \end{bmatrix} \begin{bmatrix} \mathbf{I}_2 \\ \mathbf{I}_3 \\ \boldsymbol{\Psi}_3(\mathbf{y}_{1j},x_1) \end{bmatrix}^{-1} \begin{bmatrix} g_2(\mathbf{y}_{m,j+1},\mathbf{u}_{j+1}) \\ g_3(\mathbf{y}_{m,j+1},\mathbf{u}_{j+1}) \\ \mathbf{0}_{1\times 3} \end{bmatrix} \\ &= \begin{bmatrix} \boldsymbol{\Psi}_1(\mathbf{y}_{m-1,j},x_{m-1}) \\ \boldsymbol{\Psi}_2(\mathbf{y}_{m-1,j},x_{m-1}) \\ \mathbf{0}_{1\times 3} \end{bmatrix} \mathbf{y}_{mj} - \frac{\boldsymbol{\Lambda}^+(\mathbf{y}_{m-1j},x_{m-1})\Delta t}{\Delta x} \begin{bmatrix} \boldsymbol{\Psi}_1(\mathbf{y}_{m-1,j},x_{m-1}) \\ \boldsymbol{\Psi}_2(\mathbf{y}_{m-1,j},x_{m-1}) \\ \mathbf{0}_{1\times 3} \end{bmatrix} (\mathbf{y}_{mj} - \mathbf{y}_{m-1,j}) - \begin{bmatrix} \boldsymbol{\Psi}_1(\mathbf{y}_{m-1,j},x_{m-1}) \\ \boldsymbol{\Psi}_2(\mathbf{y}_{m-1,j},x_{m-1}) \\ \mathbf{0}_{1\times 3} \end{bmatrix} \Delta t \mathbf{B}(\mathbf{y}_{m-1,j},x_{m-1}) \\ &+ \begin{bmatrix} \mathbf{0}_{1\times 3} \\ \mathbf{0}_{1\times 3} \\ \mathbf{I}_1 \end{bmatrix} \begin{bmatrix} \mathbf{I}_2 \\ \mathbf{I}_3 \\ \boldsymbol{\Psi}_3(\mathbf{y}_{1j},x_1) \end{bmatrix}^{-1} \begin{bmatrix} \mathbf{0}_{1\times 3} \\ \mathbf{0}_{1\times 3} \\ \boldsymbol{\Psi}_3(\mathbf{y}_{1j},x_1) \end{bmatrix} \mathbf{y}_{1j} - \begin{bmatrix} \mathbf{0}_{1\times 3} \\ \mathbf{0}_{1\times 3} \\ \mathbf{I}_1 \end{bmatrix} \begin{bmatrix} \mathbf{I}_2 \\ \mathbf{I}_3 \\ \boldsymbol{\Psi}_3(\mathbf{y}_{1j},x_1) \end{bmatrix}^{-1} \frac{\boldsymbol{\Lambda}^-(\mathbf{y}_{1j},x_1)\Delta t}{\Delta x} \begin{bmatrix} \mathbf{0}_{1\times 3} \\ \mathbf{0}_{1\times 3} \\ \boldsymbol{\Psi}_3(\mathbf{y}_{1j},x_1) \end{bmatrix} (\mathbf{y}_{2j} - \mathbf{y}_{1j}) \\ &- \begin{bmatrix} \mathbf{0}_{1\times 3} \\ \mathbf{0}_{1\times 3} \\ \mathbf{I}_1 \end{bmatrix} \begin{bmatrix} \mathbf{I}_2 \\ \mathbf{I}_3 \\ \boldsymbol{\Psi}_3(\mathbf{y}_{1j},x_1) \end{bmatrix}^{-1} \begin{bmatrix} \mathbf{0}_{1\times 3} \\ \mathbf{0}_{1\times 3} \\ \boldsymbol{\Psi}_3(\mathbf{y}_{1j},x_1) \end{bmatrix} \Delta t \mathbf{B}(\mathbf{y}_{1j},x_1) \end{aligned} \tag{79}$$

Equation (79) now becomes only a nonlinear function of $\mathbf{y}_{m,j+1}$ and $\mathbf{u}_{j+1}$. An iterative method is implemented to search for the zero solution of $\mathbf{y}_{m,j+1}$ using information from the previous time step. To solve Eq. (79), the boundary control vector $\mathbf{u}$ must be determined for a given time history of the auxiliary control $\mathbf{v}$ by integrating Eq. (69). Once $\mathbf{y}_{m,j+1}$ is determined, then $\mathbf{y}_{m,j+1}$ is computed from Eq. (78). Thus, the information at the system boundaries is now known and then can be used to compute all the information at the interior points by integrating Eq. (42) forward in time.

3.4 Shock Fitting. Flow with shocks in a closed-loop transport system poses a significant challenge in that a discontinuous solution of the Euler equations must be found that can predict when and where a shock structure would arise. To further complicate the solution, the discontinuous solution must also satisfy the nonlinear boundary condition (25). Most shock capturing schemes are designed for the flux-conserved form of the Euler equations because the flux variables are conserved across a shock structure. First-order shock capturing schemes such as Lax–Friedrichs and Lax–Wendroff schemes with artificial viscosity are commonly used to provide unique entropy solutions that define physical shock structures.

Since the present method is based on the quasilinear, non-flux-conserved form, the shock structure must be estimated explicitly by a shock fitting method. This means that some information must be known a priori such as the general vicinity of the shock structure and the number of normal shocks in the flow field. For each shock, the domain of solution must be decomposed appropriately to deal with the presence of multiple shocks in the flow field. Toward this end, for a single shock structure, if the flow in a closed-loop transport system is transitioned from subsonic to supersonic, the critical flow condition at Mach 1 exists at the minimum cross-sectional area A^*, or the throat area. The ensuing supersonic flow will encounter a normal shock formation at some point farther downstream in the flow from the throat area. In this situation, the flow in the closed-loop transport system can be divided into three regions: (1) Region I is defined by $0 \le x < L^*$ wherein the flow is entirely subsonic, (2) region II is defined by $L^* < x \le L_S^-$ wherein the flow is entirely supersonic, and (3) region III is defined by $L_S^- < x \le L$ wherein the flow is entirely subsonic. If more than one shock is present in the solution domain, the number of regions increases by two for each additional shock. For example, if there are two shocks, the flow is divided into five regions, and for three shocks, the number of solution regions is seven, and so on. Thus, as the number of shocks increases, the shock fitting method can become inefficient. For the analysis below, a single shock structure is assumed, but the method is general enough for extending to the case of multiple shocks present in the flow field.

The discontinuous solution across the shock region $L_S^- < x \le L_S^+$ is defined by the Rankine–Hugoniot relationship

$$(\mathbf{F}^+ - \mathbf{F}^-) = V(\mathbf{U}^+ - \mathbf{U}^-) \tag{80}$$

which can also be written as

$$(\mathbf{b}^+\mathbf{y}^+ - \mathbf{b}^-\mathbf{y}^-) = V(\mathbf{a}^+\mathbf{y}^+ - \mathbf{a}^-\mathbf{y}^-) \tag{81}$$

where the $\pm$ sign denotes $x = L_S^+$ and $x = L_S^-$, V is the speed of the moving shock, and

$$\mathbf{a}(\mathbf{y}) = \begin{bmatrix} \frac{1}{u} & 0 & 0 \\ 1 & 0 & 0 \\ 0 & -\frac{A}{\left(1 + \frac{\gamma-1}{2}\mathrm{M}^2\right)^{\gamma/(\gamma-1)}} & \frac{\dot{m}c_p}{u} \end{bmatrix}$$

$$\mathbf{b}(\mathbf{y},x) = \begin{bmatrix} 1 & 0 & 0 \\ 0 & \frac{A(1+\gamma\mathrm{M}^2)}{\left(1 + \frac{\gamma-1}{2}\mathrm{M}^2\right)^{\gamma/(\gamma-1)}} & 0 \\ 0 & 0 & \dot{m}c_p \end{bmatrix} \tag{82}$$

To obtain a physical solution, the entropy condition requires that

$$\mathrm{M}^+ - \frac{V}{c^+} = \sqrt{\frac{2 + (\gamma-1)\left(\mathrm{M}^- - \frac{V}{c^-}\right)^2}{2\gamma\left(\mathrm{M}^- - \frac{V}{c^-}\right)^2 - (\gamma-1)}} < 1 \tag{83}$$

We note that for a standing shock, the following relationship applies:

$$\mathbf{y}^+ = (\mathbf{b}^+)^{-1}\mathbf{b}^-\mathbf{y}^- \tag{84}$$

where

$$(\mathbf{b}^+)^{-1}\mathbf{b}^- = \begin{bmatrix} 1 & 0 & 0 \\ 0 & r & 0 \\ 0 & 0 & 1 \end{bmatrix} \tag{85}$$

$$r = \left[\frac{\frac{\gamma+1}{2}(\mathrm{M}^-)^2}{1 + \frac{\gamma+1}{2}(\mathrm{M}^-)^2}\right]^{\gamma/(\gamma-1)} \left[\frac{2\gamma}{\gamma+1}(\mathrm{M}^-)^2 - \frac{\gamma-1}{\gamma+1}\right]^{-1/(\gamma-1)} < 1 \tag{86}$$

The shock location L_S is determined by matching the flow conditions at the boundaries between the flow regions in order to satisfy the nonlinear forced periodic boundary condition (25). Initially, we assume a standing shock whose location is known. At each subsequent time step, an iterative solution is performed to locate the shock. Since the mass flow and enthalpy conservation prevail at the boundaries of these regions, the shock location is primarily a function of the stagnation pressure relationship and is found by determining $x = L_S$ that satisfies the following stagnation pressure balance equation:

$$\Delta p_{0,\mathrm{I}} + \Delta p_{0,\mathrm{II}} + \Delta p_{0,S} + \Delta p_{0,\mathrm{III}} = g_2(\mathbf{y}(L,t),\mathbf{u}) - p_0(L,t) \tag{87}$$

where

$$\Delta p_{0,\mathrm{I}} = p_0(0,t) - p_0(L^*,t) \tag{88}$$

$$\Delta p_{0,\mathrm{II}} = p_0(L^*,t) - p_0(L_S^-,t) \tag{89}$$

$$\Delta p_{0,S} = p_0(L_S^-,t) - p_0(L_S^+,t) = -\frac{V}{b_{22}^+}(\dot{m}^+ - \dot{m}^-) + \left(1 - \frac{b_{22}^-}{b_{22}^+}\right)p_0^- \tag{90}$$

$$\Delta p_{0,\mathrm{III}} = p_0(L_S^+,t) - p_0(L,t) \tag{91}$$

To solve for flow regions I and II, an additional boundary condition is imposed at the throat area that relates the critical mass flow to the stagnation pressure and temperature as follows:

$$\dot{m}(L^*,t) = \sqrt{\frac{\gamma}{RT_0(L^*,t)}} p_0(L^*,t) A^* \left(\frac{\gamma+1}{2}\right)^{-(\gamma+1)/2(\gamma-1)} \tag{92}$$

This boundary condition together with two characteristic boundary conditions for positive-wave speeds completely defines the boundary conditions at the throat area. Once the initial guess of the shock location at the current time step is found, the normal shock speed can be computed from the shock locations at the current and previous time steps as

$$V = \frac{L_S(t) - L_S(t-\Delta t)}{\Delta t} \tag{93}$$

Equations (81), (87), and (93) are then iterated until the shock location L_S converges. The solution for the entire transonic flow in the closed-loop transport system is then completely established.

4 Numerical Simulation

4.1 Closed-Circuit Wind Tunnel Model. The present computational method for a closed-loop transport system is applied to model fluid flow in the NASA Ames 11 ft TWT as shown in Fig. 1. Fluid flow is recirculated through a closed-circuit duct by a compressor, as illustrated in Fig. 2, that delivers air flow to a test section at a desired air speed for aerodynamic testing. The compressor is considered to be a key component of a wind tunnel system designed to match wind tunnel pressure losses due to fluid viscous losses. Fluid flow through alternating rows of stator and rotor blades within the compressor imparts a tangential velocity component in the flow. The kinetic energy associated with this swirl flow is then converted into a potential energy that creates a pressure rise across the compressor. The rotor blades are driven by a set of drive motors. In addition, a compressor in a wind tunnel may be equipped with variable-geometry inlet guide vanes designed to adjust the stagnation pressure rise at a constant compressor speed. The inlet guide vanes may have adjustable trailing edge flaps to change the air tangential velocity. Changes in the aerodynamic condition in a wind tunnel are thus accomplished by changing the compressor speed and the inlet guide vane flap angle. These two quantities are often referred to as compressor control inputs. Figure 3 shows a plot of the 11 ft TWT Mach number envelope as a function of the compressor control inputs.

The flow in a wind tunnel may be assumed to be 1D flow since we are interested in unsteady, spatially averaged flow through any given cross section of the wind tunnel. This information is useful for studying the time response of the flow condition in the test section due to control inputs from the drive motors and the inlet guide vane flap angle. Equation (22) is used to model this 1D unsteady flow. The friction factor f used in Eq. (22) is determined experimentally from wind tunnel measurements. The model also includes the heat transfer process taken place in the compressor and the aftercooler. We assume a perfect heat transfer process whereby the heat generated by the enthalpy increase across the compressor is completely removed by the aftercooler.

The forcing function $\mathbf{g}$ describes the behavior of the compressor through the boundary control vector $\mathbf{u}=[\omega\ \ \theta]^T$ where ω is the compressor speed and θ is the inlet guide vane flap angle. The compressor is a fluid device so the conservation of mass, momentum, and energy is applicable. The mass flow through the compressor must be constant. The stagnation pressure and stagnation temperature rises are due to the work input supplied by the drive motors. Let $x=0$ be the compressor exit station and $x=L$ be the compressor inlet station. Then, the performance of a turbomachine is generally described by the following similitude relationship [19]:

$$\frac{p_0(0,t)}{p_0(L,t)} = f(\dot{m}_c, \omega_c, \theta) \tag{94}$$

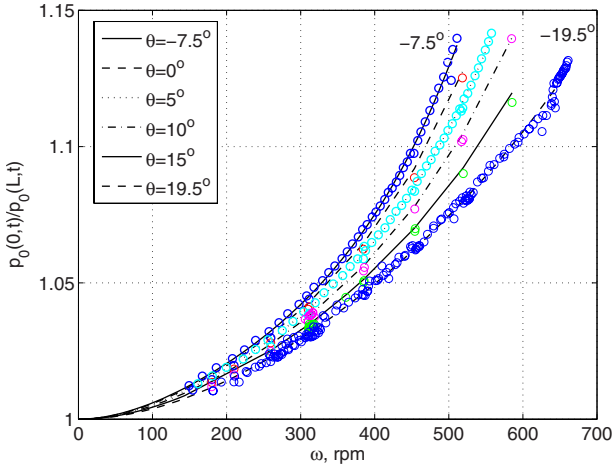

Fig. 5 Compressor pressure ratio

$$\frac{T_0(0,t)}{T_0(L,t)} = f\left(\frac{p_0(0,t)}{p_0(L,t)}, \dot{m}_c, \omega_c\right) \tag{95}$$

where $\dot{m}_c$ is the corrected mass flow and ω_c is the corrected speed defined as

$$\dot{m}_c = \dot{m}(L,t)\frac{p_{0,\text{ref}}}{p_0(L,t)}\sqrt{\frac{T_0(L,t)}{T_{0,\text{ref}}}} \tag{96}$$

$$\omega_c = \omega\sqrt{\frac{T_{0,\text{ref}}}{T_0(L,t)}} \tag{97}$$

and $p_{0,\text{ref}}$ and $T_{0,\text{ref}}$ are some reference total pressure and total temperature.

Using an empirical model, we obtain the forcing function $\mathbf{g}$ in the nonlinear forced periodic boundary condition (25) for the wind tunnel model as

$$\mathbf{g}(\mathbf{y}(L,t),\mathbf{u}) = \begin{bmatrix} \dot{m}(L,t) \\ p_0(L,t)\left(1+\sum_{i=2}^{4}\sum_{j=0}^{2} c_{ij}\theta^j\omega_c^i\right)\left(b_1 - b_2\dfrac{\dot{m}_c}{\sum_{i=1}^{3}\sum_{j=0}^{2} d_{ij}\theta^j\omega_c^i}\right) \\ T_0(L,t)\left\{1+\dfrac{b_3\omega_c}{\dot{m}_c}\left[\dfrac{p_0(0,t)}{p_0(L,t)}-1\right]\right\} \end{bmatrix} \tag{98}$$

where b_i, c_{ij}, and d_{ij} are empirical coefficients derived from experimental compressor performance measurements as shown in Fig. 5.

Equation (27) describes the time-varying process of the boundary control as influenced by the dynamics of the auxiliary process encapsulated by the transition function $\mathbf{f}$ and the auxiliary control vector $\mathbf{V}$. The coupling with Eq. (22) is due to the existence of the transport vectors $\mathbf{y}(0,t)$ and $\mathbf{y}(L,t)$ at the system boundaries. In particular, for the wind tunnel model, the drive motors and the inlet guide vane systems impose dynamic constraints on the compressor speed and the inlet guide vane flap angle. In particular, the torque equation for the drive motors is given by

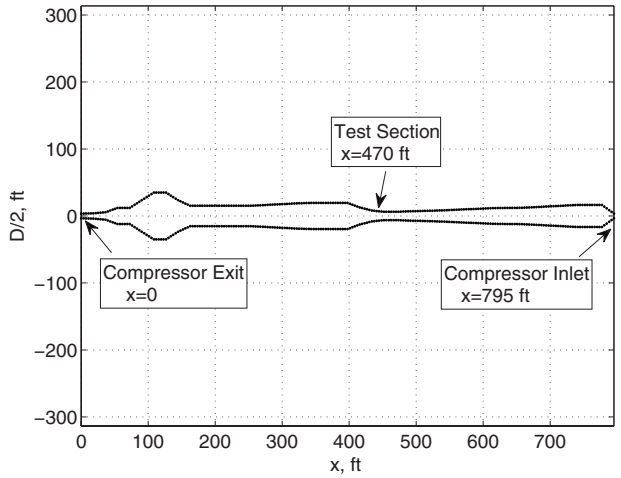

Fig. 6 Wind tunnel discretization

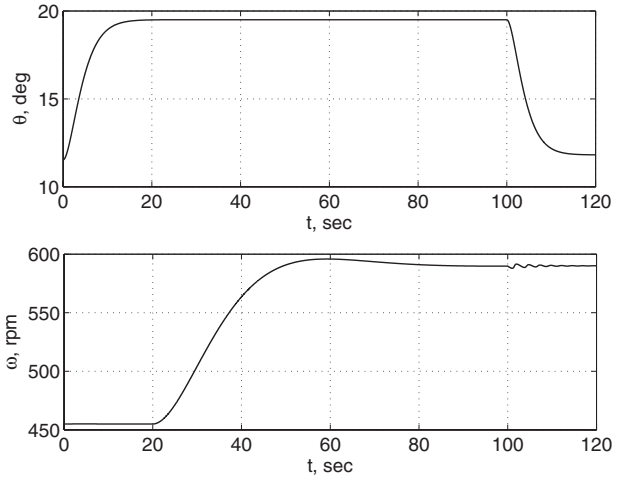

Fig. 7 Compressor speed and inlet guide vane flap angle responses

$$\dot{\omega} = \frac{a_m R_r(\omega_s - \omega)}{b_m(\omega_s - \omega)^2 + c_m R_r(\omega_s - \omega) + d_m R_r^2} - e_m[p_0(0,t) - p_0(L,t)] \tag{99}$$

where R_r is a rotor resistance that controls the motor drive speed; ω_s is the synchronous speed; and a_m, b_m, c_m, d_m, and e_m are some parameters.

Similarly, the dynamics of the inlet guide vane system is described by the following equation:

$$\dot{\theta} = q(L,t)(a_i\theta + b_i) + c_i V_a \tag{100}$$

where V_a is a field voltage that controls the inlet guide vane system; and a_i, b_i, and c_i are some parameters.

In the context of Eq. (27), the boundary control vector $\mathbf{u} = [\omega \ \ \theta]^T$ is dynamically constrained by Eqs. (99) and (100) and is controlled by the auxiliary control vector $\mathbf{v} = [R_r \ \ V_a]^T$.

5 Results

A simulation is conducted to compute the test section Mach number transition from Mach 0.6 to Mach 0.9 in the 11 ft TWT. The wind tunnel model is discretized into 221 nodes as shown in Fig. 6.

The step size $\Delta x = 3.6$ ft is chosen so that the important features of the wind tunnel such as the aftercooler and test section positions are captured in the spatial discretization. The simulation time for the Mach number transition is about 2 min. The time step $\Delta t = 0.001$ s is used in order to satisfy the CFL condition (72). The time histories of the compressor speed and the inlet guide vane flap angle during the Mach number transition from 0.6 to 0.9 are plotted in Fig. 7. The transition takes place over a 120 s interval. At the beginning of the transition, the inlet guide vane flap angle is adjusted while the compressor speed is held constant at 455 rpm. A new compressor speed set point of 590 rpm is then sought while the inlet guide vane flap angle is maintained constant at 19.5 deg. Once the compressor speed is stabilized, the inlet guide vane flap angle is adjusted in a closed-loop feedback mode using the test section Mach number error as a feedback variable. The ripples at the beginning of the final interval are due to a compressor speed proportional and integral feedback control implemented in the simulation.

The corresponding inlet guide vane field voltage and the drive motor rotor resistance that control the motion of the compressor speed and the inlet guide vane flap angle are plotted in Fig. 8.

Figure 9 illustrates the test section Mach number response computed using the wave-splitting finite-difference method as compared with the wind tunnel test data. An excellent agreement between the computed test section Mach number and the test data is observed.

The complete solution of the Euler equations is plotted in Figs. 10–13. The Mach number distribution in the wind tunnel is shown

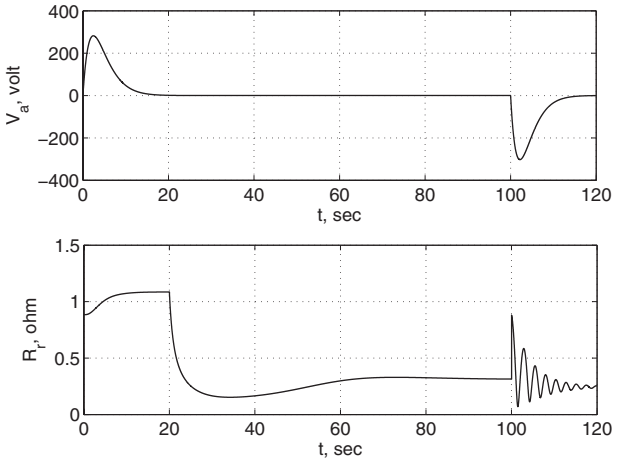

Fig. 8 Drive motor rotor resistance and inlet guide vane motor voltage

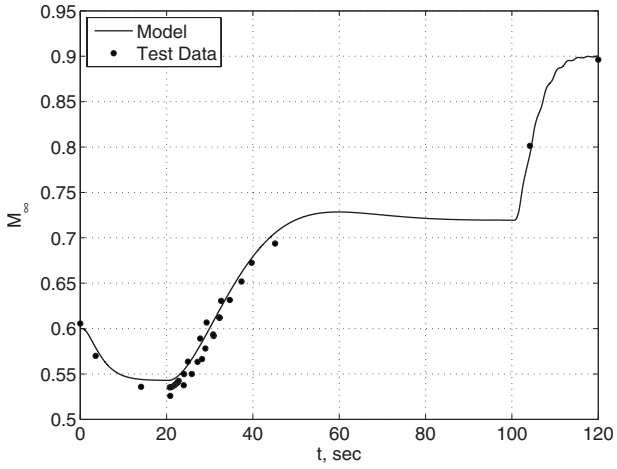

Fig. 9 Test section Mach number response

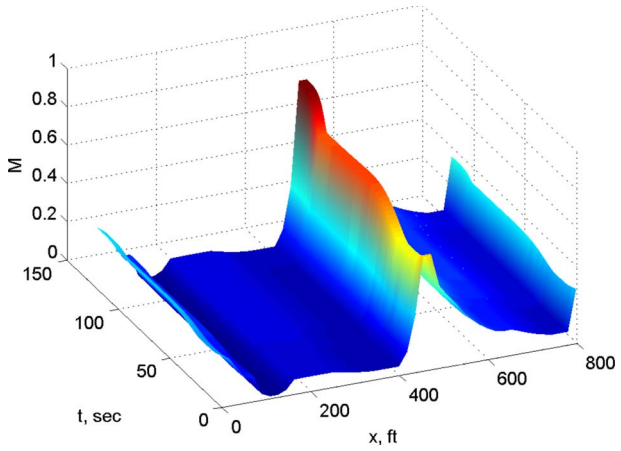

Fig. 10 Mach number distribution

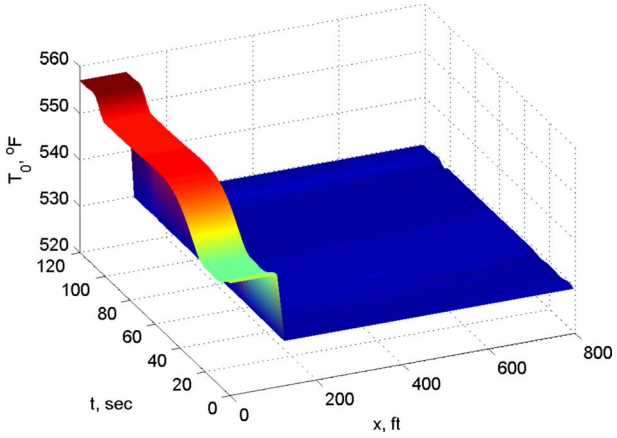

Fig. 13 Stagnation temperature distribution

in Fig. 10, showing the peaked Mach number in the test section. Elsewhere in the wind tunnel, the Mach number is nominally low and in the upper incompressible range below a Mach number of 0.35. The mass flow distribution in the wind tunnel is plotted in Fig. 11. It can be seen that the mass flow is essentially constant at all locations in the wind tunnel.

Figure 12 shows a plot of the stagnation pressure distribution in the wind tunnel. It always decreases in the x-direction due to viscous losses in the flow. The stagnation temperature distribution is plotted in Fig. 13. It can be seen that the stagnation temperature is almost constant throughout the wind tunnel except in the region between the compressor exit and the aftercooler where the heat transfer process takes place. As the Mach number increases, the stagnation temperature at the compressor exit rises due to a greater work input from the drive motors. This work input must be removed by the aftercooler in order to maintain a stable stagnation temperature in the test section for aerodynamic testing. In reality, the work input is not always completely removed by the aftercooler especially at a high supersonic flow in the test section. However, for subsonic flow, the assumption of a perfect heat transfer is quite reasonable.

Figure 14 illustrates the test section Mach number response computed by the midpoint discretization of the characteristic matrices according to Eqs. (48) and (49). The agreement between the current discretization and the midpoint discretization is quite good. However, a closer examination reveals that the midpoint method did not quite converge to the correct Mach number as the current method. This slight discrepancy is due to the inconsistency in the space discretization. The advantage with the current scheme is that the characteristic matrices are evaluated using only information at one grid point whereas the midpoint scheme requires information at two grid points. Thus, computationally, the current method is twice as less expensive than the midpoint method.

To demonstrate the shock capturing method, a simulation of transonic flow in the wind tunnel is conducted. The Mach number in the test section is maintained at Mach 1.2 at all times and the inlet guide vane flap angle is adjusted from 10 deg to 4 deg cor-

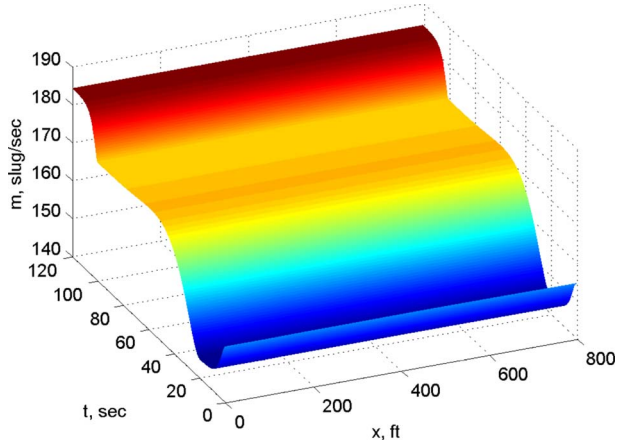

Fig. 11 Mass flow distribution

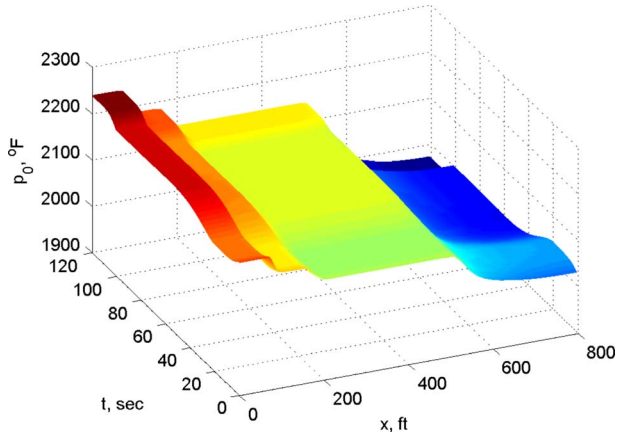

Fig. 12 Stagnation pressure distribution

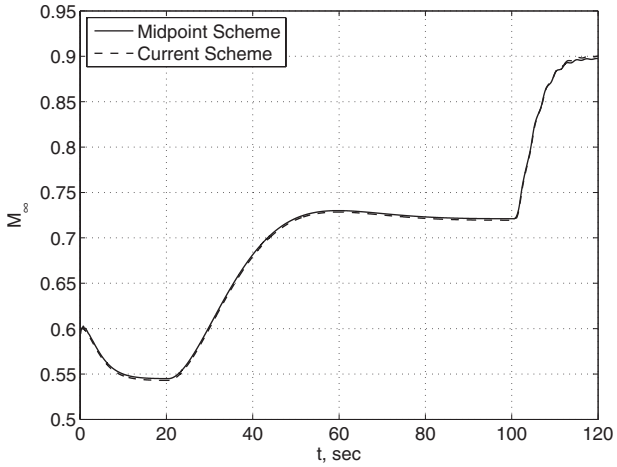

Fig. 14 Test section Mach number comparison between midpoint discretization and current discretization

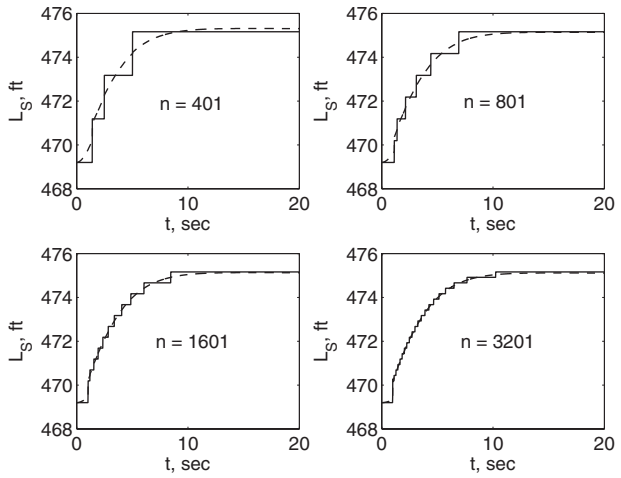

Fig. 15 Computed shock location

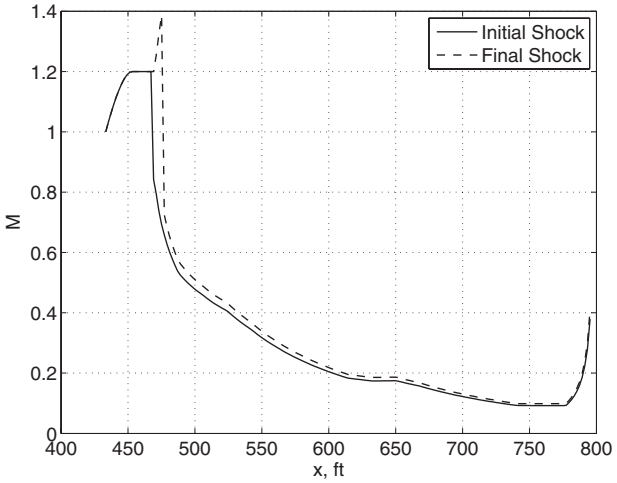

Fig. 17 Initial and final Mach number variations

responding to the Mach 1.4 setting. Since the Mach number in the test section is dictated by the area ratio between the test section and the nozzle throat, without adjusting the flexible nozzle, the effect of the inlet guide vane adjustment is to cause the normal shock to move downstream of the test section. To compute the shock location, four different numbers of grid points are used: 401, 801, 1601, and 3201. The plots of the computed shock location are shown in Fig. 15.

The stair case plots are the computed shock locations at the grid points and the smooth curves are the plots of the fitted shock locations using a first-order fitting method. Figure 16 illustrates a well-known fact that in order to accurately capture a shock location, the number of grid points must be sufficiently large. In fact, the shock location error is found to be very close to half of the Δx step size. Figure 17 shows the plot of the Mach number in the wind tunnel circuit showing the final shock location moved to downstream of the test section.

6 Conclusions

This paper has presented a computational method for a closed-loop fluid transport system based on the one-dimensional unsteady Euler equations with a dissipative source term. A quasilinear form is formulated in terms of the mass flow, the stagnation pressure, and the stagnation temperature. In this form, the mass flow and the stagnation temperature are, in fact, conserved quantities. Therefore, the present quasilinear form represents an intermediate model between the flux-conserved formulation and the primitive variable formulation. The closed-loop transport system is modeled via a nonlinear forced periodic boundary condition, which in turn is coupled to a system of ordinary differential equations that model an auxiliary system, which actually controls the behavior of the fluid conditions at the boundary. A wave-splitting, finite-difference first-order upwind method is introduced. This scheme maintains a consistency with the steady-state discretization. A numerical simulation of unsteady flow in a closed-circuit wind tunnel demonstrates an excellent agreement with experimental data. When compared with a midpoint scheme, the present scheme shows a better convergence. A shock fitting scheme is presented for the quasilinear form. A numerical simulation shows that the shock location error is very close to half of the spatial step size.

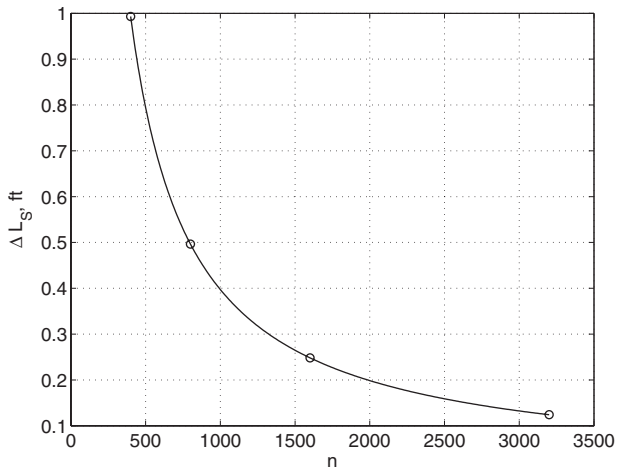

Fig. 16 Maximum shock location error versus number of grid points

Nomenclature

- $\mathbf{A}$ = characteristic matrix
- A = cross-sectional area
- A^* = minimum cross-sectional area
- $\mathbf{B}$ = nonhomogeneous source term
- c = speed of sound
- c_p = constant-pressure specific heat
- c_v = constant-volume specific heat
- D = hydraulic diameter
- $\mathbf{F}$ = flux vector
- $\mathbf{f}$ = transition function
- f = friction parameter
- $\mathbf{g}$ = periodic boundary condition forcing function
- L = length
- L_S = shock location
- L^* = minimum cross-sectional area location
- M = Mach number
- $\dot{m}$ = mass flow rate
- p = pressure
- p_0 = stagnation pressure
- $\mathbf{Q}$ = nonhomogeneous source term
- Q = heat transfer
- R = gas constant
- s = entropy
- $\mathbf{U}$ = flux-conserved form transport vector
- $\mathbf{u}$ = boundary control vector
- u = speed
- V = shock speed
- $\mathbf{v}$ = control vector
- T = temperature

T_0 = stagnation temperature
t = time
x = spatial coordinates
$\mathbf{Y}$ = steady-state transport vector
$\mathbf{y}$ = transport vector
γ = specific heat ratio
$\mathbf{\Lambda}$ = eigenvalue matrix
λ = eigenvalue
ρ = density
ρ_0 = stagnation density
$\mathbf{\Phi}$ = right eigenvector matrix
$\mathbf{\Psi}$ = inverse of right eigenvector matrix

Superscripts

$+$ = positive-wave speed
$-$ = negative-wave speed

Appendix

The Von Neumann method for stability analysis can be used to determine the CFL condition for the scalar upwind equation (39) [11]. Toward that end, let $\mathbf{\Psi}_1(\mathbf{y}_i,x_i)\mathbf{y}_i(t_k)=E_k e^{ji\phi}$ be a simple harmonic solution where E is the amplitude, $j=\sqrt{-1}$, and ϕ is the phase angle. Furthermore, we assume that $\mathbf{\Psi}_1(\mathbf{y}_{i-1},x_{i-1}) \approx \mathbf{\Psi}_1(\mathbf{y}_i,x_i)$ for small Δx. Using the Taylor series expansion, $\mathbf{\Psi}_1\mathbf{B}$ can be expressed as

$$\mathbf{\Psi}_1(\mathbf{y}_i,x_i)\mathbf{B}(\mathbf{y}_i,x_i) = \mathbf{\Psi}_1(\mathbf{0},0)\mathbf{B}(\mathbf{0},0) + \frac{\partial(\mathbf{\Psi}_1\mathbf{B})}{\partial(\mathbf{\Psi}_1\mathbf{y}_i)}\mathbf{\Psi}_1(\mathbf{y}_i,x_i)\mathbf{y}_i + \frac{\partial(\mathbf{\Psi}_1\mathbf{B})}{\partial x_i}x_i + \mathcal{O}(\mathbf{y}_i x_i,\mathbf{y}_i^2,x_i^2) \tag{A1}$$

Neglecting higher order terms, the only term in Eq. (A1) that contributes to the stability analysis is the second term in the right hand side. The Von Neumann stability analysis then results in

$$\frac{E_{k+1}e^{ji\phi}-E_k e^{ji\phi}}{\Delta t} + (u_{i-1}+c_{i-1})\frac{E_k e^{ji\phi}-E_k e^{j(i-1)\phi}}{\Delta x} - \mu_{i-1}E_k e^{j(i-1)\phi} \approx 0 \tag{A2}$$

where $\mu=-\partial(\mathbf{\Psi}_1\mathbf{B})/\partial(\mathbf{\Psi}_1\mathbf{y}_i)$ can be approximated as

$$\mu_i \approx -\frac{\mathbf{\Psi}_1(\mathbf{y}_i,x_i)\mathbf{B}(\mathbf{y}_i,x_i)-\mathbf{\Psi}_1(\mathbf{y}_{i-1},x_{i-1})\mathbf{B}(\mathbf{y}_{i-1},x_{i-1})}{\mathbf{\Psi}_1(\mathbf{y}_i,x_i)\mathbf{y}_i-\mathbf{\Psi}_1(\mathbf{y}_{i-1},x_{i-1})\mathbf{y}_{i-1}} \tag{A3}$$

Dividing Eq. (A2) by $E_k e^{ji\phi}$ yields

$$G_k - 1 + \sigma_{i-1}(1-e^{-j\phi}) - \mu_{i-1}\Delta t e^{-j\phi} \approx 0 \tag{A4}$$

where $G_k=E_{k+1}/E_k$ and

$$\sigma_{i-1} = \frac{(u_{i-1}+c_{i-1})\Delta t}{\Delta x} \tag{A5}$$

G_k can also be expressed as

$$G_k \approx 1-\sigma_{i-1}+(\sigma_{i-1}+\mu_{i-1}\Delta t)\cos\phi - j(\sigma_{i-1}+\mu_{i-1}\Delta t)\sin\phi \tag{A6}$$

The Von Neumann stability requires that $|G_k|\leq 1$. Thus

$$\sqrt{(1-\sigma_{i-1})^2+2(1-\sigma_{i-1})(\sigma_{i-1}+\mu_{i-1}\Delta t)\cos\phi+(\sigma_{i-1}+\mu_{i-1}\Delta t)^2} \leq 1 \tag{A7}$$

Neglecting the Δt^2 term, inequality (A7) is expanded as

$$(1-2\sigma_{i-1}+2\sigma_{i-1}^2)+2(1-\sigma_{i-1})(\sigma_{i-1}+\mu_{i-1}\Delta t)\cos\phi + 2\sigma_{i-1}\mu_{i-1}\Delta t \leq 1 \tag{A8}$$

The left hand side of inequality (A8) is smallest when $\phi=0$. Therefore

$$\sigma_{i-1}(\sigma_{i-1}-1+\mu_{i-1}\Delta t) \leq 0 \tag{A9}$$

This yields the CFL condition

$$0 \leq \sigma_{i-1} \leq 1-\mu_{i-1}\Delta t \tag{A10}$$

The time step requirement can be found as

$$\Delta t \leq \frac{\Delta x}{\max_i(u_{i-1}+c_{i-1}+\mu_{i-1}\Delta x)} \tag{A11}$$

References

[1] Rothfarb, B., Frank, H., Rosenbaum, D. M., Steiglitz, K., and Kleitman, D. J., 1970, "Optimal Design of Offshore Natural-Gas Pipeline Systems," J. Oper. Res. Soc. Am., **18**(6), pp. 992–1020.
[2] Bayen, A. M., Raffard, R., and Tomlin, C. J., 2004, "Adjoint-Based Constrained Control of Eulerian Transportation Networks: Application to Air Traffic Control," Proceeding of the American Control Conference, Boston, MA, pp. 5539–5545.
[3] Lee, H. Y., Lee, H.-W., and Kim, D., 1999, "Dynamic States of a Continuum Traffic Equation With On-Ramp," Phys. Rev. E, **59**(5), pp. 5101–5111.
[4] Debnath, L., 1997, *Nonlinear Partial Differential Equations for Scientists and Engineers*, Birkhauser, Boston, MA.
[5] Nguyen, N., 2006, "Model Predictive Optimal Control of a Time-Delay Distributed-Parameter System," AIAA Guidance, Navigation, and Control Conference, Keystone, CO, Paper No. AIAA-2006–6194.
[6] Wolf, T., 1998, "State of the Art in Circuit Loss Analysis of Transonic Wind Tunnels," AIAA 20th Advanced Measurement and Ground Testing Technology Conference, Albuquerque, NM, Paper No. AIAA-1998–2779.
[7] Saunder, G. H., 1991, "UPWT Modernization Final Design Test Section Model Revision for the 11-ft Tunnel Simulation," Sverdrup Technology, Contract No. NAS2-13032.
[8] Soeterboek, R. A. M., Pels, A. F., Verbruggen, H. B., and van Langen, G. C. A., 1991, "A Predictive Controller for Mach Number in a Wind Tunnel," IEEE Control Systems, **11**(1), pp. 63–72.
[9] Motter, M. A., and Principe, J. C., 1995, "Classification and Prediction of Wind Tunnel Mach Number Responses Using Both Competitive and Gamma Neural Networks," Proceedings of the World Congress of Neural Networks, Washington, DC, Vol. 2, pp. 25–29.
[10] Ben-Artzi, M., and Falcovitz, J., 2003, *Generalized Riemann Problem in Computational Fluid Dynamics*, Cambridge University Press, Cambridge, UK.
[11] Hirsch, C., 1991, *Numerical Computation of Internal and External Flows*, Vol. 1, Wiley, Brussels.
[12] Laney, C. B., 1998, *Computational Gas Dynamics*, Cambridge University Press, New York.
[13] Wendt, J. F., 1996, *Computational Fluid Dynamics—An Introduction*, Springer-Verlag, Berlin.
[14] Shapiro, A. H., 1954, *The Dynamics and Thermodynamics of Compressible Fluid Flow*, Vol. II, Ronald, New York.
[15] Wylie, E. B., and Streeter, V. L., 1978, *Fluid Transients*, McGraw-Hill, New York.
[16] Khalil, H. K., 1996, *Nonlinear Systems*, Prentice-Hall, Englewood Cliffs, NJ.
[17] Slotine, J.-J. E., and Li, W., 1991, *Applied Nonlinear Control*, Prentice-Hall, Englewood Cliffs, NJ.
[18] Eves, H., 1980, *Elementary Matrix Theory*, Dover, New York.
[19] Dixon, S. L., 1989, *Thermodynamics of Turbomachinery*, Pergamon, New York.

Numerical Study of Capillary Flow in Microchannels With Alternate Hydrophilic-Hydrophobic Bottom Wall

Auro Ashish Saha
Department of Mechanical Engineering,
Indian Institute of Technology, Bombay,
Mumbai 400076, India
e-mail: asaha@iitb.ac.in

Sushanta K. Mitra[1]
Department of Mechanical Engineering,
University of Alberta,
Edmonton, AB T6G2G8, Canada
e-mail: sushanta.mitra@ualberta.ca

A two-dimensional numerical simulation of flow in patterned microchannel with alternate layers of different sizes of hydrophilic and hydrophobic surfaces at the bottom wall is conducted here. The effect of specified contact angle and working fluid (de-ionized (DI) water and ethanol) on capillary phenomena is observed here. The volume of fluid method is used for simulating the free surface flow in the microchannel. Meniscus profiles with varying amplitude and shapes are obtained under the different specified surface conditions. Nonsymmetric meniscus profiles are obtained by changing the contact angles of the hydrophilic and hydrophobic surfaces. A meniscus stretching parameter is defined here and its relation to the capillary phenomena in the microchannel is discussed. Flow variation increases as the fluid traverses alternately between the hydrophilic and hydrophobic regions. The pattern size and the surface tension of the fluid are found to have significant influence on the capillary phenomena in the patterned microchannel. Smaller pattern size produces enhanced capillary effect with DI water, whereas no appreciable gain is observed for ethanol. The magnitude of maximum velocity along the channel height varies considerably with the pattern size and the contact angle. Also, the rms velocity is found to be higher for smaller alternate patterned microchannel. The meniscus average velocity difference at the top and bottom walls increases for a dimensionless pattern size of 0.6 and thereafter it decreases with the increase in pattern size in the case of DI water with hydrophilic-hydrophobic pattern. Using such patterned microchannel, it is possible to manipulate and optimize fluid flow in microfluidic devices, which require enhanced mixing for performing biological reactions. [DOI: 10.1115/1.3129130]

Keywords: contact angle, capillary flow, microchannel, numerical, two-dimensional

1 Introduction

Manipulating gas and liquid flows within networks of microchannels is crucial in the design and fabrication of microfluidic devices. As the surface area to volume ratio increases, fluid/surface interactions become more significant with smaller fluidic channels [1]. Flow control is essential in many of the microfluidic systems targeted for use in biochemistry analysis, drug delivery, and sequencing or synthesis of nucleic acids, among others. Such systems use microchannels to promote efficient mixing without the use of any external means. These devices typically rely upon the balance of surface tension and fluid pressure forces to perform their function. When capillary action is used for microfluidics, the wetting property of microchannels has a significant effect on the liquid behavior. It is a well known fact that a hydrophilic surface assists fluid motion, whereas a hydrophobic surface retards fluid motion inside microchannels. It is thus possible to achieve flow control of liquid inside microchannels having differential wettability characteristics. Research on patterned surfaces reveal interesting phenomena that can be exploited to control liquid motions in microfluidic devices. Hydrophobic and hydrophilic regions inside microchannels can be patterned through surface modification. However, fabrication of such patterned surfaces with selective surface characteristics is highly challenging task [2].

There have been a few studies reported for flow in patterned microchannels. Zhao et al. [3] used surface directed liquid flow to create pressure sensitive switches inside channel networks. Self-assembled monolayer chemistry is used in combination with multistream laminar flow and photolithography to pattern surface inside the microchannel networks. Kim et al. [4] carried out experimental and numerical investigation for microchannel transient filling process with surface tension. A linear relationship between the dimensionless pressure and capillary number is observed. Their experimental observations indicate that flow blockage in the narrowest width channel is enabled by the surface tension and not by viscous effect. Yang et al. [5] discussed the method to characterize the surface energy inside a microchannel by monitoring the marching velocity of capillary meniscus. They formulated one-dimensional mathematical model and performed experimental validation of liquid filling in a capillary. Parylene and silicon nitride microchannels, which are fabricated using surface micromachining technology, are used for experimentation. Their study indicates the influence of surface tension driven flow for fluid delivery in microfluidic systems.

Salamon et al. [6] used finite element based numerical method to study a three-dimensional flow of Newtonian fluid in a microchannel of height 80 μm with superhydrophobic lower and upper walls. They have shown a 40% flow enhancement over the smooth nonpatterned surface and an apparent slip length of 5.4 μm. Byun et al. [7] performed numerical visualization to investigate the effect of surface wettability in microchannel on the flow characteristics. The importance of hydrophobic and hydrophilic characteristics on a surface for the handling and control of liquid in the microsystems are emphasized. The study shows the occurrence of flow instability in the flow path when the meniscus crosses hydrophilic/hydrophobic interface. Dalton et al. [8] discussed is-

[1]Corresponding author.

Contributed by the Fluids Engineering Division of ASME for publication in the JOURNAL OF FLUIDS ENGINEERING. Manuscript received June 10, 2008; final manuscript received April 1, 2009; published online May 13, 2009. Assoc. Editor: Rajat Mittal.

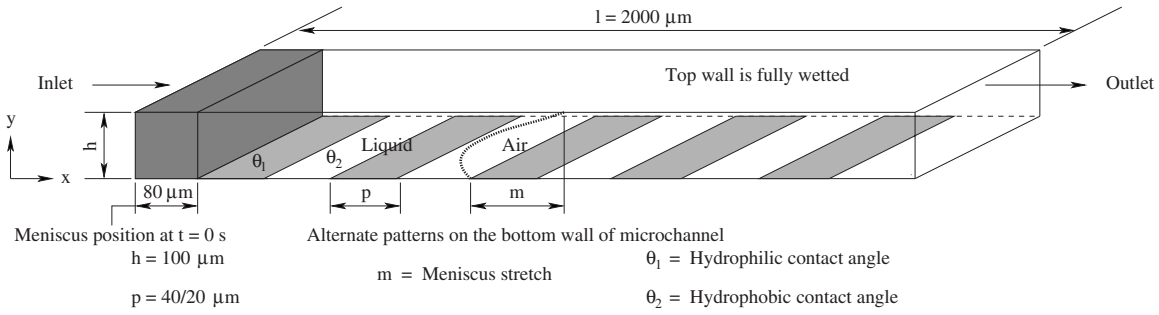

Fig. 1 Geometry of microchannel

sues in implementing superhydrophobic surfaces by nanostructured posts in a microchannel. The understanding and elimination of contact line movement effects on drag reduction are illustrated. Yang and Przekwas [9] developed the computational methodology to model surface tension effects of multifluid flow in ACE+MEMS CAD software. They present systematic validations against analytical solution for typical flows in microelectromechanical system (MEMS) devices. The unsteady motion of the free surface governed by the Hamilton–Jacobi evolution equation is solved on Eulerian grid using the volume of fluid (VOF) technique. Hirt and Nichols [10] described the concept of VOF method for treating complicated free boundary configurations. For simulation related to free surface flows, the water/air interface is characterized by surface tension and sharp changes in viscosity and density [11]. Among several general multiphase models currently in use, the VOF model has the ability to handle flows that undergo arbitrary topologic transformations [9]. Saha et al. [12] have used VOF method to study the capillary flow through microchannels with integrated pillars, which involved a complex flow geometry.

Huang et al. [13] studied theoretically and numerically the capillary filling flows inside patterned-surface microchannels: two different patterned microchannel configurations—inner walls patterned with unequal contact angles; each inner wall divided into two equal segments having different contact angles has been considered for carrying out two-dimensional and three-dimensional simulations. An equivalent contact angle model based on the surface energy method has been proposed for estimating capillary flows inside the patterned-surface microchannels and they validated the model with traditional capillary rise theories.

Recently, a new method has been developed to modify the hydrophobic and hydrophilic nature of silicon surfaces by the use of 5-(4-hydroxyphenyl)-10, 15, 20-tetra(*p*-tolyl) porphyrin self-assembled monolayer (SAM) [14]. The bare SiO_2 substrate exhibited a contact angle of 33 deg $\pm$ 2 deg showing hydrophilic nature of the surface. In the case of hydroxy-phenyl porphyrin SAM, the contact angle is found to increase up to 75 deg $\pm$ 3 deg, indicating a hydrophobic nature of the surface due to the formation of SAM on the SiO_2 surface. Until now, the studies have considered patterned surfaces that are uniform about the channel axis. In this present study, we deviate from the above restriction and study the surface dominated flow behavior in a channel with nonuniform distribution of surface characteristics with respect to channel axis. A two-dimensional numerical simulation of flow in patterned microchannels with alternate hydrophilic and hydrophobic surfaces at the bottom wall is presented. The hydrophilic surface induces the acute static contact angle, while the hydrophobic surface results in the obtuse static contact angle. The capillary driven flow phenomena in the microchannel is considered in this study. Capillary driven flows are purely governed by the forces associated with surface tension [15] and offer positive flow enhancement effect. To the best of the authors' knowledge, numerical investigation of alternate patterned microchannel with hydrophilic-hydrophobic bottom wall has not been reported so far, which accounts for the different working fluids, pattern size, and variation in the surface wettability of the patterns. The results obtained from simulations also provide the required motivation for fabricating such patterned microfluidic device.

2 Physical Problem

The geometry of the microchannel model is shown in Fig. 1. The channel considered here is a two-dimensional channel with the channel dimension perpendicular to the plane of the figure much larger than the channel height in *y*-coordinate direction. The height h of the channel is 100 μm. The model consists of a single straight segment of 2000 μm in length. The alternate patterns of hydrophilic and hydrophobic surface arrangement are shown at the bottom wall of the channel geometry, to account for the surface tension and wall adhesion effects on the flow. Two types of microchannel geometry with 40 μm and 20 μm pattern sizes (p), respectively, are considered here.

2.1 Governing Equations. Equations for numerical (VOF model) and analytical (Lucas–Washburn and reduced order model) solutions for the propagation of a liquid in a channel is presented in Secs. 2.1.1–2.1.3.

2.1.1 VOF Model. The simulations of the capillary flows in the patterned-surface microchannels are performed using a VOF method. In this method, a volume fraction transport equation is employed in addition to the continuity and momentum equations. Two phases (gas-liquid) are treated as a homogeneous gas-liquid mixture. The flow is considered to be laminar, nongravity, incompressible, Newtonian, and isothermal with velocity field $\mathbf{V}$ and governed by the Navier–Stokes and continuity equations, as provided here:

$$\nabla \cdot \mathbf{V} = 0 \tag{1}$$

$$\frac{\partial \rho \mathbf{V}}{\partial t} + \nabla \cdot (\rho \mathbf{V}\mathbf{V}) = -\nabla P + \nabla \cdot (\mu(\nabla \mathbf{V} + \nabla^T \mathbf{V})) + \mathbf{F}_s \tag{2}$$

where $\mathbf{V}$ is the velocity of the mixture, P is the pressure, t is the time, $\mathbf{F}_s$ is the volumetric force at the interface resulting from surface tension, and ρ and μ are the density and viscosity, respectively. In this equation, the accumulation and convective momentum terms in every control volume (cell) balance the pressure force, shear force, and additional surface tension force $\mathbf{F}_s$. Surface tension arises as a result of attractive forces between molecules in a fluid and it is represented as force acting only at the surface, which is required to maintain equilibrium in such instances.

The numerical simulation of free surface flows composed of two immiscible fluids involves two coupled tasks, namely, resolving the flow field and updating the position of the interface. This involves the application of SIMPLE algorithm [16] and extending it to include the VOF methodology [10,11]. The VOF method allows for the simulation of a mixture of two incompressible and immiscible fluids including surface tension effects. The VOF model includes the effects of surface tension along the interface between each pair of phases. The model can be augmented by the

additional specification of the contact angles between the phases and the walls. The fluids under consideration are DI water and ethanol as liquids and air as gas. The tracking of the interfaces between the phases is accomplished by the solution of a continuity equation for the volume fraction of any of the phases. The fields for all variables and properties are shared by the phases and represent volume-averaged values, as long as the volume fraction of each of the phases is known at each location. Thus the variables and properties in any given cell either represent one or a mixture of the phases, depending on the volume fraction values. The distribution of the liquid phase is described by using a single scalar field variable, F, which defines the fraction of the liquid volume. Here, $F=1$ represents liquid, $F=0$ represents gas, and $0<F<1$ represents the liquid/gas interface. The volume fraction distribution can be determined by solving the passive transport equation, given as

$$\frac{\partial F}{\partial t} + \mathbf{V} \cdot \nabla F = 0 \tag{3}$$

where

$$F = \frac{\text{cell volume occupied by liquid}}{\text{total volume of the control cell}} \tag{4}$$

The mixture's physical properties are derived from that of the two phases through the volume fraction function. In particular, the average value of ρ and μ in a computational cell can be computed from the value of F in accordance with

$$\rho = F\rho_2 + (1-F)\rho_1 \tag{5}$$

$$\mu = F\mu_2 + (1-F)\mu_1 \tag{6}$$

where the subscripts 1 and 2 represent the gas phase and the liquid phase, respectively.

The surface tension model follows the continuum surface force (CSF) model proposed by Brackbill et al. [17]. The surface tension is specified as a source term $\mathbf{F}_s$ in Eq. (2) according to the CSF model:

$$\mathbf{F}_s = \sigma\kappa\nabla F \tag{7}$$

The surface tension is taken to be constant along the surface and only the forces normal to the interface are considered. According to the CSF model, the surface curvature κ is computed from local gradients in the surface normal to the interface, which is given as

$$\kappa = \frac{1}{|\mathbf{n}|}\left(\left(\frac{\mathbf{n}}{|\mathbf{n}|}\cdot\nabla\right)|\mathbf{n}| - \nabla\cdot\mathbf{n}\right) \tag{8}$$

where $\mathbf{n}=\nabla F$ is the normal vector. Wall adhesion is included in the model through the contact angle:

$$\hat{\mathbf{n}} = \hat{\mathbf{n}}_w \cos\theta + \hat{\mathbf{t}}_w \sin\theta \tag{9}$$

where $\hat{\mathbf{n}}$ is the unit vector normal to the surface, $\hat{\mathbf{n}}=\mathbf{n}/|\mathbf{n}|$, and $\hat{\mathbf{n}}_w$ and $\hat{\mathbf{t}}_w$ represent the unit vector normal and tangent to the wall, respectively. It may be noted that the code calculates only the macroscopic effects of surface tension and just tracks the interface progression under this force; it does not impose the specified contact angle to the interface at the wall. The interface needs to be constructed based on the computed value of the volume fraction with the application of interpolation schemes for the identification of the interface. An upwind scheme with the piecewise linear interface construction (PLIC) method is adopted for surface reconstruction [11]. In the PLIC scheme, the liquid-gas interface is assumed to be linear and can take any orientation within the cell. The reconstructed interface is represented by line segments in a two-dimensional flow. The reconstruction is required at every time step to include the necessary backcoupling of surface forces to the momentum equations, as well as flux calculations. Equations (1)–(9) are solved iteratively to obtain the liquid volume fraction and the velocity field solution under appropriate initial and boundary conditions. No slip boundary conditions at the walls are imposed. However, this will not restrict the contact line at wall from moving, as the code integrates over the whole cell adjacent to the wall to compute the mass flux of the second phase, which, when using finite grid size, will average out to give an apparent finite interface velocity at the wall [18]. As an initial condition, a distribution of F in the microchannel needs to be specified.

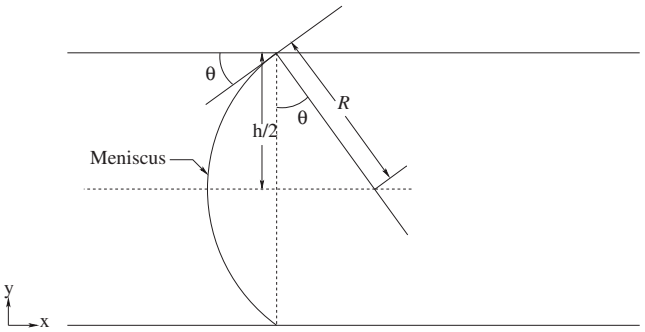

Fig. 2 Meniscus in channel in front view

2.1.2 Lucas–Washburn Model. For a fully developed capillary driven flow, the balance of viscous force, surface tension force, and gravitational force yields the classical Lucas–Washburn equation, which relates the distance traveled by the liquid meniscus L with time t [19]. The analytical solution is based on the Navier–Stokes equation for incompressible, quasi-steady, laminar, nongravity, Newtonian unidirectional horizontal flow for a two-dimensional channel:

$$-\frac{\partial P}{\partial x} = -\mu\frac{\partial^2 u}{\partial y^2} \tag{10}$$

where P is the pressure in the fluid at x, μ is the viscosity of the fluid, and u is the velocity of the fluid.

For static wetting of a liquid between two surfaces, the minimization of surface area of a liquid may result in a curved interface. The general Young–Laplace equation describes the relation for the pressure difference across the interface as

$$\Delta P = \sigma\left(\frac{1}{R_1} + \frac{1}{R_2}\right) \tag{11}$$

where ΔP is the pressure difference, σ is the liquid surface tension, and R_1 and R_2 are the radii of curvature of the interface in directions perpendicular and parallel to the liquid stream. For a two-dimensional channel $R_2=\infty$.

Therefore Eq. (11) reduces to

$$\Delta P = \sigma\frac{1}{R} \tag{12}$$

Figure 2 shows the meniscus profile in a two-dimensional channel. Here, from Fig. 2,

$$R = \frac{h}{2\cos\theta} \tag{13}$$

For steady two-dimensional Poiseuille flow, the average fluid velocity within the microchannel can be written as

$$u_{\text{avg}} = \frac{1}{12\mu}\frac{\Delta P}{L}h^2 \tag{14}$$

which can be related to the distance traveled by the liquid meniscus as

$$u_{\text{avg}} = \frac{dL}{dt} \tag{15}$$

Table 1 Boundary conditions for Cases 1 and 2

Case	Surface type	Boundary conditions on bottom wall
Case 1	Alternate hydrophilic-hydrophobic	Contact angles $\theta_1=30$ deg and $\theta_2=120$ deg
Case 2	Alternate hydrophilic-neutral	Contact angles $\theta_1=0$ deg and $\theta_2=90$ deg

Hence, the distance traveled by the liquid meniscus can be written as

$$L=\left(\frac{ht\sigma\cos\theta}{3\mu}\right)^{1/2} \tag{16}$$

Equation (16) shows that the flow time is inversely proportional to the surface tension, channel height, and the cosine of the wetting angle (θ), and directly proportional to the viscosity and the square of the flow distance.

2.1.3 Reduced Order Model. With quasisteady state assumption in the Lucas–Washburn model, the term denoting the momentum change in Navier–Stokes equation is often omitted [20]. For a microscale flow, the Reynolds number is usually very small and the surface tension force is always dominant. The quasisteady state assumption is valid except for the initial starting stage that is highly transient. In the reduced-order model, a transient solution is derived accounting for the momentum change, which is obtained by averaging the Navier–Stokes equations across the liquid length in the microchannel.

The momentum conservation may be expressed as the momentum change is balanced by the sum of the surface tension force, pressure overhead, and wall viscous force. At time t, L is the distance traveled by the liquid meniscus, u_{avg} is the average fluid velocity, and the momentum balance can be written as

$$\frac{d}{dt}(\rho hLu_{\text{avg}})=2\sigma\cos\theta+\Delta Ph-\frac{12\mu L}{h}u_{\text{avg}} \tag{17}$$

For a passive capillary filling process, $\Delta P=0$. Noting $u_{\text{avg}}=dL/dt$, the equation above can be rewritten as

$$\frac{d^2}{dt^2}L^2+B\frac{d}{dt}L^2=A \tag{18}$$

where

$$A=\frac{4\sigma\cos\theta+2\Delta Ph}{\rho h},\quad B=\frac{12\mu}{\rho h^2} \tag{19}$$

Considering initially the liquid meniscus position in the channel as L_0 and with zero velocity, the transient solution of the capillary filling problem is given as

$$L=\left(\frac{A}{B^2}\exp(-Bt)+\frac{At}{B}+\left(L_0^2-\frac{A}{B^2}\right)\right)^{1/2} \tag{20}$$

$$u_{\text{avg}}=\frac{A(1-\exp(-Bt))}{2BL} \tag{21}$$

where t is the time of the filling process, L is the distance traveled by the liquid meniscus, and u_{avg} is the average filling speed.

For the channel height of 100 μm selected in this study, the Bond number (Bo), $\rho gH^2/\sigma$, and Capillary number (Ca), $\mu U/\sigma$, are much less than unity. The contact angle dependence on the speed of the contact line will be less pronounced here [21]. Hence, the effects of gravity and dynamic contact angle are not taken into account in the present study. The research on the dynamics of capillary phenomena and their applications has been reviewed in Refs. [21–24].

2.2 Initial and Boundary Conditions. Initially, at time $t=0$, the liquid meniscus position in the channel is set as 80 μm, which is assumed to be flat. No slip boundary condition is imposed on all the walls and the boundary conditions for the surface affinity is described by the contact angle. The contact angle specified on the bottom walls of the channel is shown in Fig. 1 and summarized in Table 1 for easy reference. The top wall is considered to be fully wetted with a contact angle of 0 deg. At the bottom wall, the initial meniscus position kept at 80 μm from the inlet is also considered as fully wet. Passive capillary filling process is considered for all the cases by specifying a constant pressure (atmospheric) at channel inlet and outlet. Liquid volume fraction values of unity and zero is specified at channel inlet and outlet, respectively, for all the cases.

3 Numerical Technique

The channel geometry is created and meshed using preprocessor CFD-GEOM modeler [25]. Structured grid having 2000(10 $\times$200) square cells is used for simulations. The choice of such grid size is discussed in details in Sec. 4. CFD software CFD-ACE + based on finite volume method is used for the time dependent simulations. Flow and free surface (VOF) modules of CFD-ACE+ are used for analysis. Second-order PLIC surface reconstruction method with surface tension effect is specified for VOF with explicit time integration scheme. Explicit option is selected as it exhibits greater stability and better convergence but slightly lower accuracy as compared with the implicit scheme. However, for an accurate resolution of the interface and prediction of the interface shape and its location, this is the preferred option. Euler (first-order) scheme is applied for time accuracy. A target Courant–Friedrich–Lewy (CFL=$|v|\delta t/h$) number of 0.1 is applied for numerical stability of the simulation. This would allow the interface to cross 10% of the width of a grid cell during each time step in a VOF computation. Upwind scheme is used for spatial differencing. Semi-implicit method for pressure-linked equation consistent (SIMPLEC) algorithm is adopted for pressure-velocity coupling and pressure correction. The conjugate gradient squared plus preconditioning (CGS+Pre) solver [25] is used for velocity, while the algebraic multigrid (AMG) solver is used for pressure correction. An initial time step of 1.0×10^{-7} s is selected and the VOF module is allowed to automatically adjust the time-step size based on the CFL number and interface velocity. An automatic time-step option automatically ensures stability in the CFD-ACE+ solver. Each case is given 100 iterations per time step with a convergence criteria of 0.0001 to control the iterative solution process. The solver quits the iterative procedure when the maximum relative difference between the computed values of variables in two successive iterations is smaller than the specified convergence criteria. The physical properties of DI water and ethanol used for simulations are provided in Table 2.

Table 2 Fluid properties used in simulation

Physical property	DI water	Ethanol	Air
Density (kg/m^3)	1000	791	1.1614
Viscosity (Pa s)	1.0×10^{-3}	1.2×10^{-3}	1.846×10^{-5}
Surface tension (N/m)	72.5×10^{-3}	21.38×10^{-3}	-

4 Results and Discussion

4.1 Validation of Model. Validation of the numerical results with analytical solution has been carried out for nonpatterned microchannel 100 μm height and 2000 μm length with contact angle $\theta=45$ deg for DI water. The time evolution of meniscus displacement is considered as the parameter for validating the numerical results. Figure 3(*a*) shows the comparison of meniscus displacement obtained numerically with the analytical solution based on a reduced-order model [20]. Good agreement between numerical and analytical results is observed. It is to be noted that, in general, the meniscus displacement in a capillary follows the Lucas–Washburn equation, which predicts that the distance traveled by the meniscus is proportional to $\sqrt{t}$. The Lucas–Washburn equation is an asymptotic model for large times and is derived based on the balance of capillary and friction forces when the influence of other forces during the initial transients becomes insignificant [26]. This quasisteady state assumption is valid except for the initial starting stage, which is highly transient. The validation studies reported in literature [5,9,13] are observed for very large time scale ($t\sim$ s). However, the time scale considered for the present study is in the range of milliseconds ($t\sim$ ms) for all the cases. Therefore, the plots in Fig. 3(*a*) do not necessarily obey the Lucas–Washburn equation, but a reduced-order model [20], which accounts for the inertia, is found to be a better choice for the representation of the meniscus displacement under the given conditions. Hence, deviation between the predicted numerical results and the Lucas–Washburn model can be justified. To demonstrate this, the numerical results are also validated with experimental data [27]. The geometry considered is a two-dimensional microchannel 1 mm height and 100 mm length with contact angle $\theta=0$ deg. The liquid used in the experimental data is FC-77 with the following physical properties: the density $\rho=1789$ kg/m^3, the viscosity $\mu=0.01548$ Pa s, and the surface tension $\sigma=0.015$ N/m. Figure 3(*b*) shows the comparison of meniscus displacement obtained numerically with the experimental data. The numerical results again show good agreement with the experimental data. As the experimental data are available for a long time, we also observe that the meniscus displacement follows the Lucas–Washburn equation and is proportional to $\sqrt{t}$ within the experimental time domain.

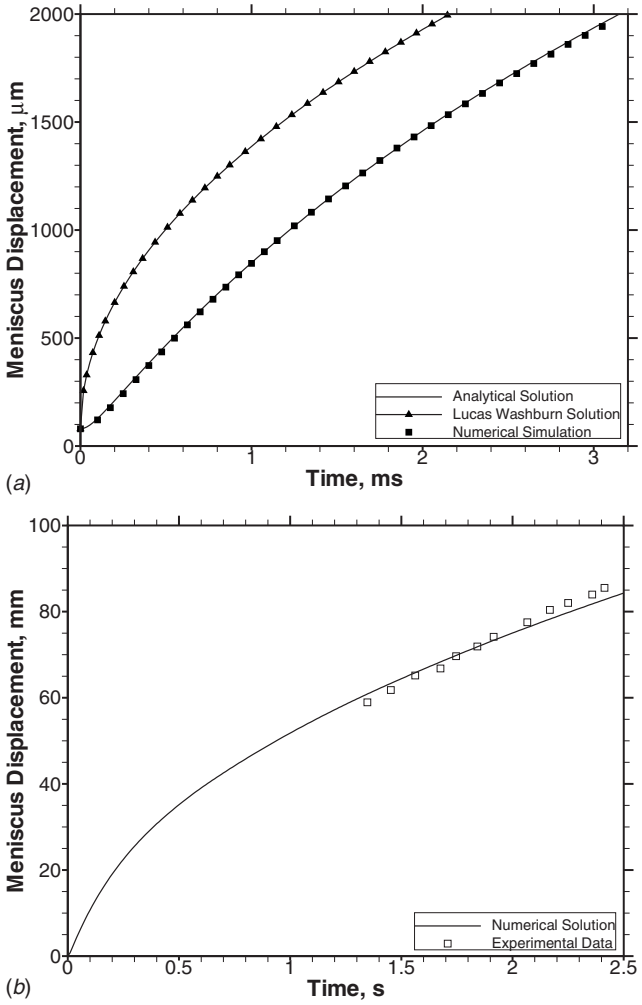

Fig. 3 Validation of numerical model with analytical solution [20] and experimental data [27]: (*a*) Verification with analytical solution and (*b*) verification with experimental data

4.2 Snapshot of Meniscus Front. Figure 4 shows the snapshot images of the meniscus front in the microchannel for Case 1 with alternate hydrophilic-hydrophobic bottom wall when the microchannel is 25%, 50%, 75%, and 90% filled. The vertical line indicates an initial liquid meniscus position at 80 μm from the channel inlet. The isocontour of $F=0.5$ is applied to identify the interfacial position for the visualization. A nonsymmetric meniscus shape is observed during the capillary flow due to the alternate contact angle ($\theta_1=30$ deg, $\theta_2=120$ deg) specified on the bottom wall. Appreciable differences in the front shapes are observed between 40 μm and 20 μm pattern geometries for both DI water and ethanol. The meniscus shapes for Case 2 with alternate hydrophilic-neutral bottom wall, as shown in Fig. 5, is also found to be nonsymmetric about the channel axis. The meniscus curvature for Case 1 is observed to be larger compared with Case 2. This is due to pronounced retarding flow effect on the bottom wall and stretching of the meniscus on the top wall. Hence Figs. 4 and 5 show that the meniscus profiles vary in amplitude and shape when alternate patterns are produced in the microchannel.

4.3 Meniscus Stretch. The nonuniform distribution of surface characteristics with respect to channel axis results in the stretching of the meniscus in the microchannel. A meniscus stretch parameter is defined for this purpose, as illustrated in Fig. 1. The meniscus stretch is defined as the difference of the x-coordinate of the meniscus front on the top and bottom walls. Figure 6 shows the variation of meniscus stretch with liquid volume fraction for Cases 1 and 2.

The meniscus stretch is observed to fluctuate with liquid volume fraction for Cases 1 and 2. The meniscus stretch for Case 1 is large compared with Case 2 for both DI water and ethanol. The pattern size and the specified surface condition are seen to have significant effect on the amplitude and frequency of fluctuation of meniscus stretch parameter. To this respect, the meniscus stretch is also plotted for nonpatterned surfaces in Fig. 7, which shows that a highly hydrophobic bottom wall ($\theta=120$ deg) causes a large meniscus stretch and a constant meniscus stretch of zero is found for fully wet walls. Therefore, it can be concluded that compared with the alternate pattern considered for Case 2 the alternate pattern for Case 1 offers higher hydrophobicity on the bottom wall. Compared with 20 μm patterned walls for both DI water and ethanol, the amplitude for Cases 1 and 2 is observed to be slightly higher for 40 μm patterned walls. The frequency of fluctuation is proportional to the number of patterns on the bottom wall. This also has its corresponding effect on the amplitude as the large number of patterns of smaller size tends to make the bottom wall less hydrophobic. This is reflected very clearly for 20 μm patterned wall, which has double the number of patterns than 40 μm patterned wall. Such effect is more pronounced with DI water than compared with ethanol.

4.4 Meniscus Displacement. The position of capillary meniscus for Cases 1 and 2 is shown in Fig. 8. As the meniscus shape is spatially distributed with respect to the x- and y-coordinate direc-

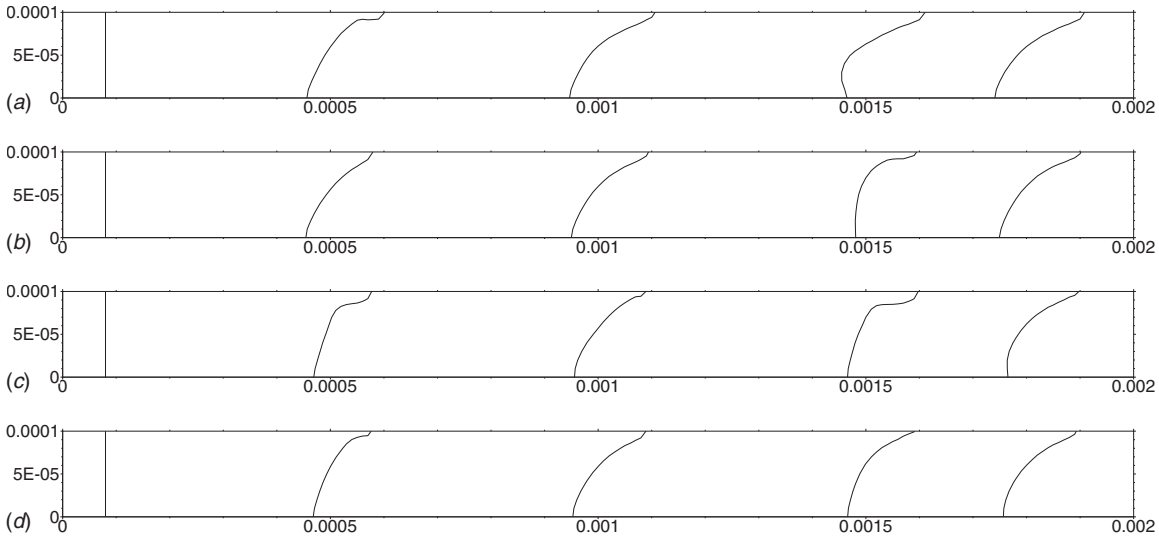

Fig. 4 The snapshot image of the evolution of meniscus front for Case 1 ($\theta_1=30$ deg, $\theta_2=120$ deg) when the microchannel is 25%, 50%, 75%, and 90% filled (isocontour of $F=0.5$ is applied to identify the meniscus): (*a*) DI water with40 μm alternate pattern; (*b*) ethanol with 40 μm alternate pattern; (*c*) DI water with 20 μm alternate pattern; and (*d*) ethanol with 20 μm alternate pattern

tions and varies considerably for all the cases, the capillary meniscus position has been normalized with respect to the x-coordinate distance [13]. The normalized capillary meniscus position is obtained by dividing the volume of the fluid in the capillary with the height of the microchannel. It is observed that the capillary driven flow produces a nonlinear displacement of the meniscus. It is found that the meniscus displacement for alternate hydrophilic-hydrophobic condition (Case 1) is lower than the hydrophilic-neutral condition (Case 2) for both DI water and ethanol, whereas the displacement magnitude is lower for ethanol. It is to be noted that the detail displacement within the initial milliseconds is shown in the inset plot, which suggests that under different surface conditions, the transient response of the meniscus displacement varies significantly. Even such response propagates at a later time instant, as shown in Table 3.

The influence of contact angle on the meniscus displacement can be observed in Fig. 9, which is obtained for nonpatterned surfaces. However, as shown in Fig. 8, the meniscus displacement for the alternate patterned microchannel (Case 1) is somewhat average of the corresponding nonpatterned surfaces with contact angles 30 deg and 120 deg, respectively, as shown in Fig. 9. The meniscus displacement may be manipulated suitably by appropriate choice of pattern size and surface contact angle, as shown in Fig. 8. In Fig. 8(*a*), it is observed that with DI water, for Cases 1 and 2, the microchannel with 20 μm patterned wall has large meniscus displacement compared with the 40 μm patterned wall. However, ethanol, having higher viscosity and lower surface tension compared with DI water, do not show pronounced difference in its meniscus displacement for patterned walls (Fig. 8(*b*)) for Cases 1 and 2.

4.5 Meniscus Instantaneous Velocity Distribution. Figure 10 shows the displacement of the capillary meniscus with time on the bottom wall with DI water (contact angles $\theta_1=30$ deg and

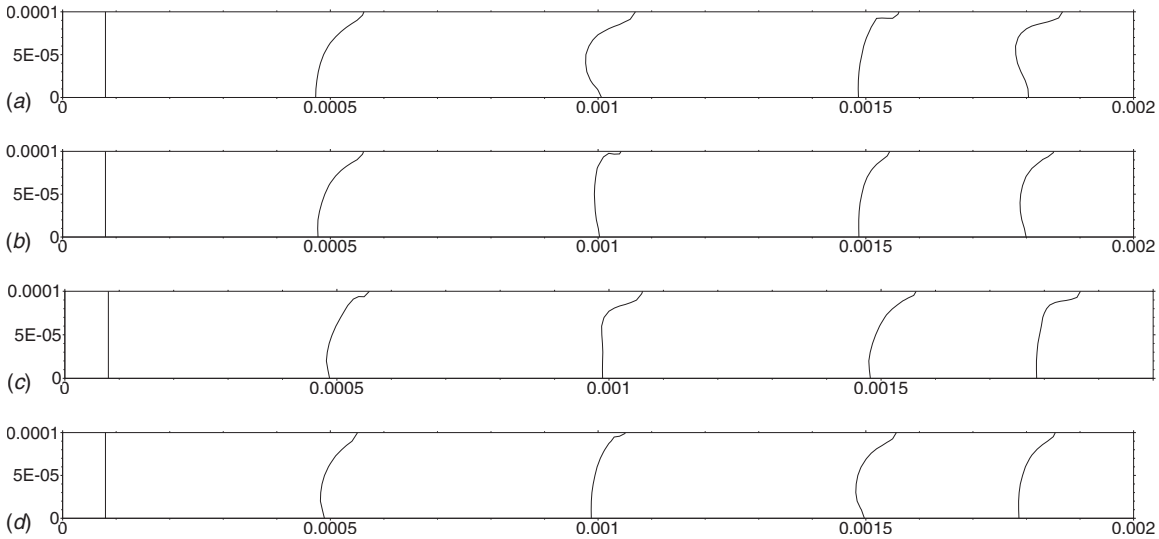

Fig. 5 The snapshot image of the evolution of meniscus front for Case 2 ($\theta_1=0$ deg, $\theta_2=90$ deg) when the microchannel is 25%, 50%, 75%, and 90% filled (isocontour of $F=0.5$ is applied to identify the meniscus): (*a*) DI water with 40 μm alternate pattern; (*b*) ethanol with 40 μm alternate pattern; (*c*) DI water with 20 μm alternate pattern; and (*d*) ethanol with 20 μm alternate pattern

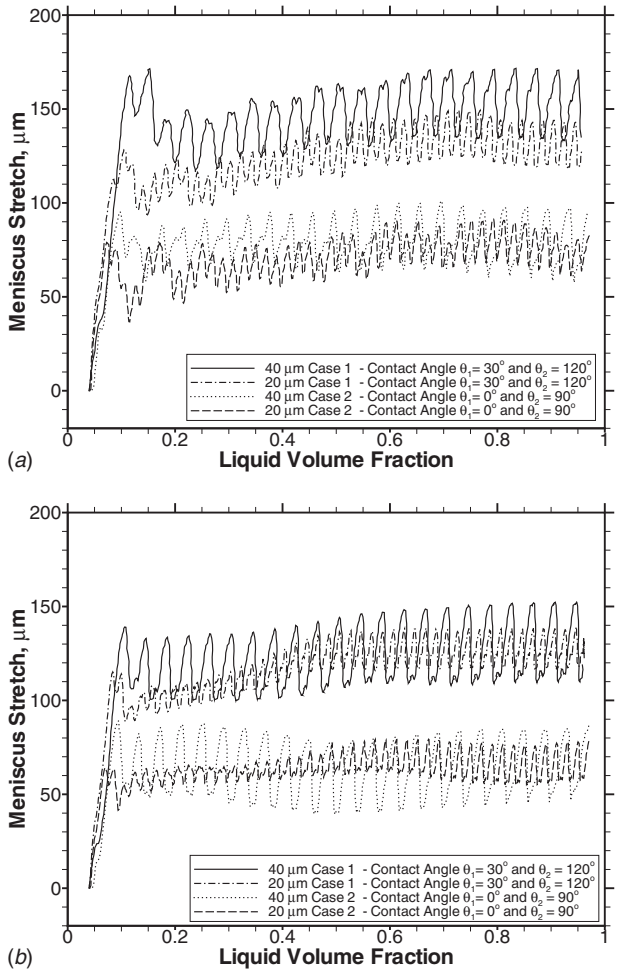

Fig. 6 The variation of meniscus stretch with liquid volume fraction for Cases 1 and 2 for two different working fluids: (*a*) DI water and (*b*) ethanol

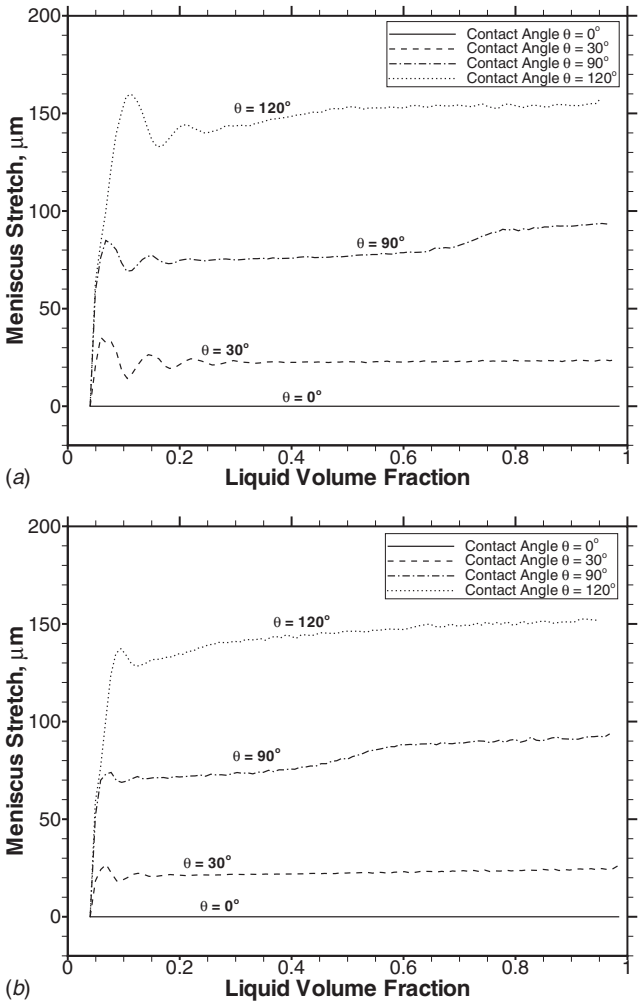

Fig. 7 The variation of meniscus stretch with liquid volume fraction for a nonpatterned microchannel for two different working fluids: (*a*) DI water and (*b*) ethanol

$\theta_2 = 120$ deg) for 20 μm and 40 μm patterned microchannels. The velocity of the advancing meniscus is also plotted in Fig. 10. The velocity of the advancing liquid front at x-position is obtained by the derivative of the liquid front position with time at time$=t$. The hydrophilic and hydrophobic regions have been marked in the plot. It is observed that the velocity of the meniscus increases/decreases when the flow reaches the hydrophilic/hydrophobic interface region on the bottom wall.

Figure 11 shows the instantaneous velocity distribution along the channel height for Cases 1 and 2 when the microchannel is 50% filled. The meniscus velocity magnitudes are observed to be higher for DI water compared with ethanol for all the cases including the 40 μm and 20 μm patterned walls. As the fluid at the bottom wall traverses alternately from hydrophilic region to hydrophobic region, the curvature of the meniscus changes very sharply and large velocity gradients are observed at the wall for Cases 1 and 2. The gradients are observed to be higher for the 20 μm patterned wall compared with the 40 μm patterned wall (Fig. 10) and also the velocity magnitude values for Case 2 is higher compared with Case 1 for both DI water and ethanol. This is due to the higher hydrophilic nature of the bottom wall in Case 2 compared with Case 1. Additionally, the smaller pattern size (20 μm patterned wall) also tends to add additional hydrophilic effect in the microchannel. Overall, this results in flow variations in the microchannel. Such flow variations will be absent in the case of nonpatterned microchannel. The position of the maximum velocity magnitude along the channel height varies considerably for all the cases. It is therefore possible to manipulate fluid flow by controlling the size of the patterned surface. Such phenomena will find applications for performing biological reactions in microfluidic devices using the capillary flow. All biological reactions need sufficient incubation time to complete the reaction. It is believed that sufficient incubation time necessary for reaction to proceed will be inherently available in the patterned microchannel. The biological fluid will come in contact with surface, which will alternately assist and retard its flow. The region where the flow is retarded can be used for the reaction zone.

4.6 Variation of Meniscus Maximum, Average, and Centerline Velocity. The maximum, average, and centerline velocity of the meniscus is observed to show very high degree of fluctuations for all the cases and their magnitude decreases with time. The meniscus root mean squared (rms) velocities are computed and is provided in Table 4 for comparison purpose. It is found that the maximum velocity with DI water occurs for Case 2, followed by Case 1. Similar trends are observed with ethanol with a lower value in its magnitude. The frequency of fluctuations is observed to be higher with ethanol compared with DI water. It is observed that the pattern size and the surface condition on the bottom wall influence the rms velocity. The rms velocity for 20 μm patterned wall is higher compared with 40 μm patterned wall for all the cases with DI water and ethanol. Figure 12 shows the meniscus displacement with time of the contact line on the top and bottom walls with DI water (contact angles $\theta_1 = 30$ deg and θ_2

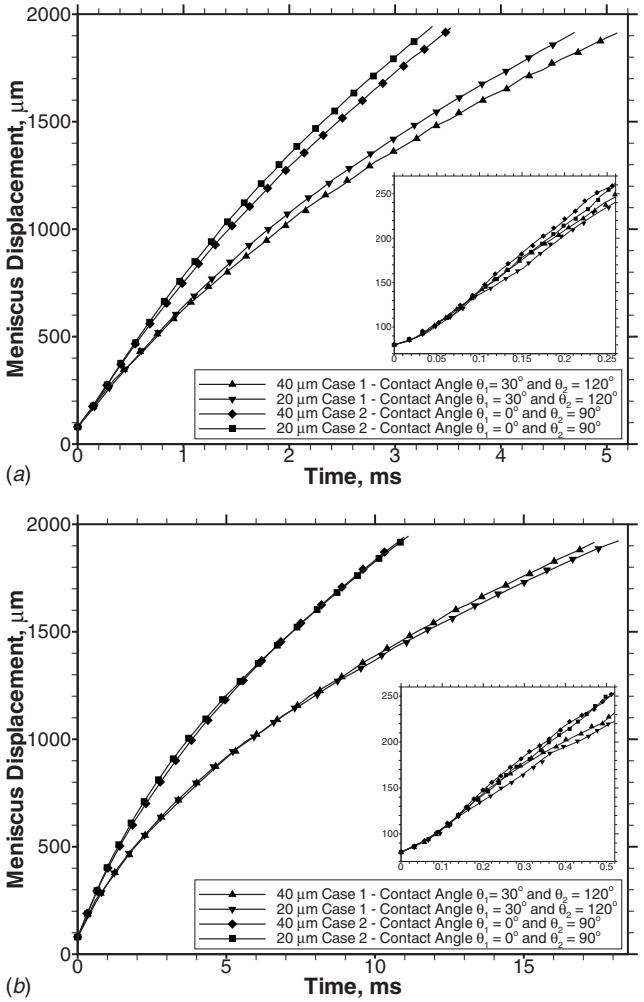

Fig. 8 The position of capillary meniscus with time for Cases 1 and 2 for two different working fluids: (*a*) DI water and (*b*) ethanol

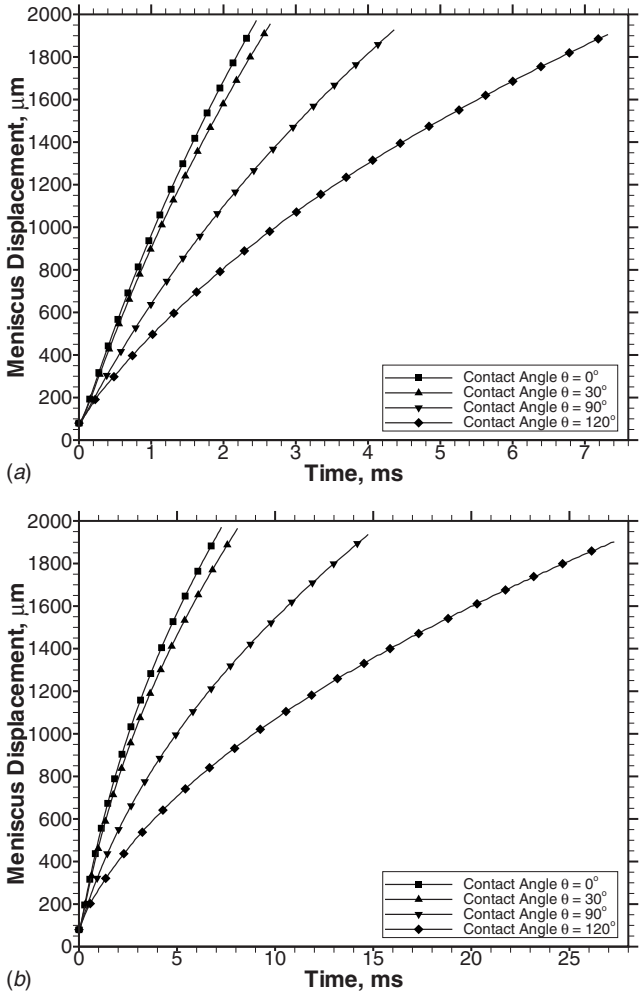

Fig. 9 The position of capillary meniscus with time for a non-patterned microchannel for two different working fluids: (*a*) DI water and (*b*) ethanol

=120 deg) for 20 μm patterned microchannel. As the top and bottom contact lines of the meniscus show different displacement profiles, the velocity difference of the top and bottom contact line motions is also plotted in Fig. 12. The hydrophilic and hydrophobic regions have been marked in the plot. It is observed that difference in velocity increases/decreases and fluctuates with time due to the presence of alternate patterns. In the hydrophilic region, the top and bottom wall velocity difference is observed to decrease, whereas the same increases in the hydrophobic region. This presents an excellent opportunity for applications in microfluidic devices, which requires enhanced mixing for fluid delivery. This will also help in innovative design of capillary driven microfluidic devices.

Table 3 Meniscus position in micrometers from the channel inlet at 1 ms

Liquid	Case	40 μm alternate pattern	20 μm alternate pattern
DI water	Case 1	604.91	626.37
	Case 2	743.77	772.80
Ethanol	Case 1	320.11	319.39
	Case 2	388.21	396.41

4.7 Effect of Large Pattern Sizes. Simulations are also performed considering 60 μm, 80 μm, and 100 μm patterns for DI water and ethanol to investigate the effect of larger pattern sizes. A dimensionless pattern size is defined (which is a ratio of pattern

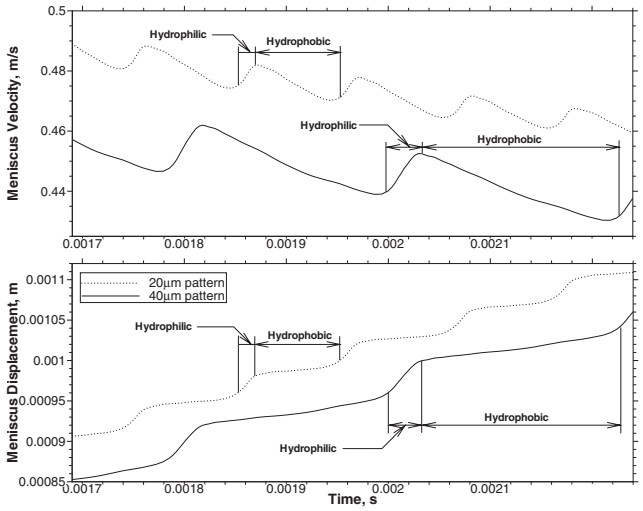

Fig. 10 Meniscus displacement of the capillary with time on the bottom wall with DI water (contact angles θ_1=30 deg and θ_2=120 deg) for 20 μm and 40 μm patterned microchannels

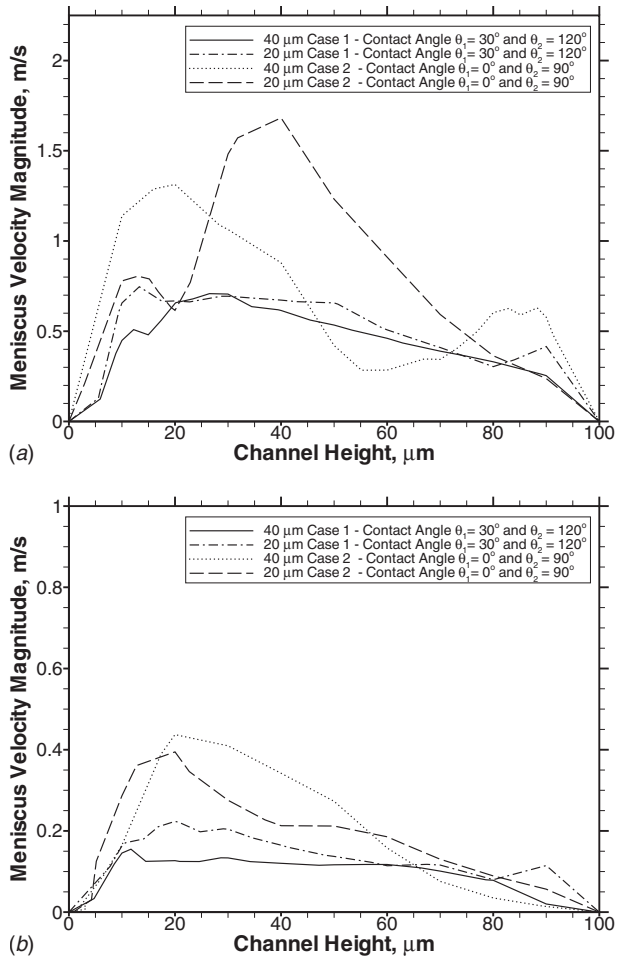

Fig. 11 Meniscus velocity distribution along the channel height for Cases 1 and 2 for two different working fluids: (*a*) DI water and (*b*) ethanol

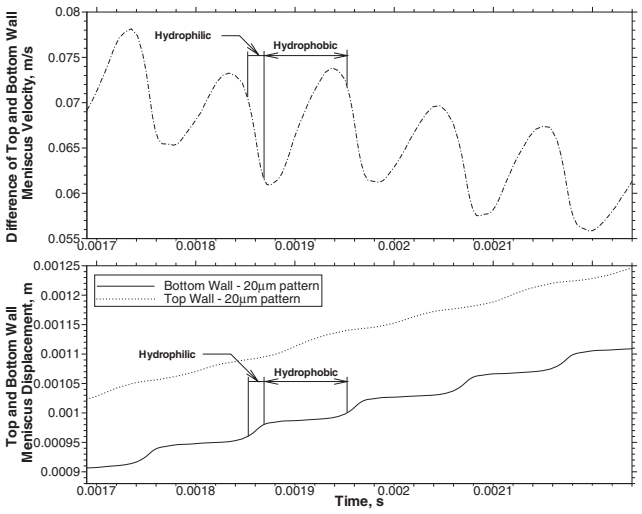

Fig. 12 Meniscus displacement of the capillary with time on the top and bottom wall with DI water (contact angles θ_1 =30 deg and θ_2=120 deg) for 20 μm patterned microchannel

size and microchannel height) here, for comparing the predicted results. Figure 13 shows the meniscus average velocity difference at top and bottom walls with dimensionless pattern size.

It is observed that, in the case of DI water with hydrophilic-hydrophobic pattern, the meniscus average velocity difference at top and bottom walls increases for a dimensionless pattern size of 0.6 and thereafter it decreases with the increase in pattern size. Whereas, for ethanol, the meniscus average velocity difference increases slightly with dimensionless pattern size and its magnitude is lower than that for DI water. It is to be noted that the top and bottom wall meniscus average velocity difference is related to meniscus stretch. With DI water as the working fluid, the meniscus stretch decreases as the pattern size is increased beyond 60 μm. However, in the case of hydrophilic-neutral pattern, the meniscus average velocity difference is observed to decrease with the increase in dimensionless pattern size for both DI water and ethanol. The above results may be useful to optimize the design of a patterned microchannel for a given application.

4.8 Grid Issues. Simulations are also conducted to study the influence of grid resolution on the numerical solution. The simulation time for 10×200 grid cells is typically around 45 min on a 2.4 GHz AMD 64 Opteron processor running Linux with an access to 4 Gbyte RAM. It is to be noted that with the increase in the grid resolution in every direction by a factor of 2, the calculation time in a two-dimensional grid increases by a factor of 8. Also, the time step under such condition needs to be decreased by a factor of 2 in order to fulfill the CFL stability criteria. The grid cells are taken as square element as per the requirement of the VOF module.

The grid convergence of the solution has been tested by imposing different inlet boundary conditions, viz., pressure inlet (zero/positive), constant velocity inlet, and time varying velocity inlet using 10×200, 12×240, 14×280, 20×400, and 40×800 grid cells. It is to be noted that, when velocity inlet boundary conditions are imposed (Fig. 14(*a*) and 14(*b*)), the meniscus displacement curves do not show any amount of error for all the grid sizes considered. However, when the pressure inlet boundary condition is imposed (Fig. 15(*a*)), an error of about 2% is observed in meniscus displacement (less than 20 μm when the microchannel is half filled) as the grid is refined. The error reduces to about 1.5% when a positive pressure of 1000 N/m^2 inlet boundary condition is imposed (Fig. 15(*b*)). Raessi et al. [28] showed that there may be errors in interface normal vectors and curvatures at high grid resolutions when modeling surface tensions. This could result in overestimating the contact angle at high grid resolutions, which tend to decrease the meniscus displacement. Hence, for capillary driven studies where the filling time and meniscus displacement

Table 4 Meniscus rms velocity

		40 μm alternate pattern			20 μm alternate pattern		
Liquid	Case	Maximum	Average	Centerline	Maximum	Average	Centerline
DI water	Case 1	1.0722	0.4793	0.6292	1.1034	0.5063	0.6531
	Case 2	1.4454	0.6119	0.7775	1.5628	0.6644	0.8174
Ethanol	Case 1	0.3246	0.1507	0.2047	0.3339	0.1517	0.1956
	Case 2	0.4569	0.2020	0.2545	0.4825	0.2065	0.2562

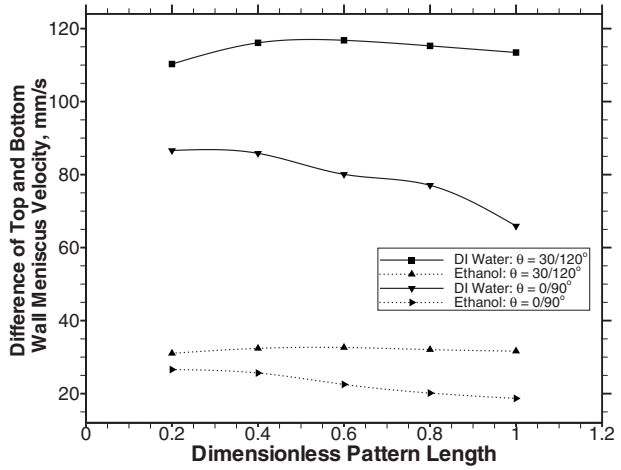

Fig. 13 Meniscus average velocity difference of top and bottom walls with dimensionless pattern size for DI water and ethanol

are important variables, it is preferable to use fewer grid nodes for simulations [7,9,12,29,13].

To study grid independence with respect to flow field variables, three simulations have been done using 2000, 2880, and 3920 grid cells. In Fig. 16, it is shown that the numerical results of total pressure and velocity magnitude as function of liquid volume fraction, with the coarsest of these three grids, are grid independent. The difference in the flow field variables are within 1.5% and 2.0%, respectively.

To check time-step independence, 2000 total grid cells (2211 nodes) are used and the simulations are executed for three time

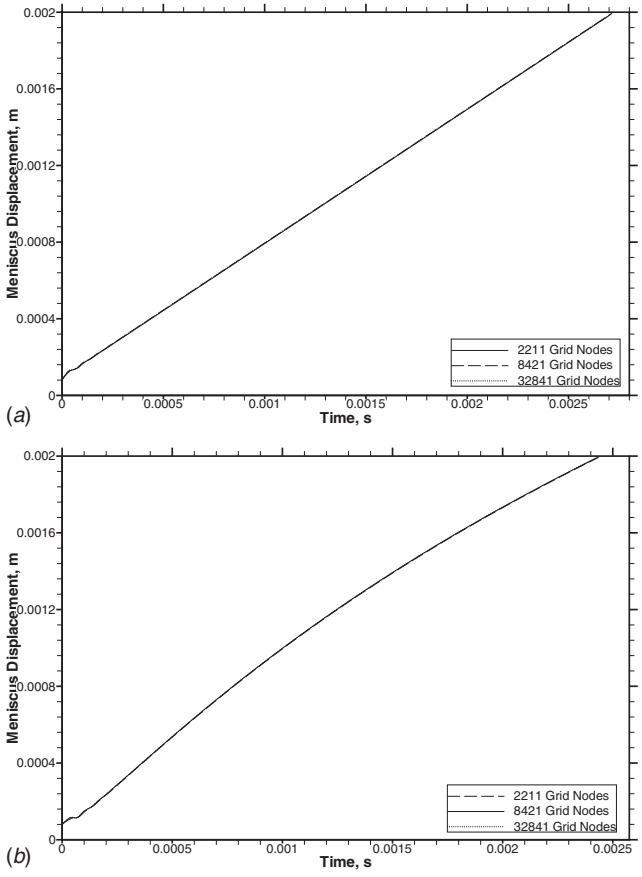

Fig. 14 Comparison of the position of the capillary meniscus with time for nonpatterned microchannel with DI water (contact angle θ=30 deg) for different velocity inlet boundary conditions with different grid sizes: (*a*) velocity inlet=constant and (*b*) velocity inlet=time varying

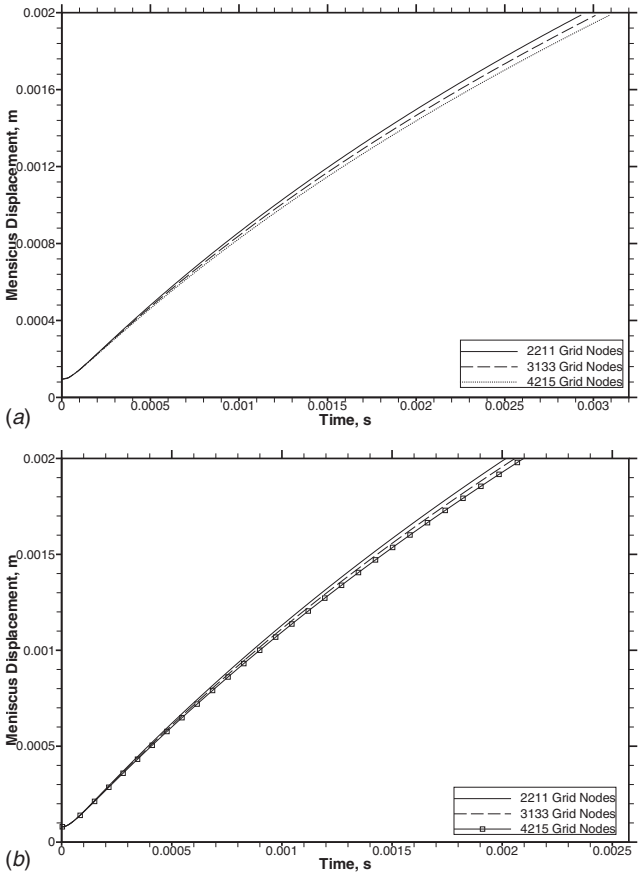

Fig. 15 Comparison of the position of the capillary meniscus with time for nonpatterned microchannel with DI water (contact angle θ=30 deg) for different pressure inlet boundary conditions with different grid sizes: (*a*) pressure=0 N/m^2 and (*b*) pressure=1000 N/m^2

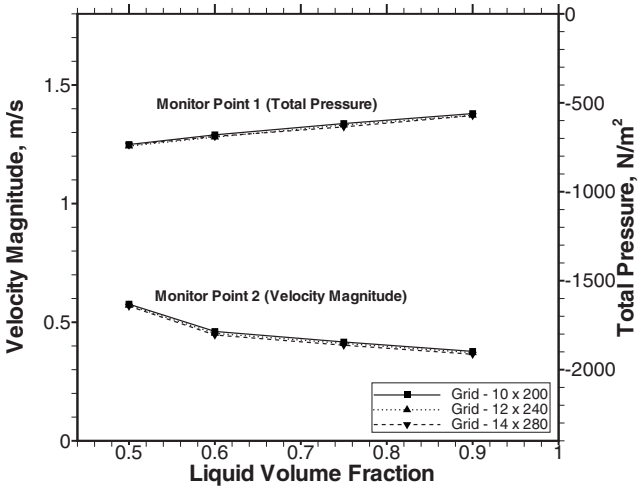

Fig. 16 Comparison of flow field variables with liquid volume fraction for nonpatterned microchannel with DI water (contact angle θ=30 deg) with different grid sizes

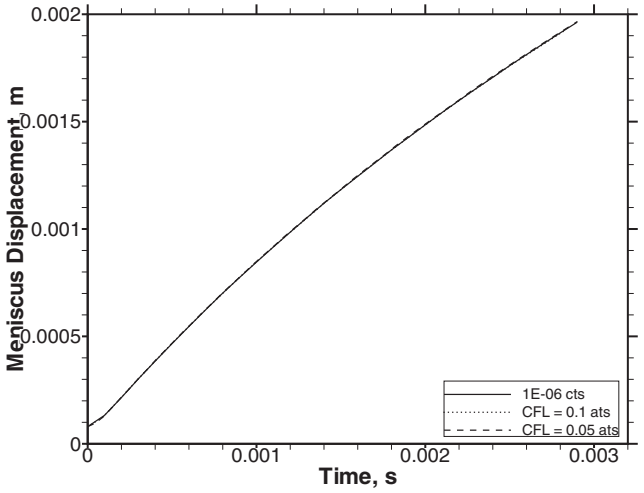

Fig. 17 Comparison of the position of the capillary meniscus with time for nonpatterned microchannel with DI water (contact angle θ=30 deg) with different time-step sizes

steps—1×10^{-6} s constant time step (cts), 0.1 CFL automatic time step (ats), and 0.05 CFL automatic time step (ats). In Fig. 17, it is shown that the results are time-step independent with 0.1 CFL automatic time step.

Figure 18 shows the profile of the capillary meniscus when the microchannel is half filled, with the three different grid sizes. It is observed that the meniscus interface is resolved well for all the grid sizes. The maximum difference of the term [30] $|(\sqrt{x_{ic}^2+y_{ic}^2})_{\text{coarse}}-(\sqrt{x_{ic}^2+y_{ic}^2})_{\text{fine}}/(\sqrt{x_{ic}^2+y_{ic}^2})_{\text{fine}}|$ was within 0.30%, where the values x_{ic} and y_{ic} denote the x and y components of the meniscus interface coordinates. Hence, a minimum of ten grid cells across the microchannel height is found to be adequate for the resolution of the meniscus interface. It is also found that by using different space discretization schemes (viz., first-order, second-order, and smart), insignificant deviation is observed in the predicted meniscus front.

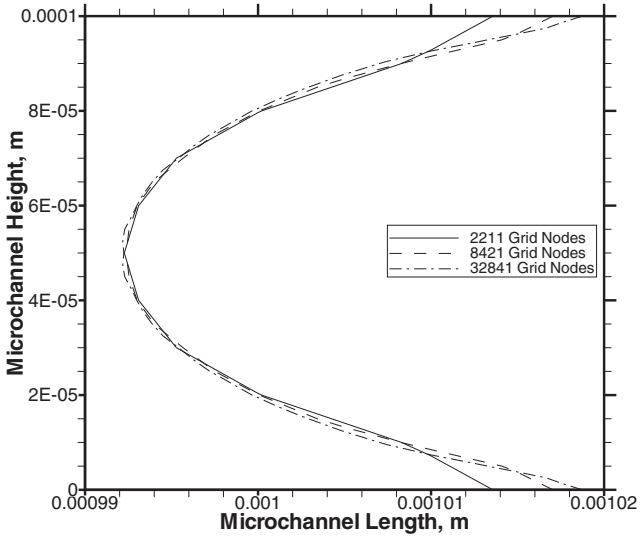

Fig. 18 Comparison of the profile of the capillary meniscus for nonpatterned microchannel with DI water (contact angle θ =30 deg) at different grid resolutions when the microchannel is half filled

5 Conclusions

A two-dimensional numerical simulation of flow through a patterned microchannel has been carried out. Two different cases—alternate hydrophilic-hydrophobic bottom wall with contact angle 30 deg and 120 deg, respectively, and alternate hydrophilic-neutral bottom wall with contact angle 0 deg and 90 deg, respectively—are considered here. The pattern size is varied between 20 μm and 40 μm for each case. The volume of fluid method is used for simulating the free surface flow in the microchannel. Meniscus profiles with varying amplitude and shapes are obtained under the different specified surface conditions. Nonsymmetric meniscus profiles are obtained by changing the contact angles of the hydrophilic and hydrophobic surfaces. The meniscus stretch is observed to fluctuate with time. Smaller pattern size produces enhanced capillary effect with DI water, whereas no appreciable gain is observed for ethanol. It is found that the meniscus displacement for alternate hydrophilic-hydrophobic surface is lower compared with the hydrophilic-neutral surface and the initial transient response of the displacement varies significantly with the surface characteristics. It is observed that the meniscus displacement can be manipulated suitably by appropriate choice of the pattern size and the contact angle for a given working fluid. It is also found that the meniscus velocity magnitude is higher for DI water and the position of the maximum velocity varies considerably for all the cases. The rms velocity for 20 μm patterned wall is found to be higher compared with the 40 μm patterned wall. The flow variations increase in the microchannel as the fluid traverses alternately between hydrophilic and hydrophobic regions due to a sharp change in the meniscus curvature at the interface. The effect of the surface tension of the fluid is shown to have significant effect on the capillary motion. Such flow phenomena in the microchannel indicate that flow control is possible by patterning the channel walls for applications related to microfluidic devices. Simulations are also performed to investigate the effect of larger pattern sizes. The meniscus average velocity difference at the top and bottom walls increases for a dimensionless pattern size of 0.6 and thereafter it decreases with the increase in pattern size in the case of DI water with hydrophilic-hydrophobic pattern. The design of a patterned microchannel may be optimized for a given application.

Acknowledgment

The support of Suman Mashruwala Advanced Microengineering Laboratory, IIT Bombay is highly appreciated.

Nomenclature

- Bo = Bond number
- Ca = Capillary number
- F = liquid volume fraction
- $\mathbf{F_s}$ = volumetric force representing the surface tension
- h = channel height, local cell dimension
- L = distance traveled by liquid meniscus
- l = channel length
- $\mathbf{n}$ = normal vector
- $\hat{\mathbf{n}}$ = unit vector normal to the surface
- $\hat{\mathbf{n}}_w$ = unit vector normal to the wall
- P = pressure
- R = radius of curvature
- t = time
- $\hat{\mathbf{t}}_w$ = unit vector tangent to the wall
- U = characteristic velocity
- u = velocity component in x-direction
- u_{avg} = average velocity
- $\mathbf{V}$ = velocity vector
- v = interface velocity
- ρ = density of fluid

σ = surface tension of fluid
θ = contact angle
μ = viscosity of fluid
κ = curvature of the surface

Subscripts

avg = average
s = surface tension
w = wall
1 = gas phase
2 = liquid phase

References

[1] Madou, M., 2002, *Fundamentals of Microfabrication*, CRC, New York.
[2] Deval, J., Umali, T. A., Lan, E. H., Dunn, B., and Ho, C. M., 2004, "Reconfigurable Hydrophobic/Hydrophilic Surfaces in Microelectromechanical Systems (MEMS)," J. Micromech. Microeng., **14**, pp. 91–95.
[3] Zhao, B., Jeffrey, M. S., and Beebe, D. J., 2001, "Surface-Directed Liquid Flow Inside Microchannels," Science, **291**, pp. 1023–1026.
[4] Kim, D. S., Lee, K. C., Kwon, T. H., and Lee, S. S., 2002, "Microchannel Filling Flow Considering Surface Tension Effect," J. Micromech. Microeng., **12**, pp. 236–246.
[5] Yang, L. J., Yao, T. J., and Tai, Y. C., 2004, "The Marching Velocity of the Capillary Meniscus in a Microchannel," J. Micromech. Microeng., **14**, pp. 220–225.
[6] Salamon, T., Lee, W., Krupenkin, M., Hodes, M., and Kolodner, P., 2005, "Numerical Simulation of Fluid Flow in Microchannels With Superhydrophobic Walls," International Mechanical Engineering Conference and Exposition, Paper No. 82641.
[7] Byun, D., Budiono, Yang, J. H., Lee, C., and Lim, K. W., 2005, "Numerical Visualization of Flow Instability in Microchannel Considering Surface Wettability," Second International Conference on Fuzzy Systems and Knowledge Discovery, Paper No. LNAI 3613.
[8] Dalton, T., Eason, C., Enright, R., Hodes, M., Kolodner, P., and Krupenkin, T., 2006, "Challenges in Using Nano Textured Surfaces to Reduce Pressure Drop Through Microchannels," Seventh International Conference on Thermal, Mechanical and Multiphysics Simulation and Experiments in Micro-Electronics and Micro-Systems, pp. 1–3.
[9] Yang, H. Q., and Przekwas, A. J., 1998, "Computational Modeling of Microfluid Devices With Free Surface Liquid Handling," First International Conference on Modeling and Simulation of Microsystems, pp. 498–505.
[10] Hirt, C. W., and Nichols, B. D., 1981, "Volume of Fluid (VOF) Method for the Dynamics of Free Boundaries," J. Comput. Phys., **39**, pp. 201–225.
[11] Kothe, D. B., Rider, W. J., Mosso, S. J., and Brock, J. S., 1996, "Volume Tracking of Interfaces Having Surface Tension in Two and Three Dimensions," AIAA Paper No. 96-0859.
[12] Saha, A. A., Mitra, S. K., Tweedie, M., Roy, S., and McLaughlin, J., 2008, "Experimental and Numerical Investigation of Capillary Flow in SU8 and PDMS Microchannels With Integrated Pillars," Microfluid. Nanofluid.
[13] Huang, W., Liu, Q., and Li, Y., 2006, "Capillary Filling Flows Inside Patterned-Surface Microchannels," Chem. Eng. Technol., **29**, pp. 716–723.
[14] Nayak, K., Kulkarni, P. D., Deepu, A., Sitaraman, V. R., Punidha, S., Saha, A. A., Ravikanth, M., Mitra, S. K., Mukherji, S., and Rao, V. R., 2007, "Patterned Microfluidic Channels Using Self-Assembled Hydroxy-Phenyl Porphyrin Monolayer," Seventh IEEE International Conference on Nanotechnology, Paper No. 404, pp. 238–240.
[15] Probstein, R. F., 1994, *Physicochemical Hydrodynamics*, Wiley, New York.
[16] Patankar, S., 1980, *Numerical Heat Transfer and Fluid Flow*, Hemisphere, New York.
[17] Brackbill, J. U., Kothe, D. B., and Zemach, C., 1992, "A Continuum Method for Modeling Surface Tension," J. Comput. Phys., **100**, pp. 335–354.
[18] Rosengarten, G., Harvie, D. J. E., and White, J. C., 2006, "Contact Angle Effects on Microdroplet Deformation Using CFD," Appl. Math. Model., **30**, pp. 1033–1042.
[19] Washburn, E. W., 1921, "The Dynamics of Capillary Flow," Phys. Rev., **17**, pp. 273–299.
[20] Zeng, J., 2007, "On Modeling of Capillary Filling," http://www.coventor.com/pdfs/on_modeling_of_capillary_filling.pdf.
[21] Ralston, J., Popescu, M., and Sedev, R., 2008, "Dynamics of Wetting from an Experimental Point of View," Annu. Rev. Mater. Res., **38**, pp. 23–43.
[22] Dussan, E. B., 1979, "On the Spreading of Liquids on Solid Surfaces: Static and Dynamic Contact Angles," Annu. Rev. Fluid Mech., **11**, pp. 371–400.
[23] de Gennes, P. G., 1985, "Wetting: Statics and Dynamics," Rev. Mod. Phys., **57**, pp. 827–890.
[24] Blake, T. D., 2006, "The Physics of Moving Wetting Lines," J. Colloid Interface Sci., **299**, pp. 1–13.
[25] ESI CFD Inc., 2007, CFD-ACE+ Software Manuals, V2007.2.
[26] Stange, M., Dreyer, M. E., and Rath, H. J., 2003, "Capillary Driven Flow in Circular Cylindrical Tubes," Phys. Fluids, **15**, pp. 2587–2601.
[27] Dreyer, M. E., Delgado, A., and Rath, H. J., 1994, "Capillary Rise of Liquid Between Parallel Plates Under Microgravity," J. Colloid Interface Sci., **163**, pp. 158–168.
[28] Raessi, M., Mostaghimi, J., and Bussmann, M., 2007, "Advecting Normal Vectors: A New Method for Calculating Interface Normals and Curvatures When Modeling Two Phase Flows," J. Comput. Phys., **226**, pp. 774–797.
[29] Trutschel, R., and Schellenberger, U., 1998, "Dynamic Simulation of Free Surfaces in Capillaries With the Finite Element Method," Int. J. Numer. Methods Fluids, **26**, pp. 485–495.
[30] Yang, A. S., 2008, "Investigation of Liquid-Gas Interfacial Shapes in Reduced Gravitational Environments," Int. J. Mech. Sci., **50**, pp. 1304–1315.

A Novel Explicit Equation for Friction Factor in Smooth and Rough Pipes

Atakan Avci
e-mail: atakan@uludag.edu.tr

Irfan Karagoz
e-mail: karagoz@uludag.edu.tr

Department of Mechanical Engineering,
Uludag University,
16059 Bursa, Turkey

In this paper, we propose a novel explicit equation for friction factor, which is valid for both smooth and rough wall turbulent flows in pipes and channels. The form of the proposed equation is based on a new logarithmic velocity profile and the model constants are obtained by using the experimental data available in the literature. The proposed equation gives the friction factor explicitly as a function of Reynolds number and relative roughness. The results indicate that the present model gives a very good prediction of the friction factor and can reproduce the Colebrook equation and its Moody plot. Therefore, the new approximation for the friction factor provides a rational, accurate, and practically useful method over the entire range of the Moody chart in terms of Reynolds number and relative roughness. [DOI: 10.1115/1.3129132]

Keywords: friction factor, turbulent flows, boundary layers, mathematical modeling

1 Introduction

Proper description of mean turbulent velocity profiles and the calculation of friction losses are of particular interest to boundary layer researchers and engineers. The difficulty to solve the turbulent flow problems lies in the fact that the friction factor is a complex function of relative surface roughness and the Reynolds number (Re). Derivation of relations for the friction factor is mostly based on the logarithmic or power law formulations of velocity profiles in boundary layers.

The first correlation for friction factor (f) is a curve fit to smooth wall data collected by Blasius for pipes in 1913. The Blasius formula is

$$f = 0.316\ \mathrm{Re}^{-0.25} \tag{1}$$

This equation has a limited range of applicability. It is widely accepted that the Blasius friction relationship gives the best representation of friction factor data of available formulations for $\mathrm{Re} < 100 \times 10^3$. Prandtl [1] derived a better formula from the logarithmic velocity profile and experimental data on smooth pipes as follows:

$$\frac{1}{\sqrt{f}} = -2.0\ \log(\mathrm{Re}\sqrt{f}) - 0.8 \tag{2}$$

Although this formula is valid for $\mathrm{Re} > 4000$, it is implicit and needs iterative solution for f. Recent studies show that the constants of Prandtl's "universal" friction factor relationship are accurate over only a limited Reynolds-number range and are unsuitable for extrapolation to high-Reynolds numbers [2,3]. McKeon et al. [3] proposed an expression, which well represents the friction factor data, including correction for the viscous deviation from the log law at the wall by

$$\frac{1}{\sqrt{f}} = 1.920\ \log(\mathrm{Re}\sqrt{f}) - 0.475 - \frac{7.04}{(\mathrm{Re}\sqrt{f})^{0.55}} \tag{3}$$

The development of approximate equations for the calculation of friction factor in rough pipes began with Nikuradse's turbulent pipe flow investigations in 1932 [4]. Using the logarithmic law with these data, the friction factor can be obtained as

$$\frac{1}{\sqrt{f}} = -2.0\ \log\left(\frac{k_s}{3.7d}\right) \tag{4}$$

for fully rough pipe flows, depending on the surface roughness k_s and pipe diameter d [5]. There are also several formulas for the transitional roughness region [6–10].

The famous relation is an implicit formula proposed by Colebrook in 1939 [11] as

$$\frac{1}{\sqrt{f}} = -2.0\ \log\left(\frac{k_s}{3.7d} + \frac{2.51}{\mathrm{Re}\sqrt{f}}\right) \tag{5}$$

The plot of this formula is known as the Moody chart and is widely used for pipe friction. As an alternative to this implicit equation, an explicit formula was given by Haaland [12] as follows:

$$\frac{1}{\sqrt{f}} = -1.8\ \log\left[\left(\frac{k_s}{3.7d}\right)^{1.11} + \frac{6.9}{\mathrm{Re}}\right] \tag{6}$$

which differs less than 2% from the Colebrook formula. More information can be found in related literature [13].

By using high-Reynolds-number pipe-flow data, McKeon concluded that power laws and logarithmic friction factor relationships well represent experimental data for limited ranges of Reynolds number.

In this study, a new formula has been developed for the friction factor in turbulent pipe flows. Derivation of this explicit formula is based on the modified mixing length theory. In order to gain insight into the model's reliability, the results of the model were compared with available experimental data. It was shown that this equation can be used for the wide ranges of Reynolds number $5 \times 10^3 < \mathrm{Re} < 1 \times 10^8$ and relative roughness $0 \le \varepsilon < 0.05$. The proposed equation can also be employed for turbulent flow in channels, by using the Reynolds number based on the hydraulic diameter.

2 Mathematical Modeling

Derivation of relations for the friction factor is mostly based on the logarithmic or power law formulations of velocity profiles in boundary layers.

Contributed by the Fluids Engineering Division of ASME for publication in the JOURNAL OF FLUIDS ENGINEERING. Manuscript received July 7, 2008; final manuscript received March 24, 2009; published online May 13, 2009. Assoc. Editor: James A. Liburdy.

It is well know that in the overlap region, velocity (u) varies logarithmically with y coordinate perpendicular to the surface and can be written in dimensionless form as [14–16]

$$\frac{u}{u_\tau} = \frac{1}{\kappa}\ln\left(\frac{yu_\tau}{\nu}\right) + B \tag{7}$$

where $u_\tau = \sqrt{\tau_w/\rho}$, τ_w is the wall shear stress, ρ is the fluid density, ν is the kinematic viscosity, κ (known as the von Karman constant) and B are constants for turbulent flow past smooth impermeable walls. Although these constants are claimed to be universal, different values for these constant are often reported in the literature [17–19].

Alternatively, the velocity profile can be assumed to obey a power law, which may be written as

$$\frac{u}{u_\tau} = C\left(\frac{yu_\tau}{\nu}\right)^\gamma \tag{8}$$

where the factor C and the exponent γ are empirically determined parameters, which are often assumed to be Reynolds number dependent [20]. However, some researchers have pointed out that both the multiplicative factor and the exponent are Reynolds number independent and given by $C=8.48$ and $\gamma=0.142$ [18,21], which are very close to the values known from Nikuradse's [4] 1/7th-power law. However, these parameters are often assumed to be Reynolds number dependent.

We propose a new relation for the velocity profile as

$$\frac{u}{u_\tau} = K(\ln(yu_\tau/\nu) + p)^n \tag{9}$$

which is a combination of logarithmic and power low velocity profiles.

For turbulent flows in pipes, taking $y=R-r$, Eq. (9) can be written as

$$\frac{u}{u_\tau} = K\left(\ln\left(\frac{(R-r)u_\tau}{\nu}\right) + p\right)^n \tag{10}$$

where n, K, and p should be determined experimentally. By inserting $r=0$ in Eq. (10), the maximum velocity can be calculated as

$$\frac{u_{\max}}{u_\tau} = K\left(\ln\left(\frac{Ru_\tau}{\nu}\right) + p\right)^n \tag{11}$$

The velocity profile represented by Eq. (10) can be used for the calculation of friction factor. For this aim, Eq. (10) should be integrated in order to get the mean velocity in a pipe, which has a radius of $R=d/2$. Since integration of this equation is not easy, it is assumed that the mean velocity (V) is a fraction of the maximum velocity and the equation for mean velocity has the same form as in Eq. (11) with different constants. Consequently, the mean velocity can be written as

$$\frac{V}{u_\tau} = a\left(\ln\left(\frac{\mathrm{Re}}{\beta}\right)\right)^b \tag{12}$$

where $\mathrm{Re}=Vd/\nu$ is the Reynolds number, and β is a parameter and might be a function of Re and the relative roughness $\varepsilon = k_s/d$. In this derivation, the term Ru_τ/ν in the parenthesis is approximated as a logarithmic function of Re number.

On the other hand, the friction factor is defined as

$$f = \frac{\tau}{\frac{1}{8}\rho V^2} = 8\left(\frac{u_\tau}{V}\right)^2 \tag{13}$$

and therefore Eq. (12) can be rewritten in terms of the friction factor as follows:

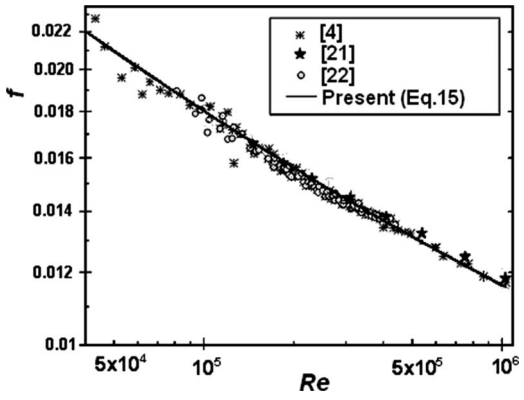

Fig. 1 Comparison of the present friction factor with literature values over an intermediate range of Reynolds numbers

$$f = \frac{8}{a^2\left(\ln\left(\frac{\mathrm{Re}}{\beta}\right)\right)^{2b}} \tag{14}$$

This equation is very simple, however the constants a, b, and β, which is a function of Re and ε, should be determined such that Eq. (14) covers the entire range of Re and ε as in the case of the Moody chart for turbulent flows in pipes and channels.

It is possible to assume that β is a constant for smooth pipes and is a function of Re and ε, otherwise. For smooth pipes, $\beta = 1$ and the values of $a \approx 1.118$ and $b \approx 1.2$ are obtained from curve fit to the experimental data available in the literature. Therefore, the friction factor is obtained as

$$f = \frac{6.4}{(\ln(\mathrm{Re}))^{2.4}} \tag{15}$$

for smooth pipes. Since the influence of the Reynolds number on the friction factor dies out and the role of the relative roughness becomes dominant at high-Reynolds number flows, the following form is proposed for β in Eq. (14):

$$\beta = 1 + c\ \mathrm{Re}\ \varepsilon(1 + d\sqrt{\varepsilon}) \tag{16}$$

where c and d are constants to be determined from experiments. This relation is also identical to Eq. (15) when $\beta=1$ for smooth pipes. Through the tests with experimental data available in the literature show that the best fit to the experimental data of Nikuradse and to the Moody chart is obtained with $c \approx 0.01$ and $d \approx 10$. Therefore, the final equation for the calculation of the friction factor can be written as

$$f = \frac{6.4}{(\ln(\mathrm{Re}) - \ln(1 + 0.01\ \mathrm{Re}\ \varepsilon(1 + 10\sqrt{\varepsilon})))^{2.4}} \tag{17}$$

which is valid for both smooth and rough pipes and channels, and covers the entire range of the Moody chart for turbulent flow. In the case of channel flows, the hydraulic diameter can be used as characteristic length to compute the Reynolds number and the relative roughness.

3 Results and Discussion

An alternative explicit equation for the friction factor is derived for turbulent pipe and channel flows. Since Eq. (15) for smooth pipes was directly derived from the mean velocity equation (Eq. (12)), justification of Eq. (15) was considered before going further. As can be seen from Fig. 1, the results obtained from this equation show very good agreement with experimental data given in the literature [4,21,22]. It should also be note that this explicit equation gives results, which are indistinguishable from the solution of the well known implicit Prandtl equation (Eq. (2)).

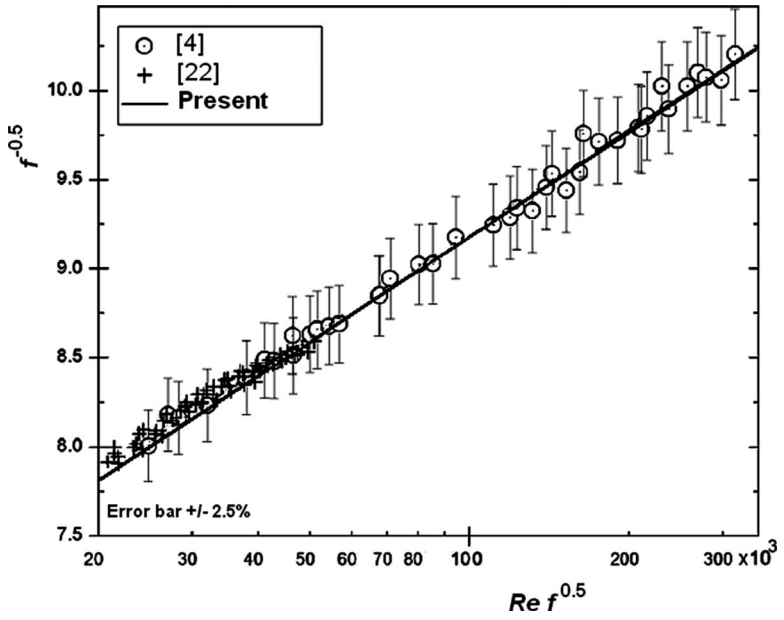

Fig. 2 Consistency check of the present formula over a wide range of Reynolds numbers

In order to obtain the constants of Prandtl's friction formula, the pipe's friction data of Zanoun et al. [22] and Nikuradse [4] were plotted as in Fig. 2. This figure was also used to test the present formula. As can be seen from Fig. 2, good agreement was also observed when the present formula was compared with the experimental data of Nikuradse and Zanoun et al., for the range of Reynolds number $2\times10^5<\mathrm{Re}<3.2\times10^6$. By using the experimental data included in Fig. 2, Zanoun et al. [22] estimated the value of the numerical constants of the Prandtl formula (Eq. (2)) to be approximately 1.93 and 0.414, instead of 2.0 and 0.8, resulting in a value of 0.421 for the von Karman constant.

The Moody chart was reproduced by using Eq. (17), which is the extension of Eq. (15) for turbulent flows in pipes or channels (Fig. 3). The Princeton superpipe data for the Reynolds number from 3.2×10^4 to 3.5×10^7 were included in the figure. A very good agreement can be observed between the predicted values and these experimental values [21] for smooth pipe flow. Some experimental values of rough walls were also included in this figure for comparison. As can be seen from the figure, the present formula produced the Moody chart well for the wide ranges of Reynolds number $5\times10^3<\mathrm{Re}<1\times10^8$, and relative roughness $0\leq\varepsilon<0.05$. Differences between the present formula and the experimental values remain no bigger than 3% for these ranges.

4 Conclusion

A new mathematical friction factor model for fully developed turbulent internal flows has been developed by using a new velocity profile, which is a combination of logarithmic and power law profiles. The formula recovers Prandtl's law of friction for smooth pipes well. The model also shows good correlation with the available data for turbulent flows in rough pipes for wide ranges of Reynolds number and surface roughness covering the entire Moody chart. The maximum relative error between the published experimental friction factors and those calculated from the developed equation was found to be less than 3%, and the proposed relationship agrees with the Blasius relationship for low Reynolds numbers to within 1%. Therefore the proposed equation can be

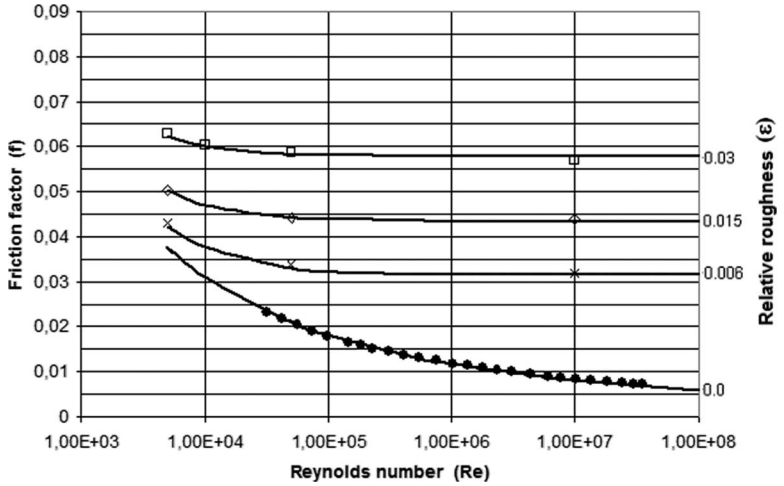

Fig. 3 Comparison of friction factor calculated from Eq. (17) (—) with the Princeton superpipe data and (●●●) and experimental data (×, ◇, □) [23]

used to calculate friction losses in smooth or rough pipes and channels as an alternative to the Moody chart and to the other implicit formulas.

References

[1] Prandtl, L., 1933, "Neuere ergebnisse der turbulenzforschung," VDI Z. (1857-1968), **77**, pp. 105–114.

[2] Zagarola, M. V., Perry, A. E., and Smits, A. J., 1997, "The Scaling in the Overlap Region," Phys. Fluids, **9**, pp. 2094–2100.

[3] McKeon, B. J., Zagarola, M. V., and Smits, A. J., 2005, "A New Friction Factor Relationship for Fully Developed Pipe Flow," J. Fluid Mech., **538**, pp. 429–443.

[4] Nikuradse, J., 1932, "Laws of Turbulent Flow in Smooth Pipes," NASA, Report No. TT F-10.

[5] White, F. M., 1999, *Viscous Fluid Flow*, 4th ed., McGraw-Hill, New York.

[6] Moody, L. F., 1947, "An Approximate Formula for Pipe Friction Factors," Trans. ASME, **69**, pp. 1005–1006.

[7] Swamee, P. K., and Jain, A. K., 1976, "Explicit Equations for Pipe Flow Problems," J. Hydr. Div., **102**(5), pp. 657–664.

[8] Chen, N. H., 1979, "An Explicit Equation for Friction Factor in Pipe," Ind. Eng. Chem. Fundam., **18**(3), pp. 296–297.

[9] Churchill, S. W., 1977, "Friction Factor Equation Spans All Fluid-Flow Regimes," Chem. Eng. J., **84**(24), pp. 91–92.

[10] Wood, D. J., 1966, "An Explicit Friction Factor Relationship," Civ. Eng. (N.Y.), **36**(12), pp. 60–61.

[11] Colebrook, C. F., 1939, "Turbulent Flow in Pipes With Particular Reference to the Transition Region Between the Smooth and the Rough Pipe Laws," J. Inst. Civ. Eng., **11**, pp. 133–156.

[12] Haaland, S. E., 1983, "Simple and Explicit Formulas for the Skin Friction in Turbulent Pipe Flow," ASME J. Fluids Eng., **105**, pp. 89–90.

[13] Romeo, E., Royo, C., and Monzon, A., 2002, "Improved Explicit Equations for Estimation of the Friction Factor in Rough and Smooth Pipes," Chem. Eng. J., **86**, pp. 369–374.

[14] Prandtl, L., 1932, "Zur turbulenten strömung in rohren und langs platten," Ergebnisse der Aerodynamischen Versuchsanstalt zu Gottingen, **4**, pp. 18–29.

[15] von Karman, T., 1930, "Mechanische ahnlichkeit und turbulenz," Nachr. Ges. Wiss. Goettingen, Math.-Phys. Kl., **5**, pp. 58–76.

[16] Millikan, C. M., 1938, "A Critical Discussion of Turbulent Flows in Channels and Circular Tubes," Proceedings of the Fifth International Congress on Applied Mechanics, pp. 386–392.

[17] Zanoun, E. S., Durst, F., and Nagib, H. M., 2003, "Evaluating the Law of the Wall in Two-Dimensional Fully Developed Turbulent Channel Flows," Phys. Fluids, **15**, pp. 3079–3089.

[18] McKeon, B. J., Li, J., Jiang, W., Morrison, J. F., and Smits, A. J., 2004, "Further Observations on the Mean Velocity Distribution in Fully Developed Pipe Flow," J. Fluid Mech., **501**, pp. 135–147.

[19] Wosnik, M., Castillo, L., and George, W. K., 2000, "A Theory for Turbulent Pipe and Channel Flows," J. Fluid Mech., **421**, pp. 115–45.

[20] Clauser, F. H., 1956, "The Turbulent Boundary Layer," Adv. Appl. Mech., **4**, pp. 1–51.

[21] Zagarola, M. V., and Smits, A. J., 1998, "Mean-Flow Scaling of Turbulent Pipe Flow," J. Fluid Mech., **373**, pp. 33–79.

[22] Zanoun, E. S., Durst, F., Bayoumy, O., and Al-Salaymeh, A., 2007, "Wall Skin Friction and Mean Velocity Profiles of Fully Developed Turbulent Pipe Flows," Exp. Therm. Fluid Sci., **32**, pp. 249–261.

[23] Moody, L. F., 1944, "Friction Factors for Pipe Flow," Trans. ASME, **66**, pp. 671–684.

A Study on Flow Transition and Development in Circular and Rectangular Ducts

E.-S. Zanoun
Department of Aerodynamics and Fluid Mechanics,
Brandenburg University of Technology Cottbus,
Siemens-Halske-Ring 14,
D-03046 Cottbus, Germany

M. Kito
Mie University,
1577 Kurimamachiya-cho,
Tsu City,
Mie Prefecture, Japan

C. Egbers
Department of Aerodynamics and Fluid Mechanics,
Brandenburg University of Technology Cottbus,
Siemens-Halske-Ring 14,
D-03046 Cottbus, Germany

The present paper reports observations on some aspects regarding the dependence of the transition Reynolds number and flow development on the inlet flow conditions and the entrance length in circular and rectangular ducts for $Re_m \leq 106 \times 10^3$, where Re_m is the Reynolds number based on the bulk flow velocity ($\bar{U}_b$) and the duct integral length scale (D). The hot-wire anemometer was used to carry out measurements close to the circular duct exit; however, the laser-Doppler anemometry was utilized for the rectangular duct measurements. Particular considerations were given to the bulk flow velocity, the mean-velocity profile, the centerline-average-velocity, and the centerline turbulence statistics to the fourth order. Transition criteria in both ducts were discussed, reflecting effects of flow geometry, entrance flow conditions, and entrance length on the transition Reynolds number. A laminar behavior was maintained up to $Re_m \approx 15.4 \times 10^3$ and $Re_m \approx 2 \times 10^3$ in the circular and rectangular ducts, respectively, and the transition was observed to take place at different downstream positions as the inlet flow velocity varied.
[DOI: 10.1115/1.3112384]

Keywords: circular and rectangular ducts, flow transition and development

1 Introduction and Aim of the Work

Transitional flows either in circular or rectangular ducts are encountered in a variety of industrial applications, and therefore a correct prediction of flow transition is of vital importance, for instance, in flow control either trying to delay or to have an early transition to turbulence. Flow transition in the circular ducts, i.e., pipes, goes back to 1883 when Osborne Reynolds performed his well-known circular pipe flow experiment. He observed that the pipe flow, depending on a dimensionless number later named the Reynolds number, consists of basically two different states, either laminar or turbulent. Reynolds also found that the transition from the laminar to turbulent state sets in intermittently by "flashes" that occur in localized regions when the Reynolds number exceeds a so-called "critical" value. As the Reynolds number increases, the frequency of these "flashes" increases until a state of fully developed turbulence is obtained in the downstream direction of the so-called core region. All these fundamental properties of the pipe flow were later found to represent some common features of wall-bounded shear flows where velocity and temperature gradients and geometry of flows change. However, the detailed process and mechanism involved in the transition of the circular pipe flow are still under progress. Significant international collaboration has been therefore recognized, trying to understand its physics of transition [1–6]. Some more detailed experimental and theoretical progress about the pipe flow transition have been reviewed by Kerswell [7] and given, recently, by Willis et al. [8]. Different scenarios, for instance, the transient growth of disturbances proposed by Trefethen et al. [9] or the so-called self-sustained process (SSP) introduced by Waleffe [10], and recently the nonlinear traveling wave [3,4], may be considered appropriate processes to explain the pipe flow transition. Besides, earlier extensive experiments have been conducted by Wygnanski and Champagne [11] and Wygnanski et al. [12], identifying two types of structures in the transitional pipe flow, which they called puffs and slugs. Figure 1 illustrates some selected samples of the streamwise traces from the hot wire, located at the pipe centerline (see Fig. 2(*a*)), for various inlet flow velocities, showing the laminar, intermittent, and fully turbulent flows. At $x/D=70.2$, for $Re_m \approx 3{,}700$ and 12,300, a laminar behavior was observed and at $x/D=27.3$ as the inlet flow velocity increases the flow transition to turbulent regime occurred passing through an intermittent flow with 0.44% intermittency for $Re_m \approx 27{,}800$. It is worth noting that the transition from the laminar to turbulent regime in the present pipe flow has been carried out naturally, i.e., without triggering the flow at the pipe entrance.

Transition of such kind of flows was found to depend, for instance, on the smoothness of the inlet contraction, triggering the flow at the entrance, the surface roughness of the test section, and therefore on the minimum entrance length (L) required for flow to develop. Hence, the flow usually reaches the fully developed state when all mean flow quantities (i.e., velocity and pressure fields) and all turbulence quantities (i.e., $\overline{u'^2}$, skewness, flatness, spectra, etc.) become invariant with the streamwise location, see Zagarola and Smits [13]. However, a discrepancy through investigations [14–19] concerning criterion on the minimum entrance length needed to assure the state of the fully developed turbulent flow still exists. For example, Nikuradse [14] concluded by comparing the mean-velocity profiles at successive streamwise distances from the pipe inlet that flow was fully developed turbulent between 25D and 40D, where D stands either for the pipe diameter or the channel full height. In a similar way, Laufer [20] claimed a pipe full development length of 30D based on the measured mean-velocity distributions. For axisymmetry disturbances, pipe flow experiments by Sarpkaya [15] yield $x/D=30$ before reaching the fully developed region, and the analysis by Haung and Chen [16,17] predicts $x/D=32$ for the fully developed state. However, for the nonaxisymmetric disturbances, a development length was found by Haung and Chen [16,17] to lie between 40D and 48D and through flow triggering at the pipe entrance using the wall fence type; their critical Reynolds number was 2300. Perry and Abel [18] observed a fully developed state at 71.9D and 86.2D with triggering the flow at the pipe entrance for $Re_m=3\times10^5$. Patel and Head [21] concluded that both the mean and the fluctu-

Contributed by the Fluids Engineering Division of ASME for publication in the JOURNAL OF FLUIDS ENGINEERING. Manuscript received February 27, 2008; final manuscript received February 17, 2009; published online May 14, 2009. Assoc. Editor: Juergen Kompenhans.

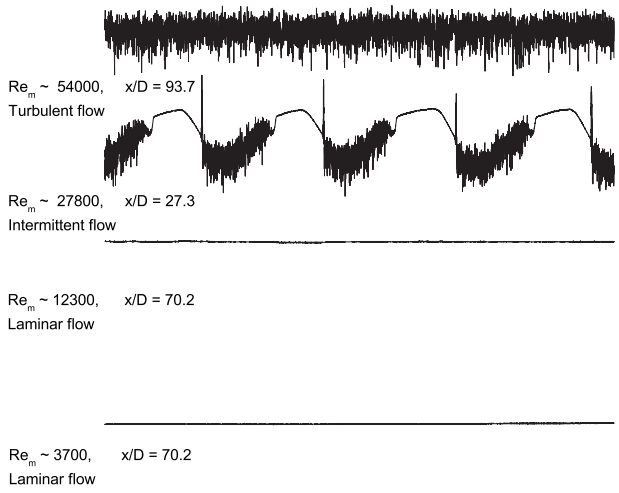

Fig. 1 Some selected samples of the streamwise traces from the hot-wire anemometer, located at the pipe centerline, for various inlet flow velocities and streamwise locations

ating velocity distributions in a turbulent pipe flow indicate a full development state for a downstream distance of $50-80D$. Lien et al. [19] indicated that a minimum channel length of $130D$ is required for flow to become sensibly constant with the streamwise direction. More recently, Doherty et al. [22] noted that the mean-velocity profiles required development length over $x/D \approx 50$ to become invariant; however, a streamwise distance of $x/D \approx 80$ for higher order statistics is needed. Figure 2(*b*) shows a summary of the normalized total pipe length (L/D) from some existing and planned experimental pipe test facilities.

In spite of the above significant efforts, no quite clear entrance length criterion was assumed for the fully developed flow either in the pipe or in the channel flows. However, it becomes common in the fluid mechanics community to exceed the entrance length by large enough x/D to assure the state of full development of the flow. Therefore, aiming at better understanding and developing criteria for flow transition and development in both the pipe and the channel facilities, a comparative study between the two types of flows was carried out. The present experimental studies are therefore carried out with particular attention being given to the centerline measurements for low range of Reynolds numbers, $\mathrm{Re}_m \leq 106 \times 10^3$, and to assure that the selection of the measuring section $L/D=85$ of Zanoun et al. [23] was appropriate and enough far away from the contraction exit to assume fully developed turbulent pipe flow.

The outline of the present paper can be briefly described as follows. Section 2 describes the pipe experimental test facility and the measuring techniques. The data presented in Sec. 3 resulted from both the present pipe experimental measurements and some available channel flow data [24]. Finally, conclusions and final remarks are drawn and suggestions for further work have been reported in Sec. 4.

2 Experimental Apparatus and Measuring Techniques

The Department of Aerodynamics and Fluid Mechanics (LAS) at BTU Cottbus maintains a high quality aeroacoustic test facility for the sake of research and development, see Fig. 3. The aeroacoustic test facility is laid out openly, i.e., free jet without direct feedback, and it is mainly designed for aeroacoustic applications; see Ref. [25] for more details. The facility uses a radial fan to provide air with a maximum velocity of 60 m/s at the nozzle exit with centerline turbulence intensity level less than 0.35%; see Fig. 4. For the sake of carrying out the present work, a pipe test section was added to the test facility in the measuring room as Fig. 3 indicates. The pipe test section was made out of a high-precision smooth acrylic-glass tube that was connected directly to a carefully machined two-cubic arcs exit nozzle, having an aspect ratio of 8. The nozzle was used between the plenum chamber and the pipe test section to assure a smooth and uniform inlet flow in addition to damping further any flow disturbances coming from the plenum chamber. The geometric dimensions of the pipe showed an internal diameter, D, of 32 mm and total length, L, of 6 m, providing total pipe length-to-diameter ratio of $L/D=187.5$. The pipe consisted of various sections connected together by custom-designed couplings. Measurements of the mean-velocity profiles, the bulk flow velocity, the centerline-average-velocity, and the centerline-velocity fluctuations were made at several stations along the pipe section between $x/D=3.9$ and 156. It is worth mentioning that all measurements were carried out without triggering the flow at the pipe inlet, and here is a summary of the different measuring locations

$$x/D = 3.90, 7.81, 11.72, 15.60, 19.53, 23.44, 27.34, 31.25, 35.16, 38.97, 46.78, 54.59, 62.40, 70.20, 78.00, 93.66, 108, 125, 140, 156$$

The pipe flow rate for each investigated case was controlled by changing the rotational speed of a 5.5 kW radial fan via a fre-

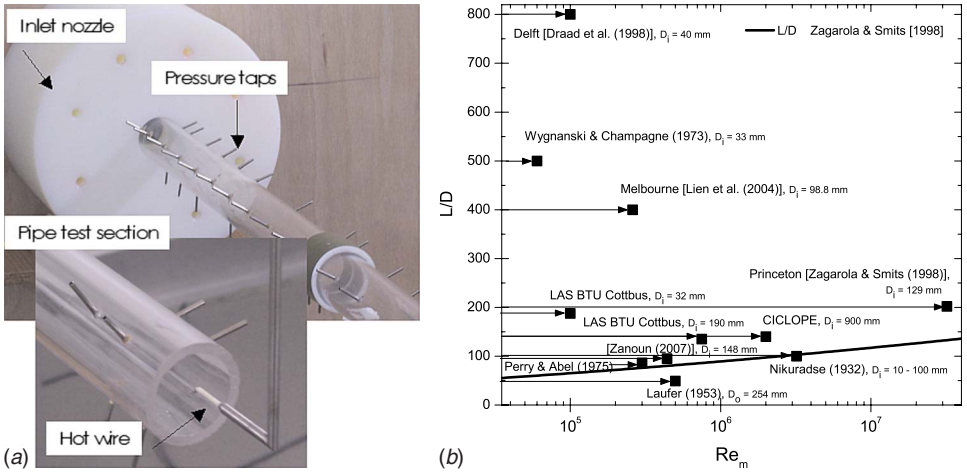

Fig. 2 (*a*) Photograph of the current pipe test section and (*b*) summary of the L/D versus the mean-based Reynolds number, Re_m, from some existing and planned pipe facilities

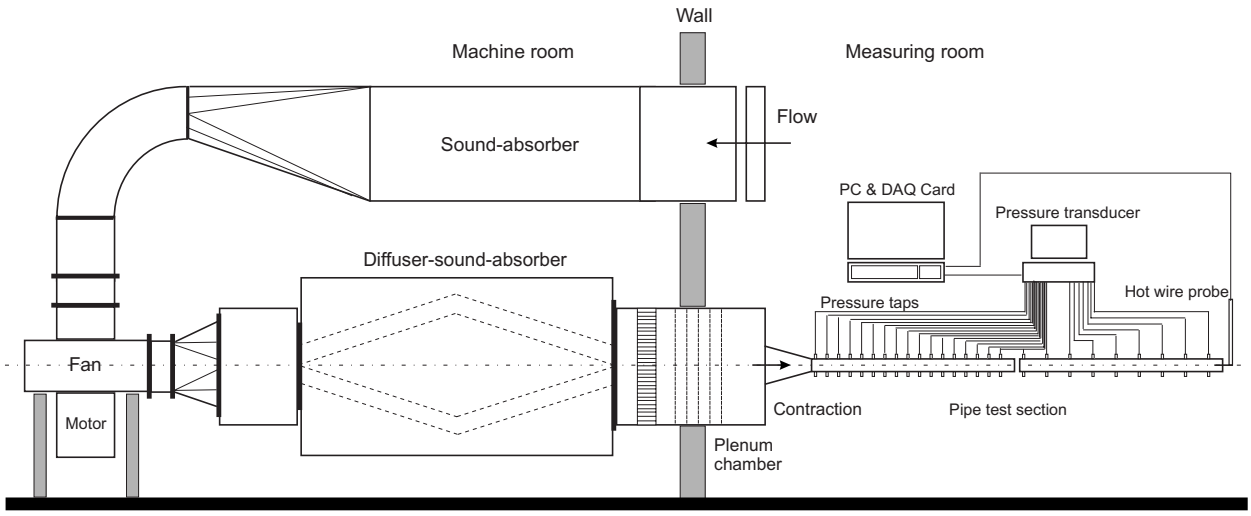

Fig. 3 Schematic of the experimental test facility

quency converter unit. A conventional one-dimensional laser-Doppler anemometry (LDA), FlowLite System Dantec Dynamics GmbH, operating in the dual-beam backscattering mode was used to calibrate the wind tunnel. The bulk flow velocity, $\bar{U}_b$, was measured using the LDA at the contraction exit, where a uniform velocity distribution exists. In addition, it was also obtained by integrating the velocity profile at the measuring location for each Reynolds number to ensure a good assessment of the bulk flow velocity for each case. Good agreement of about $\pm 1\%$ was achieved for the average velocity from both methods and the bulk flow velocity was then used to compute the bulk-velocity based Reynolds number of the flow, $\mathrm{Re}_m = \bar{U}_b D/\nu$. A low range of Reynolds numbers, i.e., $\mathrm{Re}_m \leq 106 \times 10^3$, was set up in this way. Finally, by careful installation of the pipe test section with the plenum chamber and the contraction using the laser alignment, we were able to limit any misalignment in the test facility.

Intensive measurements utilizing the hot-wire anemometer (HWA) at the above mentioned measuring locations have been carried out with particular attention being given to

- the bulk flow velocity ($\bar{U}_b$) and the centerline-average-velocity ($\bar{U}_c$)
- the centerline turbulence statistics up to the fourth moment (i.e., $\overline{u_c'^2}$, skewness, and flatness)
- the mean-velocity distributions, $\bar{U} = f(y)$
- the mean wall pressure gradient ($\mathrm{d}P/\mathrm{d}x$) and therefore the wall skin friction velocity (u_τ)

The detailed velocity measurements were carried out using a Multi-channel constant-temperature anemometer (CTA) system from Dantec Dynamics GmbH. The hot-wire measurements of the local velocity were made utilizing a boundary layer probe equipped with a 5 μm diameter wire (d) and 1.25 mm an active wire length (ℓ), providing an aspect ratio (ℓ/d) of 250. Hence the wire had a sufficiently large aspect ratio to suggest a negligible influence of the prongs on the actual velocity measurement. All calibrations and measurements were performed with an 80% overheat ratio, $a = (R_w - R_a)/R_a$, where R_w is the operational hot-wire resistance and R_a is the resistance of the cold wire, i.e., at ambient air temperature. For the statistical data analysis of the local flow, $5 \times 10^4 - 10^5$ samples were acquired over 60 s at every measuring point.

The local mean static pressure measurements were employed to evaluate the streamwise pressure gradient ($\mathrm{d}P/\mathrm{d}x$), which in turn was used to obtain the wall shear stress (τ_w) and then the wall friction velocity (u_τ) that needed to normalize the mean-velocity data

$$\tau_w = -\frac{R}{2}\frac{\mathrm{d}P}{\mathrm{d}x} \Rightarrow u_\tau = \sqrt{\frac{\tau_w}{\rho}} \tag{1}$$

where R is the pipe radius. At each x-location for the streamwise pressure measurements, three static pressure holes of 500 μm were carefully installed around the circumference of the pipe. Care was taken to ensure that the inner surface of the pipe, where the pressure holes were drilled, was free from remaining drilling defects of the holes (i.e., smoothness was ensured around the pressure tappings). The mean static pressure at each location was then obtained by averaging measurements over the three pressure holes. As a result, the wall skin friction data were computed, independently of the mean-velocity profile measurements. A temperature sensor was used to measure the temperature with high accuracy directly at the pipe exit. The ambient pressure was monitored in the laboratory and reported for each test run using Baratron 626A electronic barometric sensor, MKS Instrument GmbH. Utilizing both the mean pressure measurements and the corresponding air stream temperature in the pipe, the air density (ρ) and the kinematic viscosity (ν) were calculated using the ideal gas relationships and Sutherland's correlation [23].

3 Experimental Results and Discussion

There is no doubt that there are remarkable effects for the pipe or the channel inlet flow conditions, geometrical dimensions, and entrance length on flow development, transition location, and transition Reynolds number. To simplify the problem, we summarized here the most relevant parameters that influence the transition from the laminar to turbulent flow regime either in the pipe or in the channel as follows:

$$(x)_{\mathrm{crit}} = f(\bar{U}_c, u_c', D, \epsilon, \rho, \mu) \tag{2}$$

where f expresses a functional relationship, $(x)_{\mathrm{crit}}$ is the critical entrance length at which transition occurs, $\bar{U}_c$ is the average flow velocity at the pipe or at the channel centerline, u_c' is the centerline turbulence level, D stands either for the pipe or the channel integral length scale, ϵ is the pipe or the channel surface roughness, ρ is the fluid density, and μ is the fluid dynamic viscosity. Equation (2) can be rewritten as follows by carrying out the dimensional analysis:

$$\left(\frac{x}{D}\right)_{\text{crit}} = f\left(\text{Re}_c, \frac{u_c'}{\bar{U}_c}, \frac{\epsilon}{D}\right) \tag{3}$$

stating that the critical entrance length, i.e., transition location, needed for flow transition depends on the entrance Reynolds number (Re_c), the entrance turbulence intensity level ($u_c'/\bar{U}_c$), and the relative surface roughness (ϵ/D). On the other hand, Eq. (3) can be rewritten as follows:

$$(\text{Re}_c)_{\text{crit}} = f\left(\frac{x}{D}, \frac{u_c'}{\bar{U}_c}, \frac{\epsilon}{D}\right) \tag{4}$$

indicating that the transition Reynolds number depends on the dimensionless streamwise distance or the measuring location (x/D), the entrance turbulence intensity level ($u_c'/\bar{U}_c$), and the relative surface roughness (ϵ/D). Even, the critical turbulence intensity level $(u_c'/\bar{U}_c)_{\text{crit}}$ can be represented as a function of Re_c, x/D, and ϵ/D; see, e.g., Figs. 5, 6, 11, and 12. However, the centerline turbulence measurements at different locations have been taken, in the present study, as a transition indicator for the state of flow full development and to specify a value for the transition Reynolds number.

In nature, the pipe or the channel surface roughness does play a role in the flow transition except if the surface is hydraulically smooth. In the present study, we can neither verify nor quantify this influence because we did not change the surface roughness. Therefore, the effect of the roughness was omitted since both the present pipe and the channel of Fischer [24] were hydraulically smooth. In addition, the geometrical dimensions and the contour of the inlet contractions were not subjected to changes during either the current phase of the pipe or the channel experiments [24]. Hence the following relation holds:

$$(\text{Re}_c)_{\text{crit}} = f\left(\frac{x}{D}, \frac{u_c'}{\bar{U}_c}\right) \tag{5}$$

Figure 4 illustrates the pipe inlet turbulence intensity level $(u'/\bar{U} \equiv u_c'/\bar{U}_c)$ versus the bulk-velocity based Reynolds number (Re_m), which is equivalent to the centerline-velocity based Reynolds number (Re_c) at the contraction exit, where the velocity profile is uniform. It is natural to assume that finite and even small amplitude perturbations at the pipe or at the channel inlet sections are needed for triggering turbulence; however, these perturbations might become of less importance as the Reynolds number increases; see Fig. 4. At higher input velocities, i.e., high Reynolds numbers, the flow is less stable and therefore any small disturbances at the entrance grow fast due to the higher rate of energy production, leading to flow transition. The perturbations at the contraction exit were observed to inversely proportional to the Reynolds number, i.e., $u_c'/\bar{U}_c \propto \text{Re}_m^{-1}$, as the figure clearly illustrates. This turned out to be in good agreement with the scaling law proposed by Hof et al. [26], indicating that the amplitude of perturbation required to cause transition scales as $O(\text{Re}^{-1})$. Grossman [27] indicated also that the onset of turbulence has a double threshold: Both the initial disturbance, measured either by its energy or its amplitude, and the Reynolds number have to be large enough, i.e., the disturbance needed is the smaller the larger the Reynolds number already is and vice versa in agreement with Fig. 4.

From previous investigations we might conclude that the type, the magnitude, and the frequency of the perturbations at the pipe entrance play important roles to characterize the laminar-to-turbulent flow transition. However, in various experiments in which the perturbations of the laminar flow could be, carefully, avoided or considerably reduced, the onset of turbulence can be delayed to high Reynolds numbers. For instance, Reynolds in 1883 concluded from his pipe flow experiment that the transition from the laminar to turbulent flow forms takes place at about the same Reynolds number, i.e., $(\text{Re}_m)_{\text{crit}}=2300$. However, he observed that at low level of perturbations, the transition Reynolds number could be much larger than the most accepted critical value, i.e., $(\text{Re}_m)_{\text{crit}}=2300$. Investigations by Schiller [28], for instance, have shown laminar behavior at $\text{Re}_m=2\times10^4$. In addition, a recent work by Draad et al. [1] indicated a natural transition at locations between $x/D=788,75$ and 807,75 for $\text{Re}_m=6\times10^4$, and their setup was able to sustain a fully developed parabolic pipe flow for Reynolds number up to 14,300. A laminar pipe flow was also observed even at more higher Reynolds number, i.e., $\text{Re}_m=10^5$ [29]. Hence, we might conclude that specifying a numerical value for the transition Reynolds number depends on the boundary conditions of each individual test facility.

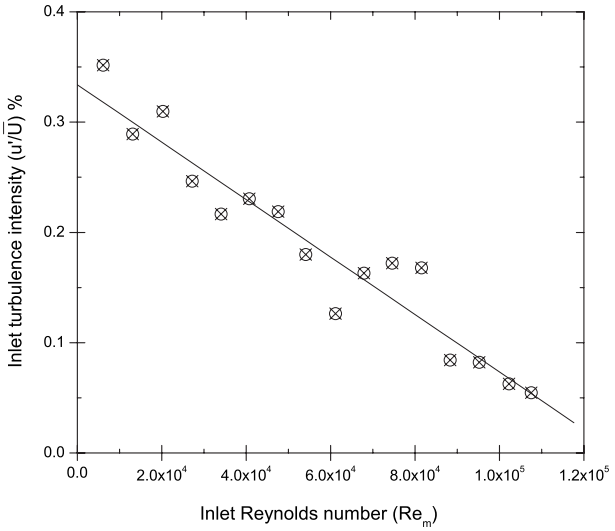

Fig. 4 The turbulence intensity level ($u'/\bar{U}$) versus the bulk-velocity based Reynolds number (Re_m) at the contraction exit without triggering the flow

Therefore, in addition to the input flow velocity, some other important factors that influence flow transition to turbulence either in the pipe or in the channel flows can be resummarized as follows:

- the level, type, and frequency of disturbances of the inlet flow
- the smoothness, geometry of the entrance, and the wall roughness
- the entrance length, and the alignment of the test section
- the pressure distribution of the internal flow

Now, an important question arises: Is it difficult to have a precise estimation for the transition Reynolds number and consequently a definition for the term fully developed flow? In the past, three different criteria have been used [21] to characterize the fully developed turbulence in pipes or channels:

1. Having a well established relationship between the wall skin friction and the Reynolds number, for instance, obeying the 1/4 power friction relation $\lambda=0.3164\ \text{Re}_m^{0.25}$ of Blasius [30].
2. For Reynolds number much higher than the transition Reynolds number, the measured mean-velocity profiles scaled with the inner wall variables (i.e., the viscous length scale $(\ell_c=\nu/u_\tau)$ and the wall friction velocity $(u_c=u_\tau=\sqrt{\tau_w/\rho})$) collapse and agree well with the well-known logarithmic law of the wall, i.e., $\bar{U}/u_\tau=1/\kappa\ln(yu_\tau/\nu)+B$, showing Reynolds number independence of the mean-velocity data, where κ and B are believed to be universal constants [31].
3. A continuously turbulent flow exists or, in other words, the intermittency factor is equal to 1 [24]. The authors of the

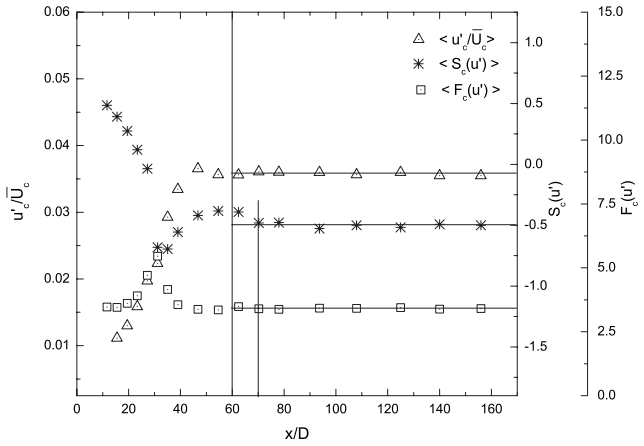

Fig. 5 The present pipe centerline turbulence statistics ($u_c'/\bar{U}_c$, $S_c(u')$, and $F_c(u')$) versus x/D for $3\times10^4 \le \mathrm{Re}_c \le 8\times10^4$ ($2.63\times10^4 \le \mathrm{Re}_m \le 7\times10^4$) and 0% tripping

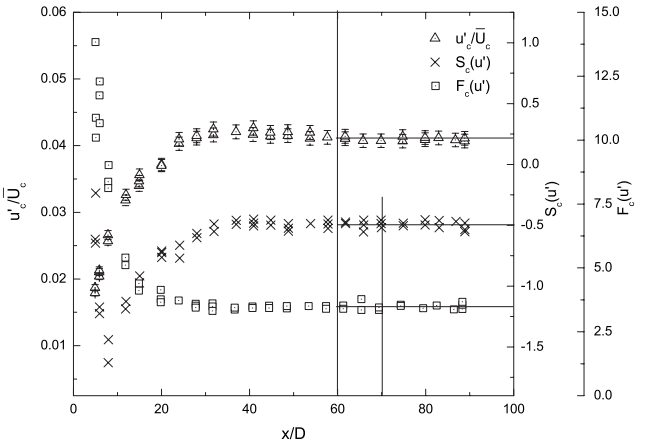

Fig. 6 The channel centerline turbulence statistics ($u_c'/\bar{U}_c$, $S_c(u')$, and $F_c(u')$) versus x/D for $\mathrm{Re}_m=10^4$ and 20% tripping [24]

present paper use rather the centerline statistics as representative of the turbulent motion to show that the flow is Reynolds number independent or does not depend further on the streamwise coordinate, x. The authors believe that reaching the constant behavior of the turbulence statistics at the pipe or at the channel centerline (i.e., the last station of turbulence across the pipe or the channel cross sectional area) is enough to state that flow is fully turbulent and intermittency disappears.

Hence, to provide an answer for the above question, the time-averaged properties of a turbulent flow are to be described by their statistical moments $\overline{M^n}$, and consequently a spatially fully developed turbulent flow is assumed if all statistical moments of the flow show invariant behavior under translation, i.e.,

$$\frac{\partial \overline{M^n}}{\partial x} = 0, \quad \forall\, x_1 > x_{1,v} \tag{6}$$

where $x_{1,v}$ can be determined experimentally by conducting intensive turbulence measurements through the flow field along the streamwise direction. The above equation represents, therefore, a good criterion to fulfill the assumption of the full development state of the flow either in the pipe or in the channel by carrying out intensive centerline measurements at different x-wise positions. This approach turns out to be in close agreement with the criteria introduced by Patel and Head [21], and recently by Zagarola and Smits [13].

In the current phase of the experimental study, the HWA and the LDA have been utilized for evaluating, quantitatively, the mean flow characteristics and the turbulence statistics in both the pipe and the channel facilities. A precise location of the hot wire at the pipe centerline was of vital importance, and therefore great care was taken to ensure a correct positioning of the wire. Hence, a calibration positioning procedure proposed by Bhatia et al. [32] and Durst et al. [33] was applied to position the wire. Without triggering the flow at the pipe entrance, i.e., turbulence was developed naturally, efforts have been therefore concentrated to provide an answer for the following question: How does the inlet flow conditions and the measuring locations influence the transition from the laminar to turbulent flow regime?

Flow transition to turbulence through the pipe was detected via the centerline measurements in a similar way to the channel flow data of Fischer [24]. The available channel flow data [24], with and without triggering the flow at the channel inlet section, were utilized to perform the comparative study versus the present pipe results. A summary of the centerline measurements (i.e., $(u_c'/\bar{U}_c)$, $S_c(u')$, and $F_c(u')$) in both the pipe and the channel test sections for different streamwise distances, x/D, is presented in Figs. 5 and 6. Figure 5 indicates that a pipe fully developed turbulent flow could be achieved for a transition length $x/D \ge 60$ and high enough Reynolds number (i.e., $\mathrm{Re}_m \ge 2.63\times10^4$), supporting Patel and Head's [21] conclusion, and turned out to be in good agreement with Zagarola and Smits [13]. Similar channel centerline measurements by 20% tripping have been carried out [24] at different x/D from the channel input, and data are presented in Fig. 6 for $\mathrm{Re}_m=10^4$. Both figures, i.e., Figs. 5 and 6, clearly show independence of the streamwise turbulence characteristics on a streamwise distance of $x/D \ge 60$ either for the circular pipe or the rectangular channel facilities. A constant behavior for both the centerline skewness $S_c(u')$ and flatness $F_c(u')$ factors was also observed; however, for a relatively long entrance length $x/D \ge 70$, i.e., $S_c(u')=-0.51$ and $F_c(u')=3.5$, which are very close to values for isotropic and homogeneous turbulence [34]. As a result, for $x/D \ge 70$, it might be concluded that there is no systematic dependence of the flow properties on the streamwise distance anymore, and therefore the state of full development of the flow was achieved.

Based on a conclusion deduced from Fig. 6, Fischer [24] carried out, for various tripping ratios and Reynolds numbers, all his channel measurements at a fixed station $x/D=80$ from the channel input that assured no dependence on the streamwise distance (x/D). On the other hand, the pipe flow measurements were carried out at different measuring locations and for various input velocities without triggering the flow. Figures 7 and 8 present the mean flow results in both the pipe for $x/D \ge 54.6$ and the channel at $x/D=80$, showing the ratio of the centerline-average-velocity to the bulk flow velocity versus the centerline-average-velocity and the bulk-velocity based Reynolds numbers. Figure 7 clearly shows almost a constant behavior of $\bar{U}_c/\bar{U}_b$ for long enough pipe test section, $x/D \ge 54.6$, and for high enough Reynolds number, $\mathrm{Re}_c \ge 3\times10^4$ ($\mathrm{Re}_m \ge 2.63\times10^4$). A similar behavior can be observed in Fig. 8; however, with slight and monotonic decrease in the ratio $\bar{U}_c/\bar{U}_b$ versus the Reynolds number for $\mathrm{Re}_c \ge 3\times10^3$ ($\mathrm{Re}_m \ge 2.46\times10^3$), reaching an asymptotic behavior for $\mathrm{Re}_c \ge 10^4$ ($\mathrm{Re}_m \ge 8.2\times10^3$).

Figures 9 and 10 present selected samples from the results in both the pipe and the channel flows for $x/D \ge 62.4$ and $x/D=80$, respectively, showing the inner scaling of the mean-velocity profiles for different Reynolds numbers. Figure 9 clearly shows that the mean-velocity distribution over the cross section of the pipe collapsed into a single curve for high enough Reynolds number

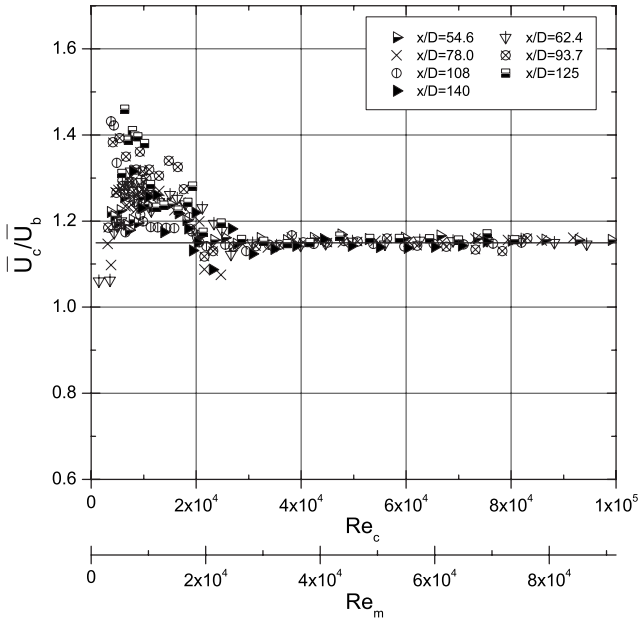

Fig. 7 The ratio of the centerline-average-velocity ($\bar{U}_c$) to the bulk flow velocity ($\bar{U}_b$) versus the centerline-average-velocity and/or the bulk-velocity based Reynolds numbers in the pipe flow for various measuring locations (x/D)

$Re_m \geq 4\times10^4$ ($R^+ \geq 1040$), and long enough entrance length $x/D \geq 62.4$ when the mean-velocity data are scaled with the wall friction flow velocity, u_τ, and the wall distance scaled with the viscous length scale, $l_c = \nu/u_\tau$. Both figures illustrate clearly that there is a too short or even no real log region since the current experiments have simply too low Reynolds numbers to show a real logarithmic character of the so-called overlap region [35]. In spite of that fact, a satisfactory agreement for the normalized mean-velocity distribution with the logarithmic line, $U^+ = 1/\kappa \ln(y^+) + B$, proposed by Perry et al. [36] with $\kappa = 0.39$ and $B = 4.42$, Nagib et al. [37,38] ($\kappa = 0.384$ and $B = 4.127$), and Zanoun et al. [23] ($\kappa = 0.384$ and $B = 4.43$), might be observed in Fig. 9. The mean-velocity data of Fischer [24] obtained using the LDA were presented in Fig. 10, showing poor agreement with the channel logarithmic line, proposed by Zanoun et al. [31] with $\kappa = 0.37$ and $B = 3.7$. On the other hand, a satisfactory agreement might be obtained for Fischer's higher Reynolds number data [24] (i.e., $R^+ \approx 481$) with the logarithmic line when higher values for both constants, i.e., $\kappa = 0.41$ and $B = 5.5$, are used; see also Fig. 4.12 in Ref. [24] for more details. Therefore, it appears from Fig. 10 that Fischer's mean-velocity data [24] did not support the accepted logarithmic velocity profile because of its low range of the Reynolds number. A displacement effect, i.e., velocity overshoot, can be also observed in Figs. 9 and 10 in the region where $y^+ \leq 150$, resulting in deviation from the logarithmic velocity profile that might be interpreted also as a result of the low Reynolds number effect. On the other hand, this bump, i.e., velocity overshoot, in the mean-velocity profile for $10 \leq y^+ \leq 150$ can be interpreted as a local power law similar to the one found by McKeon et al. [35].

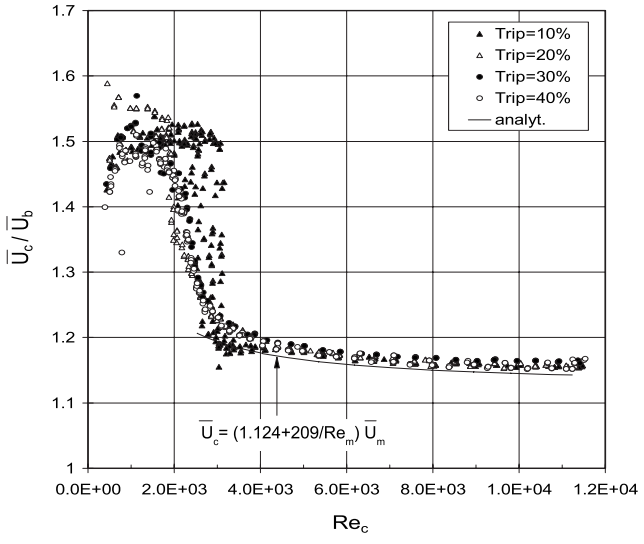

Fig. 8 The ratio of the centerline-average-velocity ($\bar{U}_c$) to the bulk flow velocity ($\bar{U}_b$) versus the centerline-average-velocity based Reynolds number in the channel flow for various tripping ratios [24]

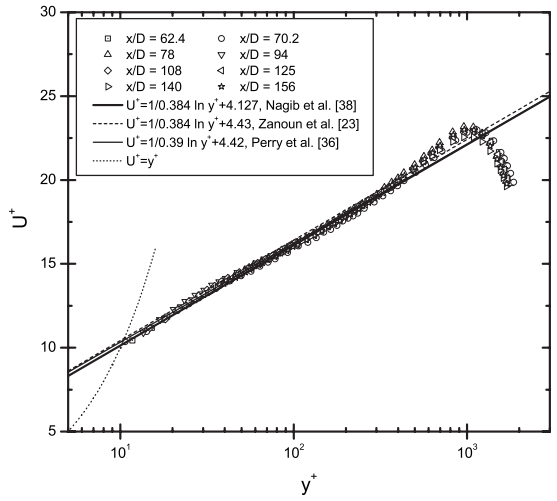

Fig. 9 The inner scaling of the present pipe mean-velocity profiles for $1040 \leq R^+ \leq 1140$

Let us now apply the centerline turbulence intensity as a transition indicator or an argument for the state of flow full development. The pipe centerline-velocity fluctuations were measured for various Reynolds numbers, $Re_c \leq 1.2\times10^5$ ($Re_m \leq 106\times10^3$), and entrance lengths, $3.9 \leq x/D \leq 156$, and the results are presented in Fig. 11. It is worth noting again that the present pipe centerline measurements were carried out using the HWA without triggering the flow at the pipe entrance, looking for the transition Reynolds number and flow development as a function of the measuring location and the input flow velocity. The pipe centerline results are then compared with the channel centerline-velocity fluctuations [24] presented in Fig. 12 for $Re_c \leq 1.2\times10^4$ ($Re_m \leq 10^4$). In Figs. 11 and 12, the centerline-velocity fluctuations were scaled with the centerline-average-velocity and presented versus the centerline-average-velocity and/or the bulk-velocity based Reynolds numbers for the pipe and the channel flows, respectively. For the low range of the pipe Reynolds number, i.e., $Re_c \leq 2\times10^4$ ($Re_m \leq 1.76\times10^4$), flow disturbances were not growing fast enough, and therefore flow remained laminar. However, for $Re_c \geq 30\times10^3$ ($Re_m \geq 26.3\times10^3$), flow disturbances grow fast due to the higher growing rate of energy production, resulting in transition to turbulent regime. The channel measurements [24] were carried out at a fixed streamwise distance $x/D = 80$, utilizing the LDA, aiming at investigating the effect of tripping the flow on the transition Reynolds number. The tripping device, i.e., an inlet fence, used by Fischer [24] was mounted at the channel entrance, i.e., $x=0$, with height ratios of $2\delta/D$

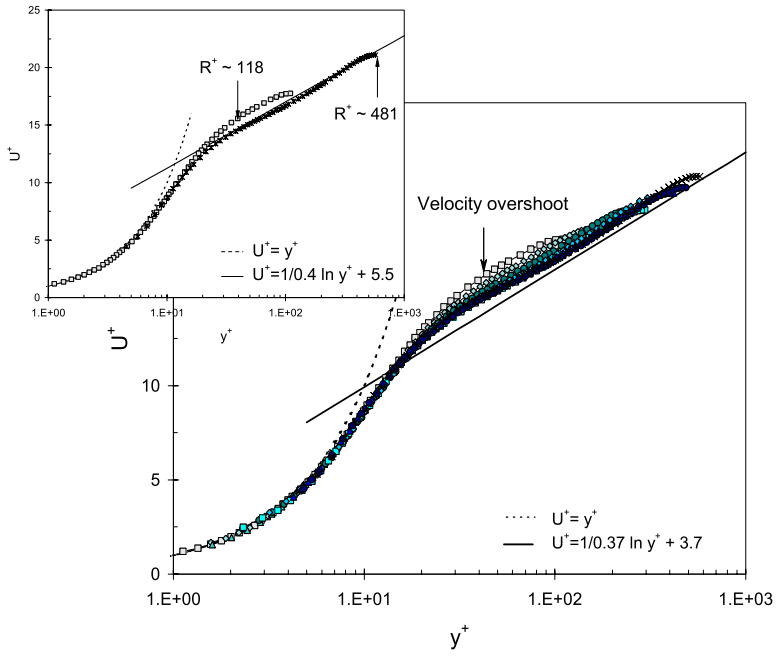

Fig. 10 The inner scaling of the channel mean-velocity profiles for 118 $\leq R^+ \leq$ 481 [24]

$=0\%, 10\%, 20\%, 30\%, 40\%$ to trigger the flow over the lower and upper walls of the channel test section. The channel results presented in Fig. 12 were obtained for 0% tripping and for a tripping device with height of $2\delta=(1/10)D$, i.e., 10% of the channel full height. For $\mathrm{Re}_c \leq 2.4\times10^3$ ($\mathrm{Re}_m \leq 2\times10^3$), Fischer [2] noticed that the laminar behavior with $2\delta/D \leq 10\%$ tripping stay unaffected, meaning that disturbances were not strong enough to grow in the downstream direction for this range of Reynolds number. On the other hand, for high enough channel Reynolds number, i.e., $\mathrm{Re}_c \geq 10^4$ ($\mathrm{Re}_m \geq 8.2\times10^3$), the channel flow was fully turbulent either with or without tripping the flow. In spite of the fact that the Reynolds number range in the current pipe and the channel [24] is different, Figs. 11 and 12 show almost the same general characteristics. A similar behavior to the channel flow was observed for the pipe flow, however, along different ranges of the Reynolds number. When the Reynolds numbers are less than the critical values, i.e., $\mathrm{Re}_c \leq 17.5\times10^3$ ($\mathrm{Re}_m \leq 15.5\times10^3$) and $\mathrm{Re}_c \leq 2.4\times10^3$ ($\mathrm{Re}_m \leq 2\times10^3$) in the pipe and in the channel, respectively, all the initial conditions are attracted to the laminar state, which is the global attractor for both systems. However, if the Reynolds numbers are higher than the above critical values, nearly all the initial conditions give rise to turbulence and the laminar state becomes a local attractor. These arguments are consistent both with Reynolds' original observations [39] and the recent experimental results of Draad et al. [1].

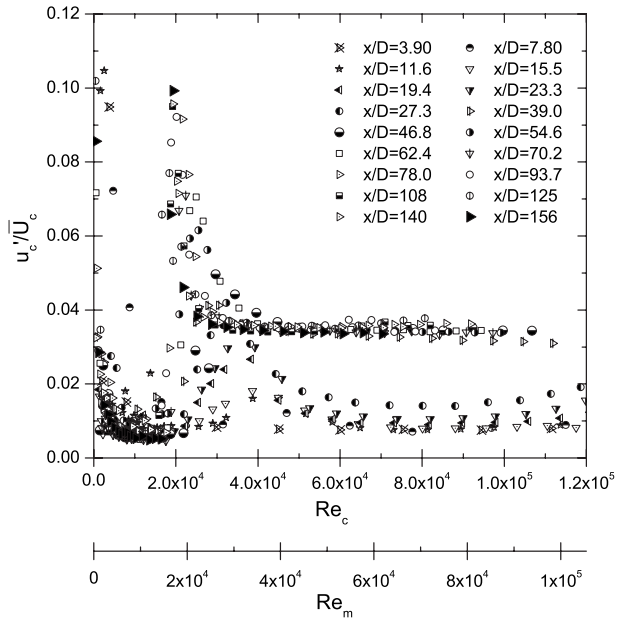

Fig. 11 The present pipe normalized centerline-velocity fluctuations ($u_c'/\bar{U}_c$) for various x/D versus the centerline-average-velocity and/or the bulk-velocity based Reynolds numbers

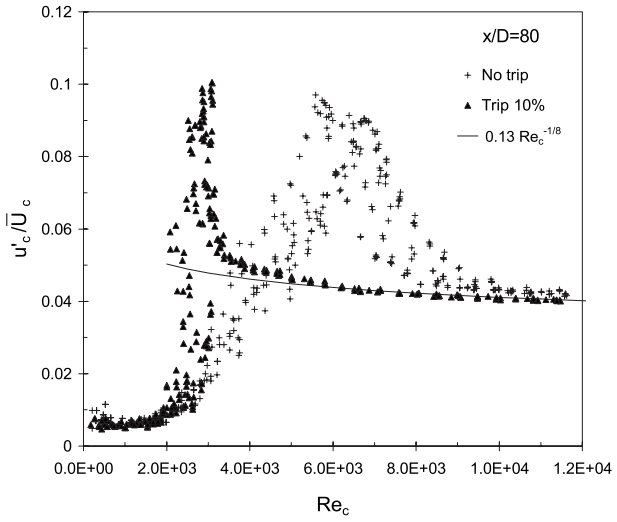

Fig. 12 The channel normalized centerline-velocity fluctuations ($u_c'/\bar{U}_c$) for 0% and 10% tripping versus the centerline-average-velocity based Reynolds number [24]

For the measuring locations at $x/D \leq 27.3$, a wide range of the transition Reynolds number was observed, i.e., $\mathrm{Re}_c \approx 17.5 \times 10^3 - 60 \times 10^3$ ($\mathrm{Re}_m \approx 15.5 \times 10^3 - 53 \times 10^3$), with lower turbulence intensity level, $u_c'/\bar{U}_c \leq 2\%$. However, for the measuring locations at $x/D \geq 39$, a narrow range of the transition Reynolds number, i.e., $\mathrm{Re}_c \approx 17.5 \times 10^3 - 45 \times 10^3$ ($\mathrm{Re}_m \approx 15.5 \times 10^3 - 39 \times 10^3$), took place. In other words, for a narrow range of inlet flow velocities, the pipe flow experiments showed that a longer streamwise entrance, i.e., $x/D \geq 39$, is needed to achieve the turbulent flow regime. On the other hand, a shorter pipe entrance, i.e., $x/D \leq 27.3$, might be used, however, with higher input flow velocity or higher Reynolds number, i.e., $\mathrm{Re}_c \geq 6 \times 10^4$ ($\mathrm{Re}_m \geq 53 \times 10^3$) to reach turbulent flow at earlier measuring position. This came in good agreement with the observation mad by Zagarola and Smits [13], indicating that at high Reynolds numbers the transition length is considerably smaller. After assuring the fully turbulent regime, the turbulent fluctuations, $u_c'/\bar{U}_c$, at the pipe or at the channel centerlines were observed to monotonically decrease, however, slightly with increasing the Reynolds number for $x/D \geq 39$ (see Fig. 11) or for high enough disturbances, i.e., $2\delta/D \geq 10\%$ tripping the flow (see Fig. 12). In case of not tripping the flow at the channel entrance, a wide range of the transition Reynolds number $\mathrm{Re}_c \approx 2 \times 10^3 - 2 \times 10^4$ ($\mathrm{Re}_c \approx 1.6 \times 10^3 - 8.2 \times 10^3$) existed as can be seen in Fig. 12. On the contrary, all the channel flow measurements collapsed into a single curve and a narrow range of the transition Reynolds number was obtained, $\mathrm{Re}_c \approx 2 \times 10^3 - 3.5 \times 10^3$ ($\mathrm{Re}_c \approx 1.6 \times 10^3 - 2.8 \times 10^3$), with 10% tripping, and therefore an earlier transition to turbulent flow regime was observed at $\mathrm{Re}_c \approx 3.5 \times 10^3$. For the pipe measurements at $x/D = 78$, which is almost equivalent to Fischer's channel measuring location $x/D = 80$ [24], and under the natural transition condition, the pipe transition Reynolds number was found to be $\mathrm{Re}_c \approx 28.8 \times 10^3$ ($\mathrm{Re}_m \approx 25 \times 10^3$), which is almost three times the transition Reynolds number in the channel flow $\mathrm{Re}_c \approx 10^4$ ($\mathrm{Re}_m \approx 8.2 \times 10^3$). One can observe also from Figs. 11 and 12 that the maximum turbulence intensity level is around 10% that took place at $\mathrm{Re}_c \approx 2 \times 10^4$ ($\mathrm{Re}_m \approx 17.5 \times 10^3$) in the pipe, however, for the channel flow under the natural transition occurred at $\mathrm{Re}_c \approx 6 \times 10^3$ ($\mathrm{Re}_m \approx 4.9 \times 10^3$) and at $\mathrm{Re}_c \approx 3 \times 10^3$ ($\mathrm{Re}_m \approx 2.4 \times 10^3$) with 10% tripping.

The centerline-velocity fluctuations, $u_c'^2$, are also presented versus the centerline-average-velocity and/or the bulk-velocity based Reynolds numbers in Figs. 13 and 14 for the pipe and the channel flows, respectively. In the pipe flow (Fig. 13), depending on the measuring location (x/D), a transition Reynolds number (Re_c) between 17.5×10^3 and 60×10^3 ($\mathrm{Re}_m \approx 15.5 \times 10^3 - 53 \times 10^3$) was observed. An earlier transition for $\mathrm{Re}_c \approx 25 \times 10^3$ ($\mathrm{Re}_m \approx 22 \times 10^3$) was obtained at larger downstream distance $x/D = 156$, in comparison to $\mathrm{Re}_c \approx 45 \times 10^3$ ($\mathrm{Re}_m \approx 39 \times 10^3$) for the shorter downstream distance $x/D = 46.8$. One could speculate that at higher input velocities, i.e., at high Reynolds numbers, the flow is more less stable and therefore disturbances are growing fast enough along a short pipe entrance due to the high rate of energy production, resulting in earlier transition to the turbulent regime. At higher Reynolds number, Zagarola and Smits [13] indicated also that the transition length is considerably smaller. On the other hand, for lower values of the inlet flow velocities, a further distant measuring location, i.e., an extended wall distance to amplify disturbances in the downstream direction, leading to transition to the turbulent flow is expected. Nishi et al. [40] obtained a pipe natural laminar-to-turbulent transition at $x/D = 533.3$ for $\mathrm{Re}_m = 11.5 \times 10^3$, utilizing Durst and Ünsal's [41] pipe facility, who had a slightly higher value $\mathrm{Re}_m = 13 \times 10^3$ for a natural transition. Nishi et al. [40] showed in their paper, Fig. 14, that a strong dependence of the laminar-to-turbulent transition on the measuring position exists, i.e., shorter pipe entrance $x/D = 260$ can achieve the laminar-to-turbulent transition if the time interval between disturbances at the pipe entrance is too small, i.e., applying inlet disturbances with higher frequency. On the other hand, if the time interval is large, a more distant measuring station is needed to achieve the transition to turbulence, similar to the effect of tripping the flow at the channel entrance as can be clearly observed in Fig. 14. For instance, earlier transition to turbulent flow in the channel at $\mathrm{Re}_c \approx 2400$ ($\mathrm{Re}_m \approx 2000$) took place if the tripping ratio is increased from 10% to 20%.

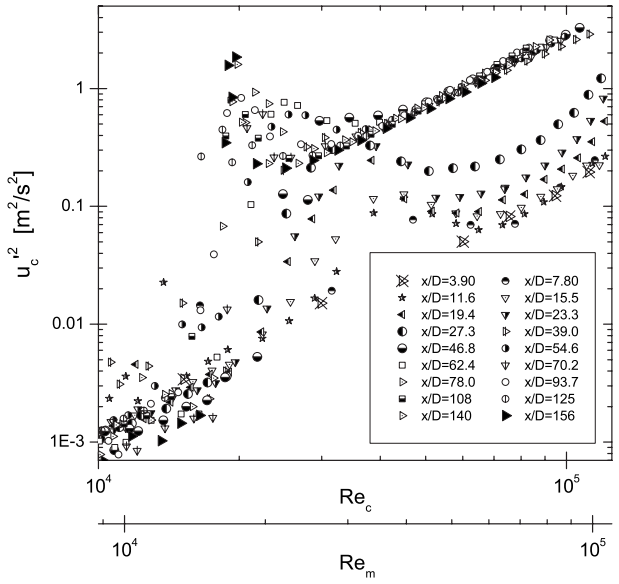

Fig. 13 The present pipe centerline-velocity fluctuations ($u_c'^2$) for various x/D versus the centerline-average-velocity and/or the bulk-velocity based Reynolds numbers

The outcome from Figs. 11–14 in both the pipe and the channel flows could be also obtained by looking at the higher order statistics, i.e., the third and the fourth moments, of the centerline measurements presented in Figs. 15–18. Conclusions extracted from Figs. 15–18 support the transition Reynolds numbers derived from Figs. 11–14 either for the pipe or the channel flows. Figures 15 and 17 clearly show independence of the streamwise turbulence higher order statistics (i.e., the skewness and the flatness), respec-

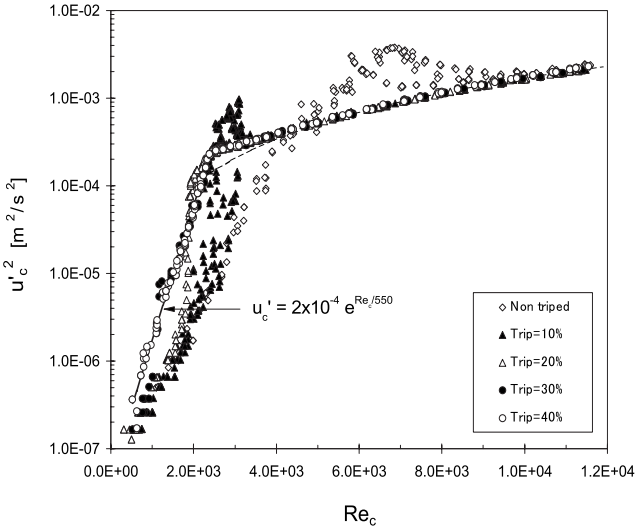

Fig. 14 The channel centerline-velocity fluctuations ($u_c'^2$) for different tripping ratios versus the centerline-average-velocity based Reynolds number [24]

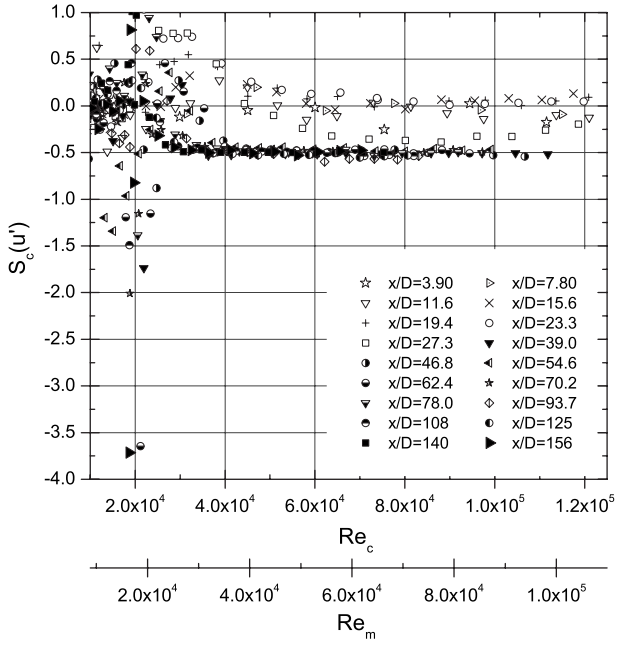

Fig. 15 The present pipe centerline skewness factor for various *x/D* versus the centerline-average-velocity and/or the bulk-velocity based Reynolds numbers

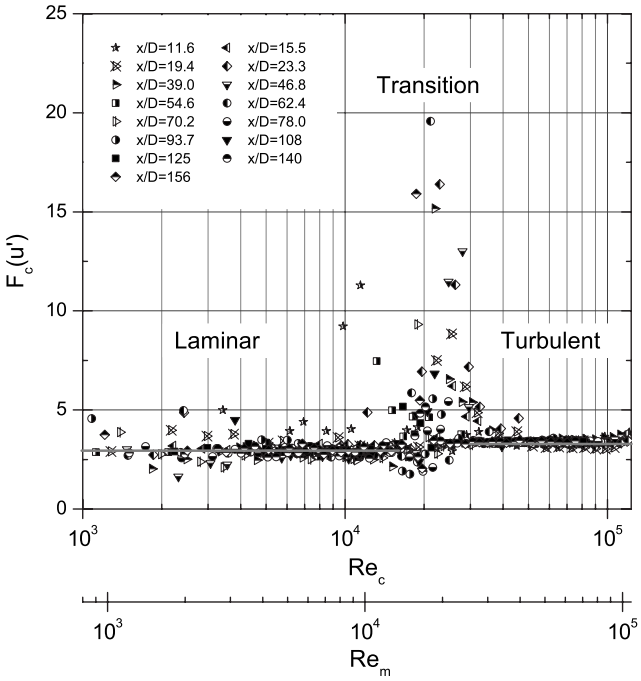

Fig. 17 The present pipe centerline flatness factor for various *x/D* versus the centerline-average-velocity and/or the bulk-velocity based Reynolds numbers

tively, on a streamwise distance of $x/D \geq 39$ for $\mathrm{Re}_c \sim 36 \times 10^3$ ($\mathrm{Re}_m \sim 3 \times 10^4$) in the circular pipe facility. However, the rectangular channel measurements of Fischer [24] have been carried out at a fixed measuring location $x/D=80$, selected based on a conclusion derived from Fig. 6. Figures 16 and 18 show also independent behaviors of both the channel streamwise skewness and flatness factors for $\mathrm{Re}_c > 3500$ and 10% tripping. A constant behavior for both the centerline skewness $S_c(u')$ (Figs. 15 and 16) and flatness $F_c(u')$ (Figs. 17 and 18) factors was observed, i.e., $S_c(u') \approx -0.51$ and $F_c(u') \approx 3.5$, which are very close to values for isotropic and homogeneous turbulence [34]. As a result, for a pipe streamwise distance $x/D \geq 40$ and high enough Reynolds number $\mathrm{Re}_c \geq 45 \times 10^3$ ($\mathrm{Re}_m \geq 39 \times 10^3$), it might be concluded that there is no systematic dependence of the pipe flow properties on the x-wise position, and therefore the state of flow full development was achieved.

4 Conclusions

By setting up a small pipe test facility at LAS, BTU Cottbus, we were able to predict the transition Reynolds number for various flow development lengths and inlet flow velocities. A comparative study of the current pipe results versus some available channel data [24] is presented, reflecting effects of flow geometry, entrance flow conditions, and measuring location on the transition Reynolds number. Hence, to well define a criterion for the flow

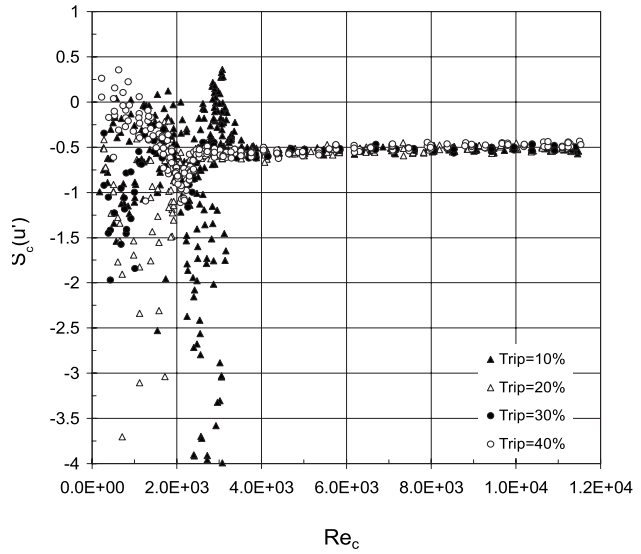

Fig. 16 The channel centerline skewness factor for different tripping ratios versus the centerline-average-velocity based Reynolds number [24]

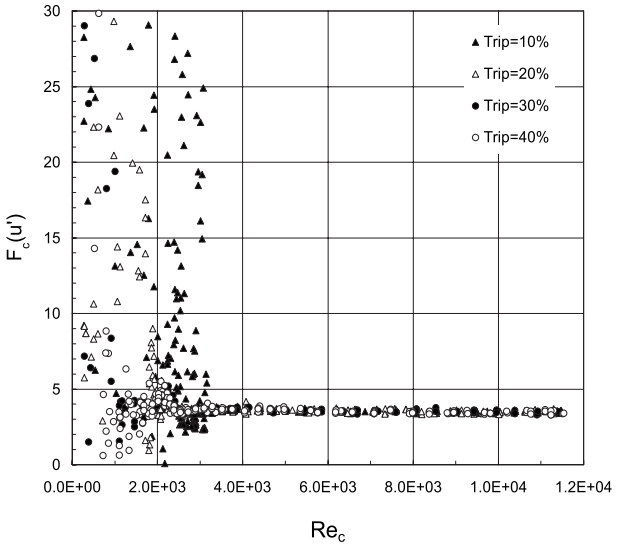

Fig. 18 The channel centerline flatness factor for different tripping ratios versus the centerline-average-velocity based Reynolds number [24]

transition and the state of flow turbulence, the effects of factors such as the entrance length/measuring location (x/D), and the inlet flow conditions, e.g., $\bar{U}_b$ or Re_m, have been taken into consideration, resulting in the following conclusions.

- Without triggering the flow at the pipe entrance, the transition Reynolds number was found to depend on the measuring location, e.g., the natural transition was found to take place for $(\mathrm{Re}_c)_{\mathrm{crit}} \approx 45 \times 10^3$ $[(\mathrm{Re}_m)_{\mathrm{crit}} \approx 39 \times 10^3]$ and $(\mathrm{Re}_c)_{\mathrm{crit}} \approx 25 \times 10^3$ $[(\mathrm{Re}_m)_{\mathrm{crit}} \approx 22 \times 10^3]$ at measuring locations $x/D=46.8$ and 156, respectively. On the other hand, for the channel flow measurements at $x/D=80$, the transition Reynolds number was found to depend on the state of flow at the channel inlet test section, e.g., $(\mathrm{Re}_c)_{\mathrm{crit}} \approx 10^4$ $[(\mathrm{Re}_m)_{\mathrm{crit}} \approx 8.2 \times 10^3]$ for the natural laminar-to-turbulent transition, and $(\mathrm{Re}_c)_{\mathrm{crit}} = 2.4 \times 10^3$ $[(\mathrm{Re}_m)_{\mathrm{crit}} \approx 2 \times 10^3]$ for 20% tripping the flow at the channel entrance.
- A laminar behavior was maintained in the present pipe facility up to $\mathrm{Re}_c \approx 17.5 \times 10^3$ ($\mathrm{Re}_m \approx 15.5 \times 10^3$). In addition, a fully developed turbulent pipe flow was achieved at $x/D \geq 60$ for high enough Reynolds number, $\mathrm{Re}_c \geq 45 \times 10^3$ ($\mathrm{Re}_m \approx 39 \times 10^3$), in close agreement with both Patel and Head [21] and Zagarola and Smits [13].
- Based on the channel flow data, it might be concluded that by triggering the flow at the pipe inlet section, the inlet turbulence intensity level will play an important role for flow transition.

In closing, the transition process to turbulence as well as defining a criterion by which the state of the turbulent flow to be specified in the pipe flow are quite complex, and therefore further research on the subject is still needed. For instance, detailed measurements of the velocity and the pressure fields in the entry section of the pipe is needed, taking effects such as alignment of the pipe, smoothness, and geometry of the contraction, as well as the surface roughness of the pipe test section, into consideration. In addition, detailed measurements of the transitional flow using the particle image velocimetry (PIV) are to be performed. This might clarify what causes the reduction in the natural transition Reynolds number with longer entrance pipe test sections.

Acknowledgment

The authors gratefully acknowledge fund received from the Department of Aerodynamics and Fluid Mechanics, BTU Cottbus to carry out the work. Thanks are also due to Professor Franz Durst for his valuable comments on a draft of the manuscript and to Dr.-Ing. Martin Fischer (LSTM-Erlangen) for providing us his channel data. The authors would also like to acknowledge Professor Dr.-Ing. Ennes Sarradj (BTU Cottbus) for allowing us to utilize the aeroacoustic test facility.

References

[1] Draad, A. A., Kuiken, G. D. C., and Nieuwstadt, F. T. M., 1998, "Laminar-Turbulent Transition in Pipe Flow for Newtonian and Non-Newtonian Fluids," J. Fluid Mech., **377**, pp. 267–312.
[2] Monin, A. S., and Yaglom, A. M., 1999, *Statistical Fluid Mechanics: The Mechanics of Turbulence*, Center for Turbulence Research-CTR Monograph Vol. I, English edition, revised, and augmented by A. M. Yaglom, Chap. 4, Stanford University, Stanford/NASA Ames Research Center, Moffett Field, CA.
[3] Faisst, H., and Eckhardt, B., 2003, "Traveling Waves in Pipe Flow," Phys. Rev. Lett., **91**, p. 224502.
[4] Wedin, H., and Kerswell, R. R., 2004, "Exact Coherent Structures in Pipe Flow: Traveling Wave Solutions," J. Fluid Mech., **508**, pp. 333–371.
[5] Hof, B., Juel, A., and Mullin, T., 2003, "Scaling of the Turbulence Transition Threshold in a Pipe," Phys. Rev. Lett., **91**(24), pp. 244502.
[6] Eckhardt, B., Schneider, T. M., Hof, B., and Westerweel, J., 2007, "Turbulence Transition in Pipe Flow," Annu. Rev. Fluid Mech., **39**, pp. 447–468.
[7] Kerswell, R. R., 2005, "Recent Progress in Understanding the Transition to Turbulence in a Pipe," Institute of Physics Publishing, Nonlinearity, **18**, pp. R17–R44.
[8] Willis, A. P., Peixinhoy, J., Kerswell, R. R., and Mullin, T., 2008, "Experimental and Theoretical Progress in Pipe Flow Transition," Philos. Trans. R. Soc. London, Ser. A, **366**(1876), pp. 2671–2684.
[9] Trefethen, L. N., Trefethen, A. E., Reddy, S. C., and Driscoll, T. A., 1993, "Hydrodynamic Stability Without Eigenvalues," Science, **261**, pp. 578–584.
[10] Waleffe, F., 1997, "On the Self-Sustaining Process in Shear Flows," Phys. Fluids, **9**, pp. 883–900.
[11] Wygnanski, I. J., and Champagne, F. H., 1973, "On Transition in a Pipe. Part 1. The Origin of Puffs and Slugs and the Flow in a Turbulent Slug," J. Fluid Mech., **59**, pp. 281–335.
[12] Wygnanski, I. J., Sokolov, M., and Friedman, D., 1975, "On Transition in a Pipe. Part 2. The Equilibrium Puff," J. Fluid Mech., **69**, pp. 283–304.
[13] Zagarola, M. V., and Smits, A. J., 1998, "Mean-Flow Scaling of Turbulent Pipe Flow," J. Fluid Mech., **373**, pp. 33–79.
[14] Nikuradse, J., 1932, "Gesetzmässigkeiten der turbulenten Strömung in glatten Rohren," Forschg. Arb. Ing.-Wes. Heft, **356**, pp. 1–36.
[15] Sarpkaya, T., 1975, "A Note on the Stability of Developing Laminar Flow Subjected to Axisymmetric and Non-Axisymmetric Disturbances," J. Fluid Mech., **68**, pp. 345–351.
[16] Huang, L. M., and Chen, T. S., 1974, "Stability of Developing Pipe Flow Subjected to Non-Axisymmetric Disturbances," J. Fluid Mech., **63**, pp. 183–193.
[17] Huang, L. M., and Chen, T. S., 1974, "Stability of the Developing Laminar Pipe Flow," Phys. Fluids, **17**, pp. 245–247.
[18] Perry, A. E., and Abel, C. J., 1975, "Scaling Laws for Pipe-Flow Turbulence," J. Fluid Mech., **67**, pp. 257–271.
[19] Lien, K., Monty, J. P., Chong, M. S., and Ooi, A., 2004, "The Entrance Length for Fully Developed Turbulent Channel Flow," *15th Australian Fluid Mechanics Conference*, Dec. 13–17, University of Sydney, Sydney, Australia.
[20] Laufer, J., 1953, "The Structure of Turbulence in Fully Developed Pipe Flow," NACA, Report No. 1174.
[21] Patel, V. C., and Head, M. R., 1969, "Some Observations on Skin Friction and Velocity Profiles in Fully Developed Pipe and Channel Flows," J. Fluid Mech., **38**, pp. 181–201.
[22] Doherty, J., Ngan, P., Monty, J., and Chong, M., 2007, "The Developments of Turbulent Pipe Flow," 16th Australian Fluid Mechanics Conference, Crown Plaza, Gold Coast, Australia, Dec. 2–7, pp. 266–270.
[23] Zanoun, E.-S., Durst, F., Bayoumi, O., and Al-Salaymeh, A., 2007, "Wall Skin Friction and Mean Velocity Profiles of Fully Developed Turbulent Pipe Flows," Exp. Therm. Fluid Sci., **32**(1), pp. 249–261.
[24] Fischer, M., 1999, "Turbulente wandgebundene Strömungen bei kleinen Reynoldszahlen," Ph.D., thesis, Universität Erlangen Nürnberg, Germany.
[25] Sarradj, E., Schulze, C., and Zeibig, A., 2005, "Identification of Noise Source Mechanisms Using Orthogonal Beam Forming," Nov., St. Raphael.
[26] Hof, B., 2004, "Transition to Turbulence in Pipe Flow," *Laminar-Turbulent Transition and Finite Amplitude Solutions*, T. Mullin and R. R. Kerswell, eds., Springer, Dordrecht, pp. 221–231.
[27] Grossmann, S., 2000, "The Onset of Shear Flow Turbulence," Rev. Mod. Phys., **72**(2), pp. 603–618.
[28] Schiller, L., 1922, "Die Entwicklung der laminaren Geschwindigkeitsverteilung und ihre Bedeutung für Zähigkeitsmessungen," Z. Angew. Math. Mech., **2**, pp. 96–106.
[29] Pfeninger, W., 1961, "Boundary Layer Suction Experiments With Laminar Flow at High Reynolds Numbers in the Inlet Length of a Tube by Various Suction Methods," *Boundary Layer and Flow Control*, G. V. Lachman, ed., Pergamon, Oxford, pp. 961–980.
[30] Blasius, H., 1913, "Das Ähnlichkeitsgesetz bei Reibungsvorgängen in Flüssikeiten," Forsch. Arb. Ing.-Wes, pp. 131–137.
[31] Zanoun, E.-S., Durst, F., and Nagib, H., 2003, "Evaluating the Law of the Wall in Two-Dimensional Fully Developed Turbulent Channel Flows," Phys. Fluids, **15**(10), pp. 3079–3089.
[32] Bhatia, J. C., Durst, F., and Jovanovic, J., 1982, "Corrections of Hot-Wire Measurements Near Walls," J. Fluid Mech., **122**, pp. 411–431.
[33] Durst, F., Zanoun, E.-S., and Pashtrapanska, M., 2001, "In Situ Calibration of Hot Wires Close to Highly Heat-Conducting Walls," Exp. Fluids, **31**, pp. 103–110.
[34] Hinze, J. O., 1975, *Turbulence*, 2nd ed., McGraw-Hill, New York.
[35] McKeon, B. J., Swanson, C. J., Zagarola, M. V., Donnelly, R. J., and Smits, A. J., 2004, "Friction Factors for Smooth Pipe Flow," J. Fluid Mech., **511**, pp. 41–44.
[36] Perry, A. E., Hafez, S., and Chong, M. S., 2001, "A Possible Reinterpretation of the Princeton Superpipe Data," J. Fluid Mech., **49**, pp. 395–401.
[37] Nagib, H. M., Chauhan, K. A., and Monkewitz, P. A., 2007, "Approach to an Asymptotic State for ZPG Turbulent Boundary Layers," Philos. Trans. R. Soc. London, Ser. A, **95**, pp. 755–770.
[38] Nagib, M. H., and Kapil, A. C., 2008, "Variations of von Kàrmàn Coefficient in Canonical Flows," Phys. Fluids, **20**, p. 101518.
[39] Reynolds, O., 1883, "On the Dynamical Theory of Incompressible Viscous Fluids and Determination of the Criterion," Philos. Trans. R. Soc. London, **186**, pp. 123–164.
[40] Nishi, M., Ünsal, B., and Durst, F., 2008, "Laminar-to-Turbulent Transition of Pipe Flows Through Slugs and Puffs," J. Fluid Mech., **614**, pp. 425–446.
[41] Durst, F., and Ünsal, B., 2006, "Forced Laminar to Turbulent Transition of Pipe Flows," J. Fluid Mech., **560**, pp. 449–464.

Particle Image Velocimetry Study of Rough-Wall Turbulent Flows in Favorable Pressure Gradient

G. F. K. Tay

D. C. S. Kuhn[1]
e-mail: dkuhn@cc.umanitoba.ca

M. F. Tachie

Department of Mechanical and Manufacturing Engineering,
University of Manitoba,
Winnipeg, MB, R3T 5V6, Canada

This paper reports an experimental investigation of the effects of wall roughness and favorable pressure gradient on low Reynolds number turbulent flow in a two-dimensional asymmetric converging channel. Flow convergence was produced by means of ramps (of angles 2 deg and 3 deg) installed on the bottom wall of a plane channel. The experiments were conducted over a smooth surface and over transitionally rough and fully rough surfaces produced from sand grains and gravel of nominal mean diameters 1.55 mm and 4.22 mm, respectively. The dimensionless acceleration parameter was varied from 0.38 $\times 10^{-6}$ *to 3.93* $\times 10^{-6}$ *while the Reynolds number based on the boundary layer momentum thickness was varied from 290 to 2250. The velocity measurements were made using a particle image velocimetry technique. From these measurements, the distributions of the mean velocity and Reynolds stresses were obtained to document the salient features of transitionally and fully rough low Reynolds number turbulent boundary layers subjected to favorable pressure gradient.* [DOI: 10.1115/1.3112389]

Keywords: particle image velocimetry, turbulent flow, wall roughness, favorable pressure gradient

1 Introduction

Turbulent flows over rough surfaces have received considerable research attention because most surfaces of fluid engineering and environmental importance are hydrodynamically rough. It is generally accepted that surface roughness would modify the near-wall turbulence structure and enhance the transport of heat, mass, and momentum. The higher values of mass and momentum deficits reported in rough-wall turbulent experiments compared with a smooth surface are explained by higher resistance to the mean flow over a rough-wall. Similarly, the turbulence levels close to the roughness elements are generally higher than if the surface were smooth. A vivid review of previous measurements over rough surfaces can be found, for example, in Refs. [1–3] and are not repeated here. Most of those experiments were conducted at moderate to high Reynolds numbers and over fully rough surfaces. In the rough-wall experiment reported by Castro [4], for example, the Reynolds number based on the boundary layer momentum thickness, Re_θ, varied from 1160 to 48,000.

Rough-wall results are often interpreted within the context of Townsend's [5] wall similarity hypothesis, which implies that smooth- and rough-wall turbulent flows are structurally similar outside the roughness sublayer at sufficiently high Reynolds number. Raupach et al. [6] argued that the roughness sublayer may extend from the wall up to $y=5k$, where k is the roughness height. Schultz and Flack [7] suggested that the equivalent sand grain roughness height k_s is a more appropriate roughness length scale (instead of k) because it provides a common measure of the influence of roughness on the mean flow. The results from a large number of previous studies (e.g., Refs. [8,9]) are consistent with the wall similarity hypothesis. However, support for the similarity hypothesis is not unanimous. For example, the measurements reported by Krogstad and Antonia [2] demonstrate that roughness effects on the turbulent structure are felt well outside the roughness sublayer.

Favorable pressure gradient (FPG) turbulent flows over a smooth surface have also been studied extensively in the past. When the FPG is large enough, the boundary layer may undergo relaminarization. Badri Nayaranan and Ramjee [10] performed measurements in strongly accelerated boundary layers for Re_θ ranging from 300 to 2000. It was found that during relaminarization, the skin friction decreases significantly and the peak values of the Reynolds stresses normalized with the freestream velocity decay substantially. The measurements reported by Blackwelder and Kovasznay [11] in a converging channel show that, except in the immediate vicinity of the wall, the relative levels of the turbulent intensities and the Reynolds stresses decay significantly with acceleration. Escudier et al. [12] performed measurements in a converging wind tunnel for $221 \leq \mathrm{Re}_\theta \leq 1700$. It was observed that δ, δ^*, and θ decrease progressively with streamwise distance x reaching minimum values at the end of relaminarization. The shape factor H decreased initially with x up to the start of relaminarization, after which it increased rapidly, reaching a maximum of 2.4. Fernholz and Warnack [13] investigated the effects of FPG and Reynolds number on the mean and turbulent quantities in an axisymmetric converging channel. The Reynolds numbers were in the range $862 \leq \mathrm{Re}_\theta \leq 5800$. They found that H and Re_θ decreased monotonically with x in the presence of the FPG. The peak values of the stresses u^{+2} and $-u^+v^+$ fall rapidly with FPG or decreasing Re_θ up to the location where Re_θ is minimum before rising again when the FPG is relaxed.

The above summary discussion indicates that surface roughness tends to enhance the mass and momentum flux deficits, shape factor, and relative turbulence levels compared with a smooth-wall. On the other hand, FPG would decrease the mass and momentum flux deficits, shape factor, and relative turbulence levels compared with a zero pressure gradient. These opposing effects of FPG and wall roughness on the mean flow and turbulence characteristics would be most felt in the near-wall region. Therefore, refined experiments are necessary to better understand the combined effects of FPG and surface roughness on the mean flow and turbulence field. The benchmark data obtained from such experi-

[1]Corresponding author.

Contributed by the Fluids Engineering Division of ASME for publication in the JOURNAL OF FLUIDS ENGINEERING. Manuscript received September 4, 2008; final manuscript received February 8, 2009; published online May 15, 2009. Assoc. Editor: Steven T. Wereley.

ments could also be used to assess the ability of turbulence models to accurately predict the mean and turbulent quantities in accelerated flows over rough surfaces in nozzles, over turbine blades, and over re-entry vehicles. To date, however, only a few studies of FPG turbulent flows over rough surfaces have been reported. Coleman et al. [14] performed hot-wire measurements in both equilibrium and nonequilibrium accelerated turbulent flows over fully rough surfaces. The acceleration parameter ($K=[(\nu/U_e^2)(dU_e/dx)]$) was varied from $K=0$ to 0.29×10^{-6}. It was found that FPG decreased the normalized turbulent kinetic energy and Reynolds stresses, and made the fully rough boundary layer rougher. The Reynolds shear stress correlation coefficient and the structure parameter were, however, not affected by surface roughness and/or FPG. Cal et al. [15,16] used laser Doppler anemometry (LDA) to study FPG turbulent flows over transitionally rough and fully rough surfaces. A 24-grit sandpaper was used to produce the rough surface and Re_θ ($=U_e\theta/\nu$) was varied from 1118 to 4927. A flat plate inclined at 3.5 deg was used to produce a mild FPG and in those experiments, the dimensionless roughness height k^+ was varied from 42.7 to 57.1. For the strong FPG experiment produced using a 15 deg inclined plane, $57\leq k^+\leq92$. It was found that in the presence of strong FPG, surface roughness increases v^2 and $-uv$ more than it increased u^2. Tachie et al. [17] used a particle image velocimetry (PIV) to study the effects of FPG and rib roughness on turbulent flow in an open-channel with converging side walls. The measurements were performed over *d*-type, intermediate, and *k*-type transverse ribs for two angles of convergence (1 deg and 2 deg). It was reported that FPG has no significant effects on the drag characteristics but it reduces the effectiveness of the ribs to enhance mass and momentum transfer. Furthermore, FPG decreased the turbulent intensities, Reynolds shear stress, and triple correlations over the *d*-type ribs more dramatically than over intermediate and *k*-type ribs.

The goal of the present study is to investigate the effects of low Reynolds number FPG turbulent flows over smooth and rough surfaces. The FPG was produced in an asymmetric converging channel and the roughness elements used were sand grain and gravel of respective nominal diameters 1.55 mm and 4.22 mm. The approach velocity and the channel geometry were varied to obtain a wide range of low Reynolds numbers ($290\leq\mathrm{Re}_\theta\leq2253$), mild flow acceleration ($0<K\leq3.93\times10^{-6}$), and both transitionally and fully rough surfaces ($9\leq k_s^+\leq142$). The velocity measurements were conducted using a PIV technique from which the mean velocities and Reynolds stresses were extracted to document the combined effects of pressure gradient and surface roughness on the flow characteristics.

2 Experimental Setup and Measurement Procedure

2.1 Test Channel and Measurement Procedure. The experiments were performed in the asymmetric converging channel shown schematically in Fig. 1. The channel was fabricated using 9 mm thick acrylic plates and its internal width was 179 mm. The first 1500 mm (OA) of the channel has parallel bottom and top walls and a constant height of 55 mm. A 2 deg ramp and a 3 deg ramp were installed at the bottom wall to produce an asymmetric converging section downstream of the parallel section. The channel was supported at its base by means of two stainless steel bars inside an existing water tunnel with a test section that was 2500 mm long, 200 mm wide, and 200 mm deep.

A PIV technique was used to conduct the velocity measurements. The flow was seeded with 5 μm polyamide seeding particles. A Nd:YAG (yttrium aluminum garnet), 120 mJ/pulse laser of 532 nm wavelength was used to illuminate the flow field. The laser sheet was located at the midspan of the channel. A 12 bit high-resolution CCD camera with 2048 pixels $\times$ 2048 pixels and a 7.4 μm pixel pitch was employed to image the instantaneous flow field. The field of view was 63.4×63.4 mm^2. In each measurement plane, 2052 instantaneous image pairs were obtained.

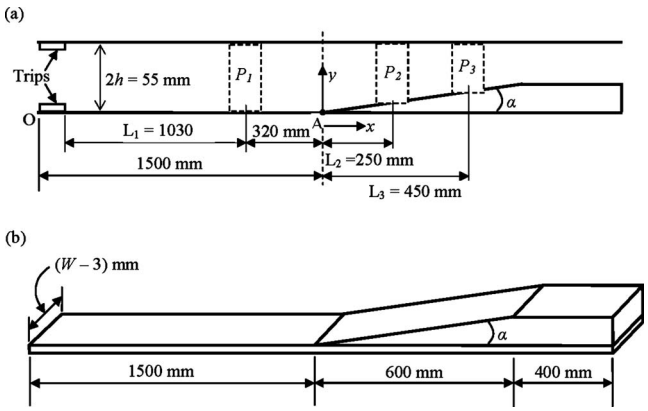

Fig. 1 Schematic of the test section: (*a*) test channel showing the converging section and the three measurement planes where data were acquired; (*b*) a three-dimensional view of the ramp used to produce the converging section; *W*=179 mm is the internal width of the test channel, and α=2 deg or 3 deg Is the angle of the ramp. In (*a*), *P* denotes measurement plane and *L* defines the exact *x*-location where profiles were extracted in a given plane.

The instantaneous images were postprocessed using the adaptive correlation option of the FlowManager software (version 4.50.17) developed by Dantec Dynamics (New Jersey). A 32 pixels $\times$ 32 pixels interrogation area (IA) with 50% overlap and moving average validation was used. The adaptive correlation used a multipass Fast Fourier Transform (FFT) correlation algorithm to determine the average particle displacement within the interrogation window with subpixel accuracy. During the image acquisition, steps were taken to ensure that the maximum particle displacement was less than $\frac{1}{4}$ of the IA size. Profiles of the mean velocities and turbulent statistics were plotted for different numbers of image pairs. The respective profiles for 1026 image pairs and greater collapsed within measurement uncertainties. Therefore, 2052 image pairs were used to compute the mean and turbulent statistics reported subsequently.

In near-wall turbulence, it is necessary to keep the IA size as small as possible in order to resolve the smallest scales in the flow. On the other hand, the dynamic range of the measured velocity values increases with interrogation area size, which implies that larger IA sizes are desirable to achieving large dynamic range. These conflicting interests require a tradeoff between spatial resolution and velocity dynamic range. The dynamic range in a PIV measurement based on a pixel displacement level is the displacement divided by the subpixel accuracy. With an IA size of 32 pixels $\times$ 32 pixels, the maximum displacement in the streamwise direction was 8 pixels and the dynamic range was of the order of 80. The particle image diameter was estimated to be $d_p=2.2$ pixels, a value that is close to the recommended optimum value of $d_p=2$ pixels to minimize peak locking [18]. The physical spacing between the velocity vectors was $l=0.494$ mm. In wall units, the spacings between the data points on the smooth test sections lie within $6<l^+<23$, while those over the sand grain and gravel are within $7<l^+<30$. Recently, Shah et al. [19] studied the effects of PIV resolution on the mean velocity and turbulent statistics up to the fourth order moments in smooth- and rough-wall turbulent flows. Based on their results, it is concluded that the spatial resolution stated above is adequate to accurately measure all the mean and turbulent quantities reported in this paper.

2.2 Test Conditions. The approach boundary layer on the top and bottom walls was tripped using a strip of closely packed gravel of nominal diameter 6 mm over a streamwise distance of 150 mm from the inlet of the test channel (Fig. 1). In addition to a smooth surface, the following two roughness conditions were

Table 1 Summary of test conditions and boundary layer parameters

Test	Plane	U_e (m/s)	dU_e/dx (s^{-1})	$K\times10^{-6}$	δ (mm)	δ^* (mm)	θ (mm)	Re_θ	H
$SMU_{0.25}$	$P_1\alpha_0$	0.247	0.024	0.38	26.3	3.55	2.60	642	1.37
	$P_2\alpha_2$	0.297	0.182	2.06	20.3	2.01	1.47	437	1.37
	$P_3\alpha_2$	0.353	0.260	2.10	14.9	1.40	0.95	335	1.47
	$P_2\alpha_3$	0.305	0.240	2.48	19.2	2.19	1.52	464	1.44
	$P_3\alpha_3$	0.403	0.614	3.60	11.8	1.12	0.72	290	1.56
$SMU_{0.50}$	$P_1\alpha_0$	0.496	0.109	0.44	24.8	3.40	2.37	1176	1.43
	$P_2\alpha_2$	0.535	0.473	1.44	20.8	2.10	1.52	813	1.38
	$P_3\alpha_2$	0.658	0.621	1.52	16.3	1.56	1.01	665	1.54
	$P_2\alpha_3$	0.631	0.594	1.49	15.8	1.56	1.08	681	1.44
	$P_3\alpha_3$	0.814	1.200	1.76	11.4	1.02	0.64	521	1.59
$SGU_{0.25}$	$P_1\alpha_0$	0.245	0.025	0.41	25.7	4.43	3.13	767	1.42
	$P_2\alpha_2$	0.298	0.274	2.96	24.1	3.33	2.43	724	1.37
	$P_3\alpha_2$	0.375	0.444	3.31	18.2	2.67	1.80	675	1.48
	$P_2\alpha_3$	0.323	0.338	3.43	17.3	2.19	1.50	485	1.46
	$P_3\alpha_3$	0.423	0.684	3.93	11.4	1.52	0.98	415	1.55
$SGU_{0.50}$	$P_1\alpha_0$	0.494	0.061	0.25	36.5	7.00	4.56	2253	1.54
	$P_2\alpha_2$	0.616	0.512	1.37	26.4	3.93	2.65	1632	1.48
	$P_3\alpha_2$	0.739	0.775	1.47	21.2	2.98	1.94	1434	1.54
	$P_2\alpha_3$	0.634	0.703	1.70	25.2	3.58	2.49	1579	1.44
	$P_3\alpha_3$	0.866	1.440	1.97	17.8	2.27	1.52	1316	1.49
$GVU_{0.25}$	$P_1\alpha_0$	0.244	0.006	0.10	26.1	4.77	3.29	803	1.45
	$P_2\alpha_2$	0.299	0.216	2.34	24.1	3.76	2.68	801	1.40
	$P_3\alpha_2$	0.363	0.367	2.70	18.2	2.46	1.70	617	1.45
	$P_2\alpha_3$	0.305	0.213	2.23	19.2	2.84	1.97	601	1.44
	$P_3\alpha_3$	0.433	0.462	2.70	11.8	1.56	1.01	437	1.54
$GVU_{0.50}$	$P_1\alpha_0$	0.490	0.035	0.15	31.8	7.04	4.40	2156	1.60
	$P_2\alpha_2$	0.615	0.323	0.89	26.8	4.49	2.85	1753	1.58
	$P_3\alpha_2$	0.732	0.515	0.95	20.9	3.45	2.20	1610	1.57
	$P_2\alpha_3$	0.636	0.682	1.68	23.1	4.12	2.49	1584	1.65
	$P_3\alpha_3$	0.851	1.800	2.38	14.4	2.45	1.37	1166	1.79

studied: (i) uniformly distributed sand grains of nominal mean diameter 1.55 mm and (ii) gravel of mean diameter 4.22 mm. The roughness elements were glued onto a 1.5 mm acrylic plate with a double-sided tape. The experiments in the two test sections were conducted at two different approach velocities of $U_e \approx 0.25$ m/s and 0.50 m/s. For each test condition, data were acquired in the following three measurement planes (see Fig. 1): P_1, which is located within the parallel section of the channel, and P_2 and P_3, which are within the converging section of the channel. As shown in Fig. 1, the specific locations at which profiles were extracted in planes P_1, P_2, and P_3 are, respectively, $L_1=1030$ mm downstream of the trips, and $L_2=250$ mm and $L_3=450$ mm from the start of convergence.

The test conditions on the smooth surfaces will be denoted by $SM\alpha_iU_jP_k$, where α denotes the angle of slope, U is the velocity of the approach flow ($j=0.25$ and 0.50), P is the plane of measurement ($k=1,2,3$), and i is the value of the angle α ($i=2$ or 3). Similarly, the tests on the sand grain and gravel will be denoted by $SG\alpha_iU_jP_k$ and $GV\alpha_iU_jP_k$, respectively. In this study, only data in the lower boundary layer over the test sections are presented and discussed. The lower boundary layer is defined as the flow region from the bottom wall to the y-location where the maximum streamwise mean velocity U_e occurs. For the rough-wall cases, $y=0$ is defined at the top plane of the roughness elements. A complete summary of the test conditions is given in Table 1. These include values of U_e, the boundary layer parameters (δ, δ^*, θ, H, and, Re_θ), and the acceleration parameters (dU_e/dx and K). The boundary layer thickness δ is defined as the distance from $y=0$ to the y-location where $U=0.99U_e$. It was found that, for a given approach velocity, the profiles of the mean and turbulent statistics obtained in the upstream plane of both the 2 deg and 3 deg test sections (i.e., $\alpha_2U_jP_1$ and $\alpha_3U_jP_1$) were identical. Therefore, only the upstream data sets over the 3 deg test section (i.e., $\alpha_3U_jP_1$) will be presented. Hereafter, these upstream data sets will be designated as $\alpha_0U_jP_1$.

2.3 Uncertainty Estimates. Measurement uncertainty analysis was made following the AIAA standard derived and explained by Coleman and Steele [20]. In general, a complete uncertainty analysis involves identifying and quantifying both the bias and precision errors in each part of the measurement chain. In PIV, the accuracy of velocity measurement is limited by the accuracy of the subpixel interpolation of the displacement correlation peak. Other sources of measurement uncertainties include particle response to fluid motion, light sheet positioning, light pulse timing, and size of interrogation area. Detailed analyses of bias and precision errors inherent in PIV are available in Refs. [21,22]. Forliti et al. [22] showed that a Gaussian peak-fitting algorithm has the lowest bias and precision errors. On the basis of the size of interrogation area and curve fitting algorithm used to calculate the instantaneous vector maps, and the large number of instantaneous images used to calculate the mean velocity and turbulent quantities, the uncertainty in the mean velocity at 95% confidence level is estimated to be $\pm2\%$. The uncertainties in the turbulent intensities and Reynolds shear stress are estimated to be $\pm5\%$ and 10%, respectively. Close to the rough surfaces, uncertainties in mean velocity and Reynolds shear stress are estimated to be

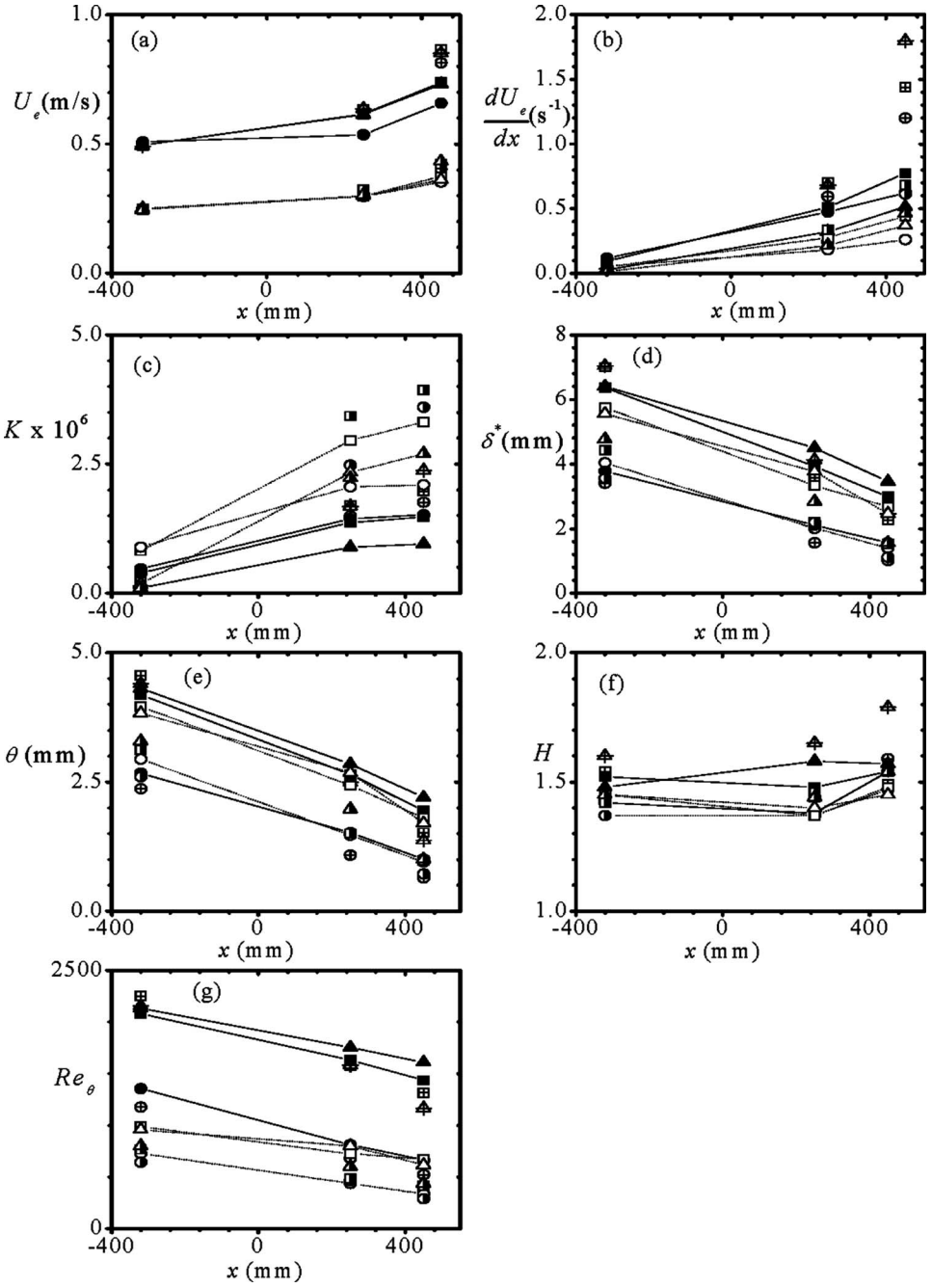

Fig. 2 Profiles of boundary layer parameters. Symbols: ○, SM$\alpha_2 U_{0.25}$; ●, SM$\alpha_2 U_{0.50}$; ◑, SM$\alpha_3 U_{0.25}$; ⊕, SM$\alpha_3 U_{0.50}$; □, SG$\alpha_2 U_{0.25}$; ■, SG$\alpha_2 U_{0.50}$; ◨, SG$\alpha_3 U_{0.25}$, ⊞, SG$\alpha_3 U_{0.50}$; △, GV$\alpha_2 U_{0.25}$; ▲, GV$\alpha_2 U_{0.50}$; ◭, GV$\alpha_3 U_{0.25}$; and ◬, GV$\alpha_3 U_{0.50}$. Lines are for visual aid only.

±2.5% and ±12.5%, respectively. In the graphs presented subsequently, error bars are used to indicate measurement uncertainty at 95% confidence level.

3 Results and Discussion

3.1 Boundary Layer Characteristics. The effects of Reynolds number, FPG, and surface roughness on the evolution of the mean flow along the channel and the boundary layer characteristics are examined using the parameters summarized in Table 1 and those plotted in Fig. 2. The acceleration parameter in each measurement plane was determined as follows: The streamwise mean velocity profiles across the channel, $U(y)$, were extracted at several x-locations at 5 mm intervals and the local maximum value, U_e, for each profile was determined. Then dU_e/dx was determined using a least-squares linear fit to U_e versus x. For a given approach velocity and surface condition, the values of U_e and dU_e/dx increased more rapidly in the 3 deg test section than in the 2 deg test section. Over the sand grain roughness, for example, the value of U_e in plane P_3 within the 3 deg test section is approximately 75% higher than in the parallel section (P_1), while that obtained in P_3 within the 2 deg test section is only 50% higher than in P_1. The percentage increase in dU_e/dx within the converging section decreases with increasing approach velocity, except for surfaces SGα_3 and GVα_3 where the increased blockage in P_3 produces a more than proportionate change in the velocity gradient. The values of the acceleration parameter K show a consistent increase with x for all the test conditions. The nonzero values of K

observed at the upstream parallel section (P_1) for the smooth- and rough-walls indicate a small but non-negligible acceleration of the approach boundary layer. Over the smooth-wall, the values of K are generally higher at the lower approach velocity than at the higher approach velocity, which should be expected since an accelerating turbulent flow at a lower Reynolds number is more likely to undergo relaminarization. The value of K for Test SM$\alpha_3 U_{0.25} P_3$ compares favorably with the value of 3.5×10^{-6} reported by Badri Nayaranan and Ramjee [10] and Escudier et al. [12].

Over the smooth surface, the boundary layer thicknesses are largest at the upstream location and decrease substantially with x within the converging section. This is consistent with the observation made in earlier studies [17,19]. Furthermore, the stronger FPG generated in the 3 deg test section produced a more substantial reduction in δ, δ^*, and θ than in the 2 deg test section. Even in the presence of surface roughness, the increased acceleration in the converging section reduced the values of δ, δ^*, and θ compared with the corresponding upstream reference values. Due to the opposing effects of surface roughness and FPG, however, the reduction in δ, δ^*, and θ due to FPG is less dramatic on the rough surface than when the surface is smooth. The momentum thickness Reynolds number Re_θ decreases with increasing dimensionless acceleration parameter. For the smooth-wall, Re_θ ranged from 290 to 1176, which is not significantly different from the Re_θ range studied by Escudier et al. [12]. The results also demonstrate that, for similar approach velocity and streamwise location, surface roughness produced consistently larger values of δ, δ^*, θ, and Re_θ than the corresponding smooth-wall values. Even though Re_θ decreases consistently with FPG, the trend in the shape factor H is less systematic. The observed values over the smooth-wall (i.e., $H\approx1.47\pm0.12$) are substantially smaller than the laminar value of 2.5. This would imply that all flows over the smooth-wall were turbulent. The higher values of the shape factor H over the rough surfaces also imply that even in the presence of FPG, surface roughness augments mass flux deficit more effectively than it enhances momentum flux deficit.

3.2 Friction Velocity and Drag Characteristics. The Clauser plot technique has been used in previous ZPG and moderate FPG measurements over smooth and rough surfaces to determine the friction velocity U_τ. In this method, the measured mean velocity data are fitted to the log-law, which, for a rough-wall, may be written as $U^+=\kappa^{-1}\ln(y+y_o)^+ + B - \Delta B^+$, where κ and B are "universal" log-law constants, ΔB^+ is the roughness shift ($\Delta B^+=0$ for a smooth-wall), and y_o ($y_o=0$ for a smooth-wall) is the virtual origin. Fernholz and Warnack [13] demonstrated that in a mild FPG, a substantial region of the overlap layer exists in which the log-law is still valid. Due to the assumption of a constant stress layer in the derivation of the log-law, it has been argued that the log-law may be susceptible to low Reynolds number effects. Simpson [23], for example, found that the log-law constant κ varies with Reynolds number. Preston [24] and Granville [25] suggested that the logarithmic region disappears at low Reynolds numbers. In DNS of turbulent boundary layers at Re_θ between 225 and 1410, Spalart [26] found that the mean velocity and shear stress profiles behave as predicted by Coles, except for the strength of the wake. Balachander and Ramachandran [27] reported that even for Re_θ as low as 180, the log layer did not disappear.

In the present study, the Clauser plot method was employed to estimate U_τ in all the smooth- and rough-wall measurements. Since the virtual origin y_o depends on the specific geometry and distribution of the roughness elements, its exact location is not known a priori. It is generally accepted, however, that $0\le y_o\le k$. In analyzing the rough-wall data, therefore, an initial estimate of $y_o=0.5k$ was made. This value was then varied slightly to ensure a reasonable collapse between the measured data and the log-law in the inner region. Figure 3 shows the mean velocity profiles in the inner coordinates for selected test conditions over the smooth and rough surfaces. The range of overlap between the upstream data and the log-law became wider as the Reynolds number increased. The wake parameter for the upstream data is negligibly small because of the high turbulence level and the slight favorable pressure gradient. The low Re_θ (due to the increasing FPG) and the diminishing channel height within the converging section reduced the logarithmic region of the measured data. It should be noted that the effect of increasing FPG on the outer layer is to make the wake more negative. The rough-wall data sets show the expected shift ΔB^+ from the smooth-wall log-law and the magnitude of the shift decreases with x within the converging section. The values of the nondimensional equivalent sand grain roughness height k_s^+ were estimated from $\Delta B^+=(1/\kappa)\ln(1+0.3k_s^+)$.

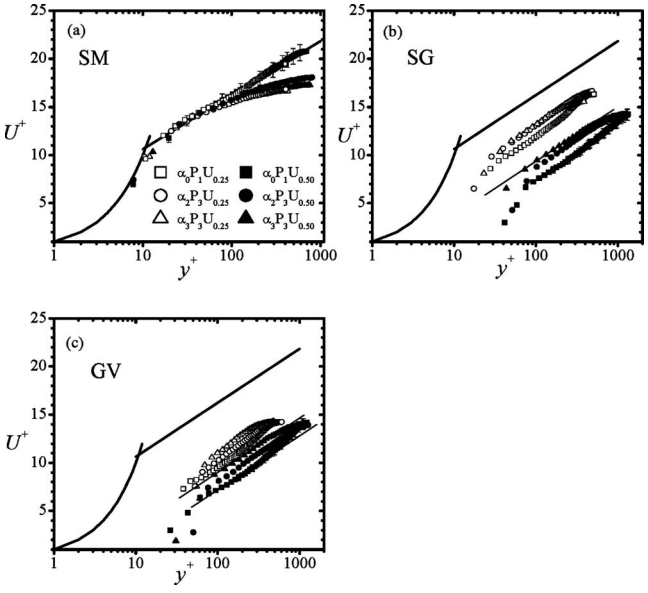

Fig. 3 Mean velocity profiles over the smooth- and rough-walls in the inner coordinates

The friction velocities and other drag and roughness parameters are summarized in Table 2. For a given approach velocity, U_τ increased consistently with x, irrespective of the surface condition. For the smooth surfaces, U_τ increased more rapidly than U_e so that the friction coefficient $C_f=2(U_\tau/U_e)^2$ increased consistently with x. A similar observation was made by Escudier et al. [12] and Fernholz and Warnack [13] prior to relaminarization in their respective FPG studies, albeit a more dramatic increase in C_f with x than observed in the present investigation. As expected, though, the C_f values decreased with increasing approach flow velocity, U_e, or Re_θ.

In the absence of FPG, the sand grain roughness increased C_f by 39% ($U_{0.25}$) and 113% ($U_{0.50}$) compared with the corresponding smooth-wall value. Corresponding changes in C_f over the gravel are, respectively, 81% and 115%. These results suggest that, for a given roughness element, increasing the Reynolds number of the approach flow would produce a more dramatic increase in surface drag. Because of the opposing effects of FPG and surface roughness on the drag characteristics, the variation in C_f values along the channel is less dramatic over the rough surfaces compared with the smooth-wall. It has been suggested that FPG increases the thickness of the viscous sublayer [11,28]. Consequently, FPG should decrease the values of k_s^+ over a rough surface and make the surface less rough. For SG$U_{0.50}$, the substantial decrease in k_s^+ from 125 at the upstream section ($P_1\alpha_0$) to $k_s^+=53$ at $P_3\alpha_3$ and $k_s^+=66$ at $P_3\alpha_2$ supports their argument. Based on Schlichting's [29] equivalent sand grain roughness criterion, the gravel and sand grain tests at $U_{0.25}$ are in the transitionally rough regime. For the higher approach velocity, the gravel and

Table 2 Summary of friction and roughness parameters

Test	Plane	U_e (m/s)	U_τ (m/s)	C_f	ΔB	k_s^+	k_s (mm)	k_s/k	k_s/δ
SM$U_{0.25}$	$P_1\alpha_0$	0.247	0.0128	0.0054					
	$P_2\alpha_2$	0.297	0.0169	0.0065					
	$P_3\alpha_2$	0.353	0.0210	0.0071					
	$P_2\alpha_3$	0.305	0.0173	0.0064					
	$P_3\alpha_3$	0.403	0.0242	0.0072					
SM$U_{0.50}$	$P_1\alpha_0$	0.496	0.0238	0.0046					
	$P_2\alpha_2$	0.535	0.0288	0.0058					
	$P_3\alpha_2$	0.658	0.0364	0.0061					
	$P_2\alpha_3$	0.631	0.0350	0.0062					
	$P_3\alpha_3$	0.814	0.0471	0.0067					
SG$U_{0.25}$	$P_1\alpha_0$	0.245	0.0150	0.0075	4.3	21	1.38	0.89	0.05
	$P_2\alpha_2$	0.298	0.0182	0.0075	3.6	11	0.62	0.40	0.03
	$P_3\alpha_2$	0.375	0.0225	0.0072	3.1	9	0.38	0.25	0.02
	$P_2\alpha_3$	0.323	0.0205	0.0081	3.4	10	0.49	0.32	0.03
	$P_3\alpha_3$	0.423	0.0272	0.0083	3.1	9	0.33	0.21	0.03
SG$U_{0.50}$	$P_1\alpha_0$	0.494	0.0346	0.0098	8.9	125	3.61	2.33	0.10
	$P_2\alpha_2$	0.616	0.0435	0.0100	7.8	78	1.80	1.16	0.07
	$P_3\alpha_2$	0.739	0.0520	0.0099	7.4	66	1.27	0.82	0.06
	$P_2\alpha_3$	0.634	0.0448	0.0100	7.4	66	1.47	0.95	0.06
	$P_3\alpha_3$	0.866	0.0606	0.0098	6.9	53	0.88	0.57	0.05
GV$U_{0.25}$	$P_1\alpha_0$	0.244	0.0171	0.0098	6.7	49	2.85	0.67	0.11
	$P_2\alpha_2$	0.299	0.0209	0.0098	6.2	39	1.87	0.44	0.08
	$P_3\alpha_2$	0.363	0.0255	0.0099	5.9	34	1.34	0.32	0.07
	$P_2\alpha_3$	0.305	0.0214	0.0098	5.6	30	1.39	0.33	0.07
	$P_3\alpha_3$	0.433	0.0303	0.0098	5.1	24	0.78	0.18	0.07
GV$U_{0.50}$	$P_1\alpha_0$	0.490	0.0345	0.0099	9.2	142	4.12	0.98	0.13
	$P_2\alpha_2$	0.615	0.0438	0.0100	8.2	93	2.12	0.50	0.08
	$P_3\alpha_2$	0.732	0.0525	0.0102	8.1	88	1.68	0.40	0.08
	$P_2\alpha_3$	0.636	0.0455	0.0102	7.8	78	1.71	0.41	0.07
	$P_3\alpha_3$	0.851	0.0611	0.0103	7.3	63	1.03	0.24	0.07

sand grain were fully rough at the upstream location but less rough within the converging section. The present results are at variance with the findings of Coleman et al. [14] who reported that their fully rough test surface became rougher as the FPG increased.

The ratio k_s/k compares the equivalent sand grain roughness height to the physical height of the roughness elements. The values of k_s/k decrease with increasing acceleration, suggesting that FPG reduces the effectiveness of sand grain and gravel to generate drag in comparison with monodisperse sand grains. The ratio k_s/δ is usually used in rough-wall flows to assess the degree of scale separation between the small and large scales in the flow. Jiménez [30] argued that if the scale separation is insufficient, roughness effects may be observed well into the outer layer. For $k_s/\delta = 0.0025$, Schultz and Flack [7] observed no roughness effects in the outer parts of the flow over an epoxy-coated acrylic plate scratched with a 12-grit sandpaper. For a woven mesh roughness with $k_s/\delta = 0.067$, Krogstad et al. [31] observed significant roughness effects well into the outer layer. The present values of k_s/δ for Tests SG$U_{0.50}$ and GV$U_{0.50}$ in the absence of FPG are large enough for the effects of the sand grain and gravel roughness to be felt outside the roughness sublayer. It should be noted that under these conditions, the roughness sublayer ($y = 5k_s$) is 50% of the boundary layer over the sand grain and 60% of the boundary layer over the gravel. In general, k_s/δ decreased with x for all the roughness elements.

3.3 Reynolds Number, Pressure Gradient, and Roughness Effects. As indicated in the Introduction, wall roughness and favorable pressure gradient may cause significant changes in the near-wall structure. In addition to these effects, the distributions of the mean velocity and turbulent statistics in a turbulent boundary layer may depend on Reynolds number. For example, the DNS results presented by Spalart [26] showed that u^+, v^+, and $-u^+v^+$ increased by 8%, 15%, and 16%, respectively, as Re_θ increased from 300 to 1410. Antonia and Kim [32] also observed 11%, 29%, and 36% increases, respectively, in u^+, v^+, and $-u^+v^+$ as Re_τ $(=hU_\tau/\nu)$ increased from 180 to 400. These Reynolds number effects were attributed to the increased stretching of the quasi-streamwise vortices in the wall region as the Reynolds number increases. On the other hand, the low Reynolds number experiments conducted in a fully developed turbulent channel [33] and in an open-channel [27] showed that the mean and turbulent characteristics are unaffected by the Reynolds number. Similarly, Bakken et al. [1] conducted measurements in a channel roughened on both walls and found that the mean velocity, Reynolds stresses, and triple correlations are little affected by the Reynolds number outside the roughness sublayer. In view of the possible effects of Reynolds number, favorable pressure gradient, and surface roughness on the present measurements, it was decided to first examine how each of these individual effects may affect the mean velocity defect, turbulent intensities, and Reynolds shear stress. For the mean velocity defect, both the friction velocity (U_τ) and the

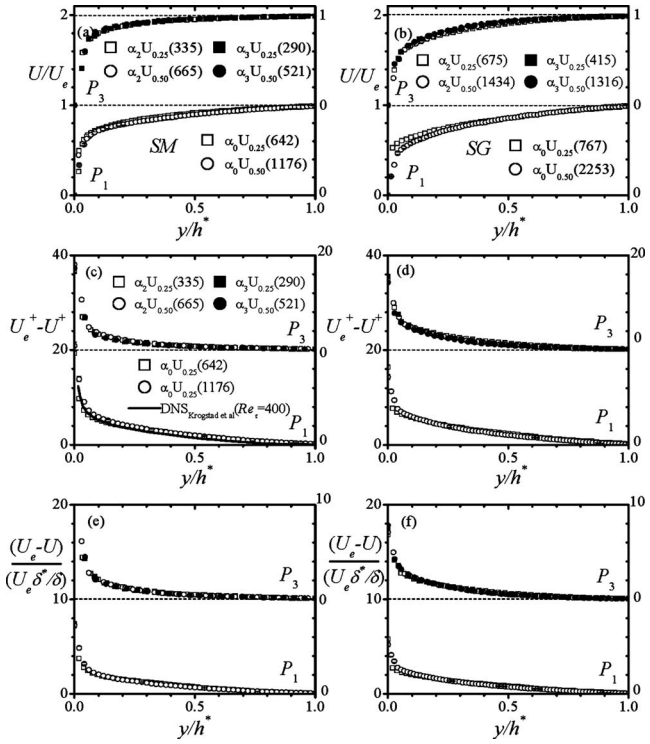

Fig. 4 Distributions of the mean velocity and mean velocity defect over the smooth-wall and the sand grain roughness. The numbers in parentheses correspond to the value of Re_θ for the particular test conditions.

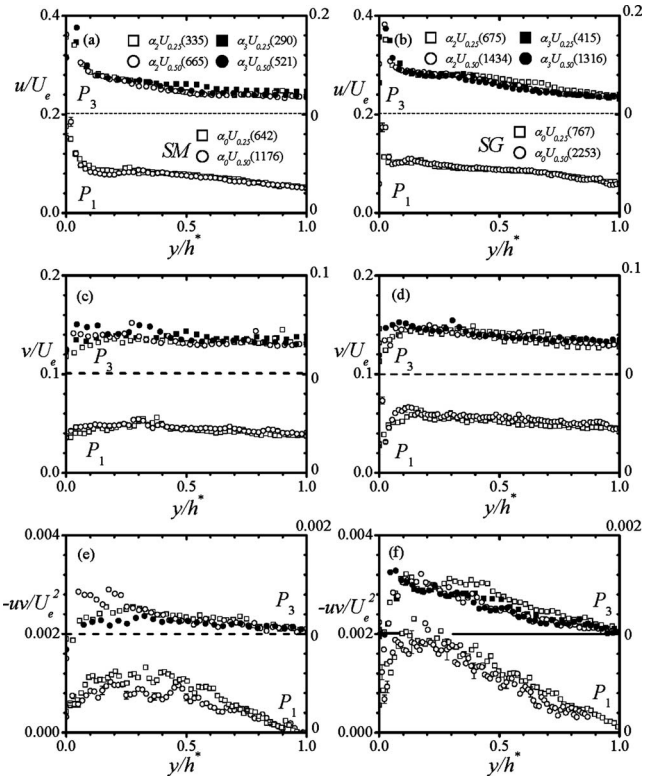

Fig. 5 Turbulent intensities and Reynolds shear stress over the smooth-wall and sand grain

mixed outer scaling ($U_e\delta^*/\delta$) proposed by Zagarola and Smit [34] are used to interpret the data. For the turbulent quantities, both outer and inner scalings are employed.

3.3.1 Reynolds Number Effects. The measurements conducted over the smooth surface (Test SM) and sand grain roughness (Test SG) at the two approach velocities are used to examine the effects of Reynolds number on the flow characteristics. Since Reynolds number effects on the mean velocity and turbulent statistics over the gravel and sand grain are the same, only profiles over the sand grain are plotted to avoid data congestion. The gravel profiles omitted in this paper are, however, presented in Ref. [35]. The profiles over the smooth surface and sand grain are plotted separately so as to isolate roughness effects. Furthermore, pressure gradient effects are isolated by plotting together profiles in plane P_1, and those in P_3, which are staggered relative to those in P_1. The mean velocity and velocity defect profiles are presented in Fig. 4. The wall-normal position is normalized by h^*, the y-location where the Reynolds shear stress changes sign from positive to negative. For the smooth surface, regardless of the nearly twofold increase in Re_θ in P_1 and P_3, the mean velocity shows no dependence on Reynolds number. It should be noted that within the converging section (P_3), the value of Re_θ changed in the following two ways: with increasing approach flow velocity and decreasing α. Even with a more than twofold increase in Re_θ by varying U_e and α (or FPG), the profiles were still Re_θ invariant. The collapse among the mean velocity defect profiles is also excellent in the upstream and converging sections irrespective of the velocity scaling used. Furthermore, there is a good agreement between the present results in the parallel section and the DNS result of Ref. [31] (see Fig. 4(c)). Similarly, the mean velocity and defect profiles obtained in the upstream and converging sections over the sand grain do not vary with Reynolds number. These results imply that the mean velocity profiles over a particular surface and measurement plane are truly independent of Reynolds number.

Figure 5 shows profiles of the turbulent intensities and Reynolds shear stress in outer coordinates. Similar to the mean velocity and defect profiles, the turbulent quantities obtained over a particular surface condition, measurement plane, and test section exhibit Reynolds number similarity. The relative turbulent intensities at the edge of the upstream boundary layer over the smooth and rough surfaces are $u/U_e \approx 0.05$. This value is similar to typical values of $u/U_e = 0.04 \pm 10\%$ reported at the channel centerline in previous experiments [33]. Since the absolute values of u did not change significantly along the channel, the increase in U_e within the converging section decreased the relative turbulent intensity to approximately 0.04.

The Reynolds stresses measured over the smooth surface and in the upstream section (a_0P_1) of the channel are compared with DNS data from Ref. 31 in Fig. 6. The Reynolds stresses are normalized by U_τ^2 while the y values are normalized by either h^* or ν/U_τ. In the DNS study, h^* coincides with the channel centerline ($h^*=h$). Near the smooth-wall, the measured values of u^{+2} decrease more rapidly than the DNS. The relatively higher measured values are possibly due to the higher background turbulence in the experiment. The wall-normal stress v^{+2} (Fig. 6(b)), on the other hand, increased more significantly with increasing Reynolds number. Since v^{+2} is closely related to the diffusion of turbulent energy across the channel, differences observed in the measured data may indicate a more intense turbulent transport at the higher Reynolds number. The profile for $SMU_{0.25}$ compares well with the DNS except close to the edge of the boundary layer. For the Reynolds shear stress $-u^+v^+$ (Fig. 6(c)), the measured data showed no dependency on Reynolds number. However, when compared with the DNS, the maximum values are much smaller than observed in the DNS, possibly due to the relatively low values of the correlation coefficient (Fig. 6(d)). In the present study,

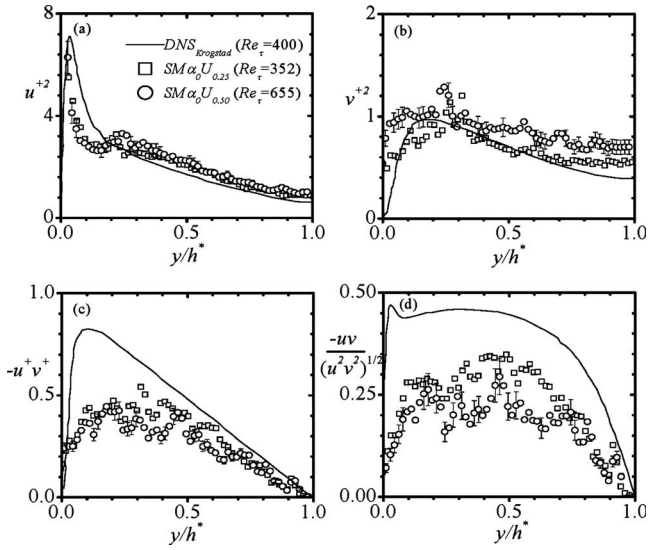

Fig. 6 Distributions of the Reynolds stresses and stress ratios over the smooth surface compared with DNS from Ref. [31]

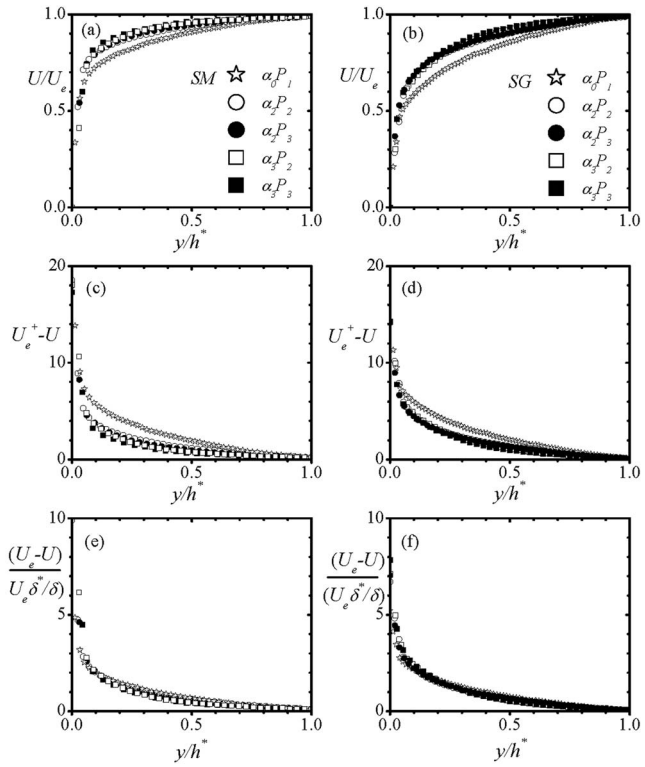

Fig. 7 Effects of FPG on the distributions of the mean velocity and the mean velocity defect over the smooth surface ((*a*), (*c*), and (*e*)) and sand grain roughness ((*b*), (*d*), and (*f*)) in the outer coordinates

the peak value of $-uv/(u^2v^2)^{0.5}$ for test SM$U_{0.25}$ was approximately 0.34 compared with 0.46 in the DNS study. The low values of $(-u^+v^+)_{\max}$ suggest that the viscous stresses constitute a significant portion of the total shear stress in the near-wall region.

3.3.2 Pressure Gradient Effects. In this section, the mean velocity, turbulent intensities, and Reynolds shear stress obtained at an approach velocity of $U_e \approx 0.5$ m/s over the various surfaces and test sections are used to examine FPG effects on the flow characteristics. Note that the strength of the pressure gradient (or K) increases as α increases from 0 deg at the upstream section through 2 deg to 3 deg within the converging section. The results are only presented for the smooth surface and sand grain roughness since the gravel roughness and sand grain exhibit similar trends. As expected, the mean velocity U/U_e becomes more uniform within the converging section (Figs. 7(*a*) and 7(*b*)), even over the sand grain and gravel roughness (not shown). The profiles of the mean velocity defect in classical scaling (i.e., $U_e^+ - U^+$) are shown in Figs. 7(*c*) and 7(*d*). A strong FPG effect is evident in the defect profiles over all surfaces. This is consistent with the trend in the mean velocity, since the effect of FPG is to increase the local mean velocity, thereby decreasing the velocity deficit. When the mixed outer scaling is used, both the smooth- and rough-wall profiles showed no FPG effects. The ability of the mixed scaling to collapse the defect profiles in ZPG and FPG turbulent flows over smooth and rough surfaces has been demonstrated in previous studies [15,16].

Figure 8 demonstrates the effects of FPG on the turbulent intensities and Reynolds shear stress normalized with (U_e, h^*). For all surfaces, the streamwise turbulent intensity is unaffected by FPG near the wall, but decays rapidly with FPG in the outer layer. The wall-normal turbulent intensity (Figs. 8(*c*) and 8(*d*)), on the other hand, decreased more dramatically with flow acceleration, suggesting that the "active" motion is more sensitive to external pressure gradients than the "inactive" motion. This is also demonstrated by the profiles of the Reynolds shear stress (Figs. 8(*e*) and 8(*f*)), where the decay in $-uv/U_e^2$ is even more dramatic than observed in the turbulent intensities. The reduction in the Reynolds shear stress can be explained as follows: In a two-dimensional incompressible flow, FPG would produce positive $\partial U/\partial x$ and negative $\partial V/\partial y$. Townsend [36] suggested that negative $\partial V/\partial y$ tends to flatten the large eddies and reduce their contribution to the Reynolds stresses. As a result, FPG should decrease the Reynolds stresses. The reduced amplitude of the eddies also implies that kinetic energy would be transferred from the turbulence field to the mean motion, resulting in substantially attenuated turbulence levels.

In the mixed coordinates (U_τ, h^*), as in Fig. 9, the turbulent intensities and Reynolds shear stress still decayed in the presence of increasing FPG, but less rapidly over the rough surfaces. For example, the overall decay in $(-u^+v^+)_{\max}$ over the smooth surface, sand grain, and gravel (not shown) were approximately 80%, 40%, and 23%, respectively. These results imply that rough surfaces reduce the turbulent intensity and Reynolds shear stress less dramatically than the smooth surface. The lower reduction over the rough-walls should be expected because of the opposing influence of wall roughness and the imposed FPG.

For a low Reynolds number smooth-wall turbulent boundary layer, the influence of flow acceleration on the Reynolds shear stress correlation coefficient was investigated by Fernholz and Warnack [37]. They found that with increased FPG, the correlation coefficient decreases in the inner layer and increases in the outer layer when compared with data in a ZPG at corresponding Re_θ. In the present study, the correlation coefficient decreases over the smooth-wall for $0.1 \le y/h^* \le 0.65$. The trend in the presence of surface roughness is less consistent since the correlation coefficient decreases with flow acceleration over the gravel (not shown) but remains relatively invariant over the sandpaper.

3.3.3 Roughness Effects. The experiments conducted with an approach velocity of $U_e \approx 0.5$ m/s are also used to examine the effects of surface roughness on the mean velocity and turbulent quantities. In this section, profiles obtained over the three different surfaces at a particular plane (P_1 and P_3) are plotted together. Note that in order to isolate pressure gradient effects from roughness effects, the profiles obtained in P_3 are staggered relative to those in P_1. In some of the following plots, a vertical line will be used to denote the edge of the roughness sublayer for Test

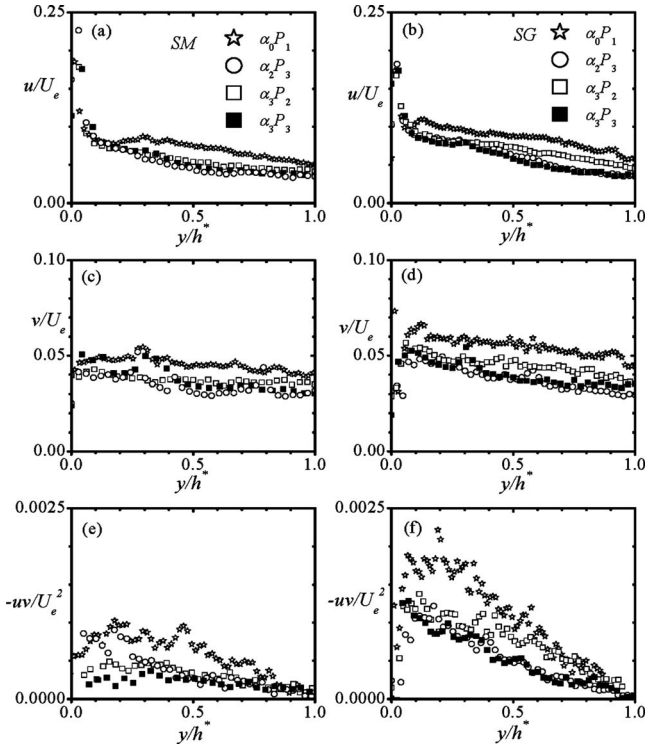

Fig. 8 Effects of FPG on the distributions of the turbulent intensities and Reynolds shear stress over the smooth surface ((*a*), (*c*), and (*e*)) and sand grain roughness ((*b*), (*d*), and (*f*)) in the outer coordinates

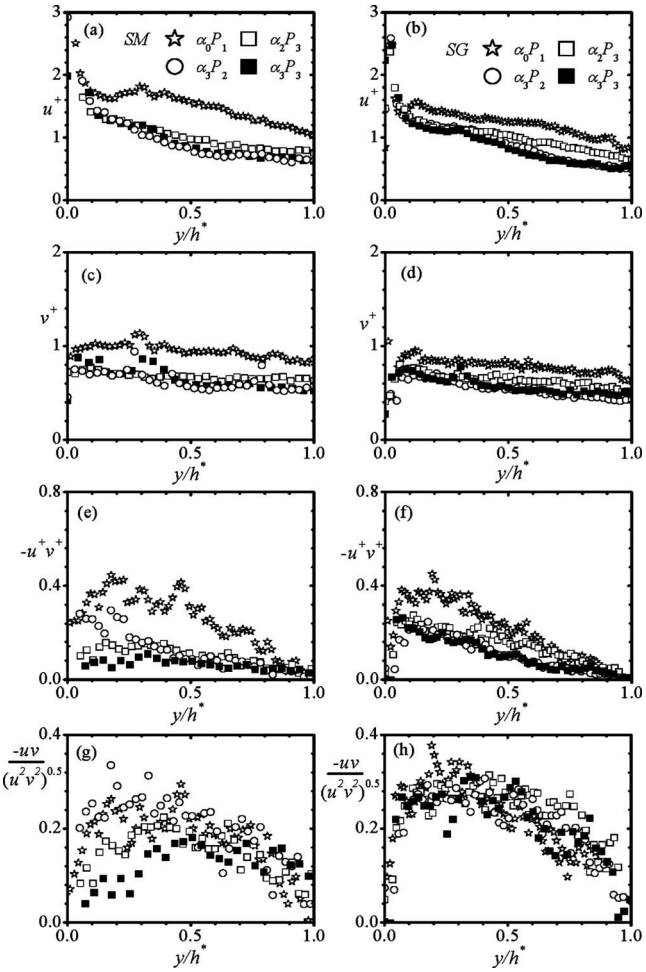

Fig. 9 Effects of FPG on the turbulent intensities and Reynolds shear stress normalized by (U_τ, h^*), and correlation coefficient over the smooth surface ((*a*), (*c*), (*e*), and (*g*)) and sand grain roughness ((*b*), (*d*), (*f*), and (*h*))

GV$\alpha_3U_{0.50}P_1$. As shown in Fig. 10(*a*), the effects of surface roughness were to make the mean velocity profiles normalized by U_e less uniform even in the presence of FPG. For the mean velocity defect, no roughness effects were observed when the mixed outer scaling was used. This observation is true at the upstream and converging sections. The turbulent intensities when normalized by U_e (Figs. 10(*c*) and 10(*e*)) are substantially higher over the rough surfaces than on the smooth surface. In the absence of FPG (P_1), roughness effects on the turbulent intensities are highest in the inner-half of the boundary layer. Significant differences are also observed between the Reynolds shear stress distributions over the smooth and rough surfaces (Fig. 10(*g*)). In a similar fashion to the FPG, it appears that the effect of surface roughness on $(v/U_e)_{\max}$ and $(-uv/U_e^2)_{\max}$ is more dramatic than observed for u/U_e. For example, the gravel roughness increased $(v/U_e)_{\max}$ and $(-uv/U_e^2)_{\max}$, respectively, by 155% and 130% at the upstream location. The results obtained from previous numerical and experimental studies in fully developed channel and ZPG turbulent boundary layers show that turbulent intensities and Reynolds shear stress increase with roughness effect (i.e., k_s^+).

It is now obvious that surface roughness substantially increased both the Reynolds shear stress ($-\rho uv$) and wall shear stress (ρU_τ^2) compared with the corresponding smooth-wall values. However, the ratio of the Reynolds shear stress to the wall shear stress ($-u^+v^+$) is independent of surface roughness at the upstream location (Fig. 10(*h*)). This would imply that the sand grain and gravel roughness increased both stresses proportionately in the absence of FPG. For the Reynolds shear stress, it is surprising that even within the roughness sublayer the stresses are not affected by surface roughness. In accordance with the wall similarity hypothesis, the Reynolds shear stress, with the exception of the data in P_3, is also universal outside the roughness sublayer.

Although surface roughness increased the turbulent intensities and Reynolds shear stress, the distributions of shear stress correlation coefficient, $-uv/(u^2v^2)^{0.5}$, and the stress ratios, v^2/u^2, $-uv/u^2$, and $-uv/v^2$, across the boundary layer (Fig. 11) are not significantly affected by surface roughness outside the roughness sublayer. The lack of sensitivity to roughness in the absence of the pressure gradient is consistent with the observations made by Ligrani and Moffat [38] in a ZPG turbulent boundary layer over densely packed copper spheres but at higher values of Re_θ (i.e., $6310 \leq \mathrm{Re}_\theta \leq 18{,}700$). According to Ligrani and Moffat [38], this should be expected since the processes involved in the production of turbulence do not change with surface roughness. The universal distribution of v^2/u^2 in P_1 would also suggest that the mechanism responsible for redistributing turbulent kinetic energy into the various components of the normal stresses is also not affected by surface roughness. The DNS data of Krogstad et al. [31] show differences between the rough- and smooth-wall values of v^2/u^2 only outside the roughness sublayer, while $-uv/v^2$ increased appreciably close to the ribbed wall.

3.3.4 Combined Pressure Gradient and Roughness Effects. The present section considers the combined effects of FPG and surface roughness on the flow characteristics. Cal et al. [15,16] noted that in a combined FPG and wall roughness, the roughness effect tends to predominate over the FPG. Tachie et al. [17] observed that the effects of FPG are less severe on fully rough surfaces (*k*-type ribs) than transitionally rough (*d*-type ribs) and

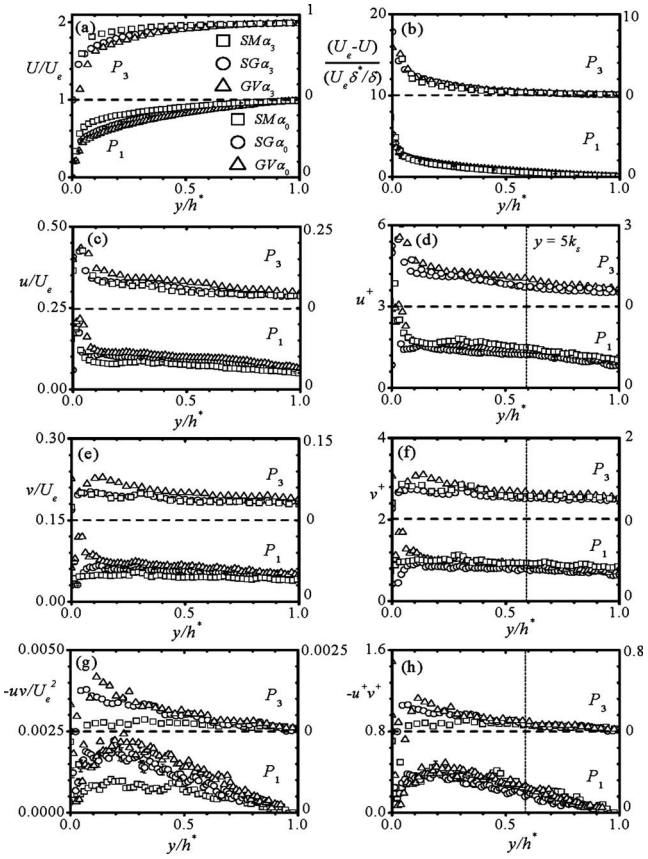

Fig. 10 Effects of surface roughness on the mean velocity defect, turbulent intensities, and the Reynolds shear stress. The vertical lines in (*b*), (*d*), (*f*), and (*h*) correspond to the edge of the roughness sublayer.

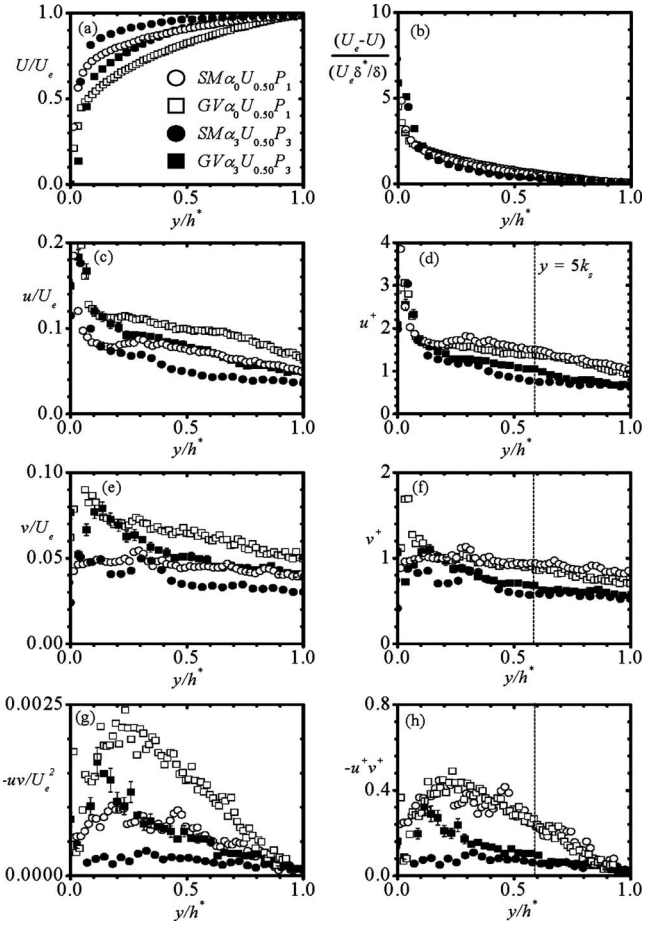

Fig. 12 Effects of combined FPT and surface roughness on the mean velocity, turbulent intensities, and the Reynolds shear stress

smooth surfaces. To study the combined effects of FPG and roughness, profiles at P_1 and P_3 over the smooth and rough surfaces are plotted together as in Fig. 12.

It should be recalled from the earlier analysis that the greatest effect of FPG (both in mean velocity and turbulent statistics) was produced over the smooth surface. It should also be recalled that, for a given test section (i.e., α_2 or α_3), the changes due to FPG were less dramatic over the rough-walls than observed over the smooth-wall. This would imply that in this flow where both the FPG and surface roughness increase, the flow statistics would show a stronger dependence on surface roughness. Figure 12(*a*) shows that this argument is valid where, for example, the profiles of U/U_e demonstrate a stronger roughness effect over the gravel in comparison with the smooth surface. When the mean velocity defect is scaled with the mixed outer scale the collapse of the profiles is excellent, but with the friction velocity (not shown), the effect of FPG appears to be stronger.

The profiles of the turbulent intensities in the outer coordinates are presented in Figs. 12(*c*) and 12(*d*). There is an increase in u/U_e and v/U_e within the roughness sublayer as the FPG increased. When the same quantities were scaled with the friction velocity, u^+ and v^+ decreased substantially under the influence of combined FPG and surface roughness. This may be due to the combined effects of FPG and surface roughness on the friction velocity. Note that in Table 2, U_τ increased with increasing FPG and surface roughness. The combined FPG and roughness effects on the Reynolds shear stress when normalized with U_e were to increase $-uv/U_e^2$ close to the rough-walls. As obvious in Fig. 12(*g*), this net increase is due to the more dramatic increase in $(-uv/U_e^2)_{\max}$ over the gravel roughness (130%) compared with the corresponding reduction by FPG over the smooth surface (i.e., 72%). In Fig. 12(*h*), on the other hand, FPG and roughness decreased $-u^+v^+$ over a considerable portion of the boundary layer.

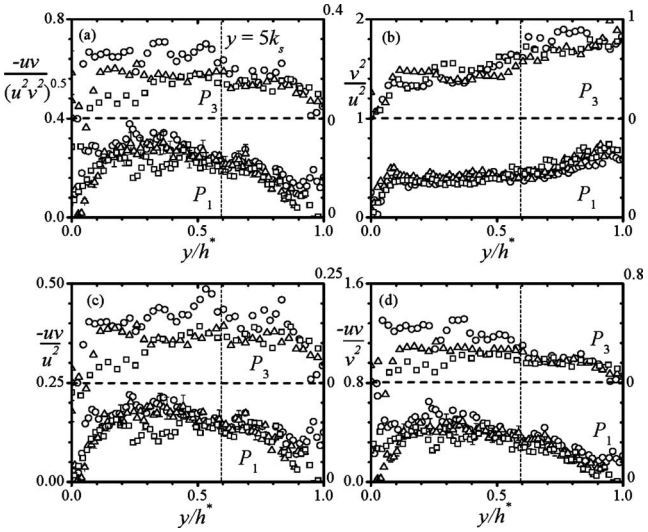

Fig. 11 Effects of surface roughness on the stress ratios. (*a*) $\rho_{uv}=-uv/(u^2v^2)^{0.5}$, (*b*) v^2/u^2, (*c*) $-uv/u^2$, and (*d*) $-uv/v^2$. The symbols are as in Fig. 10.

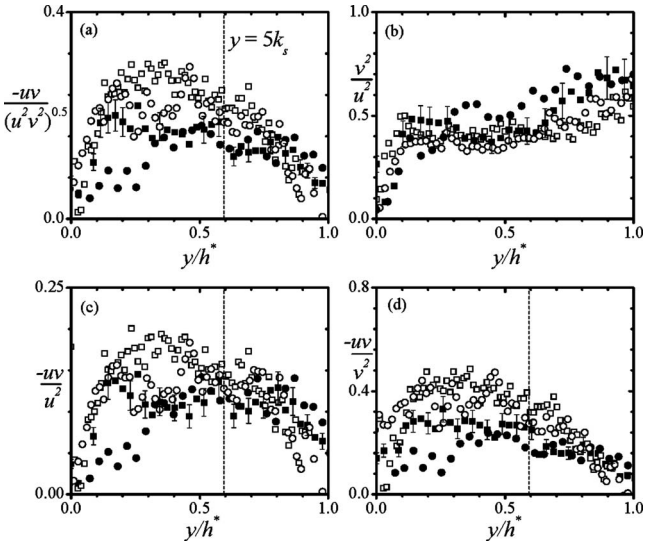

Fig. 13 Effects of combined FPG and surface roughness on the stress ratios. The symbols are as in Fig. 12.

Coleman et al. [14] reported a 23% reduction in the Reynolds shear stress as k_s^+ increased from 77 to 93.

The stress ratios are depicted in Fig. 13. Notwithstanding the scatter in the data sets, it appears the stress ratios are not significantly affected by a combination of FPG and surface roughness. The implication of this observation for v^2/u^2 is that in an increasing FPG, changing the surface roughness produces a negligible effect on turbulent mixing.

4 Summary and Conclusions

PIV measurements of moderate FPG over sand grain and gravel roughness in a asymmetric converging channel have been compared with reference smooth cases. Two angles of convergence have been investigated ($\alpha=2$ deg and 3 deg) in order to document the effects of increased FPG on the mean velocity and turbulent statistics.

The results demonstrate that, in the absence of a pressure gradient, surface roughness increases the mass and momentum flux deficits in comparison with the smooth-wall values. Due to the opposing influence of surface roughness and the imposed favorable pressure gradient, it was found that FPG reduces the effectiveness of roughness to increase mass and momentum flux deficits over the test sections. The mean velocity profiles over the smooth-wall show a diminishing outer wake region with increasing FPG, which is typical of most smooth FPG boundary layers at low Reynolds number.

The friction velocity and skin friction coefficient increased with surface roughness and FPG. However, the drag characteristics of the sand grain and gravel roughness decreased consistently in the presence of FPG. This resulted in lower roughness shift in the converging section and smaller values of k_s^+ and k_s/k. This implies that the boundary layer over the sand grain and gravel roughness became less rough when subjected to an increasing FPG.

With increasing FPG, the turbulent intensities and Reynolds shear stress decayed significantly irrespective of the surface condition. Distributions of the Reynolds stress ratios over the rough surfaces are unaffected by FPG outside the roughness sublayer. In the absence of FPG, however, the effects of surface roughness were confined to the roughness sublayer for u^+ and v^+, but $-u^+v^+$ remained invariant across the entire boundary layer.

Under the influence of combined FPG and wall roughness, both the mean velocity and turbulent statistics show a dominance of wall roughness over FPG. The correlation coefficient was invariant with increasing FPG over the sand grain and gravel roughness outside the roughness sublayer. Over all, the data analysis presented in this investigation suggests that in a turbulent flow subjected to a combined roughness and favorable pressure gradient, the roughness exerts a stronger influence on the mean and turbulent statistics than the pressure gradient.

Acknowledgment

The support of this work by the Natural Sciences and Engineering Research Council of Canada and The Canada Foundation for Innovation is gratefully acknowledged.

Nomenclature

C_f = skin friction coefficient
H = boundary layer shape factor
h^* = wall-normal location where the Reynolds shear stress changes sign from positive to negative
k = roughness height
k_s = equivalent sand grain roughness height
K = acceleration parameter
Re_θ = Reynolds number based on maximum velocity and boundary layer momentum thickness
U = streamwise component of mean velocity
U_e = maximum velocity
U_τ = friction velocity
u, v = streamwise and wall-normal turbulent intensities
$-uv$ = Reynolds shear stress
x, y = streamwise and wall-normal coordinates
y_o = virtual origin

Greeks

δ = boundary layer thickness
δ^* = boundary layer displacement thickness
κ = von Karman constant
θ = boundary layer momentum thickness
ΔB^+ = roughness shift

Superscript

$( )^+$ = normalization by inner variables

Subscript

$( )_{\max}$ = maximum or peak value

Abbreviations

CCD = charge coupled device
DNS = direct numerical simulation
GV = gravel roughness
SG = sand grain roughness
SM = smooth surface
ZPG = zero pressure gradient

References

[1] Bakken, O. M., Krogstad, P.-Å., Ashrafian, A., and Andersson, H. I., 2005, "Reynolds Number Effects in the Outer Layer of the Turbulent Flow in a Channel With Rough Walls," Phys. Fluids, **17**(6), p. 065101.
[2] Krogstad, P.-Å., and Antonia, R. A., 1999, "Surface Roughness Effects in Turbulent Boundary Layers," Exp. Fluids, **27**(5), pp. 450–460.
[3] Keirsbulck, L., Labraga, L., Mazouz, A., and Tournier, C., 2002, "Surface Roughness Effects on Turbulent Boundary Layer Structures," ASME J. Fluids Eng., **124**, pp. 127–135.
[4] Castro, I. P., 2007, "Rough-Wall Boundary Layers: Mean Flow Universality," J. Fluid Mech., **585**, pp. 469–485.
[5] Townsend, A. A., 1976, *The Structure of Turbulent Shear Flow*, 2nd ed., Cambridge University Press, Cambridge.
[6] Raupach, M. R., Antonia, R. A., and Rajagopalan, S., 1991, "Rough-Wall Turbulent Boundary Layers," Appl. Mech. Rev., **108**, pp. 1–25.
[7] Schultz, M. P., and Flack, K. A., 2007, "The Rough-Wall Turbulent Boundary Layer From the Hydraulically Smooth to the Fully Rough Regime," J. Fluid Mech., **580**, pp. 381–405.
[8] Grass, A. J., 1971, "Structural Features of Turbulent Flow Over Smooth and Rough Boundaries," J. Fluid Mech., **50**, pp. 233–255.
[9] Connelly, J. S., Schultz, M. P., and Flack, K. A., 2006, "Velocity-Defect Scaling for Turbulent Boundary Layers With a Range of Relative Roughness,"

Exp. Fluids, **40**, pp. 188–195.
[10] Badri Nayaranan, M. A., and Ramjee, V., 1969, "On the Criteria for Reverse Transition in a Two-Dimensional Boundary Layer Flow," J. Fluid Mech., **35**(2), pp. 225–241.
[11] Blackwelder, R. F., and Kovasznay, L. S. G., 1972, "Large-Scale Motion of a Turbulent Boundary Layer During Relaminarization," J. Fluid Mech., **53**, pp. 61–83.
[12] Escudier, M. P., Abdel-Hameed, A., Johnson, M. W., and Sutcliffe, C. J., 1998, "Laminarisation and Re-Transition of a Turbulent Boundary Layer Subjected to Favorable Pressure Gradient," Exp. Fluids, **25**, pp. 491–502.
[13] Fernholz, H. H., and Warnack, D., 1998, "The Effects of a Favourable Pressure Gradient and of the Reynolds Number on an Incompressible Axisymmetric Turbulent Boundary Layer. Part 1. The Turbulent Boundary Layer," J. Fluid Mech., **359**, pp. 329–356.
[14] Coleman, H. W., Moffat, R. J., and Kays, W. M., 1977, "The Accelerated Fully Rough Turbulent Boundary Layer," J. Fluid Mech., **82**(3), pp. 507–538.
[15] Cal, R. B., Brzek, B., Johansson, T. G., and Castillo, L., 2006, "Upstream Condition Effects on Rough Favourable Pressure Gradient Turbulent Boundary Layers," Collection of Technical Papers, 44th Aerospace Sciences Meeting and Exhibit.
[16] Cal, R. B., Brzek, B., Johansson, T. G., and Castillo, L., 2006, "LDA Measurements on Rough Turbulent Boundary Layers Subject to Strong Favourable Pressure Gradients," Proceedings of FEDSM.
[17] Tachie, M. F., Agelinchaab, M., and Shah, M. K., 2007, "Turbulent Flow Over Transverse Ribs in Open Channel With Converging Side Walls," Int. J. Heat Fluid Flow, **28**, pp. 683–707.
[18] Westerweel, J., 1997, "Fundamentals of Digital Particle Image Velocimetry," Meas. Sci. Technol., **8**, pp. 1379–1392.
[19] Shah, M. K., Agelinchaab, M., and Tachie, M. F., 2008, "Influence of PIV Interrogation Area on Turbulent Statistics up to 4th Order Moments in Smooth and Rough Wall Turbulent Flows," Exp. Therm. Fluid Sci., **32**, pp. 725–747.
[20] Coleman, H. W., and Steele, W. G., 1995, "Engineering Applications of Experimental, Uncertainty Analysis," AIAA J., **33**, pp. 1888–1896.
[21] Prasad, A. K., Adrian, R. J., Landreth, C. C., and Offut, P. W., 1992, "Effect of Resolution on the Speed and Accuracy of Particle Image Velocimetry Interrogation," Exp. Fluids, **13**, pp. 105–116.
[22] Forliti, D. J., Strykowski, P. J., and Debatin, K., 2000, "Bias and Precision Errors of Digital Particle Image Velocimetry," Exp. Fluids, **28**, pp. 436–447.
[23] Simpson, R. L., 1970, "Characteristics of Turbulent Boundary Layers at Low Reynolds Numbers With and Without Transpiration," J. Fluid Mech., **42**, pp. 769–802.
[24] Preston, J. H., 1958, "The Minimum Reynolds Number for a Turbulent Boundary Layer and the Selection of a Transition Device," J. Fluid Mech., **3**, pp. 373–384.
[25] Granville, P. S., 1977, "Drag and Turbulent Boundary Layers at Low Reynolds Numbers," J. Ship Res., **21**, pp. 30–39.
[26] Spalart, P. R., 1988, "Direct Simulation of a Turbulent Boundary Layer up to R_θ=1410 ," J. Fluid Mech., **187**, pp. 61–98.
[27] Balachandar, R., and Ramachandran, S. S., 1999, "Turbulent Boundary Layers in Low Reynolds Number Shallow Open Channel Flows," ASME J. Fluids Eng., **121**(3), pp. 684–689.
[28] Finnicum, D. S., and Hanratty, T. J., 1988, "Effect of Favourable Pressure Gradient on Turbulent Boundary Layers," AIChE J., **34**(4), pp. 529–540.
[29] Schlichting, H., 1979, *Boundary-Layer Theory*, 7th ed., McGraw-Hill, New York.
[30] Jiménez, J., 2004, "Turbulent Flows Over Rough Walls," Annu. Rev. Fluid Mech., **36**, pp. 173–196.
[31] Krogstad, P.-Å., Andersson, H. I., Bakken, O. M., and Ashrafian, A., 2005, "Experimental and Numerical Study of Channel Flow With Rough Walls," J. Fluid Mech., **530**, pp. 327–352.
[32] Antonia, R. A., and Kim, J., 1994, "Low-Reynolds-Number Effects on Near-Wall Turbulence," J. Fluid Mech., **276**, pp. 61–80.
[33] Durst, F., Fischer, M., Jovanovic, J., and Kikura, H., 1998, "Methods to Set Up and Investigate Low Reynolds Number, Fully Developed Turbulent Plane Channel Flows," ASME J. Fluids Eng., **120**(3), pp. 496–503.
[34] Zagarola, M. V., and Smits, A. J., 1998, "Mean-Flow Scaling of Turbulent Pipe Flow," J. Fluid Mech., **373**, pp. 33–79.
[35] Tay, G. F. K., 2009, "Rough-Wall Turbulent Flows in Adverse and Favourable Pressure Gradients," MSc thesis, University of Manitoba, Winnipeg, MB, Canada.
[36] Townsend, A. A., 1961, "Equilibrium Layers and Wall Turbulence," J. Fluid Mech., **11**, pp. 97–120.
[37] Fernholz, H. H., and Warnack, D., 1998, "The Effects of a Favourable Pressure Gradient and of the Reynolds Number on an Incompressible Axisymmetric Turbulent Boundary Layer. Part 2. The Boundary Layer With Relaminarization," J. Fluid Mech., **359**, pp. 357–381.
[38] Ligrani, P. M., and Moffat, R. J., 1986, "Structure of Transitionally Rough and Fully Rough Turbulent Boundary Layers," J. Fluid Mech., **162**, pp. 69–98.

Development of a Novel Oil Cavitation Jet Peening System and Cavitation Jet Erosion in Aluminum Alloy, AA 6063-T6

A. Sahaya Grinspan[1]
Senior Engineer
Technical Centre,
Advanced Engineering,
Ashok Leyland,
Chennai 600103, India
e-mail: sahayagrinspan.a@ashokleyland.com

R. Gnanamoorthy
Professor Deputy Director
Indian Institute of Information Technology,
Design and Manufacturing
(IIITD&M) Kancheepuram,
IIT Madras Campus,
Chennai 600 036, India

Compressive residual stresses that improve fatigue strength of material are obtained by peening the surface. Unlike traditional processes, a novel process of oil cavitation jet peening was developed. The process is based on implosion generated by the oil cavitation jet that plastically deforms the surface, imparting compressive residual stresses. The process developed involves injection of a high-speed oil jet (~230 m/s) through a suitably designed nozzle, into an oil-filled chamber containing the specimen to be peened. The region of cavitation generation, growth, and collapse, at the various cavitation numbers, was recorded using high-speed photography. To optimize the process parameters, a simple erosion test was performed in aluminum alloy, AA 6063-T6, specimens. The impact pressure generated during the implosion of cavitation bubbles causes plastic deformation and erosion of the surface. The surface deformation and cavitation jet erosion in the exposed specimens were characterized using optical and scanning electron microscopies. The standoff distance, which measures jet impact zone of the specimen from nozzle, was optimized at 15 mm in a cavitation number (which is a measure of pressure ratio across the nozzle) of 0.0017. The surface deformation produced by collapse of the oil bubble was similar to impact of oil droplet on the surface. The material removal mechanism during implosion of the bubble is predominately by ductile shear deformation. [DOI: 10.1115/1.3129134]

Keywords: cavitation jet, cavitation jet peening, oil jet peening, erosion

1 Introduction

Aerospace and automobile industries call for good fatigue resistant materials. Fatigue resistance of metallic materials is usually increased by introducing compressive residual stress at the surface. Compressive residual stress delays crack initiation and propagation, thus enhancing component life [1,2]. Mechanical surface modification processes, such as shot peening, laser shock peening, deep rolling, and roller burnishing, introduce the beneficial compressive residual stress. Liquid jet peening processes, such as water jet peening and oil jet peening, were developed to peen the surfaces more uniformly, and even inaccessible component contours can be effectively peened [3–5]. The liquid jet processes involve water or oil droplets impinging the specimen surface at high velocities. The oil droplet generates an impact pressure, at the surface, that exceeds the yield strength of the materials. At every drop impingement, the impact pressure builds up within a few milliseconds and causes local plastic deformation. The compressive residual stress formed at the surface was about 85% of yield strength of materials [6]. In addition, the introduction of compressive residual stress was similar to that resulted in conventional shot peening process [7]. Oil jet peening improves the fatigue strength of medium carbon steel, AISI 1040, by about 17% compared with the unpeened specimen [8]. This process, however, has loss of oil during the peening processes.

Water cavitation jet peening is another process used for manganese steel, carbonized steel, tool steel, aluminum alloys, and titanium alloy [9–11]. The advantage of cavitation jet peening process was that the peened surface was less rough compared with shot peening, since there was no solid body collisions involved [11]. Odhiambo and Soyama [12] reported that fatigue strength improved by water cavitation jet peening was 4% higher than that of shot peening. The increase in fatigue strength was attributed to good surface finish and compressive residual stress imparted, which delayed crack initiation and retardation of fatigue crack growth propagation. Compared with shot peening and laser shock peening, water cavitation jet peening has more potential to treat the surface of complex shaped components, such as gear, shaft, turbine blades, and grooves [13].

Oil cavitation jet peening process developed in this study is derived from the principle of mechanical surface treatment, where implosion generated by an oil cavitation jet is allowed to deform the surface, which introduces compressive stresses in the sample. The process involves injection of a high-speed oil jet through a nozzle, into an oil-filled chamber containing the specimen to be peened reducing significant oil loss. The process is useful to peen surface of both low yield strength metallic materials (aluminum alloys, copper, and magnesium alloy) and high yield strength metallic materials (stainless steels, carbon steels, alloy steels, and titanium alloys). The potentials of oil cavitation jet peening, in terms of the compressive residual stress formation, hardening, and surface morphological changes in aluminum alloy, were investigated and reported elsewhere [14].

The present study is focused on the development of a suitable experimental setup for oil cavitation jet peening process, and optimization of the operating parameters in aluminum alloy AA6063-T6. The characteristics of the oil cavitation jet have been assessed using high-speed photography, in which the regions of bubble formation, growth, and collapse at various upstream pressures (or cavitation numbers) have been determined.

[1]Corresponding author.

Contributed by the Fluids Engineering Division of ASME for publication in the JOURNAL OF FLUIDS ENGINEERING. Manuscript received September 19, 2008; final manuscript received March 23, 2009; published online May 14, 2009. Assoc. Editor: Theodore Heindel.

2 Cavitation

Cavitation normally causes severe damage in hydraulic machinery such as pumps, valves, and hydroturbine. However, over the past few years, cavitation has received a considerable attention, primarily with laboratory experiments, in order to understand their behavior and to determine the feasibility of their use in various applications such as peening [9–11,15] and cutting [15].

2.1 Cavitation Mechanisms. Cavitation is defined as the phenomenon of the formation of vapor bubbles of a flowing liquid in a region where the pressure of the liquid falls below its vapor pressure, P_v [16]. When the liquid that contains cavities is subjected to high hydrostatic pressure, the bubbles can collapse. When this collapse occurs at a surface, the associated pressure can cause surface deformation. Tomita and Shima [17] studied the mechanism of surface deformation caused by the collapse of bubbles. This study concluded that implosion of bubbles generated microjets that impacts the surface at a speed of about 100 m/s leading to surface deformation. The diameter of the microjet generated was estimated to be one-tenth of the initial bubble diameter [18]. The collapse of a spherical bubble results in a shock wave pressure of about 1000 MPa [18]. However, this pressure attenuates within a distance that is approximately the radius of the bubble [18]. Such repeated impact loads on a small area of the component surface cause surface deformation. The impact pressure, P_{imp}, developed by the collapse of bubble can be described as [19]

$$P_{\text{imp}} \approx \rho V_j C \tag{1}$$

where ρ and C are the density and velocity of sound in liquid, respectively, and V_j is the velocity of the micro jet. However, a complete detail of the mechanism behind cavitation impact is still unknown.

There are other processes that generate cavitation such as ultrasonic generator and high-speed water (liquid) tunnels. The advantage of the oil cavitation jet (high-speed submerged jet) in the present study is that there is a control over the cavitation number using independent hydrostatic parameters, such as upstream pressure and downstream pressure of nozzle. Thus, the cavitation jet apparatus can simulate several cavitating conditions [20] and more specifically preferred for peening [9–11,15] and cutting [15].

2.2 Cavitation in a Submerged Nozzle. The oil flow rate in a nozzle is influenced by parameters such as pressure difference across the nozzle (i.e., ΔP=upstream pressure P_1 and downstream pressure P_2), geometry of the nozzle, and diameter and length of the nozzle [21]. The shape of the inlet corner of the nozzle decides the flow path of the liquid. The liquid flowing through the nozzle forms a jet, whose area of cross section is less than that of the nozzle [22]. The area of the jet of liquid goes on and decreases as it progresses from the nozzle to get a small area (Section *C-C* in Fig. 1) known as vena contracta [22]. At this section, the steam lines are straight, parallel to each other, and perpendicular to the plane of the nozzle. The velocity of the liquid is higher than the initial velocity of the liquid. Beyond the vena contracta, the liquid jet diverges. When the pressure difference across the nozzle, ΔP, increases sufficiently, cavitation occurs in the exit flow. When the upstream pressure of the nozzle increases, the cavitation builds up enlarging the cavitation region beyond the exit of the nozzle. The high velocity of liquid in the vena contracta drastically decreases the static pressure. When the static pressure decreases below the vapor pressure, P_v, of a liquid, cavitation forms in the region. The formation of cavitation (vapor bubbles) starts from boundary layers of the nuclei, minute solid particles or gas bubbles entrain the fluid. Recovery of the pressure after the vena contracta raises the pressure above the liquid vapor pressure, causing collapse of the vapor bubbles (i.e., cavities, which are traveling along the flow, collapse when they enter into higher-pressure region of the flow).

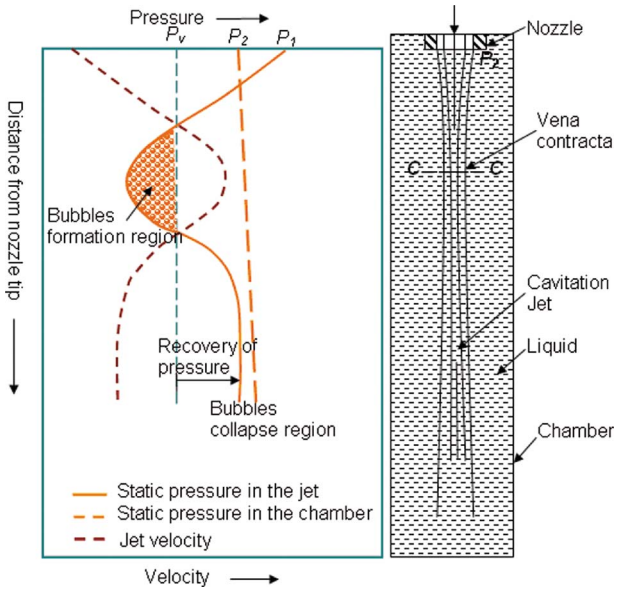

Fig. 1 Pressure and velocity change in a jet in the cavitation condition.

2.3 Cavitation Erosion. Cavitation jet erosion is the material removal of a solid surface caused by impact of cavitation jet [23]. The degree of the cavitation jet erosion depends on various factors such as intensity of cavitation, geometry of cavitation jet, pressure and temperature in a system, properties of fluid such as viscosity and density, and material properties such as hardness, work hardening capability, and grain size [21].

Pai and Hargreaves [24] performed cavitation jet erosion experiments on various metals, including aluminum alloy, AA5005, using hydraulic fluids and reported that an increasing viscosity of the oil led to decrease in the rate of growth and collapse of bubble and hence reduce erosion on the surface of the specimen. Talks and Moreton [25] and Tsujino et al. [26] reported that the cavitation jet erosion rate by mineral oil on different steels was less than that by water. These studies reported that sudden implosion of oil bubble at a surface, local stress in the surface exceeds the yield strength of materials. As the surface is subjected to repeated implosions of oil bubbles in the cavitation jet, a severe plastic deformation occurred, followed by surface erosion.

Flow visualization technique is an important tool in fluid dynamics research. With the help of the flow visualization and simple erosion test, it is possible to identify where the preferred collapse points are located and how the location and density of the bubbles changed with cavitation number [15]. Many researchers have made efforts to observe and to visualize the cavitation jet in order to understand its behavior, the mechanisms of formation of the cavitation. Yamaguchi and Shimizu [27] observed the structure of cavitation jet of high water base fluid (HWBF) and tap water. The study reported that the cavity clouds appear to be continuous near the jet exit but separate and develop into lumps as they travel with the jet. After impingement, the cavity clouds splash radially. Soyama et al. [28] reported that cavitation region shedding and the breakdown of the cloud of the cavitation jet in water took place periodically, with frequency in the range 0.5–2 kHz. The frequency depends on the cavitation numbers of the cavitation jet but does not depend on the nozzle geometry.

The failure mode by cavitation is influenced by strain-rate sensitivity of the material [16]. Generally, cavitation failure occurs as a ductile or brittle failure. The ductile failure mechanism predominates in metals with face-centered cubic (fcc) structure (Al, Cu, Ni, Ag, and austenitic stainless steels), which have low values of strain-rate sensitivity as against body-centered cubic (bcc) structure (ferritic steel, Cr, and W), which have high values of strain-

rate sensitivity. Metals with hexagonal close-packed (hcp) structure (Mg) may be strain-rate sensitive. Metals with high strain-rate sensitivity work harden rapidly and are influenced by peening operation and fail with cleavage facets. A comparison between response of several metallic materials to liquid (water) jet impact and their response to cavitation impact [23] shows that aluminum alloys, Al–0.45% Mg, Al–1.02%Mg, and Al–1.0% Cu respond in a very ductile manner to both cavitation and liquid jet impact [23]. Undulations and craters developed all over the sample surfaces as a result of extensive plastic deformation and erosion occurred by ductile shearing of the rims of craters. In contrast, the erosion of bcc iron by both cavitation and liquid jet impact was a mixture of ductile shear and brittle cleavage.

In order to determine the evolution of cavitation erosion (i.e., erosion rate), many experiments were performed [29]. From these studies, it was found that there are various stages in the cavitation erosion process. Experimental studies reported that a little mass loss was observed in the early stage of the cavitation (i.e., incubation period) [29]. The incubation stage is the initial period of time during which damage of the materials is not apparent. Cavitation jet peening should be performed at the incubation stage [9]. This stage was often followed by a period of large increase in erosion rate (i.e., accumulation period) and a constant mass loss (i.e., steady state). After that, a decrease in erosion rate was often observed (i.e., attenuation stage). Rao and Buckley [30] performed investigations in the early stage of the cavitation on materials such as aluminum alloy, AA 6061-T6, copper, brass, and bronze. The investigations were conducted in a viscous mineral oil (density of $\rho=869$ kg/m^3 and kinematic viscosity at 20°C $=1.1\times10^{-4}$ m^2/s). The study reported that erosion occurred by shearing and necking of the surface undulations caused by plastic deformation.

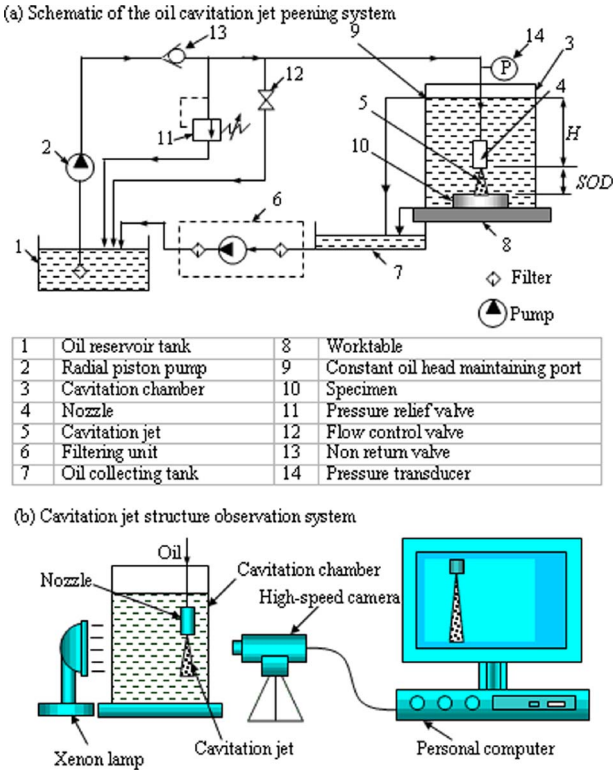

1	Oil reservoir tank	8	Worktable
2	Radial piston pump	9	Constant oil head maintaining port
3	Cavitation chamber	10	Specimen
4	Nozzle	11	Pressure relief valve
5	Cavitation jet	12	Flow control valve
6	Filtering unit	13	Non return valve
7	Oil collecting tank	14	Pressure transducer

Fig. 2 Schematic of the oil cavitation jet peening system developed: (*a*) oil cavitation jet peening system and (*b*) illustration of cavitation jet structure observation system employed

3 Experimental Setup and Procedures

3.1 Oil Cavitation Jet Peening Setup. The design and development oil jet peening system were reported elsewhere [5]. In order to perform oil cavitation jet peening, the oil jet peening system was modified. A cavitation chamber and an oil filtering unit were additionally incorporated to the oil jet peening system. Figure 2(*a*) shows the schematic of the setup. A radial piston pump was used, which was driven by a three-phase induction motor with a power of 11.2 kW. It can deliver oil pressure up to maximum of 100 MPa with an oil flow rate of 1.13×10^{-5} m^3/s. The oil reservoir tank had a volume of 0.75 m^3. In order to recycle the oil that comes after erosion/peening, the filtering unit was developed. The filtering unit comprised of three components: a suction filter (5 μm), a gear pump, and a discharge filter (5 μm). The gear pump was driven by a motor with a power of 0.37 kW. The inlet of the filtering unit was connected to the oil-collecting tank and the outlet of the filtering unit was connected to the oil reservoir tank. The oil-collecting tank has a volume of 0.5 m^3. During oil cavitation jet peening or erosion operation, the filter unit delivers the filtered oil to the oil reservoir tank for further use. As the oil was filtered using the well filter (5 μm), the surface would not be damaged by impact of particles. The cavitation chamber was fitted to the worktable of the oil jet peening unit. The cavitation chamber was made of Plexiglas to perform flow visualization. The cavitation chamber has a volume of 0.25 m^3. A specimen fixture (i.e., specimen holder) was fixed into the cavitation chamber. In order to maintain a constant head, H, of oil in the cavitation chamber, a hole was provided in the cavitation chamber. A cylindrical nozzle was used for generating the cavitation jet. The nozzle was made of alloy steel (En 31 steel) with a throat diameter of 0.25 ± 0.1 mm and length of 2 ± 0.1 mm. The geometry of the nozzle was reported elsewhere [5]. The discharge coefficient, C_d, of the nozzle was 0.61 ± 1. The nozzle was oriented perpendicular to the specimen surface. The jet flow behavior was characterized in terms of cavitation number, which is defined as a measure of the resistance of flow to cavitation [12]. The cavitation number was varied by controlling the upstream pressure, P_1 of the nozzle (i.e., oil injection pressure) and standoff distance. The cavitation number, σ, depends on the downstream pressure of the nozzle, P_2, and the upstream pressure, P_1, of the nozzle as follows:

$$\sigma \cong \frac{P_2}{P_1} \tag{2}$$

The upstream pressure of the nozzle was measured by using a pressure transducer with an accuracy of 0.1 MPa. The downstream pressure of the nozzle was calculated from the oil head in the cavitation chamber (i.e., oil head above the nozzle exit). Therefore,

$$P_2 = P_{\text{atm}} + \rho g H \tag{3}$$

where P_{atm} is the atmosphere pressure (=0.103 MPa) and g is the acceleration due to gravity (=9.81 m/s^2). The oil reservoir tank and cavitation chamber were filled with antiwear hydraulic oil, ISO VG 68. Table 1 shows the specification of antiwear hydraulic oil, ISO VG 68, used for this study. The hydraulic oil was injected at a desired constant pressure into the cavitation chamber through

Table 1 Specification of antiwear hydraulic oil VG 68 used

Density at 15°C (kg/m^3)	884 ± 0.1
Kinematic viscosity at 40°C (mm^2/s)	68 ± 5
Kinematic viscosity at 100°C (mm^2/s)	8.5 ± 0.02
Viscosity index	95 ± 0.2
Pour point (°C)	-6 ± 0.5
Flash point (°C)	210 ± 2
Vapor pressure at 20°C (N/m^2)	<133.42

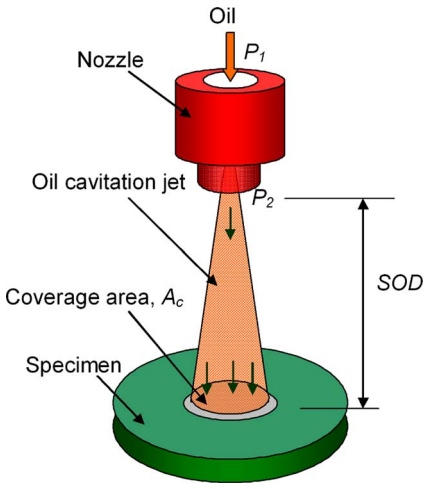

Fig. 3 Parameters involved in oil cavitation jet peening

the cylindrical nozzle.

The nozzle tip was placed at a constant head, H, 200 mm (i.e., P_2=0.1050 MPa). The structure of the cavitation jet was observed at various upstream pressures, P_1, 10 MPa, 20 MPa, 30 MPa, 40 MPa, 50 MPa, and 60 MPa, and the corresponding cavitation numbers, σ, are 0.0105, 0.0052, 0.0035, 0.0026, 0.0021, and 0.0017, respectively. Figure 2(*b*) shows the illustration of the cavitation jet structure observation system employed. Cavitation jet images were captured at a speed of 200 fps (frames per second) by using a high-speed camera (EPIX, Model Name: Silicon Video 642), so that the interval between the two frames was about 5 ms. For a light source, a xenon arc lamp was employed. Reflective kind illumination was used. The camera and the xenon arc lamp were set on the same side against the oil cavitation jet. Images were captured five times repeatedly at each upstream pressure. The images were calibrated by using image analyzer software DEWINTER MATERIALS PLUS. The cavitation jet diameter and axial length of jet were determined from the images using the image analyzer software.

3.2 Optimization of Standoff Distance. The parameters involved in oil cavitation jet erosion process are shown in Fig. 3. The standoff distance (SOD) is defined as the distance from the nozzle tip to the surface of specimen. The standoff distance is the major parameter that influences the impact pressure developed on the surface. The optimum standoff distance, SOD_{opt}, is a distance at which the cavitation jet generates high impact pressures on the specimen surface due to large numbers of implosion of bubbles. At this region, therefore, maximum erosion takes place on a specimen. In order to find the optimum standoff distance, a simple erosion test was conducted. Samples made of aluminum alloy, AA6063-T6, were machined to the shape of disk with a diameter of 8 mm and a thickness of 4 mm, according to ASTM standards [20]. The surfaces were polished using silicon carbide abrasive paper No. 1200. Table 2 and 3 show the chemical composition and mechanical properties of aluminum alloys, AA 6063-T6, used, respectively. This alloy has applications such as automobile wheels and many structural members. The microhardness on the surface of the specimens is determined at a load of 100 g (0.98 N) using microhardness tester (Tukon, Model 300) with a diamond indenter. The average Vickers hardness measured on the surface of

Table 2 Chemical composition (in wt %) of test material

Material	Cu	Mg	Si	Fe	Mn	Zn	Ti	Al
AA6063-T6	0.1	0.4–0.9	0.3–0.7	0.6	0.3	0.2	0.2	Bal.

Table 3 Mechanical properties of test material

Material	σ_{YS} (MPa)	σ_{UTS} (MPa)	HV	% El
AA6063-T6	150 ± 4	185 ± 6	83 ± 3	7 ± 0.1

specimens was about 83. The specimens were exposed to oil cavitation jet at the standoff distances varied between 10 mm to 35 mm in the interval of 5 mm. A constant upstream pressure, P_1, of 60 MPa was maintained. The nozzle tip was kept at a constant head, H, of 200 mm. Each test specimen is exposed to the cavitation jet for an exposure time, t_e, of 500 s. The standoff distances were selected from the results obtained from the high-speed camera. Five specimens were exposed subsequently at each condition. The mass of specimen was measured by using a precision electronic balance with an accuracy of 0.01 mg. The mass of specimen was measured before, m_1, and after the erosion test, m_2. Thus, the mass loss, Δm, was calculated as

$$\Delta m = m_1 - m_2 \tag{4}$$

4 Results and Discussion

The uncertainties in the experiments are as follows: the SOD ±0.1 mm, the mass loss (Δm) ±0.01 mg, and the upstream pressure (P_1) ±0.1 MPa. The constant head of oil in the cavitation chamber, H, is ±0.1 mm, the length of cavitation jet, L_j, is ±0.1 mm, the diameter of cavitation jet, Dj, is ±0.1mm, the cavitation number, σ, is ±0.0001 mm, and the exposure time, t_e, is ±5 ms.

4.1 Structure of Oil Cavitation Jet. Figure 4 shows the sequence of images (at the time of 25 ms, 125ms, 225 ms of 325 ms) of cavitation jet structures at various upstream pressures. In general, cavitation originates in the regions of low vapor pressure in liquid. The clouds of bubbles appear as white color in the images. Clouds appear continuously near the nozzle at all tested pressures. The structure of cavitation jet depends on the upstream pressure (or cavitation number). Many bubbles were generated at the upstream pressures of 50 MPa and 60 MPa, due to the low cavitation numbers. Figure 5 shows the cavitation jet length at various pressures as a function of time. At all upstream pressures, the length of oil cavitation jet increases rapidly at initial stages, and then it stabilizes after a few milliseconds. The times were about 105 ms, 155 ms, 215 ms, 255 ms, and 275 ms for the upstream pressures of 20 MPa, 30 MPa, 40 MPa, 50 MPa, and 60 MPa, respectively. A similar trend was observed at all upstream pressures. The cavitation jet lengths observed from the images varied about ±6%. Figure 6 shows the cavitation jet diameter, D_j, as a function of distance from nozzle tip, L. When the upstream pressure of nozzle increases, the quantity of bubble generation was increased; therefore, the cavitation jet diameter increased. No significant difference was observed in the cavitation jet lengths and jet diameters of the upstream pressures 50 MPa and 60 MPa. The cavitation jet diameters observed from the images varied about ±4%.

Figure 7 illustrates the cavitation jet structure at various upstream pressures. At low pressure (10 MPa), few spherical bubbles were generated just below the nozzle tip. At the region just below the nozzle, the jet was the combination of liquid jet and bubbles. Whereas at the high upstream pressures (50 MPa and 60 MPa), many bubbles were generated at the nozzle tip with a diameter of about five times higher than the nozzle diameter due to the low cavitation number. When a high-speed cavitation jet propagates in liquid, the jet diverges due to high drag force. As a result, the bubbles traveling velocity was decreased. However, no significant difference was observed in jet diameters of upstream pressures 50 MPa and 60 MPa (Fig. 6). In addition, a high white color intensity region was seen at a certain distance from the

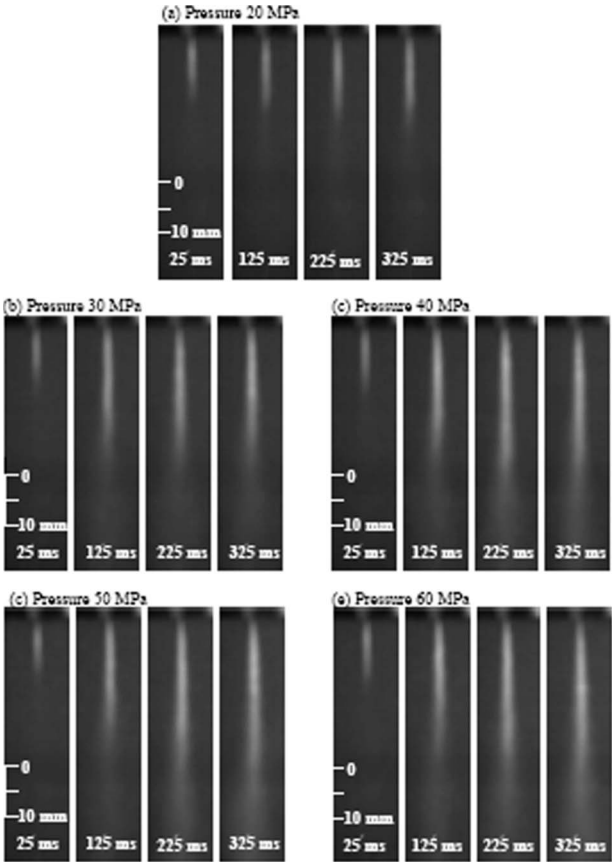

Fig. 4 Sequence of images showing the oil cavitation jet structures at various upstream pressures: (*a*) 20 MPa, (*b*) 30 MPa, (*c*) 40 MPa, (*d*) 50 MPa, and (*e*) 60 MPa

nozzle tip in the images. It indicates the large quantity of bubble region in cavitation jet. The region, where large quantity of bubble was observed, is suitable for peening because a high impact pressure would be generated. In the diffusion region, the cavitation region was entirely disintegrated into individual bubbles, which disappear quickly.

4.2 Optimum Standoff Distance. Surface deformation is a localized plastic deformation, which occurs on the surface due to implosion of an oil bubble. Cavitation erosion is defined as the progressive loss of material from the solid surface due to continuous exposure to cavitation jet [20]. The mass losses in the specimens exposed to the standoff distances 10 mm and 15 mm were about 0.9 mg and 1.6 mg, respectively. The mass losses, Δm, in the specimens exposed at the standoff distances 10 mm and 15 mm varied about $\pm 6\%$. The mass losses observed in specimens exposed at the standoff distances of 25 mm and 35 mm are negligible. However, the surface deformation occurred in specimen exposed at the standoff distance of 25 mm was larger than that in specimen exposed at standoff distance of 35 mm. It indicates that the impact pressure developed by the cavitation jet is maximum at a distance from the nozzle tip. It confirms the result, which was observed from the structure of oil jet (i.e., the region, where a large quantity of bubble was generated). Yamuchi et al. [15] and Sun et al. [31] reported a similar result from their studies on water cavitation jet erosion.

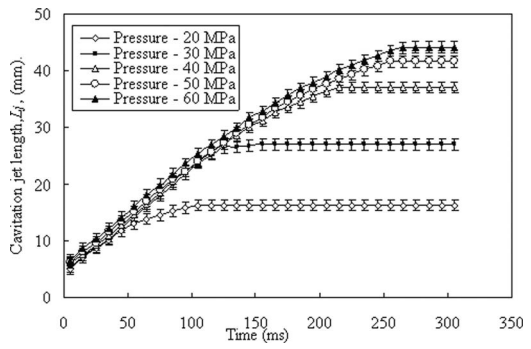

Fig. 5 Cavitation jet length at various upstream pressures

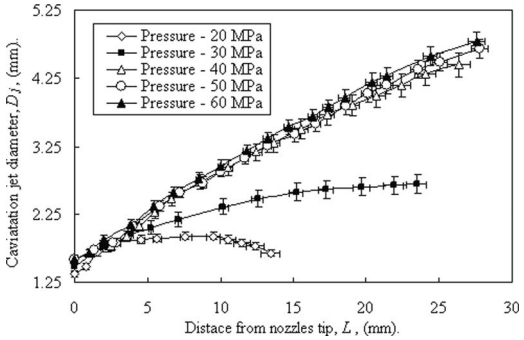

Fig. 6 Cavitation jet diameter at various upstream pressures

The surface of aluminum alloy, AA 6063-T6, eroded by oil cavitation jet at an upstream pressure of 60 MPa (i.e., cavitation number of 0.0017) under various standoff distances is shown in Fig. 8. The standoff distance influences significantly the surface deformation and erosion. In specimens exposed at the standoff distance of 15 mm, severe erosion occurred due to impact of high intensity cavitation. A number of large size craters with rims were observed within the impacted region. As the surface experiences multiple and repeated impacts, the rim or shear lip develops around the crater. The crater size was about 10–100 μm. It confirms the region, where a large quantity of bubble was generated. Moderate size craters with rims ($\sim$10–60 μm) was observed in specimens exposed at standoff distances of 10 mm and 25 mm. Specimens exposed at the standoff distance of 35 mm, very small craters of size of about 7–20 μm, were observed. As the surface roughness increases during successive repeated impact of microjets, shear stress develops at the rim of craters. Consequently, the rims break in the form of small fragments. As the erosion occurs

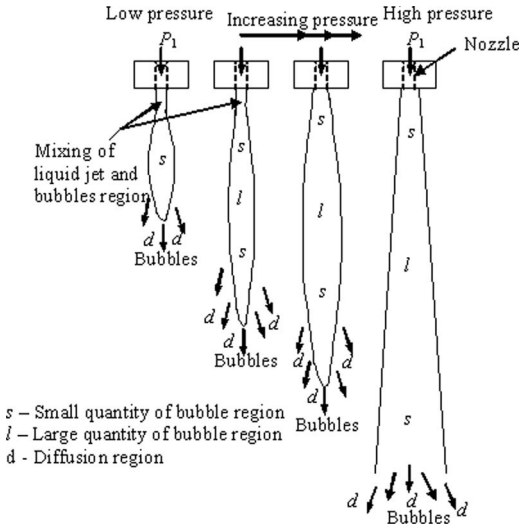

Fig. 7 Schematic depicting the oil cavitation jet structures under different upstream pressures

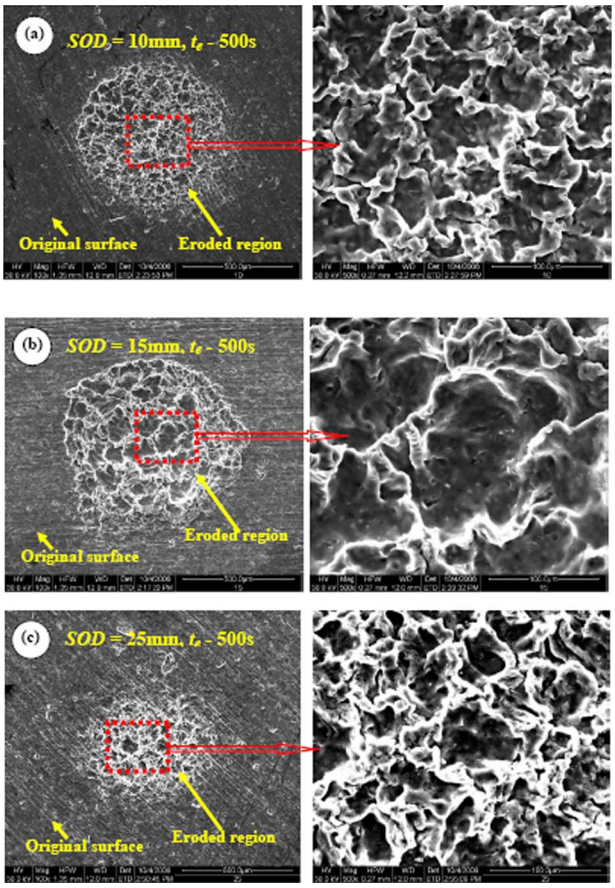

Fig. 8 Micrographs showing the surface of aluminum alloy, AA6063-T6, eroded by oil cavitation jet under various SODs: (*a*) SOD=10 mm, (*b*) SOD=15 mm, and (*c*) SOD=25 mm

continuously, the size of damage region and depth of penetration were increased (Fig. 9). Many irregular shaped craters with rims were also observed. At the center of exposed region, the size of crater was larger than that observed at the outer zone, indicating a large intensity of clouds at the center of cavitation jet. At the high standoff distance, 35 mm, the pressure wave was attenuated as it travels 35 mm to the single bubble that implodes in from microjet.

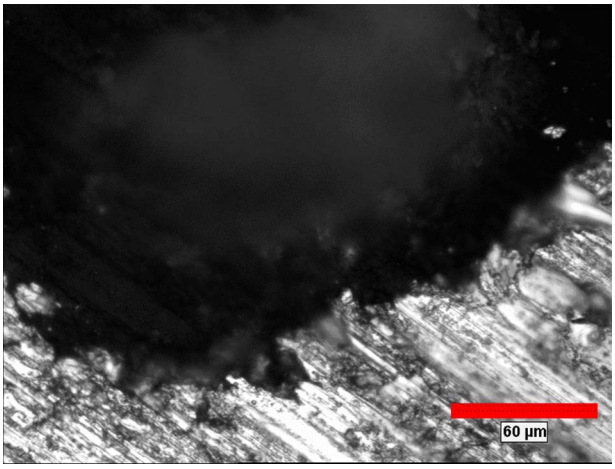

Fig. 9 Micrograph showing the sectional view of aluminum alloy, AA6063-T6, eroded by oil cavitation jet under a SOD of 15 mm

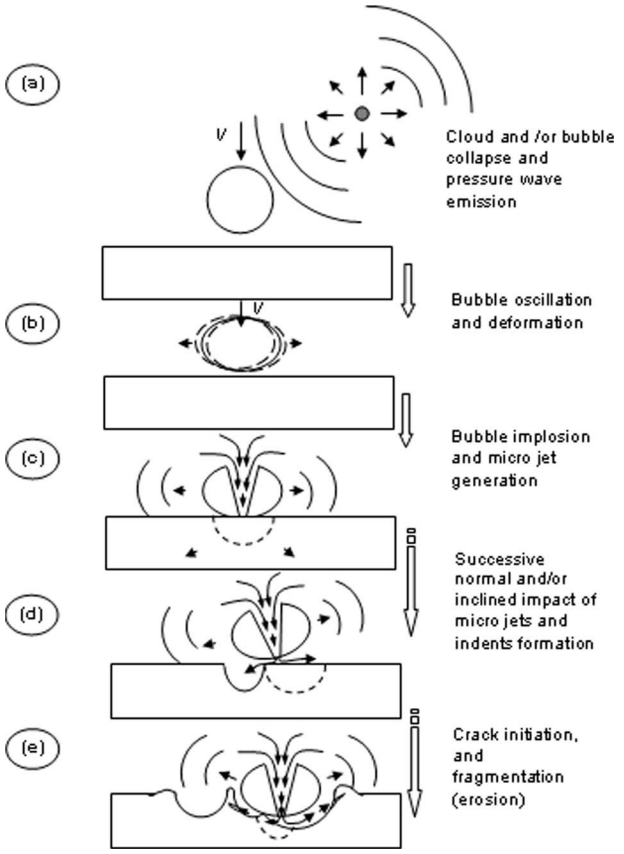

Fig. 10 Mechanism of oil jet cavitation erosion on ductile materials: (*a*) collapse of clouds and/or bubbles, and pressure wave emission; (*b*) bubble oscillates and deforms near the surface; (*c*) implosion of bubble and micro jet formation; (*d*) subsequent implosion of another bubble of oil cavitation jet forms craters; and (*e*) initiated the cracks in the rims, crack growth, and fragmentation of rims due to radial force

Therefore, many small size craters were observed. The craters developed on the specimens surfaces are due to large plastic deformation and erosion.

4.3 Mechanism of oil Cavitation Jet Erosion. Aluminum alloy, AA 6063-T6, responds in a ductile manner during oil cavitation jet impact. The mechanism of material removal was complex. Figure 10 shows the mechanism of oil cavitation jet erosion in a ductile material. When the bubbles collapse, the potential energy present in bubbles transfers into acoustic energy and radiates strong acoustic pulsations in the fluid. The magnitude of this shock wave was attenuated with traveling distance and reached the bubble existing near the clouds. As the pressure wave reaches another bubble, it oscillates and deforms simultaneously [19]. At the same time, the bubble travels with certain velocity and impacts the surface. Therefore, the bubble imploded near the surface. The microjet generated during implosion affects the surface. As a result, an impact pressure was developed at the interface between the microjet and surface. Simultaneously, the shock wave was also radiated near the surface. When the magnitude of impact pressure exceeds the yield strength of material, plastic deformation occurs at the surface. In cavitation jet impact, there will be numerous cavitation bubbles being generated and imploded repeatedly on the surface. Due to this, many small indents were formed with irregular shapes on the exposed surface. The craters have rims indicating a severe ductile deformation. The irregular shape was due to the overlap between the craters. Impact and radial flow of microjet result in shear stress and shock wave. The rims, as well as the sharp edges of the deformed material, shear during succes-

sive impact of microjet. Once the surface becomes very rough, the effect of radial flow and the shock wave was pronounced. The surface experiences a fatigue loading due to repeated impact of microjets, and many fatigue striations were observed on the eroded surfaces. From the study, it was concluded that the material removal mechanism during implosion of bubble was predominately by ductile shear deformation. A similar mechanism was reported in water cavitation jet erosion of aluminum alloy [23].

A comparison study has been made between the oil cavitation jet impingement and previous studies of oil jet peening on aluminum alloys [7]. During droplet impact on a solid surface, the liquid behaves in a compressible manner and develops an impact pressure at the interface between droplet and surface [32,33]. Appearance of rims depends on the impingement direction of liquid droplet and microjet. Oil jet peening studies reported that a symmetrical concentric rim was formed around the indent, indicating the normal impingement direction of liquid droplet. Whereas specimens exposed to oil cavitation jet showed rims with dissymmetrical feature (Fig. 8), indicating the inclined impact of microjet on the surface. Aluminum alloy, AA6063-T6, responds in a ductile manner in both oil cavitation jet and droplet jet impact. In oil jet peening process, the surface was repeatedly hit by multiple impacts of oil droplet. At every impingement of oil droplet, an impact pressure was developed on the surface. During dynamic loading, this impact pressure induces shock wave and it rapidly propagates into the target [6]. When the impact pressure exceeds the elastic limit for a few milliseconds, the metal yields and plastically deforms at the surface. In both processes, the indents or craters develop all over the exposed area due to extensive plastic deformation and erosion. Whereas in cavitation jet impact, the surface experienced the impact of microjets caused by implosion of bubbles. The microjet generates an impact pressure that exceeds the yield strength of the materials. Although both oil jet and cavitation jet impingement processes have different mechanism to generate impact pressure on the surface, eroded aluminum alloy surfaces have more or less similar erosion features. A similar result was reported in the studies of water jet and water cavitation jet erosion of aluminum alloys [23,34].

5 Conclusions

The structure of oil cavitation jet was investigated at various cavitation numbers. The cavitation jet length increases rapidly at the initial stage and then it stabilizes after a few milliseconds. The time to reach the stabilized jet increases with increasing upstream pressures. The times were about 105 ms, 155 ms, 215 ms, 255 ms, and 275 ms for the upstream pressures of 20 MPa, 30 MPa, 40 MPa, 50 MPa, and 60 MPa, respectively. The standoff distance influences significantly the surface deformation and erosion. In specimens exposed at the standoff distance of 15 mm, a severe erosion occurred due to impact of high intensity cavitation. A number of large size craters with rims occurred randomly on the impact region. The mass losses in the specimens exposed to the standoff distances of 10 mm and 15 mm were about 0.9 mg and 1.6 mg, respectively. The standoff distance 15 mm was found to be the optimum for the cavitation number of 0.0017. Severe erosion occurred in specimens exposed at the standoff distance of 15 mm due to impact of high intensity cavitation. A number of craters with rims occurred in the cavitation jet impacted region. The crater size of about 10–100 μm occurred in the specimens exposed at the standoff distance 15 mm. Moderate size craters with rims ($\sim$10–60 μm) were observed in specimens exposed at standoff distances of 10 mm and 25 mm, whereas specimens exposed at the standoff distance of 35 mm, very small craters of size of about 7–20 μm were observed. The material removal mechanism in aluminum alloy, AA6063-T6, during implosion of bubble was predominated by ductile shear deformation. The mechanism of oil cavitation jet erosion was similar to oil droplet impact erosion.

Acknowledgment

This research work was carried out as a part of the author's (A.S.G.) doctoral research work performed in IIT Madras, Chennai, India. The authors are grateful to Dr. G. Balachandran, Technical Centre, Ashok Leyland for his cooperation in preparing this manuscript.

Nomenclature

Δm = mass loss (mg)
ΔP = pressure difference across the nozzle ($P_1 - P_2$)
ρ = density of liquid (kg/m^3)
σ = cavitation number
σ_{YS} = yield strength of material (MPa)
σ_{UTS} = ultimate tensile strength of material (MPa)
A_c = coverage area of cavitation jet on the specimen (mm^2)
C = sound velocity of liquid (m/s)
C_d = discharge coefficient of nozzle
D_n = diameter of nozzle (mm)
D_j = cavitation jet diameter (mm)
d = diffusion region
g = acceleration due to gravity (m/s^2)
H = head of oil in the cavitation chamber (mm)
HV = Vickers microhardness
L = distance from nozzles tip (mm)
L_j = cavitation jet length (mm)
l = large quantity bubble region
m_1 = mass of the specimen before erosion (mg)
m_2 = mass of the specimen after erosion (mg)
P_1 = upstream pressure (i.e., oil injection pressure) (MPa)
P_2 = downstream pressure (MPa)
P_{atm} = atmosphere pressure (MPa)
P_{imp} = impact pressure (MPa)
P_v = vapor pressure (MPa)
SOD = standoff distance (mm)
SOD_{opt} = optimum standoff distance (mm)
s = small quantity bubble region
t_e = exposure time (s)
V_j = velocity of micro jet (m/s)

References

[1] Mutoh, Y., Fair, G. H., Noble, B., and Water House, R. B., 1987, "The Effect of Residual Stresses Induced by Shot Peening on Fatigue Crack Propagation in Two High Strength Aluminum Alloys," Fatigue Fract. Eng. Mater. Struct., **10**, pp. 261–272.
[2] Benedetti, M., Bortolamedi, T., Fontanari, V., and Frendo, F., 2004, "Bending Fatigue Behavior of Differently Shot Peened Al 6082-T5 Alloy," Int. J. Fatigue, **26**, pp. 889–897.
[3] Tönshoff, H. K., Kroos, F., and Marzenell, C., 1997, "High-Pressure Water Peening—A New Mechanical Surface Strengthening Process," CIRP Ann., **46**(1), pp. 113–116.
[4] Daniewicz, S. R., and Cummings, S. D., 1999, "Characterization of a Water Peening Process," ASME J. Eng. Mater. Technol., **121**, pp. 336–340.
[5] Grinspan, A. Sahaya, and Gnanamoorthy, R., 2006, "A Novel Surface Modification Technique for the Introduction Compressive Residual Stress and Preliminary Studies on Aluminum Alloy AA6063," Surf. Coat. Technol., **201**, pp. 1768–1775.
[6] Grinspan, A. Sahaya, and Gnanamoorthy, R., 2006, "Surface Modification by Oil Jet Peening in Aluminum Alloys AA 6063-T6 and AA 6061-T4: Residual Stress and Hardening," Appl. Surf. Sci., **253**, pp. 989–996.
[7] Grinspan, A. Sahaya, and Gnanamoorthy, R., 2006, "Surface Modification by Oil Jet Peening in Aluminum Alloys AA 6063-T6 and AA 6061-T4: Surface Morphology, Erosion and Mass Loss," Appl. Surf. Sci., **253**, pp. 997–1006.
[8] Grinspan, A. Sahaya, and Gnanamoorthy, R., 2007, "Surface Modification and Fatigue Behavior of High-Pressure Oil Jet Peened Medium Carbon Steel, AISI 1040," ASME J. Manuf. Sci. Eng., **129**, pp. 601–606.
[9] Soyama, H., 2004, "Introduction of Compressive Residual Stress Using a Cavitating Jet in Air," ASME J. Eng. Mater. Technol., **126**, pp. 123–128.
[10] Soyama, H., and Asahara, H., 1999, "Improvement of Corrosion Resistance of a Carbon Steel Surface by a Cavitation Jet," J. Mater. Sci. Lett., **18**, pp. 1953–1955.
[11] Soyama, H., 2000, "Improvement in Fatigue Strength of Silicon Manganese

Steel SUP7 by Using a Cavitation Jet," JSME Int. J., Ser. A, **43**, pp. 173–178.
[12] Odhiambo, D., and Soyama, H., 2003, "Cavitation Shot Less Peening for Improvement of Fatigue Strength of Carbonized Steel," Int. J. Fatigue, **25**, pp. 1217–1222.
[13] Qin, M., Ju, D. Y., and Oba, R., 2006, "Investigation of Influence of Incident Angle on the Process Capability of Water Cavitation Peening," Surf. Coat. Technol., **201**, pp. 1409–1413.
[14] Grinspan, A. Sahaya, and Gnanamoorthy, R., 2007, "Effect of Nozzle Traveling Velocity on Oil Cavitation Jet Peening of Aluminum Alloy, AA6063-T6," ASME J. Eng. Mater. Technol., **129**, pp. 609–614.
[15] Yamuchi, Y., Soyama, H., Adachi, Y., Sato, K., Shindo, T., Oba, R., Oshima, R., and Yamabe, M., 1995, "Suitable Regions of High Speed Submerged Water Jets for Cutting and Peening," JSME Int. J., Ser. B, **38**, pp. 31–38.
[16] Chen, Y. M., and Mongs, J., 2005, "Cavitation Wear in Plain Bearing: Case Study," Mecanique & Industries, **6**, pp. 195–201.
[17] Tomita, Y., and Shima, A., 1986, "Mechanism of Impulse Pressure Generation and Damage Pit Formation by Bubble Collapse," J. Fluid Mech., **169**, pp. 535–564.
[18] Vyas, B., and Preece, C. M., 1976, "Stress Produced in a Solid by Cavitation," J. Appl. Phys., **47**, pp. 5133–5138.
[19] Dular, M., Stoffel, B., and Sirok, B., 2006, "Development of a Cavitation Erosion Model," Wear, **261**, pp. 642–655.
[20] 2006, "Standard Test Method for Erosion of Solid Materials by a Cavitation Liquid Jet," Annual Book of ASTM Standard 03.02, ASTM G 134-95, Philadelphia, PA.
[21] Koilvula, T., 2000, "On Cavitation in Fluid Power" Proceedings of the First FPNI-PhD Symposium, Hamburg, pp. 371–382.
[22] Bansal, R. K., 1996, *Fluid Mechanics and Hydraulic Machines*, 5th ed., Laxmi, New Delhi, India, Chap. 7.
[23] Preece, C. M., and Brunton, J. H., 1980, "A Comparison of Liquid Impact Erosion and Cavitation Erosion," Wear, **60**, pp. 269–284.
[24] Pai, R., and Hargreaves, D. J., 2002, "Performance of Environment-Friendly Hydraulic Fluids and Material Wear in Cavitation Conditions," Wear, **252**, pp. 970–978.
[25] Talks, M. G., and Moreton, G., 1981, "Cavitation Erosion of Fire Resistant Hydraulic Fluids," Proceedings of the ASME Symposium on Cavitation Erosion Fluid System, pp. 139–152.
[26] Tsujino, T., Shima, A., and Oikawa, Y., 1990, "Cavitation Damage and Generated Noise in High Water Base Fluids," Trans. Jpn. Soc. Mech. Eng., Ser. B, **56**, pp. 3592–3596.
[27] Yamaguchi, A., and Shimizu, S., 1987, "Erosion Due to Impingement of Cavitation Jet," ASME Trans. J. Fluids Eng., **109**, pp. 442–447.
[28] Soyama, H., Yanauchi, Y., Saito, K., Ikohagi, T., Oba, R., and Oshima, R., 1996, "High Speed Observation of Ultrahigh-Speed Submerged Water Jets," Exp. Therm. Fluid Sci., **12**, pp. 411–416.
[29] Rao, P. V., and Buckley, D. H., 1987, "Unfield Empirical Relations for the Cavitation and Liquid Impingement Erosion Processes," Wear, **120**, pp. 253–288.
[30] Rao, B. C. S., and Buckley, D. H., 1984, "Deformation and Erosion of FCC Metals and Alloys Under Cavitation Attack," Mater. Sci. Eng., **67**, pp. 55–67.
[31] Sun, Z., Kang, X. Q., and Wang, X. H., 2005, "Experimental System of Cavitation Erosion with Water Jet," Mater. Des., **26**, pp. 59–63.
[32] Field, J. E., 1999, "ELSI Conference: Invited Lecture Liquid Impact: Theory, Experiment, Applications," Wear, **233–235**, pp. 1–12.
[33] Haymann, F. J., 1992, "Liquid Impingement Erosion," *ASM HandBook*, Vol. 18, Friction, Lubrication, and Wear Technology, ASM International, Materials Park, OH, pp. 221–232.
[34] Karimi, A., and Avellan, F., 1986, "Comparison of Erosion Mechanisms in Different Types of Cavitation," Wear, **113**, pp. 305–322.

Implicit Large Eddy Simulation of Two-Dimensional Homogeneous Turbulence Using Weighted Compact Nonlinear Scheme

Keiichi Ishiko
e-mail: k.ishiko@cfd.mech.tohoku.ac.jp

Naofumi Ohnishi

Kazuyuki Ueno

Keisuke Sawada

Department of Aerospace Engineering,
Tohoku University,
6-6-01 Aramaki-Aza-Aoba, Aoba-ku,
Sendai, Miyagi 980-8579, Japan

For the aim of computing compressible turbulent flowfield involving shock waves, an implicit large eddy simulation (LES) code has been developed based on the idea of monotonically integrated LES. We employ the weighted compact nonlinear scheme (WCNS) not only for capturing possible shock waves but also for attaining highly accurate resolution required for implicit LES. In order to show that WCNS is a proper choice for implicit LES, a two-dimensional homogeneous turbulence is first obtained by solving the Navier–Stokes equations for incompressible flow. We compare the inertial range in the computed energy spectrum with that obtained by the direct numerical simulation (DNS) and also those given by the different LES approaches. We then obtain the same homogeneous turbulence by solving the equations for compressible flow. It is shown that the present implicit LES can reproduce the inertial range in the energy spectrum given by DNS fairly well. A truncation of energy spectrum occurs naturally at high wavenumber limit indicating that dissipative effect is included properly in the present approach. A linear stability analysis for WCNS indicates that the third order interpolation determined in the upwind stencil introduces a large amount of numerical viscosity to stabilize the scheme, but the same interpolation makes the scheme weakly unstable for waves satisfying $k\Delta x \approx 1$. This weak instability results in a slight increase in the energy spectrum at high wavenumber limit. In the computed result of homogeneous turbulence, a fair correlation is shown to exist between the locations where the magnitude of $\nabla \times \omega$ becomes large and where the weighted combination of the third order interpolations in WCNS deviates from the optimum ratio to increase the amount of numerical viscosity. Therefore, the numerical viscosity involved in WCNS becomes large only at the locations where the subgrid-scale viscosity can arise in ordinary LES. This suggests the reason why the present implicit LES code using WCNS can resolve turbulent flowfield reasonably well.
[DOI: 10.1115/1.3077141]

Keywords: implicit large eddy simulation, weighted compact nonlinear scheme, two-dimensional homogeneous turbulence

1 Introduction

It is conjectured that wall erosion at the nozzle throat of a solid rocket motor (SRM) is caused by complicated turbulent effect [1]. According to Daimon et al. [1, solid rocket motors employ thermoresistive materials at the nozzle throat in order to have the throat diameter unchanged throughout the burning period. On the other hand, thermo-insulative materials are used to protect the nozzle wall upstream/downstream of the throat region from heat load. The nozzle surface is made of different material recesses in different rates in the burning period, and forms a backward-facing step at the joint in the downstream of the throat. This backward-facing step causes boundary layer separation, which reattaches in the downstream side of the step, where shock waves, as well as a number of strong longitudinal vortices, appear. The surface recession is supposed to be enhanced by the interaction with these longitudinal vortices. This nozzle erosion mechanism, however, is poorly understood because of the lack of experimental data. In order to determine the precise mechanism of nozzle erosion in SRM, numerical simulations of the turbulent flowfield involving shock waves over the entire nozzle region are certainly needed.

LES is one of the major techniques used to predict turbulent flowfields in practical engineering problems. LES directly resolves eddies in the flowfield larger than the computational mesh size. The eddy structures smaller than the mesh size are dissipated according to the subgrid-scale (SGS) model. This approach has successfully reproduced the energy spectrum for three-dimensional (3D) homogeneous turbulence [2]. However, it is difficult to find a rational SGS model when one applies LES to complicated flowfields, such as compressible turbulent flowfield involving solid particles that appears in SRM applications. No universal SGS model is yet known, and hence a suitable SGS model should be constructed for each problem that we may concern.

Implicit LES approaches, on the other hand, have broad applicability to complicated turbulent flowfields because they do not need any specific SGS models [3]. In the monotonically integrated LES (MILES) proposed by Boris et al. [4], the flux-corrected transport (FCT) algorithm is used as a monotonicity preserving higher order scheme. Besides the molecular viscosity, the numerical viscosity inherently involved in the scheme is shown to dissipate the shortest wavelength component of numerical oscillations associated to the given mesh system. As a result, MILES can give a reasonable energy spectrum of homogeneous turbulence with a natural truncation occurring at the maximum wavenumber. Examples of MILES applications for high Reynolds number turbu-

Contributed by the Fluids Engineering Division of ASME for publication in the JOURNAL OF FLUIDS ENGINEERING. Manuscript received April 18, 2008; final manuscript received December 17, 2008; published online May 13, 2009. Assoc. Editor: Dimitris Drikakis.

lent flowfields can be found in the study of Grinstein et al. [5]. According to the concept of MILES, monotonicity preserving higher order schemes for compressible flows, such as the monotone upstream scheme for conservation law (MUSCL) [6], essentially nonoscillatory (ENO) [7,8], or weighted ENO (WENO) [9,10] reconstruction, should be able to replace FCT. Indeed, implicit LES of Burgers turbulence was examined by Drikakis [11,12] using TVD Godunov-type scheme without using any SGS models. See also the results given by Garnier et al. [13].

Recently, the compact schemes [14] have attracted attention as suitable numerical schemes for DNS and LES because they can achieve higher spatial accuracy using relatively narrow stencils. Although traditional compact schemes have only dispersive error, the modern compact schemes with biased interpolation do possess a dissipative property. However, these modern compact schemes with biased interpolation are not necessarily suitable for implicit LES because they are not monotonicity preserving schemes. In order to achieve the monotonicity preserving property, Deng and Mao [15] and Deng and Zhang 16] developed WCNS in which a WENO-like weighted technique was introduced in biased interpolation. WCNS is one of the higher order monotonicity preserving schemes, which can stably capture shock waves. It is noted that the weighted interpolation in WCNS corresponds to fifth order biased interpolation in the smooth flowfield, and also to third order WENO-like interpolation at discontinuities.

In our previous study, we explored the applicability of WCNS for implicit LES by solving the one-dimensional (1D) Burgers turbulence [17]. In the Burgers turbulence, any smooth initial velocity profile develops to form triangular waves, resulting in an inertial range in the energy spectrum in proportion to k^{-2}. This property is often utilized to examine newly developed SGS models [18,19]. We note that this property is also useful for examining the applicability of a particular scheme to MILES approach because such triangular wave pattern can be captured correctly only when the scheme is high-order accurate and monotonicity preserving. It was shown that WCNS captured the triangular wave shape quite sharply without numerical oscillations, and that the energy spectrum was truncated smoothly at high wavenumber limit [17].

The ultimate purpose of the present work is to solve the complicated turbulent flowfield involving both shock waves and solid particles at the nozzle throat of SRM, and to try to identify the erosion mechanism. Before doing so, we obviously need to examine whether WCNS is really suitable for implicit LES of turbulent flowfield. The objective of the present study, therefore, is to explore the applicability of WCNS to implicit LES by solving the two-dimensional (2D) homogeneous turbulence. In Sec. 2, the formulation of the present implicit LES code based on WCNS is given. While examining the developed implicit LES code, we noticed a weak numerical instability even when the fully upwind stencil was chosen in the weighted interpolation. We therefore conducted a linear stability analysis of the scheme for a scalar advective equation. The obtained results are shown in this section together with accuracy verification of the scheme. Then, in Sec. 3, we first compute 2D incompressible homogeneous turbulence and compare the obtained results with that given by DNS and also with those given by the different LES approaches. We then obtain the same homogeneous turbulence by solving the equations for compressible flow. It is known that the inertial range of the energy spectrum for 2D homogeneous turbulence is proportional to $(\log k)^{-1/3}k^{-3}$ [20]. It is examined, as in the 1D case, whether such inertial range appears in the energy spectrum [20], and how the energy spectrum is truncated at high wavenumber limit. From the computed results, we attempted to identify where the lower order interpolation is chosen to stabilize the scheme, and found that such location has a fair correlation with the location where the magnitude of $\nabla \times \omega$ becomes large. This will be discussed also in this section. Finally, we give the conclusions of this study in Sec. 4.

2 Numerical Methodology

In this work, we consider the 2D Navier–Stokes equations both for incompressible and compressible flows as the governing equations of 2D homogeneous turbulence. The governing equations for incompressible flow case can be written as

$$\frac{\partial u_i}{\partial t} + \frac{\partial}{\partial x_j}(u_i u_j) = -\frac{\partial p}{\partial x_i} + \frac{\partial}{\partial x_j}(2\nu S_{ij}) \tag{1}$$

$$\frac{\partial u_i}{\partial x_i} = 0 \tag{2}$$

where $u_i=(u_1,u_2)=(u,v)$ denotes the Cartesian velocity component, p is the pressure, and ν is the kinematic viscosity. The strain rate tensor S_{ij} is given by

$$S_{ij} = \frac{1}{2}\left(\frac{\partial u_i}{\partial x_j} + \frac{\partial u_j}{\partial x_i}\right) \tag{3}$$

The convective terms of the Navier–Stokes equations $\partial(u_i u_j)/\partial x_j$ can be rewritten as $\partial f(q)/\partial x$, where $q=u_i$ is the conservative variables and $f=u_i u_j$ is the flux. The first derivative of the numerical flux in WCNS is approximated in the following three steps. First, the conservative variables defined at a grid point are interpolated to the staggered grid point by using WENO-like weighted technique. Hereafter, the staggered point is referred to as cell-edge. Second, the numerical flux at a cell-edge is given by an upwind method using the interpolated conservative variables. Third, derivatives of the numerical flux at a grid point are calculated by the compact scheme. A detailed description of these steps will be given in Sec. 2.1.

The governing equations for viscous compressible flow can be written as

$$\frac{\partial \mathbf{Q}}{\partial t} + \frac{\partial(\mathbf{E}-\mathbf{E}_v)}{\partial x} + \frac{\partial(\mathbf{F}-\mathbf{F}_v)}{\partial y} = 0 \tag{4}$$

where $\mathbf{Q}$ denotes the conservative variable, and $\mathbf{E}$ and $\mathbf{F}$ are the convective flux vectors given, respectively, by

$$\mathbf{Q} = \begin{pmatrix} \rho \\ \rho u \\ \rho v \\ e \end{pmatrix}, \quad \mathbf{E} = \begin{pmatrix} \rho u \\ \rho u^2 + p \\ \rho uv \\ (e+p)u \end{pmatrix}, \quad \mathbf{F} = \begin{pmatrix} \rho v \\ \rho uv \\ \rho v^2 + p \\ (e+p)v \end{pmatrix} \tag{5}$$

in which ρ denotes the density and e is the total energy per unit volume. In Eq. (4), $\mathbf{E}_v$ and $\mathbf{F}_v$ are viscous flux vectors denoted, respectively, by

$$\mathbf{E}_v = \begin{pmatrix} 0 \\ \tau_{xx} \\ \tau_{xy} \\ u\tau_{xx} + v\tau_{xy} - \dot{q}_x \end{pmatrix}, \quad \mathbf{F}_v = \begin{pmatrix} 0 \\ \tau_{yx} \\ \tau_{yy} \\ u\tau_{xy} + v\tau_{yy} - \dot{q}_y \end{pmatrix} \tag{6}$$

with

$$\tau_{xx} = \frac{2}{3}\mu\left(2\frac{\partial u}{\partial x} - \frac{\partial v}{\partial y}\right)$$

$$\tau_{yy} = \frac{2}{3}\mu\left(2\frac{\partial v}{\partial y} - \frac{\partial u}{\partial x}\right)$$

$$\tau_{xy} = \tau_{yx} = \mu\left(\frac{\partial u}{\partial y} + \frac{\partial v}{\partial x}\right)$$

$$\dot{q}_x = -\kappa\frac{\partial T}{\partial x}, \quad \dot{q}_y = -\kappa\frac{\partial T}{\partial y}$$

where T denotes the temperature, μ is the coefficient of molecular viscosity, and κ is the heat conduction coefficient defined by

$$\kappa = \frac{\mu C_p}{\mathrm{Pr}} \tag{7}$$

where C_p denotes the specific heat at constant pressure and Pr is the Prandtl number.

The derivatives of the numerical flux at a grid point are similarly obtained as for the incompressible flow case. The conservative variables at a grid point are interpolated to a cell-edge using characteristic variables defined by

$$W_{j,p} = \mathbf{l}_n^p \cdot \mathbf{Q}_j \tag{8}$$

where $\mathbf{l}_n^p$ denotes the pth left eigenvector at a fixed grid point n, which is typically taken as the middle grid point of the local stencil. The WENO-like interpolation method for obtaining the characteristic variables at the cell-edge $\tilde{W}^{\omega}_{Lj+1/2,p}$ and $\tilde{W}^{\omega}_{Rj-1/2,p}$ will be given in Sec. 2.1. Then the conservative variables at the left and right of cell-edge $\tilde{\mathbf{Q}}_{Lj+1/2}$ and $\tilde{\mathbf{Q}}_{Rj-1/2}$ are restored by

$$\tilde{\mathbf{Q}}_{Lj+1/2} = \sum_{p=1}^{3} \tilde{W}^{\omega}_{Lj+1/2,p} \mathbf{r}_n^p \tag{9}$$

$$\tilde{\mathbf{Q}}_{Rj-1/2} = \sum_{p=1}^{3} \tilde{W}^{\omega}_{Rj-1/2,p} \mathbf{r}_n^p \tag{10}$$

where $\mathbf{r}_n^p$ denote the pth right eigenvector. For more details, see Refs. [15,16]. The numerical flux is then determined by the AUSM-DV upwind scheme [21]. Finally, the derivatives of the numerical flux at a grid point are calculated by the compact scheme.

2.1 Weighted Compact Nonlinear Schemes. The original compact scheme gives the first derivative of the numerical flux f'_j at jth grid point as

$$\kappa f'_{j-1} + f'_j + \kappa f'_{j+1} = \frac{a}{h}(\tilde{f}_{j+1/2} - \tilde{f}_{j-1/2}) + \frac{b}{h}(\tilde{f}_{j+3/2} - \tilde{f}_{j-3/2}) \tag{11}$$

with the parameters

$$a = \tfrac{3}{8}(3 - 2\kappa), \quad b = \tfrac{1}{24}(22\kappa - 1) \tag{12}$$

where $\tilde{f}_{j+1/2}$ is the numerical flux at the cell-edge $x_{j+1/2}$ for the flux function $f(q)$, and h is the grid interval. Equation (11) obtains a fifth order spatial accuracy when $\kappa = 9/62$. The numerical flux $\tilde{f}_{j+1/2}$ is given by

$$\tilde{f}_{j+1/2} = \begin{cases} f(\tilde{q}_{Lj+1/2}) & \text{for } \alpha_{j+1/2} \geq 0 \\ f(\tilde{q}_{Rj+1/2}) & \text{for } \alpha_{j+1/2} < 0 \end{cases} \tag{13}$$

where $\alpha_{j+1/2}$ is the convection velocity at the cell-edge determined by

$$\alpha_{j+1/2} = \frac{f(\tilde{q}_{Rj+1/2}) - f(\tilde{q}_{Lj+1/2})}{\tilde{q}_{Rj+1/2} - \tilde{q}_{Lj+1/2}} \tag{14}$$

The conservative variables at the left and the right sides of the cell-edge are denoted by $\tilde{q}_{Lj+1/2}$ and $\tilde{q}_{Rj+1/2}$, respectively. The fifth order biased interpolations give

$$\tilde{q}_{Lj+1/2} = \tfrac{1}{128}(3q_{j-2} - 20q_{j-1} + 90q_j + 60q_{j+1} - 5q_{j+2}) \tag{15}$$

$$\tilde{q}_{Rj-1/2} = -\tfrac{1}{128}(5q_{j-2} - 60q_{j-1} - 90q_j + 20q_{j+1} - 3q_{j+2}) \tag{16}$$

respectively. Hereafter this scheme is referred to as CS5.

Instead of Eqs. (15) and (16), we can use the WCNS developed by Deng and Mao [15] and Deng and Zhang [16], in which a weighted interpolation is employed to determine the cell-edge value. In this scheme, the third order interpolations are given by

$$\tilde{q}^l_{Lj+1/2} = q_j + \frac{1}{1!}\left(\frac{h}{2}\right) q'^l_j + \frac{1}{2!}\left(\frac{h}{2}\right)^2 q''^l_j + O(h^3) \tag{17}$$

$$\tilde{q}^l_{Rj-1/2} = q_j - \frac{1}{1!}\left(\frac{h}{2}\right) q'^l_j + \frac{1}{2!}\left(\frac{h}{2}\right)^2 q''^l_j + O(h^3) \tag{18}$$

where q'_j and q''_j denote the first and the second derivatives of q_j, respectively. The index l (l takes 1, 2, and 3) is designated to indicate one of the available stencils $S_1 \in [x_{j-2}, x_{j-1}, x_j]$, $S_2 \in [x_{j-1}, x_j, x_{j+1}]$, and $S_3 \in [x_j, x_{j+1}, x_{j+2}]$, in which three consecutive grid points are assigned from the five grid points ranging from $j-2$ to $j+2$. The second order approximations of the derivatives q'_j and q''_j in each S_l are given by

$$q'^1_j = \frac{1}{2h}(q_{j-2} - 4q_{j-1} + 3q_j) \tag{19}$$

$$q'^2_j = \frac{1}{2h}(q_{j+1} - q_{j-1}) \tag{20}$$

$$q'^3_j = \frac{1}{2h}(-3q_j + 4q_{j+1} - q_{j+2}) \tag{21}$$

and

$$q''^1_j = \frac{1}{h^2}(q_{j-2} - 2q_{j-1} + q_j) \tag{22}$$

$$q''^2_j = \frac{1}{h^2}(q_{j+1} - 2q_j + q_{j-1}) \tag{23}$$

$$q''^3_j = \frac{1}{h^2}(q_j - 2q_{j+1} + q_{j+2}) \tag{24}$$

Substituting Eqs. (19)–(24) into Eqs. (17) and (18), one obtains the following three different third order interpolations

$$\tilde{q}^1_{Lj+1/2} = \tfrac{1}{8}(3q_{j-2} - 10q_{j-1} + 15q_j) \tag{25}$$

$$\tilde{q}^2_{Lj+1/2} = \tfrac{1}{8}(-q_{j-1} + 6q_j + 3q_{j+1}) \tag{26}$$

$$\tilde{q}^3_{Rj+1/2} = \tfrac{1}{8}(3q_j + 6q_{j+1} - q_{j+2}) \tag{27}$$

and

$$\tilde{q}^1_{Rj-1/2} = -\tfrac{1}{8}(q_{j-2} - 6q_{j-1} - 3q_j) \tag{28}$$

$$\tilde{q}^2_{Rj-1/2} = -\tfrac{1}{8}(-3q_{j-1} - 6q_j + q_{j+1}) \tag{29}$$

$$\tilde{q}^3_{Rj-1/2} = -\tfrac{1}{8}(-15q_j + 10q_{j+1} - 3q_{j+2}) \tag{30}$$

Hereafter the scheme that gives $\tilde{q}^1_{Lj+1/2}$ and $\tilde{q}^1_{Rj-1/2}$ is denoted as CS3-1, $\tilde{q}^2_{Lj+1/2}$ and $\tilde{q}^2_{Rj-1/2}$ as CS3-2, and $\tilde{q}^3_{Lj+1/2}$ and $\tilde{q}^3_{Rj-1/2}$ as CS3-3. The conservative variables at the cell-edge are obtained by the weighted combination of three interpolated values with the weights $\omega_{L(R)l}$

$$\tilde{q}^{\omega}_{Lj+1/2} = \sum_{l=1}^{3} \omega_{Ll} \tilde{q}^l_{Lj+1/2} \tag{31}$$

$$\tilde{q}^{\omega}_{Rj-1/2} = \sum_{l=1}^{3} \omega_{Rl} \tilde{q}^l_{Rj-1/2} \tag{32}$$

where the weights satisfy the conditions

$$\sum_{l=1}^{3} \omega_{Ll} = 1, \quad \sum_{l=1}^{3} \omega_{Rl} = 1 \tag{33}$$

Following Refs. [15,16], the weights are given by

$$\omega_{Ll} = \frac{\beta_{Ll}}{\sum_{m=1}^{3} \beta_{Lm}}, \quad \omega_{Rl} = \frac{\beta_{Rl}}{\sum_{m=1}^{3} \beta_{Rm}} \tag{34}$$

where

$$\beta_{Ll} = \frac{C_{Ll}}{(\epsilon + IS_l)^2}, \quad \beta_{Rl} = \frac{C_{Rl}}{(\epsilon + IS_l)^2} \tag{35}$$

The optimum weights $C_{L(R)l}$ are given by

$$C_{L1} = C_{R3} = \tfrac{1}{16}, \quad C_{L2} = C_{R2} = \tfrac{10}{16}, \quad C_{L3} = C_{R1} = \tfrac{5}{16} \tag{36}$$

A small number ϵ in Eq. (35) is to avoid the denominator becoming zero ($\epsilon = 10^{-6}$ in the present work), and IS_l is a smoothness measure, which depends on both the gradient and the curvature at x_j as

$$IS_l = (hq_j'^l)^2 + (h^2 q_j''^l)^2 \tag{37}$$

In the smooth region where $q_j'^1 = q_j'^2 = q_j'^3$ and $q_j''^1 = q_j''^2 = q_j''^3$, the weight $\omega_{L(R)l}$ approaches $C_{L(R)l}$ with a truncation error of second order magnitude, and therefore Eqs. (31) and (32) give the fifth order biased interpolations of Eqs. (15) and (16). In contrast, at steep gradient or at large curvature, the weights automatically determine a third order interpolation in properly chosen stencil.

2.2 Linear Analysis. In this section, we examine the linear stability of WCNS, and show how dispersive and dissipative properties change for different interpolation methods. As stated in Sec. 2.1, WCNS utilizes the fifth order interpolations in the smooth region, and turns to employ the third order interpolations determined by WENO-like weighted combination of the three distinct third order interpolations in the nonsmooth region. In the linear stability analysis, therefore, these fifth order biased and three distinct third order interpolations are separately considered.

The scalar linear advection equation is given by

$$\frac{\partial u}{\partial t} + c\frac{\partial u}{\partial x} = 0 \tag{38}$$

where c is a constant advection velocity of positive value. Assuming a periodicity in x, the semidiscrete form of Eq. (38)

$$\frac{\partial u_j}{\partial t} + cu_j' = 0 \tag{39}$$

with an initial condition for a sinusoidal wave shape

$$u(x) = \exp(ikx) \tag{40}$$

has a solution of the form

$$u_j = \exp(ck_i^* t)\exp\left[ik\left(x_j - c\frac{k_r^*}{k}t\right)\right] \tag{41}$$

where $k^* = k_r^* + ik_i^*$ is a modified wavenumber. The real part of the modified wavenumber corresponds to dispersion property of the scheme, while the imaginary part to that of dissipation.

For the fifth order original compact scheme indicated in Eq. (11), the modified wavenumber can be written as

$$k^*\Delta x = \frac{2\tilde{k}\left[a\sin\left(k\frac{\Delta x}{2}\right) + b\sin\left(k\frac{3\Delta x}{2}\right)\right]}{[1 + 2\kappa\cos(k\Delta x)]} \tag{42}$$

where $\tilde{k}$ is a factor given by

$$\tilde{k}_{5\text{th}} = \frac{1}{128}\left[150\cos\left(k\frac{\Delta x}{2}\right) - 25\cos\left(k\frac{3\Delta x}{2}\right) + 3\cos\left(k\frac{5\Delta x}{2}\right)\right] + \frac{i}{128}\left[-30\sin\left(k\frac{\Delta x}{2}\right) + 15\sin\left(k\frac{3\Delta x}{2}\right) - 3\sin\left(k\frac{5\Delta x}{2}\right)\right] \tag{43}$$

In above equation, we assume that the flux function $f = cu$ is given by $\tilde{f}_{j+1/2} = c\tilde{q}_{Lj+1/2}$ because the advection velocity c is assumed positive. For each third order interpolation that gives $\tilde{q}^1_{Lj+1/2}$, $\tilde{q}^2_{Lj+1/2}$, and $\tilde{q}^3_{Lj+1/2}$, the factor $\tilde{k}$ in Eq. (42) becomes

$$\tilde{k}^1_{3\text{rd}} = \frac{1}{8}\left[15\cos\left(k\frac{\Delta x}{2}\right) - 10\cos\left(k\frac{3\Delta x}{2}\right) + 3\cos\left(k\frac{5\Delta x}{2}\right)\right] + \frac{i}{8}\left[-15\sin\left(k\frac{\Delta x}{2}\right) + 10\sin\left(k\frac{3\Delta x}{2}\right) - 3\sin\left(k\frac{5\Delta x}{2}\right)\right] \tag{44}$$

$$\tilde{k}^2_{3\text{rd}} = \frac{1}{8}\left[9\cos\left(k\frac{\Delta x}{2}\right) - \cos\left(k\frac{3\Delta x}{2}\right)\right] + \frac{i}{8}\left[-3\sin\left(k\frac{\Delta x}{2}\right) + \sin\left(k\frac{3\Delta x}{2}\right)\right] \tag{45}$$

$$\tilde{k}^3_{3\text{rd}} = \frac{1}{8}\left[9\cos\left(k\frac{\Delta x}{2}\right) - \cos\left(k\frac{3\Delta x}{2}\right)\right] + \frac{i}{8}\left[3\sin\left(k\frac{\Delta x}{2}\right) - \sin\left(k\frac{3\Delta x}{2}\right)\right] \tag{46}$$

respectively. The weighted linear combination of these factors gives

$$\tilde{k}_w = \omega_{L1}\tilde{k}^1_{3\text{rd}} + \omega_{L2}\tilde{k}^2_{3\text{rd}} + \omega_{L3}\tilde{k}^3_{3\text{rd}} \tag{47}$$

Obviously, we have $\tilde{k}_w = \tilde{k}_{5\text{th}}$ in the smooth region.

Figure 1 shows the comparison of the modified wavenumber for the fifth order compact scheme with fifth order biased interpolation (CS5), and with three different third order interpolations (CS3-1, CS3-2, and CS3-3). The upper figure shows the real part and the lower one the imaginary part. The solid lines show the exact cases of zero dispersion and zero dissipation. Therefore, any deviation from the solid lines corresponds either to dispersive error or to dissipative error. Note that the dispersion curve for CS3-1

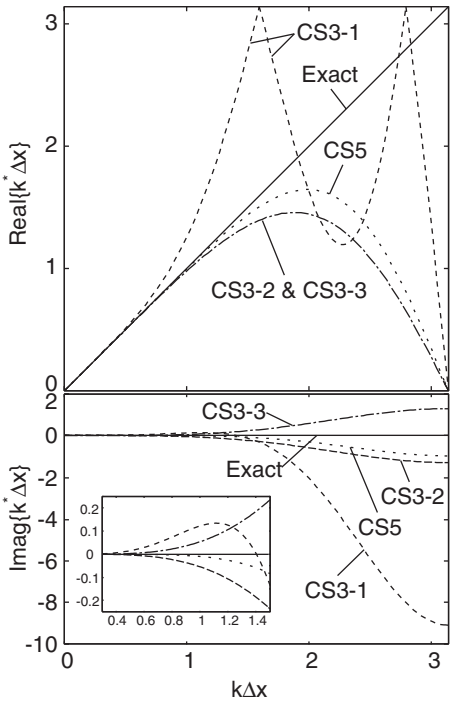

Fig. 1 The modified wavenumber of fifth order compact schemes with various interpolations. The upper figure shows the real part and the lower one the imaginary part. A closeup view of the imaginary part near $k\Delta x \approx 1$ is shown together.

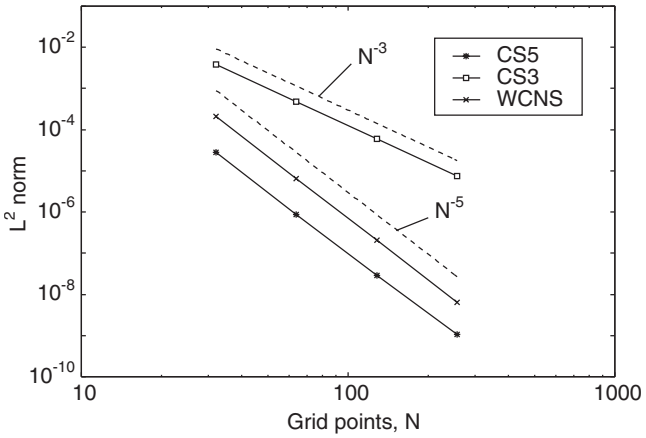

Fig. 2 L^2**-norms of the difference between the exact solution for a linear advection problem and that given by fifth order compact scheme with various interpolations**

is reflected across Real $\{k^*\Delta x\}=\pi$ due to aliasing error. It can be seen that CS5 and CS3-2 give similar dispersive and dissipative features, although CS5 obviously gives less dispersive and dissipative errors due to higher spatial accuracy. The imaginary part of the wavenumber for CS3-3 becomes positive in the region $k\Delta x \approx 1$ or larger, suggesting that CS3-3 becomes unstable. This is because the stencil S_3 is positioned downwind side to the cell-edge. On the other hand, CS3-1 has significantly larger dissipation and dispersion errors. Therefore, even if high wavenumber oscillations are excited, large dissipation of CS3-1 can damp out such components. However, one should note that the dissipation curve for CS3-1 becomes slightly positive near $k\Delta x \approx 1$, suggesting that CS3-1 is weakly unstable in this region. Consequently, when the weights are biased toward S_1 in WCNS, high wavenumber components may be excited due to dispersion, but the scheme remains stable due to large numerical dissipation, except for the region near $k\Delta x \approx 1$, where the scheme can be weakly unstable. On the other hand, when the weights are biased toward S_3, the scheme becomes unstable because of negative dissipation in the high wavenumber regime. Although the WENO-like weighted technique in WCNS excludes the latter case, we note that WCNS can still be weakly unstable at near $k\Delta x \approx 1$.

The choice of interpolation method obviously has significant influence on the dispersive and dissipative features, and therefore on the spatial accuracy of the scheme. The numerical accuracy of WCNS for a linear advection problem is examined for different interpolation methods. We solve the 1D linear advection problem with an advection velocity of unity. The computational domain is [0,1], and the periodic boundary condition is imposed at both ends. The initial condition is given by $u(x,t=0)=\sin(2\pi x)$. For the time integration, a fourth order Runge–Kutta method is employed. The CFL number is 0.4 for all cases. Figure 2 shows the variation in L^2 errors at $t=2.0$ obtained through successive mesh refinement. The slope of L^2 errors plotted in log-log scale gives the actual spatial accuracy of the scheme. It is found that both CS5 and WCNS achieve fifth order spatial accuracy, though the truncation error for WCNS is larger than that of CS5. A third order accuracy is attained for CS3-2, as is expected, but heavy oscillations appeared in the numerical solution of CS3-1, and an evaluation of the spatial accuracy could not be made. The solution of CS3-3 blew up immediately.

2.3 Navier–Stokes Solver. The developed numerical scheme for solving the Navier–Stokes equations is described briefly. For both incompressible and compressible flow cases, the convective term is calculated by WCNS. The viscous flux is obtained by the fourth order central difference scheme. For time integration, the fourth order Runge–Kutta method is used.

For incompressible flow case, a fractional step method is employed for enforcing the divergence-free condition. The Poisson equation is solved by the fast Fourier transform (FFT) algorithm. Because the differential operation in the physical space is replaced by the algebraic operation in the Fourier space, solving the Poisson equations using FFT is computationally less demanding when the periodic boundary condition is employed.

3 Computation of 2D Homogeneous Turbulence

A 2D homogeneous turbulence is an energy decaying system and is known to have an inertial range in the energy spectrum that is proportional to $(\log k)^{-1/3}k^{-3}$ for the incompressible flow case [20]. This property is often utilized to verify numerical methods for LES. In this work, we therefore solve the 2D homogeneous turbulence to examine the present implicit LES using WCNS and to determine whether the inertial range correctly appears and to also determine whether the energy spectrum is truncated smoothly at high wavenumber limit.

3.1 Initial Conditions. The computational domain is a square region whose edge has a length of 2π. The periodic boundary condition is set at the four edges of the square region.

Let us describe briefly how the initial velocity field is determined. We first consider an energy spectrum written in the Fourier space as

$$E(k) = \frac{1}{2}\int \hat{u}_i(\mathbf{k})\hat{u}_i^*(\mathbf{k})dS(k) = \pi k \hat{u}_i(\mathbf{k})\hat{u}_i^*(\mathbf{k}) \tag{48}$$

where $\hat{u}_i(\mathbf{k})$ denotes the Fourier transform of the velocity component $u_i(\mathbf{x})$, and $\hat{u}_i^*(\mathbf{k})$ is the complex conjugate of $\hat{u}_i(\mathbf{k})$. Integration is understood to be done along a circle with a radius of $|\mathbf{k}| = \sqrt{k_1^2+k_2^2}=k$. The initial energy spectrum is given by [22]

$$E(k) = \frac{1}{2}a_s U_0^2 k_p^{-1}\left(\frac{k}{k_p}\right)^{2s+1}\exp\left[-\left(s+\frac{1}{2}\right)\left(\frac{k}{k_p}\right)^2\right] \tag{49}$$

where U_0 denotes the root-mean-square value of the initial velocity that satisfies the condition $U_0 \equiv U(t=0)=\langle|\mathbf{u}(t=0)|^2\rangle^{1/2}=1$. The maximum value of the initial energy spectrum occurs at the wavenumber of k_p. This wavenumber also determines the dominant eddy size. In this study, we assume $k_p=12$. The coefficient a_s normalizes the initial kinetic energy to satisfy $K \equiv \int_0^\infty E(k)dk = (1/2)U_0^2$, and is given by

$$a_s = \frac{(2s+1)^{s+1}}{2^s s!} \tag{50}$$

where $s(=0,1,2,\ldots)$ is a parameter that shapes the energy spectrum. In this work, we assume that $s=3$. The resulting initial energy spectrum is shown in Fig. 3.

By combining the equation of continuity and the definition of vorticity in the Fourier space, one obtains the velocity components

$$\hat{u}_1(\mathbf{k}) = \sqrt{-1}\frac{k_2}{k^2}\hat{\omega}_3(\mathbf{k}) \tag{51}$$

$$\hat{u}_2(\mathbf{k}) = -\sqrt{-1}\frac{k_1}{k^2}\hat{\omega}_3(\mathbf{k}) \tag{52}$$

where $\hat{\omega}_3(\mathbf{k})$ is the Fourier transform of vorticity $\omega_3(\mathbf{x})$. Substituting Eqs. (51) and (52) into Eq. (48), the magnitude of vorticity is related to the assumed energy spectrum as

$$|\hat{\omega}_3(\mathbf{k})| = \sqrt{\frac{k}{\pi}E(k)} \tag{53}$$

The initial vorticity distribution in the Fourier space is then obtained using the magnitude $|\hat{\omega}_3(\mathbf{k})|$ and a phase $\zeta(\mathbf{k})$ as follows:

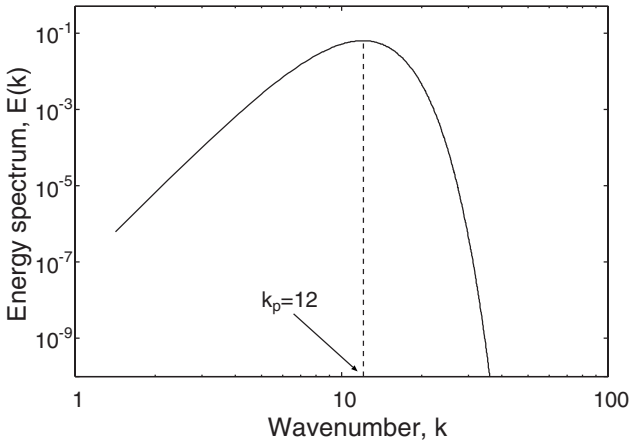

Fig. 3 Initial energy spectrum. The maximum value in the energy spectrum appears at the wavenumber of k_p. Eddies with this size are dominant in the initial vorticity distribution.

$$\hat{\omega}_3(\mathbf{k}) = \sqrt{\frac{k}{\pi}E(k)}\exp[\sqrt{-1}\zeta(\mathbf{k})] \tag{54}$$

The initial velocity distribution in the physical space is given by the inverse Fourier transform of Eqs. (51) and (52) using FFT.

The randomness of the initial vorticity distribution is assured by choosing a random phase $\zeta(\mathbf{k})$ in Eq. (54). In the present work, this phase is given by $\zeta(\mathbf{k})=\xi(\mathbf{k})+\eta(\mathbf{k})$, where $\xi(\mathbf{k})$ and $\eta(\mathbf{k})$ are independent random values chosen in $[0,2\pi]$ at each coordinate point in the first quadrant of the k_1-k_2 plane. We assume that these $\xi(\mathbf{k})$ and $\eta(\mathbf{k})$ have different conjugate relations given as follows:

$$\begin{aligned}
\xi(-k_1,k_2) &= -\xi(k_1,k_2)\\
\xi(-k_1,-k_2) &= -\xi(k_1,k_2)\\
\xi(k_1,-k_2) &= \xi(k_1,k_2)
\end{aligned} \tag{55}$$

$$\begin{aligned}
\eta(-k_1,k_2) &= \eta(k_1,k_2)\\
\eta(-k_1,-k_2) &= -\eta(k_1,k_2)\\
\eta(k_1,-k_2) &= -\eta(k_1,k_2)
\end{aligned} \tag{56}$$

respectively.

The domain of integration for the inverse Fourier transform is $[-k_{\max},k_{\max}]$, where the maximum wavenumber $k_{\max}$ corresponds to the given mesh interval as

$$k_{\max} = \frac{2\pi N}{2L} \tag{57}$$

in which L denotes the length of computational domain ($L=2\pi$) and N is the number of grid points for DNS ($N=4096$). Figure 4 shows the initial vorticity distribution. The initial vorticity distribution for LES is given simply by coarsening the distribution for DNS calculation.

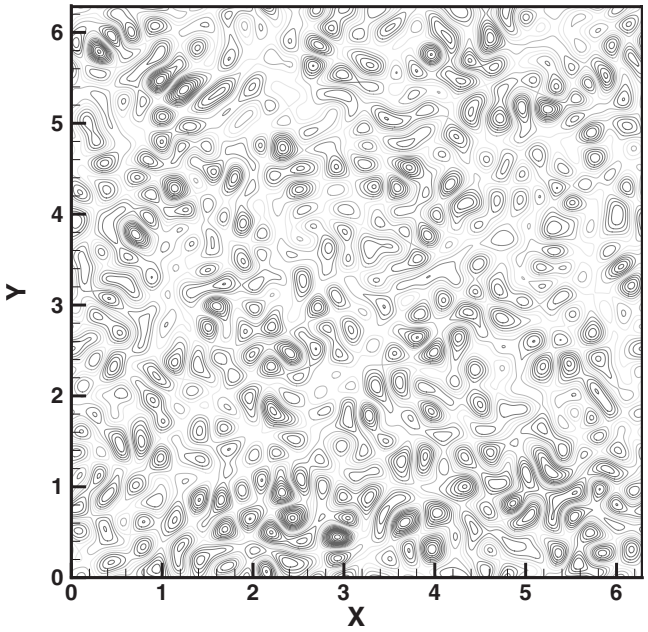

Fig. 4 Initial vorticity distribution

The kinematic viscosity ν is determined from the Reynolds number defined by

$$\mathrm{R}(t) = \frac{U(t)L(t)}{\nu} \tag{58}$$

In the above equation, $L(t)=U(t)/\Omega(t)$ denotes the characteristic length of microscale, where $\Omega(t)$ is the root-mean-square of vorticity. At $t=0$, they are given by

$$\Omega_0 \equiv \Omega(t=0) = \sqrt{\frac{2s+2}{2s+1}}U_0 k_p, \quad L_0 \equiv L(t=0) = \sqrt{\frac{2s+1}{2s+2}}k_p^{-1} \tag{59}$$

respectively. In the present study, we assume the initial Reynolds number $\mathrm{R}(t=0)=U_0L_0/\nu$ to be 2048.

3.2 Results and Discussions. Let us first show the computed results for the case of incompressible homogeneous turbulence. Table 1 summarizes the numerical schemes for incompressible flow case. The implicit LES code that utilizes WCNS is denoted as ILES-WCNS and another implicit LES code that employs the fifth order interpolation as ILES-CS5. The implicit LES code that uses the third order interpolation is denoted as ILES-CS3. The conventional LES that employs the dynamic Smagorinsky SGS model is referred to as LES-DSM, where a fourth order central difference scheme is used in the evaluation of the convective

Table 1 Numerical methods

	Scheme	Interpolation	SGS model	Filter	Grid points
ILES-WCNS	Fifth-CS (WCNS)	Weighted	-	-	1024^2
ILES-CS5	Fifth-CS	Fifth-biased	-	-	1024^2
ILES-CS3	Fifth-CS	Third-biased	-	-	1024^2
LES with DSM	Fourth-CDS	-	DSM	BF	1024^2
DNS	Fourth-CDS	-	-	-	4096^2

ILES: implicit LES, WCNS: weighted compact nonlinear scheme, fifth-CS: fifth order compact scheme, fourth-CDS: fourth order central difference scheme, weighted: weighted interpolation, fifth-biased: fifth order biased interpolation, third-biased: third order biased interpolation, DSM: dynamic Smagorinsky model, and BF: box filter.

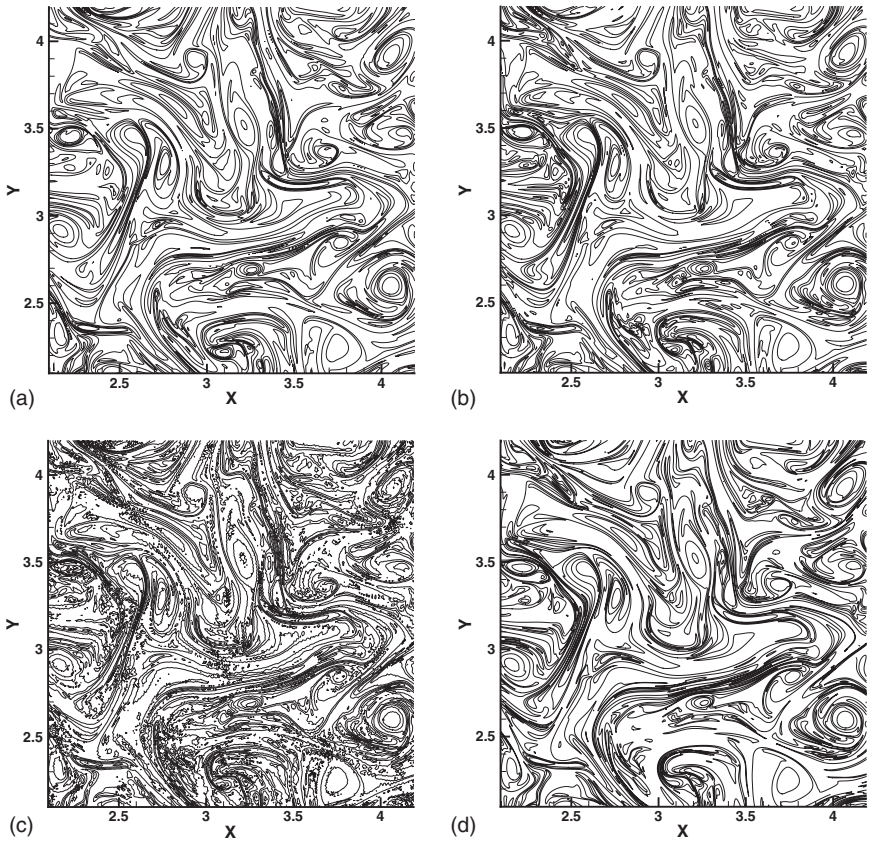

Fig. 5 Computed vorticity distribution at $t=2.0$. (*a*) ILES-WCNS, (*b*) ILES-CS5, (*c*) LES-DSM, and (*d*) DNS.

terms. A box filter is employed for each x- and y-coordinate in order to separate subgrid-scale components from the flowfield. The same scheme is also used in DNS, where the SGS model is removed.

Figure 5 shows a closeup view of the obtained vorticity contours at $t=2.0$. One finds that the vorticity patterns obtained by ILES-WCNS and ILES-CS5 reproduce that by DNS quite well. The vorticity contours obtained by LES-DSM show that overall vorticity contour patterns are well reproduced, but obviously numerical wiggles appear everywhere. These wiggles can be attributed to dispersive error of the central difference scheme used in LES-DSM. Figure 6 shows the obtained vorticity contours at $t=6.0$. Because of the chaotic nature of turbulence, the obtained vorticity contours are different from each other at this moment. Both ILES-WCNS and ILES-CS5 give vorticity distributions without numerical oscillations, while that given by LES-DSM suffers from numerical wiggles severely.

In Fig. 7, the computed energy spectra obtained at $t=2.0$ and $t=6.0$ are shown. We can find that an inertial range appears in each energy spectrum and that all the energy spectra follow the power law of $E(k) \propto (\log k)^{-1/3} k^{-3}$ for 2D homogeneous turbulence reasonably well. The inertial range computed by LES-DSM extends slightly more to the higher wavenumber than that by the three implicit LES approaches, but begins to deviate rapidly from that of DNS at a high wavenumber limit. We can also find that the energy spectrum is diminished with time over the entire range because the present turbulence is energy decaying due to dissipation. In addition, an excitation of energy occurs in the lower wavenumber regime at the later time due to the inverse cascade that is dominant for 2D turbulence. We note that each LES code gives a slightly different behavior of the energy spectrum in the lower wavenumber range at the later time due to different vorticity distributions, as shown in Fig. 6.

As stated above, the energy spectrum given by LES-DSM turns to deviate from that of DNS and rapidly increases at high wavenumber limit. This behavior is due to numerical wiggles that appeared in the numerical solutions. Although the numerical solution obtained by LES-DSM does not blow up, the dynamic Smagorinsky SGS model is obviously insufficient to suppress numerical oscillations for 2D turbulent flowfield. This seems rather reasonable because the dynamic Smagorinsky SGS model is originally developed for a 3D turbulent flowfield in which energy cascade can be induced by eddy stretching effect, while such effect is absent in 2D flowfield. In contrast, the energy spectra computed by the three implicit LES approach gradually deviating from that of DNS and decrease naturally toward the maximum wavenumber limit. This indicates that the inherent numerical viscosity in these implicit LES codes favorably suppresses numerical oscillations. Note that ILES-CS3 gives a smaller energy spectrum than that of ILES-CS5 at the high wavenumber region, suggesting that ILES-CS3 is more dissipative. Likewise, ILES-WCNS should give a smaller energy spectrum because more dissipative third order interpolations are employed in places to maintain monotonicity. However, the computed result indicates that this is not the case at high wavenumber limit. The reason for this is suggested in the linear stability analysis that WCNS can be weakly unstable when the stencil for the third order interpolation is chosen toward the fully upwind side. Later we will identify where the weighted average of the third order interpolations in WCNS deviates from the fifth order one used in ILES-CS5.

In Fig. 8, the temporal histories of (a) the normalized kinetic energy and (b) the normalized enstrophy are shown. Reasonable agreements are obtained for all the normalized kinetic energy profiles with that of DNS, but a close inspection reveals that ILES-CS5 and LES-DSM give good agreements, while those ILES-WCNS and ILES-CS3 show slightly more dissipative profiles at

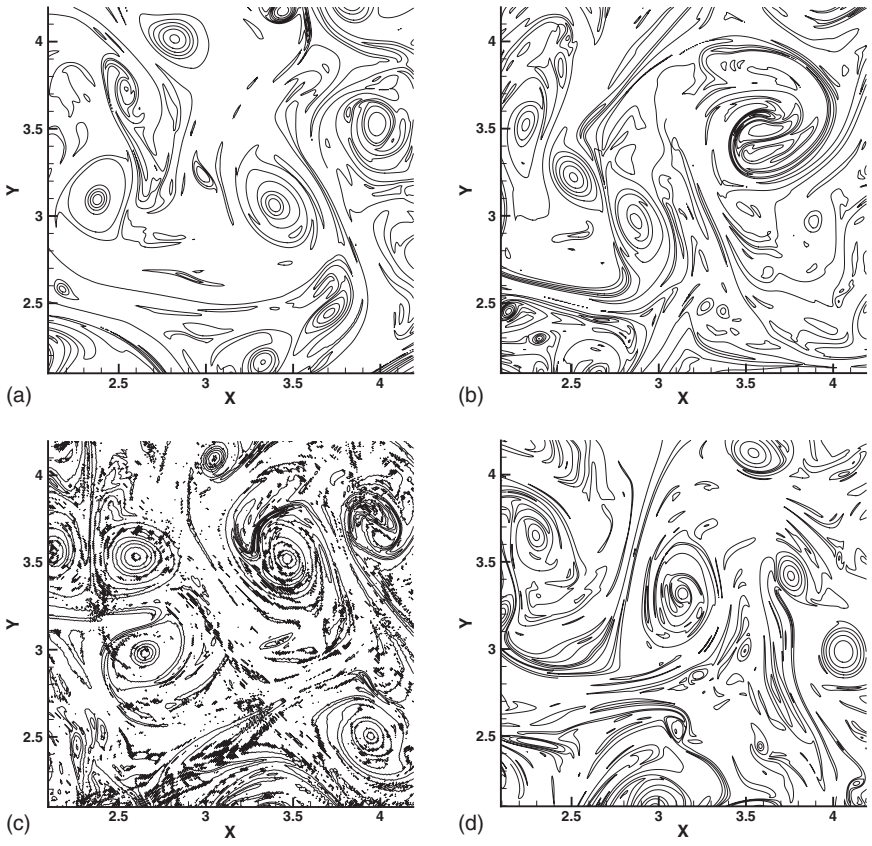

Fig. 6 Computed vorticity distribution at $t=6.0$. (*a*) ILES-WCNS, (*b*) ILES-CS5, (*c*) LES-DSM, and (*d*) DNS.

an early time. This indicates that the initially assumed velocity field is smoothed out to a certain level by the third order interpolations employed in these schemes. The situation seems almost the same for the normalized enstrophy profiles. Indeed, LES-DSM gives the best agreement with the result of DNS for this case, and that of ILES-CS5 follows. Those given by ILES-WCNS and ILES-CS3 give slightly smaller values. All the profiles except for that of ILES-CS3 seem to approach asymptotically that of the DNS result at a later time.

Figure 9 shows the temporal variations in Reynolds number and enstrophy plotted in logarithmic scales. It is found from the least square fitting for $t>2.0$ that the Reynolds number varies as $\mathrm{R}(t) \propto t^{0.41}$ and the enstrophy as $\langle\omega^2\rangle/\langle\omega_0^2\rangle \propto t^{-0.85}$. Because the Reynolds number can be rewritten as

$$\mathrm{R}(t) = \frac{U(t)L(t)}{\nu} = \frac{[U(t)]^2}{\nu\Omega(t)} \tag{60}$$

one obtains a relation

$$\mathrm{R}(t) \propto \left[\frac{\langle\omega^2\rangle}{\langle\omega_0^2\rangle}\right]^{-1/2} \tag{61}$$

when $U(t)$ can be assumed to be time independent for high Reynolds number flow. Therefore, we can say that the present result amply satisfies this relation for $t>2.0$. As to the enstrophy, the present result suggests the value of $\langle\omega^2\rangle/\langle\omega_0^2\rangle \propto t^{-0.85}$, which agrees reasonably well with the result of $t^{-0.8}$ given by Chasnov [22]. On the other hand, the Reynolds number and the enstrophy were found to be proportional to $t^{0.5}$ and t^{-1}, respectively, in the work of Das et al. [23], while Batchelor [24] suggested from a dimensional analysis that the enstrophy should be t^{-2} when $\nu\to 0$. Recently, van Bokhoven et al. [25] suggested from their numerical simulations that the power law exponent for the enstrophy was affected by the size of initially assumed vortices. Our result is close to that of Chasnov because the same formulation is employed to give the initial energy spectrum.

In this study, both ILES-WCNS and ILES-CS5 are shown to give reasonable solutions of 2D homogeneous turbulence. However, the computed results of ILES-WCNS slightly differ from that of ILES-CS5 in terms of the energy spectrum at high wavenumber limit, as shown in Fig. 7, and also of the temporal history of the kinetic energy, as shown in Fig. 8(*a*). In ILES-WCNS, the weighted interpolation is sometimes biased toward one of the third order interpolations for monotonicity preservation. It is interesting to identify where such biased interpolation is chosen in ILES-WCNS. For this purpose, let us introduce a residual velocity vector $(u_{i,j}^{\mathrm{res}}, v_{i,j}^{\mathrm{res}})$ defined by

$$u_{i,j}^{\mathrm{res}} = \tfrac{1}{4}(\bar{u}_{Ri-1/2,j} + \bar{u}_{Li+1/2,j} + \bar{u}_{Ri,j-1/2} + \bar{u}_{Li,j+1/2}) \tag{62}$$

$$v_{i,j}^{\mathrm{res}} = \tfrac{1}{4}(\bar{v}_{Ri-1/2,j} + \bar{v}_{Li+1/2,j} + \bar{v}_{Ri,j-1/2} + \bar{v}_{Li,j+1/2}) \tag{63}$$

where $\bar{u}$ and $\bar{v}$ denote $\bar{u}=\tilde{u}^{\omega}-\tilde{u}^{\mathrm{CS5}}$ and $\bar{v}=\tilde{v}^{\omega}-\tilde{v}^{\mathrm{CS5}}$, respectively. These $(\tilde{u}^{\mathrm{CS5}}, \tilde{v}^{\mathrm{CS5}})$ are obtained from Eqs. (15) and (16) for the left-hand side and the right-hand side of the cell-edge, respectively, and $(\tilde{u}^{\omega}, \tilde{v}^{\omega})$ are similarly determined from Eqs. (31) and (32). The absolute value of $\nabla\times\omega$ and the magnitude of residual velocity vector defined by $\sqrt{(u_{i,j}^{\mathrm{res}})^2+(v_{i,j}^{\mathrm{res}})^2}$ are plotted in Figs. 10(*a*) and 10(*b*), respectively. The cross-correlation value between $|\nabla\times\omega|$ and $\sqrt{(u_{i,j}^{\mathrm{res}})^2+(v_{i,j}^{\mathrm{res}})^2}$ becomes 0.43, which indicates that a certain correlation between them exists. It should be noted that the explicit SGS term in the conventional LES formulation is approximated by the eddy viscosity model as

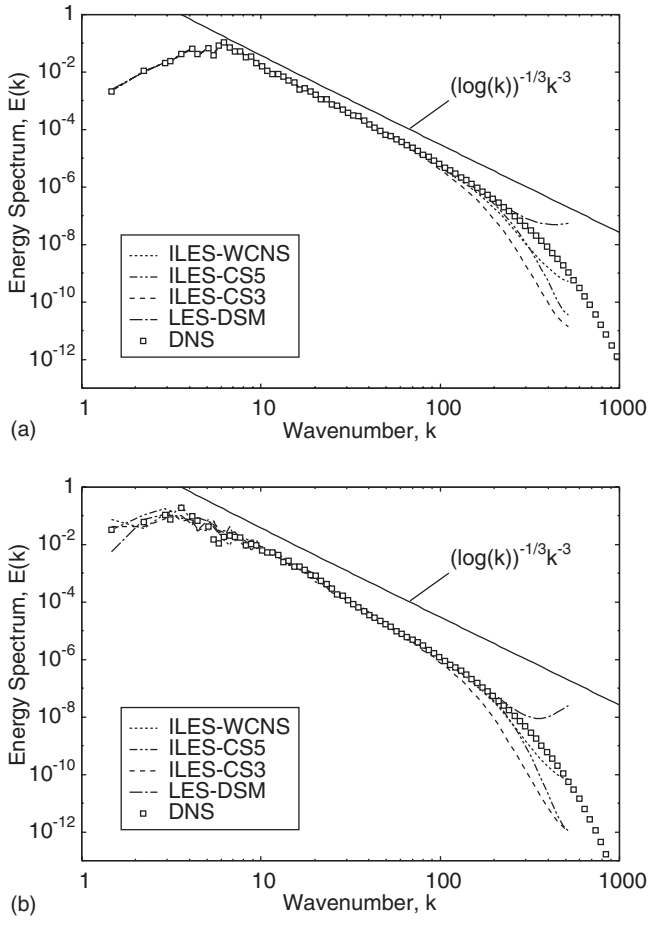

Fig. 7 Comparison of energy spectra. (*a*) $t=2.0$ and (*b*) $t=6.0$.

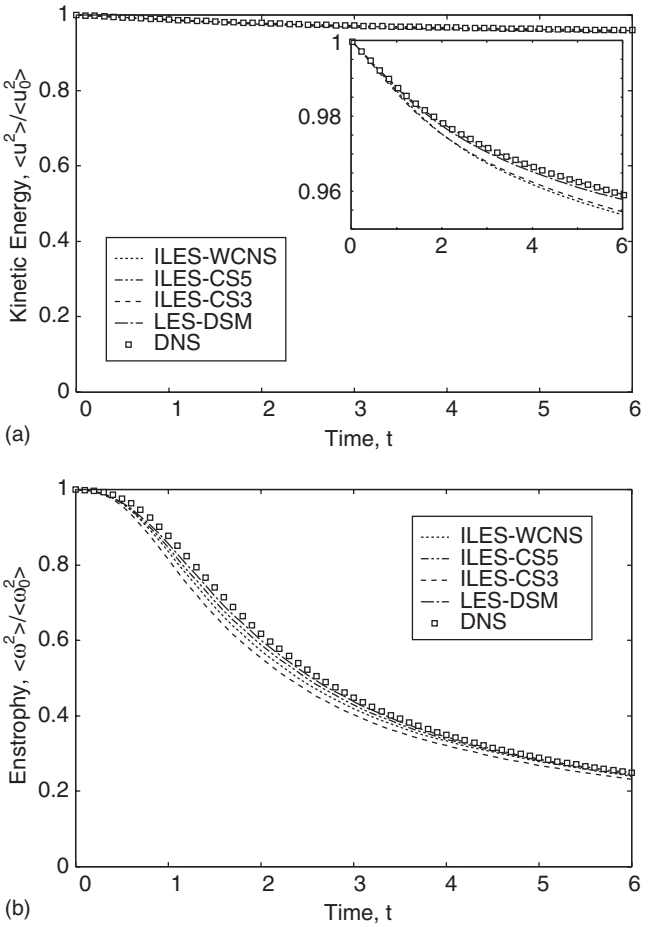

Fig. 8 Comparison of (*a*) kinetic energy and (*b*) enstrophy

$$-\frac{\partial \tau_{ij}}{\partial x_j} = -\frac{\partial}{\partial x_j}(-2\nu_e \bar{S}_{ij}) = \nu_e \nabla^2 \bar{\mathbf{u}} = -\nu_e \nabla \times \bar{\omega} \qquad (64)$$

where τ_{ij} denotes the SGS stress, ν_e is the eddy viscosity coefficient, and $\bar{S}_{ij}$ is the strain rate tensor, respectively. The overlined variable indicates that it is a filtered value. Therefore, the enhanced numerical diffusion effect due to the use of the third order interpolations in ILES-WCNS appears at the location where the explicit SGS term can arise in the conventional LES. This is probably the reason why ILES-WCNS gives a reasonable resolution for turbulent flowfield, while it attains a monotone preservation property needed for the computation of compressible flowfield.

The effect of grid resolution for this problem is also explored for ILES-WCNS. The obtained results using 512^2 grid points are denoted as ILES-WCNS-512, while those using 2048^2 grid points are ILES-WCNS-2048. The computed results shown so far utilize 1024^2 grid points, and are denoted as ILES-WCNS-1024 where needed.

As shown in Fig. 11, both ILES-WCNS-512 and ILES-WCNS-2048 give the vorticity contours at $t=6.0$ that exhibit no numerical oscillation. In Fig. 12, the computed energy spectra at $t=6.0$ are compared for different grid resolutions. We can find in all cases that the inertial range appears and that smooth truncation of the energy spectrum occurs in the maximum wavenumber region. Obviously, ILES-WCNS-512 gives the energy spectrum that begins to deviate from the result of DNS at longer wavelength. As the grid is refined, the inertial range extends to the shorter wavelength region, and seems to converge to that of DNS. Note that the energy spectrum given by ILES-WCNS-2048 becomes slightly larger than that given by DNS at high wavenumber limit due to the weak instability stated earlier. However, the deviation occurs already in dissipation range, and therefore no influence is expected for the flowfield.

In Fig. 13, we also compare the temporal variations of (a) the normalized kinetic energy and (b) the normalized enstrophy for different grid resolutions. Again, ILES-WCNS-512 gives the most dissipative results and, as the grid is refined, the computed results tend to those given by DNS.

Now let us show the computed results for the case of compressible homogeneous turbulence. The initial velocity profile for the computation of 2D compressible turbulence is the same as that for the incompressible case. In addition, the initial density is assumed to be $\rho_0=1.0$. By assuming the Mach number to be $M_0=U_0/c_0=0.1$, where c_0 denotes the constant sound velocity for the initial flowfield, the total energy for a unit volume can be determined. The ratio of the constant specific heat is $\gamma=1.4$, and the Prandtl number is unity.

Table 2 summarizes the numerical schemes considered for this case. The implicit LES code that utilizes WCNS for compressible flow is denoted as ILES-WCNS-C and the implicit LES code that employs the fifth order interpolation as ILES-CS5-C. The results are compared with those given by ILES-WCNS, ILES-CS5, ILES-CS3, and DNS for incompressible flow.

The computed vorticity contours are very similar to those shown in Figs. 5 and 6, and therefore we omit showing them. Figure 14 shows the computed energy spectra obtained at $t=2.0$ and $t=6.0$. We can find that the inertial range in each energy spectrum appears correctly, and that truncation of the energy spectrum occurs smoothly at high wavenumber limit. Note that the energy spectra obtained by ILES-WCNS-C and ILES-CS5-C become lower than those corresponding ones given by ILES-WCNS

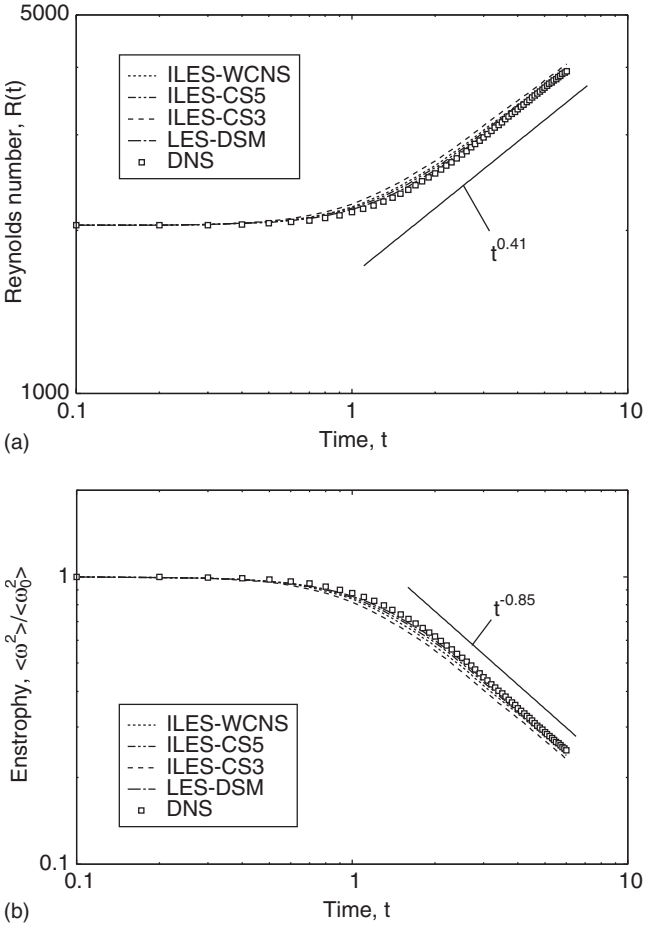

Fig. 9 Comparison of (*a*) Reynolds number and (*b*) enstrophy in logarithmic scale. The solid lines indicate the fitted power laws.

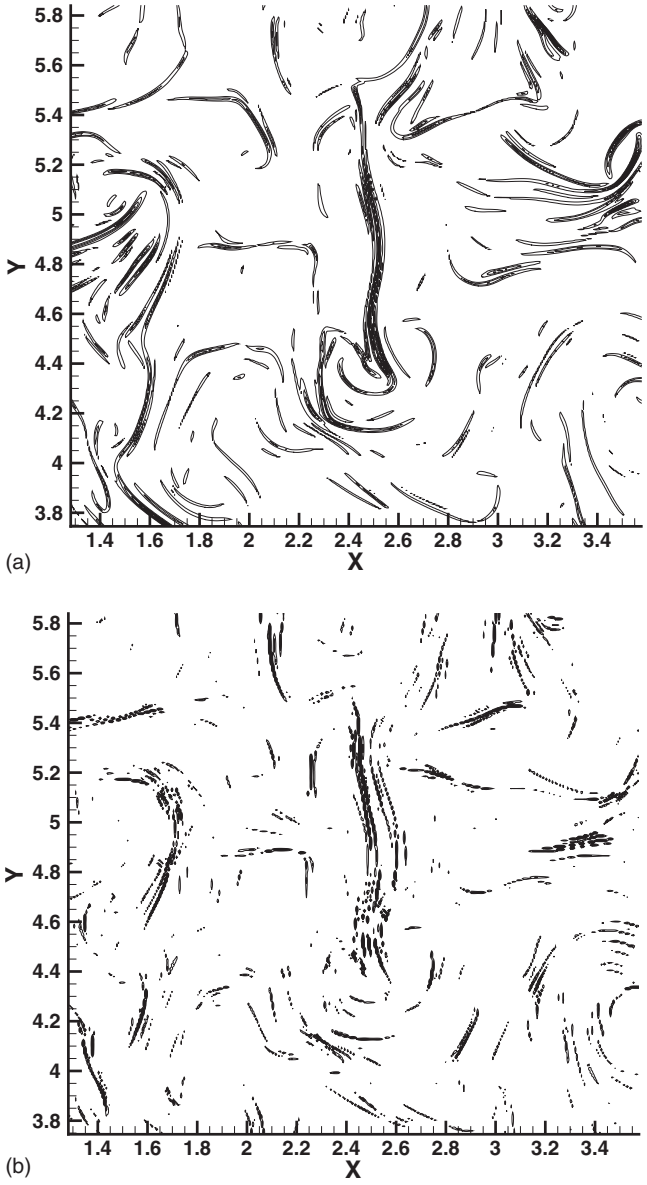

Fig. 10 Contours of (*a*) $|\nabla \times \omega|$ and (*b*) weights $\sqrt{(u_{i,j}^{res})^2+(v_{i,j}^{res})^2}$ for interpolation in WCNS

and ILES-CS5 for incompressible flow case. This obviously implies that these schemes for compressible flow are more dissipative than those for incompressible flow due to the fact that numerical viscosity is involved not only in the momentum equations, but also in the mass and the energy conservation equations. Therefore, the kinetic energy for compressible flow case is more dissipated than that for incompressible flow case.

In Fig. 15, the temporal histories of (a) the normalized kinetic energy and (b) the normalized enstrophy are shown. All the normalized kinetic energy profiles obtained by implicit LES agree reasonably well with that obtained by DNS. However, those ILES-WCNS-C and ILES-CS5-C give the curves that deviate quickly from that of DNS at the beginning of the computation. Although the density and the pressure are initially constant in the entire region, the total energy per unit volume is not constant due to kinetic energy component, which seems to introduce dissipative effect particularly at the beginning of the computation. A comparison of the kinetic energy profiles given by ILES-WCNS-C and ILES-CS5-C shows that ILES-WCNS-C is more dissipative, as is expected, due to the use of the third order interpolation. As to the enstrophy plots, ILES-WCNS-C gives a very similar profile with that given by ILES-CS3 again indicating that a larger dissipative effect is involved in the computation of compressible flow case. As to the temporal variations in the Reynolds number and the enstrophy, plotted curves are very similar to those for incompressible flow case and therefore they are omitted.

Recently, Thornber et al. [26] showed that dissipation of kinetic energy of the flowfield computed by high resolution shock capturing scheme was directly linked to temperature multiplied by change in entropy at low Mach numbers. It is interesting to observe whether such relation is also established in the present result. Figure 16 shows the comparison of temporal variation in kinetic energy with the initial kinetic energy KE_0 minus $T\Delta S$ for the present result, where T denotes the temperature and ΔS the change of entropy determined by [26]

$$\Delta S = \frac{\mathrm{R}}{\gamma - 1} \ln\left[\left(\frac{p}{\rho^{\gamma}}\right)^{n+1}\left(\frac{\rho^{\gamma}}{p}\right)^{n}\right] \tag{65}$$

in which n denotes the time step. One can find that $KE_0 - T\Delta S$ agrees fairly well with temporal variation in the kinetic energy, indicating that the present result is consistent with that of Thornber et al. Note that the initial kinetic energy is assumed as the value at $t=0.1$ in Fig. 16 because the initial velocity field is slightly damped out by WCNS at the beginning of computation.

Thornber et al. also pointed out that the dissipation of kinetic energy occurs more rapidly as the flow Mach number decreases. It is very difficult, however, to confirm the possible Mach number dependence for the present case because it requires a prohibitively

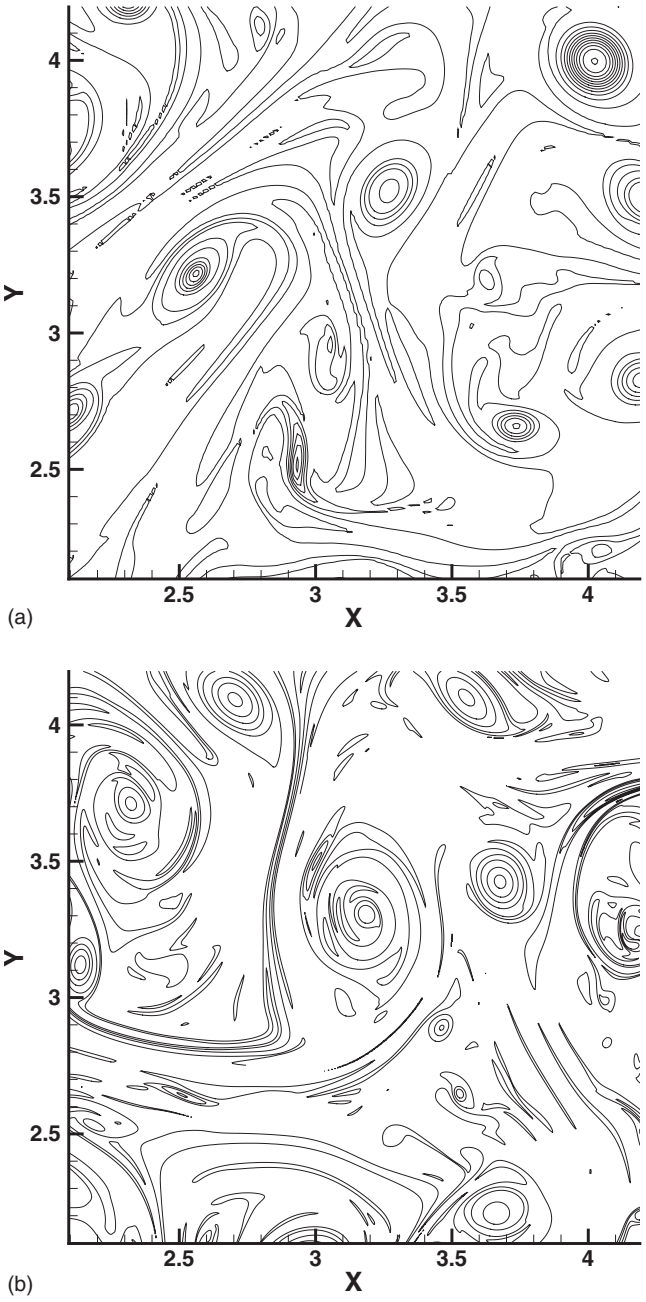

Fig. 11 Computed vorticity distribution at $t=6.0$. (*a*) ILES-WCNS-512 and (*b*) ILES-WCNS-2048.

large CPU time for obtaining the flowfield for small Mach numbers. Therefore, we have examined this point by solving a 2D double shear layer problem for inviscid flowfield.

The governing equations for this problem are given by Eq. (4) where the viscous terms, as well as thermal conduction, are all removed. The computational domain is a square region whose edge has a length of 2π. The periodic boundary condition is assumed at four edges. The initial velocity field is given by

$$u(x,y) = \begin{cases} 1 & \text{for } -\frac{\pi}{2} \le y \le \frac{3\pi}{2} \\ -1 & \text{for } y < -\frac{\pi}{2}, \frac{3\pi}{2} < y \end{cases} \tag{66}$$

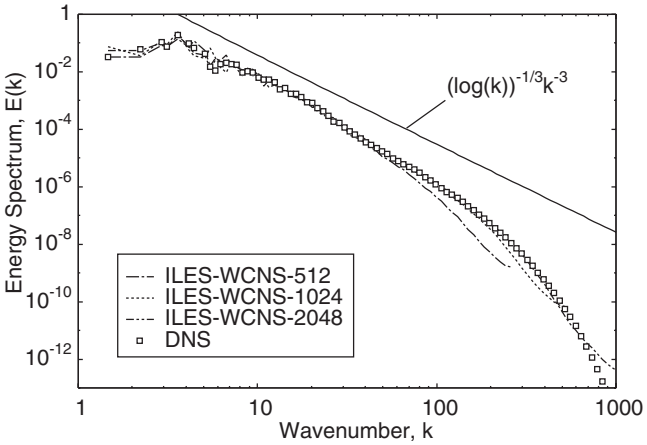

Fig. 12 Comparison of energy spectra at $t=6.0$

$$v(x,y) = \delta \sin(x) \tag{67}$$

where we assume $\delta=0.05$. We also assume that the initial density is $\rho_0=1.0$ and the ratio of constant specific heats $\gamma=1.4$. The initial Mach number is given by

$$\mathrm{M}_0 = \frac{U_0}{c_0} \tag{68}$$

where U_0 denotes the root-mean-square value of the initial velocity, and c_0 the constant sound velocity for the initial flowfield. The

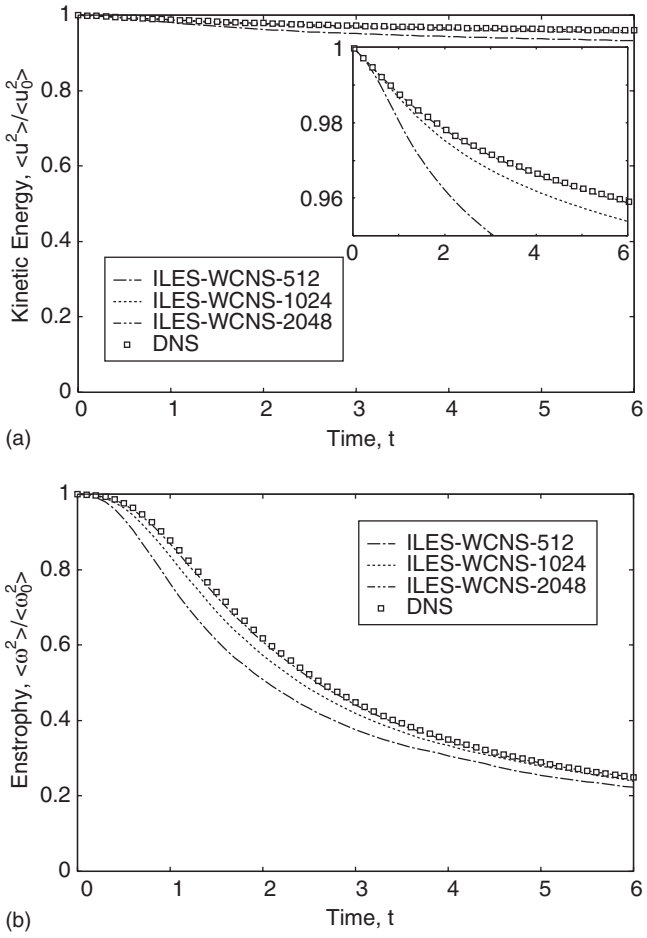

Fig. 13 Comparison of (*a*) kinetic energy and (*b*) enstrophy

Table 2 Numerical methods

	Governing eqs.	Scheme	Interpolation	Grid points
ILES-WCNS-C	NS-comp	Fifth-CS (WCNS)	Weighted	1024^2
ILES-CS5-C	NS-comp	Fifth-CS	Fifth-biased	1024^2
ILES-WCNS	NS-incomp	Fifth-CS (WCNS)	Weighted	1024^2
ILES-CS5	NS-incomp	Fifth-CS	Fifth-biased	1024^2
ILES-CS3	NS-incomp	Fifth-CS	Third-biased	1024^2
DNS	NS-incomp	Fourth-CDS	-	4096^2

ILES: implicit LES, NS-comp: compressible Navier–Stokes equations, NS-incomp: incompressible Navier–Stokes equations, WCNS: weighted compact nonlinear scheme, fifth-CS: Fifth order compact scheme, fourth-CDS: fourth order central difference scheme, weighted: weighted interpolation, fifth-biased: fifth order biased interpolation, and third-biased: third order biased interpolation.

results are obtained for three different Mach numbers $M_0=0.1$, 0.05, and 0.01.

Figure 17 shows the temporal variations in kinetic energy and $KE_0-T\Delta S$ computed by WCNS and CS5. For all cases, the temporal variations in $KE_0-T\Delta S$ agree fairly well with those of the corresponding kinetic energy. We note that the dissipation of kinetic energy given by CS5 becomes smaller as the Mach number is increased. This agrees with what Thornber et al. pointed out in their study. However, the dissipation of kinetic energy given by WCNS is more apparent as the Mach number is increased.

In WCNS, the overall numerical viscosity can be regarded as a sum of the one given by baseline CS5 scheme and the other due to third order biased interpolation. Even though the former decreases, the latter grows rapidly, as the Mach number is increased to make overall numerical viscosity increase. Because the density is initially assumed constant, any increase in density fluctuation causes third order biased interpolation. The magnitude of this density fluctuation becomes larger as the Mach number is increased due to compressibility. A modification of the smoothness measure given in Eq. (37) may alleviate the rapid increase in dissipative effect in WCNS at low Mach number. However, a detailed exploration of implicit SGS viscosity involved in the present high resolution scheme linked with the Mach number is beyond the scope of the present study.

4 Conclusions

In this study, an implicit LES method for computing 2D homogeneous turbulence is examined. Evaluation of the convective terms is made by WCNS, which utilizes the fifth order accurate interpolations in the smooth region, and turns to employ a

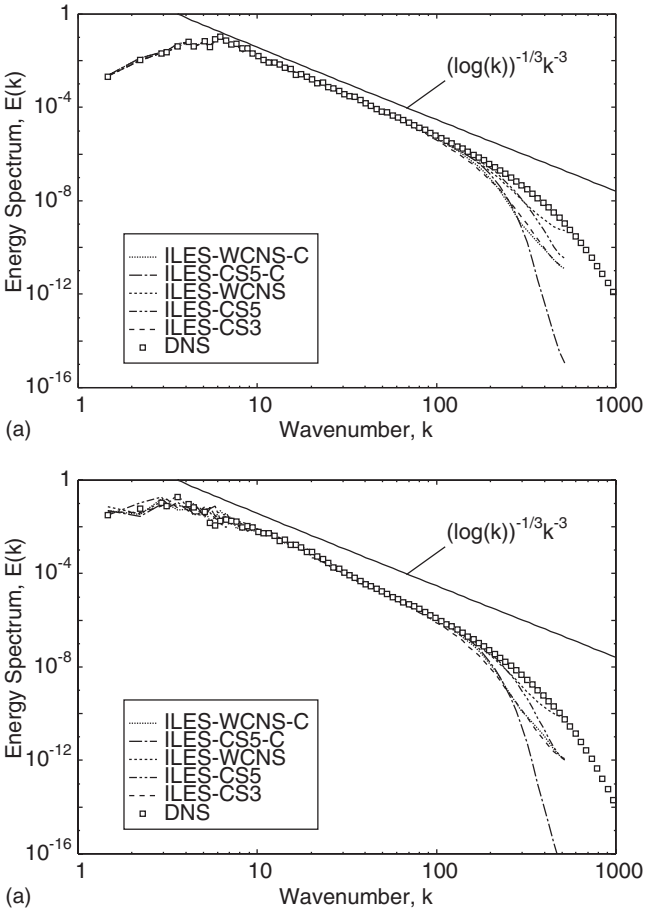

Fig. 14 Comparison of energy spectra. (*a*) *t*=2.0 and (*b*) *t*=6.0.

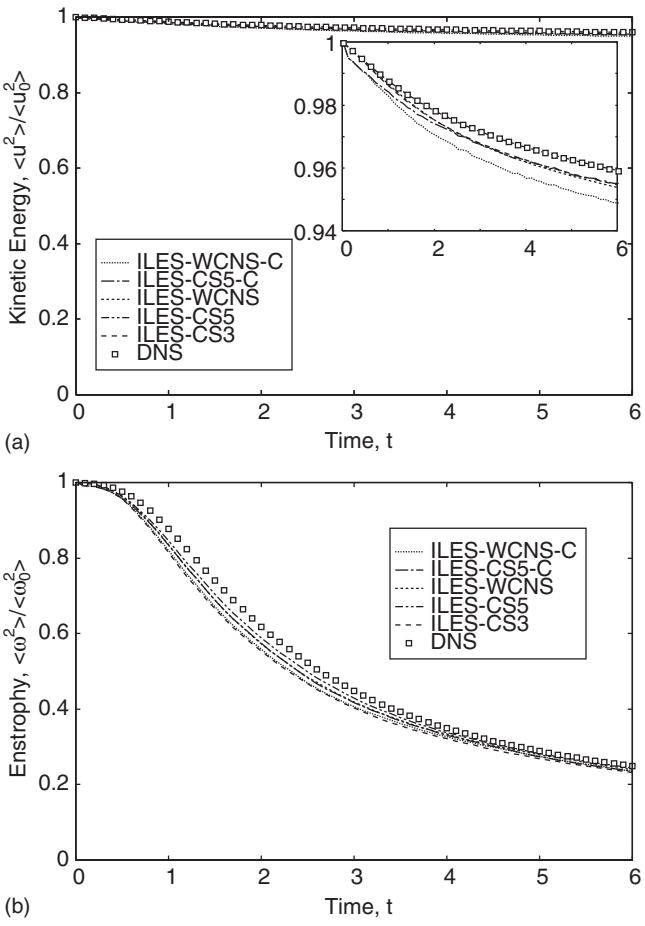

Fig. 15 Comparison of (*a*) kinetic energy and (*b*) enstrophy

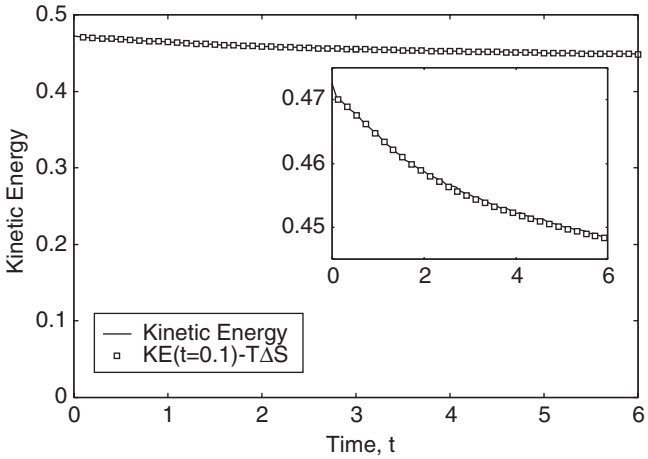

Fig. 16 Temporal history of kinetic energy with the predicted change using the initial kinetic energy KE_0 minus $T\Delta S$

weighted average of the third order interpolations where needed to maintain monotonicity. The result of a linear stability analysis of the scheme for a linear advection problem shows that the third order interpolation chosen in an upwind stencil provides a fairly large numerical dissipation to stabilize the scheme. However, the same third order interpolation is shown to make the scheme weakly unstable for waves satisfying $k\Delta x \approx 1$.

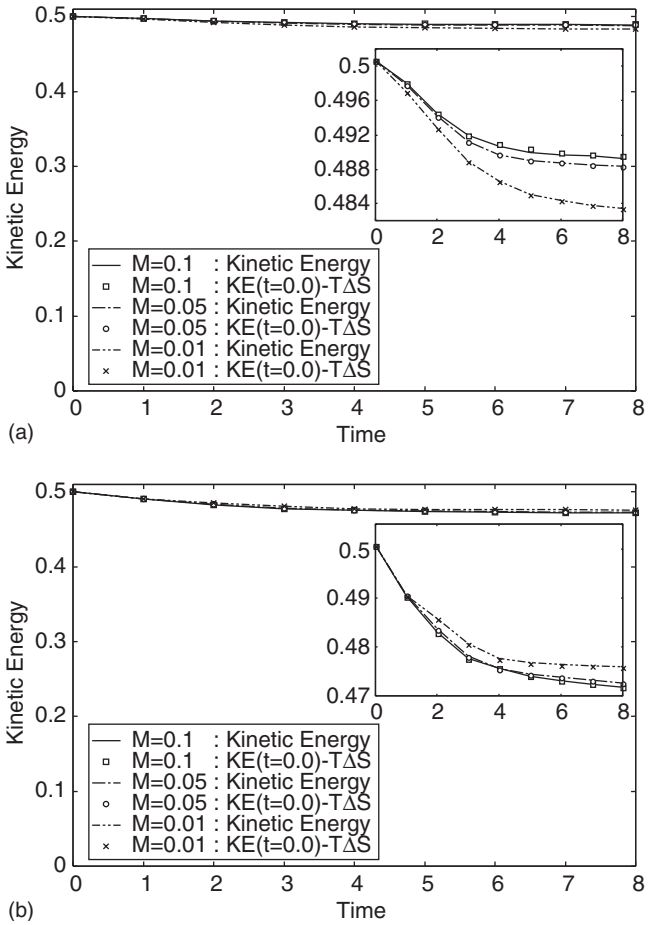

Fig. 17 Comparison of temporal variation of kinetic energy with the initial kinetic energy KE_0 minus $T\Delta S$ for three different Mach numbers, M_0=0.1, 0.05, and 0.01. (*a*) CS5 and (*b*) WCNS.

At first, the obtained results for 2D incompressible homogeneous turbulence in a square domain computed by several implicit LES codes are compared with those given by LES-DSM and DNS. It is shown that the vorticity contours given by ILES-WCNS and ILES-CS5 agree fairly well with that given by DNS solution at earlier time. A fair agreement is also obtained for LES-DSM, though numerical wiggles appear everywhere in the flowfield. The cause of the numerical wiggles is attributed to improper use of the dynamic Smagorinsky SGS model for 2D flowfield. At a later time, all solutions of these LES codes and that of DNS are different from each other due to chaotic nature of turbulence. It is shown that ILES-WCNS and ILES-CS5 give the energy spectra that agree fairly well with that of DNS, though numerical viscosity causes the energy spectra to be slightly lower than that of DNS at the high wavenumber region. A natural truncation of the energy spectrum occurs for these implicit LES codes at high wavenumber limit. The computed energy spectrum of ILES-WCNS increases slightly from that of ILES-CS5 at high wavenumber limit, suggesting that the third order interpolation chosen in the weighted combination results in a weak numerical excitation, which is a consequence of the weak instability indicated in the linear stability analysis. For the compressible flow case, a favorable agreement with the result of DNS is also maintained, though the dissipative effect is slightly significant if compared with those given by implicit LES methods for incompressible flow case.

It is shown that where the weighted average of the third order interpolations deviate from the optimum combination reasonably agrees with the location where $|\nabla \times \omega|$ becomes large, and hence where the explicit SGS term can arise in the conventional LES. This suggests the reason why ILES-WCNS can resolve turbulent flowfield reasonably well, why it can maintain numerical stability at discontinuities.

Acknowledgment

All the computations are carried out by SX-8 supercomputer in the Advanced Fluid Information Research Center, Institute of Fluid Science, Tohoku University. K.I. gratefully acknowledges Nicholas Williamson and Steve Armfield for their help in conducting large eddy simulation while he was staying at the University of Sydney in Australia.

References

[1] Daimon, Y., Shimada, T., Takaki, R., Fujita, K., and Takekawa, K., 2006, "Evaluation of Ablation and Longitudinal Vortices in Solid Rocket Motor by Computational Fluid Dynamics," AIAA Paper No. 2006-5243.
[2] Lesieur, M., Metais, O., and Comte, P., 2005, *Large-Eddy Simulations of Turbulence*, Cambridge University, Cambridge.
[3] Grinstein, F. F., Margolin, L. G., and Rider, W. J., 2007, *Implicit Large Eddy Simulation*, Cambridge University, Cambridge.
[4] Boris, J. P., Grinstein, F. F., Oran, E. S., and Kolbe, R. L., 1992, "New Insights Into Large Eddy Simulation," Fluid Dyn. Res., **10**, pp. 199–288.
[5] Grinstein, F. F., Fureby, C., and DeVore, C. R., 2005, "On MILES Based on Flux-Limiting Algorithms," Int. J. Numer. Methods Fluids, **47**, pp. 1043–1051.
[6] van Leer, B., 1979, "Towards the Ultimate Conservative Difference Scheme. V. A Second-Order Sequel to Godunov's Method," J. Comput. Phys., **32**, pp. 101–136.
[7] Shu, C. W., and Osher, S., 1988, "Efficient Implementation of Essentially Non-Oscillatory Shock-Capturing Schemes," J. Comput. Phys., **77**, pp. 439–471.
[8] Shu, C. W., and Osher, S., 1989, "Efficient Implementation of Essentially Non-Oscillatory Shock-Capturing Schemes, II," J. Comput. Phys., **83**, pp. 32–78.
[9] Liu, X. D., Osher, S., and Chan, T., 1994, "Weighted Essentially Non-Oscillatory Schemes," J. Comput. Phys., **115**, pp. 200–212.
[10] Jiang, G. S., and Shu, C. W., 1996, "Efficient Implementation of Weighted ENO Schemes," J. Comput. Phys., **126**, pp. 202–228.
[11] Drikakis, D., 2002, "Embedded Turbulence Model in Numerical Methods for Hyperbolic Conservation Laws," Int. J. Numer. Methods Fluids, **39**, pp. 763–781.
[12] Drikakis, D., 2003, "Advances in Turbulent Flow Computations Using High-Resolution Methods," Prog. Aerosp. Sci., **39**, pp. 405–424.
[13] Garnier, E., Mossi, M., Sagaut, P., Comte, P., and Deville, M., 1999, "On the Use of Shock-Capturing Schemes for Large-Eddy Simulation," J. Comput. Phys., **153**, pp. 273–311.

[14] Lele, S. K., 1992, "Compact Finite Difference Schemes With Spectral-Like Resolution," J. Comput. Phys., **103**, pp. 16–42.
[15] Deng, X. G., and Mao, M. L., 1997, "Weighted Compact High-Order Nonlinear Schemes for the Euler Equations," AIAA Paper No. 97-1941.
[16] Deng, X. G., and Zhang, H. X., 2000, "Developing High-Order Weighted Compact Nonlinear Schemes," J. Comput. Phys., **165**, pp. 22–44.
[17] Ishiko, K., Ohnishi, N., and Sawada, K., 2005, "Implicit LES of Turbulence Using Weighted Compact Scheme," Nagare, **24**(5), pp. 515–523.
[18] Das, A., and Moser, R. D., 2002, "Optimal Large-Eddy Simulation of Forced Burgers Equation," Phys. Fluids, **14**(12), pp. 4344–4351.
[19] Aprovitola, A., and Denaro, F. M., 2004, "On the Application of Congruent Upwind Discretizations for Large Eddy Simulations," J. Comput. Phys., **194**, pp. 329–343.
[20] Kraichnan, R. H., 1971, "Inertial-Range Transfer in Two- and Three-Dimensional Turbulence," J. Fluid Mech., **47**, pp. 525–535.
[21] Wada, Y., and Liu, M. S., 1994, "A Flux Splitting Scheme With High-Resolution and Robustness for Discontinuities," AIAA Paper No. 94-0083.
[22] Chasnov, J. R., 1997, "On the Decay of Two-Dimensional Homogeneous Turbulence," Phys. Fluids, **9**(1), pp. 171–180.
[23] Das, C., Kida, S., and Goto, S., 2001, "Overall Self-Similar Decay of Two-Dimensional Turbulence," J. Phys. Soc. Jpn., **70**(4), pp. 966–976.
[24] Batchelor, G. K., 1969, "Computation of the Energy Spectrum in Homogeneous Two-Dimensional Turbulence," Phys. Fluids, **12**, pp. 233–239.
[25] van Bokhoven, L. J. A., Trieling, R. R., Clercx, H. J. J., and van Heijst, G. J. F., 2007, "Influence of Initial Conditions on Decaying Two-Dimensional Turbulence," Phys. Fluids, **19**, p. 046601.
[26] Thornber, B., Drikakis, D., Williams, R. J. R., and Youngs, D., 2008, "On Entropy Generation and Dissipation of Kinetic Energy in High-Resolution Shock-Capturing Schemes," J. Comput. Phys., **227**, pp. 4853–4872.

Drag Reduction Due to Cut-Corners at the Front-Edge of a Rectangular Cylinder With the Length-to-Breadth Ratio Being Less Than or Equal to Unity

Mitsuo Kurata
Department of Mechanical Engineering,
College of Engineering,
Setsunan University,
17-8 Ikedanaka-Machi,
Neyagawa, Osaka 572-8508, Japan

Yoshiaki Ueda
Division of Materials Science and Engineering,
Graduate School of Engineering,
Hokkaido University,
Nishi 8, Kita 13, Kita-Ku,
Sapporo, Hokkaido 060-8628, Japan
e-mail: y-ueda@eng.hokudai.ac.jp

Teruhiko Kida
Professor Emeritus
Division of Mechanical Engineering,
Graduate School of Engineering,
Osaka Prefecture University,
1-1 Gakuen-Cho,
Sakai, Osaka 599-8531, Japan

Manabu Iguchi
Division of Materials Science and Engineering,
Graduate School of Engineering,
Hokkaido University,
Nishi 8, Kita 13, Kita-Ku,
Sapporo, Hokkaido 060-8628, Japan

The flow past a rectangular cylinder with small cut-corners at the front-edge is investigated to discuss a relation between drag reduction and the cutout dimension. The rectangular shape is selected in eleven kinds of the length-to-breadth ratio from 2/6 to 6/6 (square prism) with the small rectangular-shaped cut-corners at the front-edge. The wind tunnel experiment is carried out to obtain time-averaged hydrodynamic forces measured by the force transducer at Re≈50,000. The contour map of the hydrodynamic coefficients with respect to the cutout dimension are shown to investigate the relation between the drag reduction and the cutout shape. In the contour map for the zero angle of attack, the region of the effective drag reduction achieved, in which the value of the drag coefficient is less than that of a circular cylinder at the same Reynolds number, is observed to become wide with the increase in the length-to-breadth ratio and it is independent of the angle of attack, α, within α being small. Furthermore, it is shown that there is a condition in which the drag reduction of $C_D \lessapprox 1.5$ can be achieved even when the Strouhal number is less than 0.2. [DOI: 10.1115/1.3129123]

Contributed by the Fluids Engineering Division of ASME for publication in the JOURNAL OF FLUIDS ENGINEERING. Manuscript received February 20, 2008; final manuscript received March 11, 2009; published online May 13, 2009. Assoc. Editor: Zvi Rusak.

1 Introduction

Drag reduction is an intriguing subject because saving of energy is one of the primary issues in modern developed society. The familiar methods of a drag reduction are classified into (i) a boundary-layer control by a tripping wire over a body surface to reduce a separated shear layer from the body and (ii) a geometrical modification to remove a strong separated flow; for example, a sharp corner is made into a rounded one with a moderately small curvature as mentioned in Ref. [1]. The drag reduction is known to be achieved as well in a square prism with cut-corners at the front-edge at the Reynolds number being approximately 50,000 (see Ref. [2]). To investigate the drag reduction, the present work selects a rectangular cylinder, having the length-to-breadth ratio being less than or equal to unity, with or without small rectangular-shaped cut-corners at the front-edge.

The present authors have already reported the drag reduction in a square prism with cut-corners and the zero angle of attack at $\mathrm{Re} \approx 50,000$ and showed a detailed contour map of the hydrodynamic forces (see Ref. [3]). One can refer to the typical references in the previous articles [2–5]. Following the series of articles [2–5], Igarashi et al. [6] reconfirmed their results and proposed a geometrical-based formula about the dimension of the rectangular-shaped cut-corners to obtain the remarkable drag reduction for a few kinds of the length-to-breath ratios being less than unity. Their predicted formula is obtained by the identification of the turbulent separation point of the cutout cylinder with one of the circular cylinders. The verification of their proposed formula has been unfortunately done for only two cases of the length-to-breadth ratios with a few kinds of cutout dimensions. The Strouhal number, St, was observed to jump from between 0.14 and 0.16 to 0.25 at the critical Reynolds number about $\mathrm{Re}_c \approx 8000$ using the smoke flow and oil flow visualizations, which was carried out by Igarashi et al. [6]. They implied that the jump of the Strouhal number relates to the drag reduction. In visualizations, the separation was also observed to be turbulent for $\mathrm{Re} > \mathrm{Re}_c$. Okajima et al. [7] also visualized a separated shear layer from the front-corner of the rectangular cylinder using the smoke flow technique. Their visualization was carried out in a wide range of the Reynolds number about a rectangular cylinder, having the various length-to-breadth ratios, with a few kinds of small cut-corners. The separated shear layer from the front corner was observed to completely separate in $\mathrm{Re} < \mathrm{Re}_c$ and to re-attach on the side surface of the cylinder in $\mathrm{Re} > \mathrm{Re}_c$. They concluded that the jump of the Strouhal number (from between 0.17 and 0.20 to between 0.23 and 0.25) is caused by the transition of the separated shear layer at Re_c. Unfortunately, Okajima et al. [7] did not show any results on the drag force. Unlike Igarashi et al. [6], our previous experiments [3] showed the drag reduction of $C_D \approx 1.5$ in the Strouhal number being even less than 0.18. Therefore, the present paper gives a detailed contour map about the drag force with respect to the cutout dimensions or the angle of attack and discusses the relation between the drag force and Strouhal number. The selected length-to-breadth ratio is less than or equal to unity.

2 Experimental Methodology

Figure 1 shows the Cartesian coordinate system and an experimental model. A rectangular cylinder with the breadth of $a = 30$ mm and 11 kinds of the length, $b = 5.0, 7.5, 10, \ldots, 30$ mm, having cut-corners at the front-edge, is 360 mm long in the spanwise direction. Then, the length-to-breadth ratio is calculated as $b/a = 2/12, 3/12, 4/12, \ldots, 12/12$. The dimensions of the cut-corner shape are denoted as c_1 and c_2 in the y- and x-directions, respectively. In this experiment, c_1/a was varied, by 0.05 spacing, between 0.00 and 0.20, and c_2/a was also varied between 0.00 and 0.25. Thus, 21 sets of the experimental model were adopted.

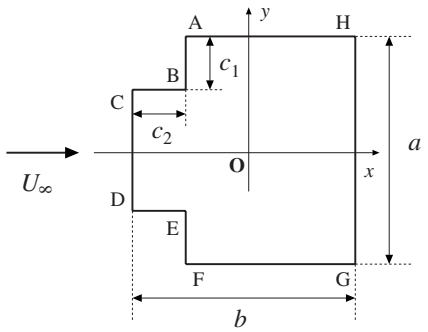

Fig. 1 Coordinate system and physical settings

The drag force and the Strouhal number were measured by using the open-type wind tunnel whose cross section is 380 $\times$380 mm^2. The turbulence intensity of the wind tunnel is between 0.8% and 1.2%. The rectangular cylinder was set inside the sidewall consisting of two parallel plates of which the front-edges were cut out in 45 deg to reduce separation from the edge. The uniform flow was varied in 25 m/s, 30 m/s, and 35 m/s. The Reynolds number, based on the breadth of the cylinder a, is then calculated as 5×10^4, 6×10^4, and 7×10^4. The drag force was measured through the force transducer on which the rectangular cylinder was set. The sampling data were conducted to the fast Fourier transform (FFT) analyzer equipped with the personal computer through the analog/digital (A/D) converter. The resolution of the FFT is 0.98 Hz. The Strouhal number, St, was calculated by using the frequency analyzer from the measured values by the X-type hot-wire anemometer. The position of the hot-wire anemometer was approximately at $x/a\approx4.0$ and $y/a\approx1.5$, and it was chosen as the appropriate point where the frequency became clear. The base pressure was measured at the pressure hole, which was made at the center on the base face of the rectangular cylinder.

3 Experimental Results

3.1 Effect of Length-to-Breadth Ratio for the Zero Angle of Attack. Figure 2 shows the drag and lift coefficients, C_D and C_L, the Strouhal number, St, and the base pressure coefficient, C_{Pb}, for the various length-to-breadth ratios being less than or equal to unity. This experiment has been done for the zero angle of attack. Three kinds of the cut-corner shape are selected; (open circle) $c_1/a=c_2/a=0.00$, namely, without cutout; (open square) $c_1/a=0.10$ and $c_2/a=0.15$; and (open triangle) $c_1/a=0.10$ and $c_2/a=0.20$. Each coefficient is, respectively, defined as follows:

$$C_D := \frac{D}{\frac{1}{2}\rho U_\infty^2 a}, \quad C_L := \frac{L}{\frac{1}{2}\rho U_\infty^2 a}, \quad \mathrm{St} := \frac{fa}{U_\infty}, \quad C_{\mathrm{Pb}} := \frac{P_b - P_\infty}{\frac{1}{2}\rho U_\infty^2} \tag{1}$$

where D is the drag force, L is the lift force, f is the frequency, P_b is the base pressure, and P_∞ is a reference pressure as $x\to\infty$, respectively.

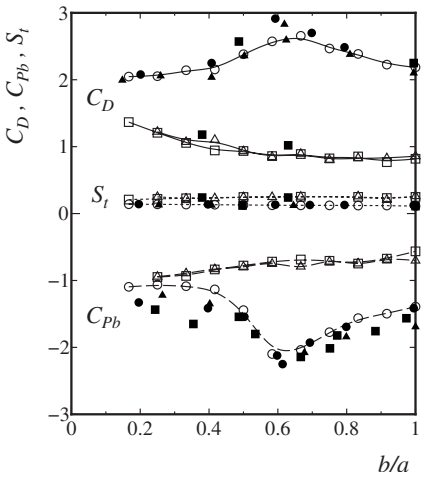

Fig. 2 Length-to-breadth ratio, b/a, versus hydrodynamic coefficients: (solid line) C_D, (dashed line) C_{Pb}, (dotted line) St for various cutout shapes, (circle) $c_1/a=c_2/a=0.0$; (square) $c_1/a=0.1$ and $c_2/a=0.15$, and (triangle) $c_1/a=0.1$ and $c_2/a=0.2$. The solid symbols are earlier comparative results for $c_1/a=c_2/a=0.0$ by (solid circle) Bearman and Trueman [8], (solid square) Igarashi [9], and (solid triangle) Nakaguchi et al. [10].

In this figure, the present results are compared with earlier experimental results for the case without the cutout given by Bearman and Trueman [8], Igarashi [9], and Nakaguchi et al. [10]. The present results seem to be in good agreement with the earlier ones. The C_D profile of the no cut-corner case exhibits the maximum value around $b/a=0.68$. By contrast to the no cut-corner case, the cut-corner case exhibits a flat profile of C_D and the critical change of C_D cannot be observed although being observed around $b/a\approx0.68$ in the no cut-corner case. In terms of St, the remarkable change of St cannot be observed for any c_1/a even in the no cut-corner case.

3.2 Effect of Dimension of Cut-Corners for the Zero Angle of Attack. Figure 3 shows the hydrodynamic coefficients for various y-components of the cut-corner dimension. As mentioned in Sec. 2, c_1/a was varied, by 0.05 spacing, between 0.00 and 0.20. To make it easy to see, every plot is traced by the B-spline curve. These figures show that the C_D profile is convex downward with respect to c_1/a, and the minimum value of C_D exists in the adopted range $0.0\le c_1/a\le0.2$ for all cases of b/a. Also, the drag reduction seems to gradually change against c_1/a. The c_1/a-dependence of the C_{Pb} seems to be almost the same in property as the C_D. The Strouhal number is also thought to be related to the drag force. Indeed, the Strouhal number is totally observed to be large for the highly achieved drag reduction case. Of particular interest is, however, that the strong drag reduction, $C_D\lessapprox1.5$, occurs even for $20\mathrm{St}\le4.0$, namely, $\mathrm{St}\le0.2$ (for example, look at the results of $c_1/a=0.10$ and $c_2/a=0.10$ for $b/a=4/6$ or $b/a=6/6$ in Fig. 3). As mentioned in Sec. 1, Okajima et al. [7] and Igarashi et al. [6] found that the Strouhal number jumps from between 0.14 and 0.20 to between 0.23 and 0.25 at around Re_c, and the separated shear layer changes from laminar to turbulent flow due to the cutout beyond Re_c. Furthermore, Igarashi et al. [6] insisted on that the drag reduction can be achieved for $\mathrm{Re}>\mathrm{Re}_c$, in which the separated shear layer is turbulent. However, the present results would imply a possibility of the drag reduction for a lower Reynolds number than Re_c unlike the findings of Igarashi et al. [6]. We will also discuss the possibility of the drag reduction for $\mathrm{Re}<\mathrm{Re}_c$ for nonzero values of the angle of attack in Sec. 3.3.

Figure 4 (top side) shows the contour map of the drag coefficient with respect to the cut-corner shape. Utilizing the contour map, one can easily determine the most effective shape of the cut-corner in the case of $b/a=6/6$, 4/6, and 2/6 in an engineering use. The thick dashed line indicates the value of $C_D^*=1.2$, which is the same as the drag coefficient of the circular cylinder at the same Reynolds number ($\mathrm{Re}\approx50,000$). We can see that the effective drag reduction region, in which the drag coefficient is less than C_D^*, becomes wide with the increase in b/a. The flow visualization for the corresponding rectangular cylinders to Fig. 4 will be presented in the associated article [11]. It seems that the most appropriate cut-corner shape is almost independent of the length-to-breadth ratio within $2/6\le b/a\le6/6$. Figure 4 (bottom side)

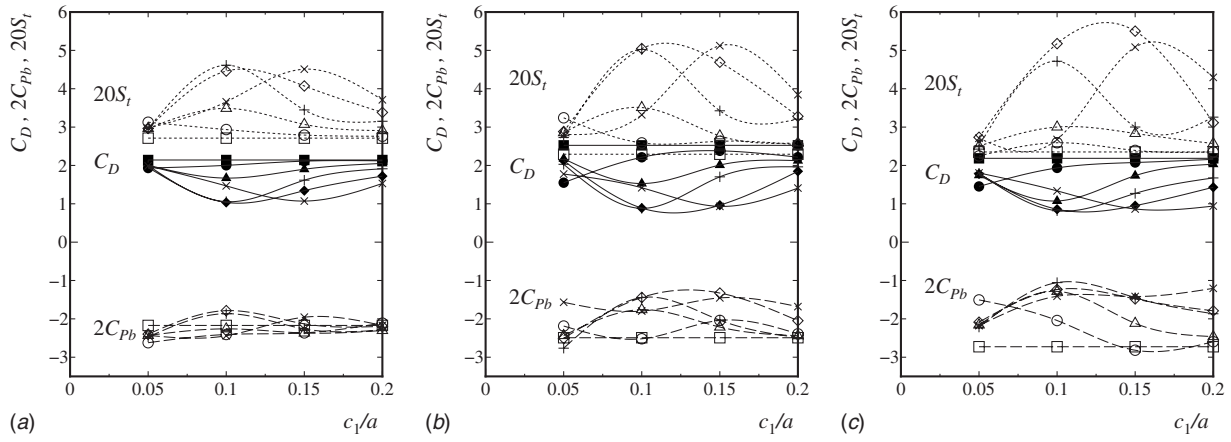

Fig. 3 Hydrodynamic coefficients: (solid line) C_D, (dashed line) C_{Pb}, and (dotted line) St versus c_1/a for (left) $b/a=2/6$, for (center) $b/a=4/6$, and for (right) $b/a=6/6$. (Square) $c_2/a=0.0$, (circle) $c_2/a=0.05$, (triangle) $c_2/a=0.1$, (plus) $c_2/a=0.15$, (rhombus) $c_2/a=0.2$, and (cross) $c_2/a=0.25$

shows the contour map of the base pressure coefficient. The thick dashed line also indicates the value of $C_{Pb}^{*}=1.2$, which is the same as the base pressure coefficient of the circular cylinder at the same Reynolds number ($\mathrm{Re}\approx 50,000$).

3.3 Effect of Length-to-Breadth Ratio for Nonzero Values of Angle of Attack. Figure 5 shows the drag and lift coefficients with respect to the angle of attack, α, for the rectangular cylinder with the cut-corners of $c_1/a=0.10$ and $c_2/a=0.15$. The drag coefficient is observed to be almost constant with respect to α within about $\alpha=5$ deg or a little less than 5 deg. The lift coefficient is, in contrast, observed to increase with the increase in α up to about 4 deg and after about 4 deg to exponentially decrease up to about 7 deg. After $\alpha=7$ deg, the C_L profile exhibits different properties for each b/a; (i) when $b/a=2/6$, C_L gradually decreases; (ii) when $b/a=4/6$, C_L is almost constant; and (iii) when $b/a=6/6$, C_L gradually increases.

Figure 6 shows the hydrodynamic coefficients, C_D, C_L, C_{Pb}, and St, of the rectangular cylinder with the cut-corners of $c_1/a=0.10$ and $c_2/a=0.15$ against the angle of attack, α, between ± 25 deg. It seems that C_D, C_{Pb}, and St are symmetric with respect to α although C_L is antisymmetric. In addition, the effective drag reduction is found to be achieved in a range $|\alpha| \lessapprox 5$ deg in all cases of b/a.

Figure 7 shows the contour map of C_D with respect to c_2/a and α for three cases of the length-to-breadth ratio, $b/a=2/6$, 4/6, and 6/6. In addition, c_1/a is fixed at 0.1. The thick dotted line indicates the values of $C_D \approx 1.0$, 1.5, and 2.0, respectively. With respect to a set of parameters c_2/a and α, the effective drag reduction region, in which the value of C_D exhibits $C_D < 1.5$, is observed to be wide within almost $\alpha=5$ deg, and the effective drag reduction is achieved in $0.15 \lessapprox c_2/a \lessapprox 0.20$.

Figure 8 shows the relation between the drag coefficient, C_D, and the Strouhal number, St, in three cases of the length-to-breadth ratio, $b/a=2/6$, 4/6, and 6/6 and two cases of the cut-corner shape, $c_1/a=c_2/a=0.00$ and $c_1/a=0.10$, and $c_2/a=0.15$. The values of C_D and St were measured for the angle of attack being in the range $-25 \leq \alpha \leq +25$ deg. We can observe that there are some conditions in which the drag coefficient becomes less

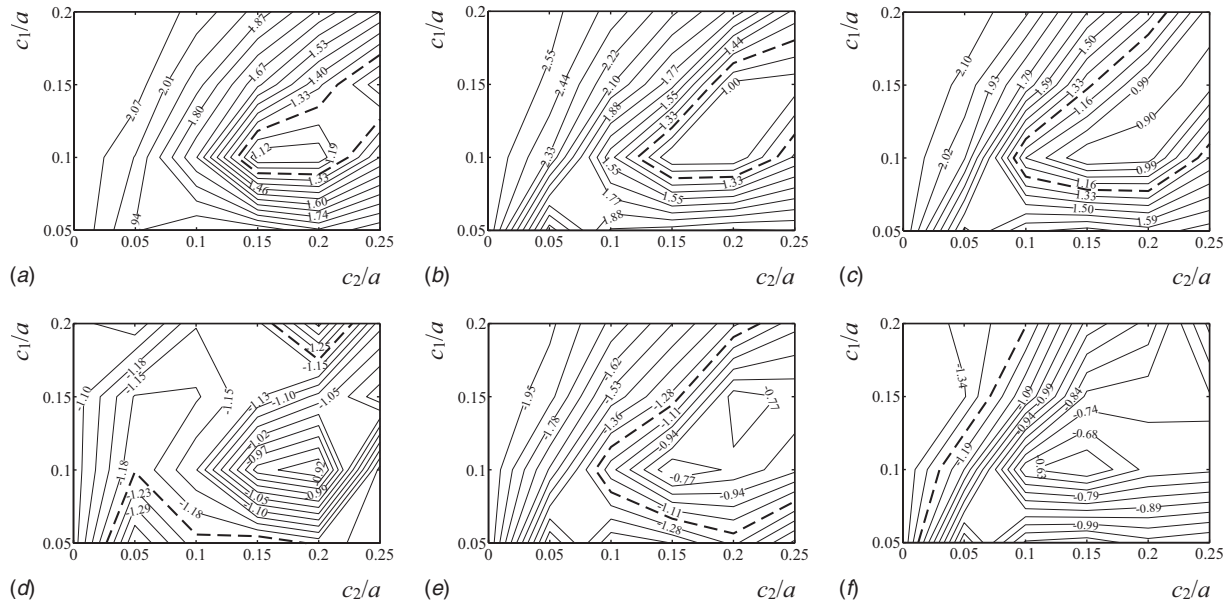

Fig. 4 Contour map of (top) C_D and (bottom) C_{Pb} with respect to cutout dimension. (Left) $b/a=2/6$, (center) $b/a=4/6$, and (right) $b/a=6/6$

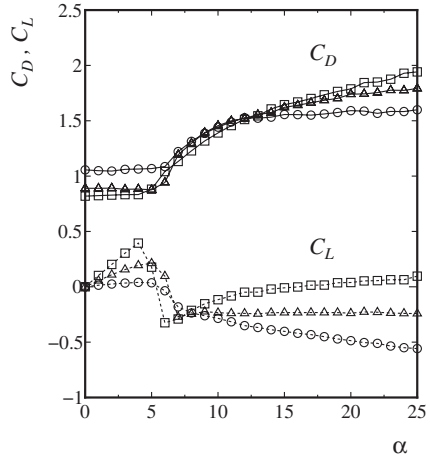

Fig. 5 Drag and lift coefficients, C_D and C_L, of a rectangular cylinder with cut-corners of $c_1=0.10$ and $c_2=0.15$ against the angle of attack of α degree. (Circle) $b/a=2/6$, (triangle) $b/a=4/6$, and (square) $b/a=6/6$.

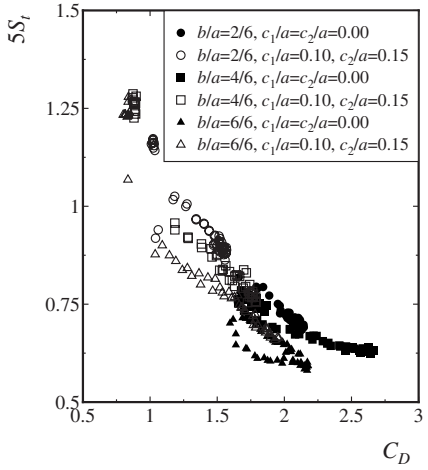

Fig. 8 Strouhal number, St, versus drag coefficient, C_D, for various values of the length-to-breadth ratio, b/a

than 1.5 for $St<0.2$. As mentioned in Sec. 3.2, the previous work of Igarashi et al. [6] insisted on that the drag reduction can be achieved under a turbulent separated shear layer (not a laminar separated one) beyond the critical Reynolds number, $Re>Re_c \approx 8,000$, in which the Strouhal number jumps from between 0.14 and 0.16 to 0.25. However, the present results imply that the remarkable drag reduction occurs even for the separated *laminar* shear layer if we would select an appropriate shape of the cut-corner.

4 Conclusions

Drag reduction of a rectangular cylinder with cut-corners has been investigated using a wind tunnel experiment. The length-to-breadth ratio, b/a, has been varied in 11 kinds from 2/6 to 6/6 (square prism). The primary results for a detailed contour map of the hydrodynamic coefficients with respect to the cut-corner dimension or the angle of attack has been given for three kinds of $b/a=2/6$, 4/6, and 6/6. Other main findings are summarized as follows.

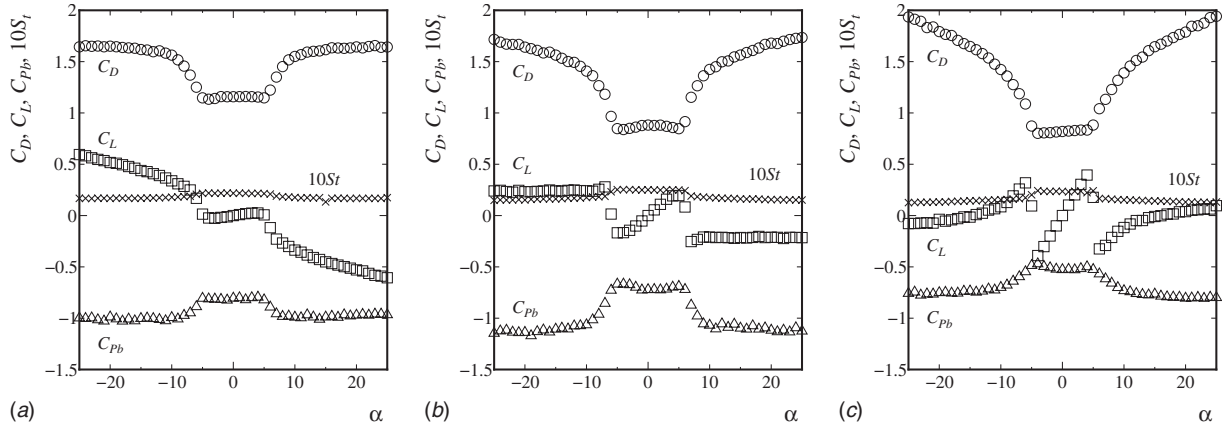

Fig. 6 Hydrodynamic coefficients against the angle of attack of α degree in the case of $c_1/a=0.10$ and $c_2/a=0.15$. (Left) $b/a=2/6$, (center) $b/a=4/6$, and (right) $b/a=6/6$

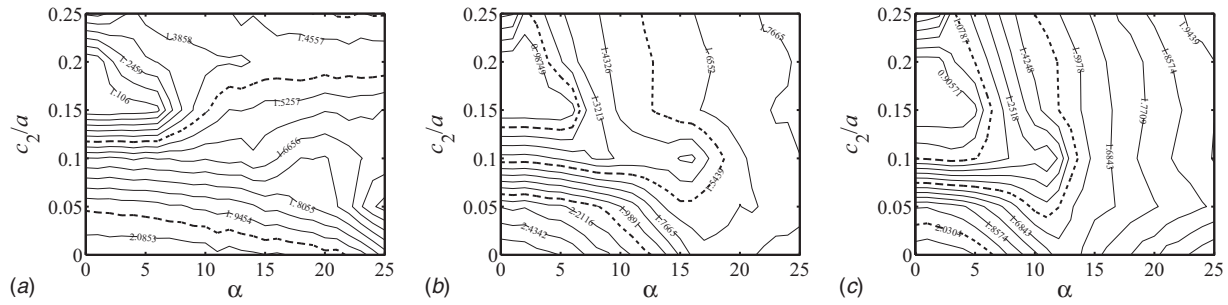

Fig. 7 Contour map of C_D with respect to the angle of attack of α degree and c_2/a in the case of $c_1/a=0.10$. (Left) $b/a=2/6$, (center) $b/a=4/6$, and (right) $b/a=6/6$

- The drag reduction was experimentally achieved even for the length-to-breadth ratio being less than unity at Re $=50,000$. Further attention should be paid to that a remarkable drag reduction occurs even in $St<0.2$.
- The detailed contour map of C_D for the zero angle of attack showed an existence of the appropriate dimension of the cut-corner at $Re=50,000$, and the effective cut-corner dimension was found to be almost independent of the length-to-breadth ratio.
- The contour map against the angle of attack, α, showed that the region of the effective drag reduction achieved is independent of α within α being almost 5 deg although being dependent on the length-to-breadth ratio. The region of the effective drag reduction is fairly wide with respect to the cut-corner shape.

References

[1] Tamura, T., Miyagi, T., and Kitagishi, T., 1998, "Numerical Prediction of Unsteady Pressures on a Square Cylinder With Various Corner Shapes," J. Wind. Eng. Ind. Aerodyn., **74–76**, pp. 531–542.

[2] Kurata, M., Morisawa, T., Hirakawa, K., Yasutomi, Z., and Kida, T., 1998, "Drag Reduction of a Bluff Body With Small Cutout at Its Edges (Case of Prism With Square Cross Section)," JSME Int. J., Ser. B, **64**(618), pp. 397–404.

[3] Kurata, M., Hirakawa, K., Yasutomi, Z., and Kida, T., 1999, "Effect of Cutout at Front Edges to Drag Reduction of Square Prism," Trans. Jpn. Soc. Aeronaut. Space Sci., **47**(543), pp. 174–181.

[4] Kurata, M., Hirakawa, K., Yasutomi, Z., and Kida, T., 1999, "Relationship Between Near Wake and Drag Reduction of Square Prism Due to Cutout at Front Edges," Trans. Jpn. Soc. Aeronaut. Space Sci., **47**(550), pp. 403–410.

[5] Kurata, M., Yamato, H., Yasutomi, Z., and Kida, T., 2002, "Effect of Cutout at Edges to Drag Reduction of Square Prism With Angle of Attack," JSME Int. J., Ser. B, **68**(668), pp. 1087–1094.

[6] Igarashi, T., Muranaka, N. and Nakamura, H., 2005, "Drag Reduction of a Rectangular Cylinder With Small Rectangular Cutout at Its Edges Normal to Air-Stream," Annual Conference of Japan Society of Fluid Mechanics, Paper No. AM05-04-016.

[7] Okajima, A., Ueno, H., and Abe, A., 1992, "Influence of Reynolds Number on Flow and Aerodynamics Characteristics of Bluff Bodies With Rectangular Section of Cut Corners," J. Wind. Eng. Ind. Aerodyn., **49**, pp. 1–13.

[8] Bearman, P. W., and Trueman, D. M., 1972, "An Investigation of the Flow Around Rectangular Cylinders," Aeronaut. Q., **23**, pp. 228–237.

[9] Igarashi, T., 1984, "Characteristics of the Flow Around Rectangular Cylinders (The Case of the Angle of Attack 0 deg)," Trans. Jpn. Soc. Mech. Eng., Ser. B, **50**(460), pp. 3185–3192.

[10] Nakaguchi, H., Hashimoto, K., and Muto, S., 1968, "An Experimental Study on Aerodynamic Drag of Rectangular Cylinders," Trans. Jpn. Soc. Aeronaut. Space Sci., **16**(168), pp. 1–5.

[11] Ueda, Y., Kurata, M., Kida, T., and Iguchi, M., 2008, "Visualization of Flow Past a Square Prism With Cut-Corners at the Front-Edge," J. Visualization, to be published.

Erratum: "Fiber Orientation Control Related to Papermaking" [ASME J. Fluids Eng., 2007, 129(4), pp. 457–465]

Allan Carlsson, Fredrik Lundell, and L. Daniel Söderberg

Three errors have been detected in a further analysis of the data.

- The first error is that the reported frame rate of the camera is incorrect. This means that the velocities of the fibers should be divided by two. Another consequence is that the wall normal distance from the wall y will be roughly (velocity gradient not constant) half of the previously reported values.
- The second error is that the computed theoretical concentration profile is incorrect.
- The third error is that the reported fiber diameter is incorrect.

These errors do not affect the two main results: (i) fibers near the smooth wall orient themselves perpendicular to the flow direction at the wall and (ii) near the structured wall fibers oriented perpendicular to the flow direction are absent. Nevertheless, the corrections affect Figs. 14–16 and Secs. 2.3, 2.4.3, 2.5, 4.1, 4.2.2, 4.2.3, and 5.

Section 2.3 Fiber Suspension:

- The fiber diameter, given in the second sentence of the second paragraph, should be changed to $d \approx 70$ μm.

Section 2.4.3 Particle Tracking Velocimetry:

- The correct value of the frame rate is $f=5.13$ Hz ± 0.05 Hz.

Section 2.5 Velocity Profile of Fibers:

- The fiber diameter in line number nine of the section should be changed to $d \approx 70$ μm.

Section 4.1 Jeffery Orbits Close to the Wall:

- In the first sentence of the section "… *one fiber length away from the wall*…" should be changed to "… *half a fiber length away from the wall*…."

Section 4.2.2 Wall-Normal Concentration Distribution:

- Due to the incorrect computation of the theoretical concentration profile (corrected in Fig. 14) the discussion on this, as well as the comparisons between the theoretical and experimental profiles, is faulty. Thus, ten lines of text should be disregarded. This is the text, in the first paragraph in the second column, that reads "*The assumptions above… becomes steeper and steeper.*"
- The second paragraph in the second column should be changed to "*The experimental data from the flow over the smooth surface in Fig. 14 (solid) show a high concentration close to the wall (i.e., a lot of slow fibers), followed by a decrease and then an increase up to* $nl^3 \approx 0.5$ at $y/l \approx 0.6$. Above $y/l \approx 0.6$, the number of fibers found in the images decreases."
- The first sentence in the third paragraph in the second column should be changed to "*For the flow over the structured surface, the concentration profile in Fig. 14 looks different and does not have the sharp peak close to the wall.*" In the second sentence of the same paragraph "*These differences have to be…*" should be replaced with "*This difference has to be….*"

Section 4.2.3 Orientations at Various Distances From the Wall:

- The last sentence of the second paragraph on page 464 (lines 21–22 in the column) "… $y/l=0.2-1$…" should be changed to "… $y/l=0.2-0.5$…."
- The second last sentence of the third paragraph on page 464 should be replaced with "*For* $y/l > 0.5$, most of the fibers are oriented in the flow direction, in the region $0.2 < y/l < 0.5$ the distribution is more homogeneous."

Section 5 Conclusions:

- In the second paragraph "… *less than about a quarter of a fiber length…*" should be replaced with "… *less than about an eighth of a fiber length….*"

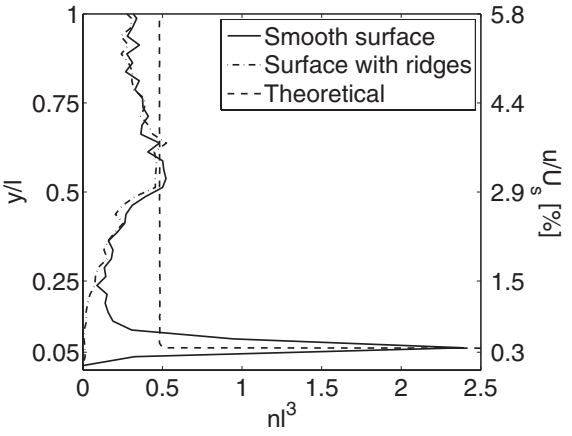

Fig. 14 Variations in concentration as a function of the distance from the wall (camera position P4)

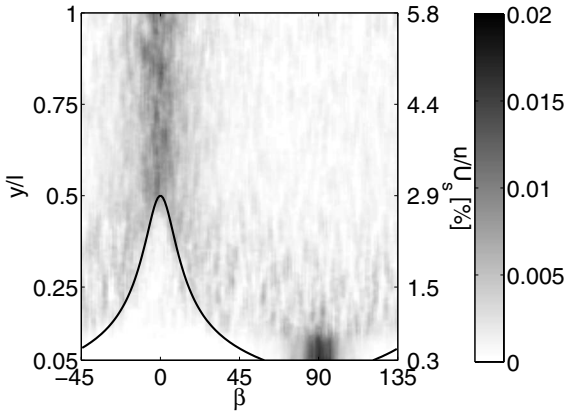

Fig. 15 Fiber fraction as a function of β for different distances from the wall. Measurements performed on smooth surface (camera position P4).

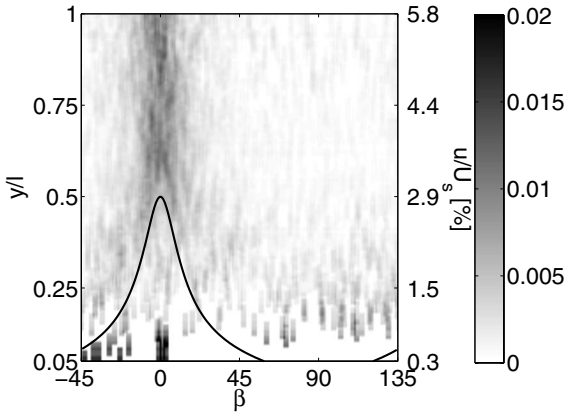

Fig. 16 Fiber fraction as a function of β for different distances from the wall. Measurements performed on surface with ridges (camera position P4).